

Université
de Liège



FACULTE DES SCIENCES

Laboratoire de Physique Atmosphérique et Planétaire (LPAP)

**A 3D model of ocean biogeochemical cycles and
ocean ventilation studies**



Année académique
2010-2011

Dissertation présentée par
Anne MOUCHET
en vue de l'obtention du grade de
Docteur en Sciences

Université
de Liège



FACULTE DES SCIENCES

Laboratoire de Physique Atmosphérique et Planétaire (LPAP)

**A 3D model of ocean biogeochemical cycles and
ocean ventilation studies**

Année académique
2010-2011

Dissertation présentée par
Anne MOUCHET
en vue de l'obtention du grade de
Docteur en Sciences

Cover photo: Sea smoke blankets the water in the Atlantic Ocean.
Picture taken by a sailor of the U.S. Navy. Copyright © public domain.

Remerciements

Au moment d'écrire ces quelques lignes et de terminer cette thèse, je prends conscience du temps écoulé depuis le jour où le projet de ce travail a germé et j'éprouve aujourd'hui un immense sentiment de gratitude.

Je pense particulièrement à toutes celles et ceux qui, au cours de ces années, ont été présents à mes côtés, m'ont soutenue, ont cru en moi et en la réalisation de ce travail.

Certains, tels ceux qui ont créé les bases sur lesquelles j'ai pu m'appuyer solidement, ont été mes mentors scientifiques. D'autres, ou parfois les mêmes, ont mis leurs connaissances, leurs compétences, leurs savoirs et leurs savoir-faire à ma disposition. Conseillers infatigables autant que critiques inflexibles, ils ont su me soutenir dans les périodes de doute et d'incertitude traversées au cours de la réalisation de cette recherche.

Beaucoup ont tout simplement été là, attentionnés et attentifs. Me soulageant de problèmes techniques, administratifs ou d'intendance, ils ont su donner avec générosité leur plus grande richesse : une partie d'eux-mêmes. Ils ont été les essentiels soutiens, toujours présents aux moments les plus difficiles.

Je ne citerai aucun nom, tant la liste serait longue et tant est grande ma crainte d'oublier l'une ou l'autre personne pourtant irremplaçable. Chacun se reconnaîtra dans ces remerciements et que tous sachent combien, par delà leur contribution à la réalisation de ce texte, ils resteront chers à mon cœur.

Je terminerai par un hommage reconnaissant à ceux qui, malheureusement, n'ont pas vécu assez longtemps pour voir l'aboutissement de ce travail.

Anne Mouchet

Quand nul ne la regarde
La mer n'est plus la mer
Elle est ce que nous sommes
Lorsque nul ne nous voit.

Elle a d'autres poissons,
D'autres vagues aussi.
C'est la mer pour la mer
Et pour ceux qui en rêvent
Comme je fais ici.

J. Supervielle

Abstract

The pace at which ocean surface waters are renewed, or the ocean ventilation, determines the long-term response to climate changes caused by human activity. The analysis and prediction of that response can only be done with numerical modelling tools.

In the first part of this work we examine the dominant mechanisms by which three-dimensional ocean general circulation models (OGCM) reproduce the ocean ventilation. For this purpose we develop a simplified tool that reduces the complexity of the problem and summarizes the characteristics of the circulation produced by an OGCM in a few parameters. An excellent agreement is observed between the water age responses predicted by this tool and two OGCMs. Our results suggest that low Peclet numbers are associated with the large scale circulation in OGCMs. A further study confirms that diffusion processes play a significant role in the ventilation modes of OGCM.

The second part of the work focuses on the ocean carbon cycle. We developed an ocean carbon cycle model and coupled it to an Earth system model of intermediate complexity. We examine the performance of the ocean carbon cycle model and its sensitivity to different parameterizations of biological processes.

In a final case study we analyze how two ocean models reproduce the removal of the excess radiocarbon from the atmosphere that was produced by nuclear weapons testing mainly between 1950 and 1960. The bomb radiocarbon inventories predicted by the two ocean models differ significantly from the estimates based upon data gathered during global ocean surveys. Our study has identified two causes for this disagreement. On one hand, the method used to determine the amount of radiocarbon absorbed by the ocean from the observational data leads to an underestimate; on the other hand, the diffusion that is intrinsic to numerical models leads to an overestimate of this quantity.

Our results confirm the role that ocean dynamics, as it is produced by OGCMs, plays in shaping the response of models of biogeochemical cycles. The latter, as well, have their own limitations, due to their simplified representation of natural processes. It is, however, difficult to clearly identify the causes of their failures, which seem to be, at least partially, linked to weaknesses in the physical models.

Résumé

L'allure à laquelle les eaux océaniques de surface se renouvellent, ou, en d'autres termes, la ventilation océanique, détermine la réponse climatique à long terme aux modifications engendrées par l'activité humaine. L'analyse et la prévision de cette réponse ne peuvent se faire qu'à l'aide d'outils de modélisation numérique.

Dans la première partie de ce travail nous examinons les mécanismes dominant la manière dont des modèles tri-dimensionnels de la circulation océanique (OGCM) reproduisent la ventilation océanique. A cette fin nous développons des outils simplifiés. Ceux-ci permettent de réduire la complexité du problème et de résumer à l'aide de quelques grandeurs physiques les caractéristiques de la circulation telle que prédite par un OGCM. L'analyse révèle que les processus de diffusion jouent un rôle non négligeable dans les modes de ventilation des OGCMs.

La deuxième partie du travail est consacrée au cycle du carbone. Un modèle du cycle océanique du carbone est développé et couplé à un modèle de complexité intermédiaire du système climatique terrestre. Nous examinons la sensibilité de la réponse du modèle de carbone océanique à différentes paramétrisations des processus biologiques.

Dans un dernier cas d'étude nous analysons comment deux modèles océaniques reproduisent l'absorption de l'excès de radiocarbone atmosphérique provoqué par les essais nucléaires effectués durant les années 1950–1960. Ces modèles prédisent des quantités de radiocarbone absorbées par l'océan qui diffèrent significativement des estimations établies sur base de campagnes de mesures en mer. Notre étude indique que deux causes seraient à l'origine de cet écart. D'une part, la méthode utilisée pour établir la quantité de radiocarbone absorbée par les océans à partir des observations conduirait à une sous-évaluation de celle-ci. D'autre part, la diffusion intrinsèque aux modèles numériques entrainerait une sur-évaluation de cette quantité.

Les résultats de ce travail confirment le rôle déterminant joué par la dynamique océanique, telle que reproduite dans les OGCMs, dans la réponse des modèles de cycles biogéochimiques. Ces derniers, représentant de manière simplifiée les processus naturels, sont également limités dans leurs performances. Il est cependant difficile d'identifier avec certitude les causes de leurs défaillances puisqu'une

partie de ces dernières semble pouvoir être attribuée aux faiblesses des modèles physiques.

Contents

Remerciements	iii
Abstract	vii
Résumé	ix
1 Context	1
2 Assessing ocean ventilation	11
2.1 Diagnosing ocean ventilation: age tracers	12
2.1.1 Constituent-oriented Age and Residence time Theory . . .	12
2.1.2 Timescales of use in ventilation studies and their relationship	16
2.2 A simple analog – the leaky funnel model	18
2.2.1 The leaky funnel model, a metaphor of the ventilation of the World Ocean as simulated in an OGCM	20
2.2.2 The leaky funnel revisited	20
2.2.3 On the role of numerical diffusivity and its assessment . .	59
2.2.4 Conclusion	65
2.3 Age bias and mixing in OGCMs	68
2.3.1 A 1-D upwelling diffusion model	68
2.3.2 Experiments with 3-D ocean models	72
2.3.3 Age biases analysis of the 3-D OGCM results	74
2.3.4 Conclusion	78
2.3.A Semi-infinite domain	81
2.3.B Analytical solutions	83
3 Modelling the Ocean Carbon Cycle	85
3.1 Overview of the ocean carbon cycle	85
3.1.1 Control on atmospheric CO ₂ levels	87
3.1.2 Atmospheric adjustment time	89
3.2 Modelling the ocean carbon cycle	91
3.2.1 Speciation	91

3.2.2	Organic carbon pump	94
3.2.3	Shells	95
3.2.4	3-D equations	97
3.2.5	Boundary conditions	99
3.2.6	Atmosphere	100
3.3	LOCH performances	100
3.3.1	Export production	101
3.3.2	Air-sea pCO ₂ difference	102
3.4	Sensitivity studies	108
3.4.1	Si dissolution profiles	108
3.4.2	Particulate organic matter flux	110
3.4.3	Mouchet & Francois (1996)	111
4	Modern times and carbon isotopes	119
4.1	Bomb radiocarbon	119
4.1.1	Methods	123
4.1.2	Results	129
4.1.3	Discussion and conclusions	136
4.2	Modelling carbon isotopes	143
4.2.1	Sources and sinks terms due to biological activity	143
4.2.2	Sensitivity to fractionation during photosynthesis	145
5	Conclusions	149
A	Model descriptions	153
A.1	Main features of the OGCMs used in this study	153
A.1.1	UL-OM	153
A.1.2	LSG-OM	154
A.2	LOVECLIM	154
	Bibliography	187

Chapter 1

Context

“Tiens
Se dit le lac Saint-Sébastien
Ils s’improvisent magiciens
Ils déracinent et ils bétonnent
Ils font le vide et ils s’étonnent
Que les saisons aillent de travers
Et que s’étende le désert.”

A. Sylvestre

In the second part of the 20th century concern has been growing about climate change and its consequences which might endanger water resources, human health, genotype preservation, and many other factors (*Schmitz, 1992*). There is growing evidence that the current way of living of a fraction of the world population is causing planetary wide modifications of the natural environment (*Hegerl et al., 2007; Peters and Hertwich, 2008*).

In order to be able to evaluate the magnitude of the potential changes and mitigate them a more complete understanding of the climate system is necessary. Assessing the amplitude and pace of the response to perturbations, anthropogenic or natural, by the climate system components is essential in this context.

Complex and intricate processes relate the world ocean and atmospheric CO₂, two of the key components of the Earth’s climate system.

Throughout Earth history climate has been varying on all timescales. Geological, faunal and isotopic records show that a succession of cold to warm climatic transitions occurred frequently in the past (*Jansen et al., 2007*). Natural climate variability is concomitant with atmospheric CO₂ level changes (*Bradley, 1999*). Deep-sea sediments (*Shackleton and Pisias, 1985*) and the Vostok ice core (*Petit et al., 1999*) records provide the best evidence for the link between climate transitions and atmospheric CO₂ levels. Abrupt climate transitions are also related to ocean circulation changes (*Rahmstorf, 2002*). A reduction of deep water

formation in the North Atlantic, consecutive to massive freshwater discharge, is associated with low temperatures in the northern hemisphere (*Boyle and Keigwin, 1987; Alley, 2000; Maslin et al., 2001; McManus et al., 2004*). These regional phenomena have, by means of several teleconnections, worldwide impacts (*Mikolajewicz et al., 1997; Broecker, 1998; Maslin et al., 2001; Jouzel et al., 2007; Okazaki et al., 2010*).

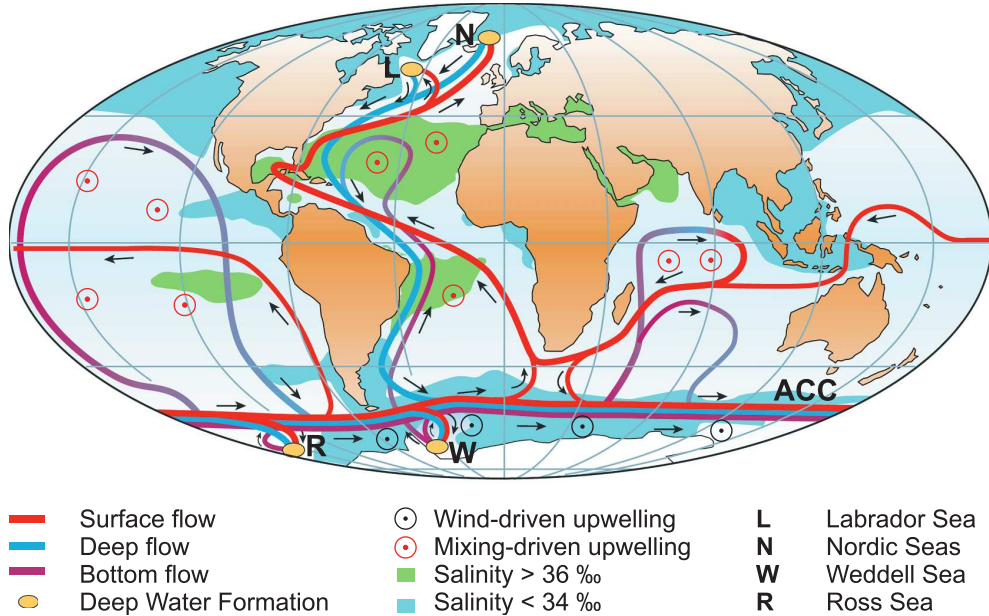


Figure 1.1: Schematic representation of the global overturning circulation. Deep water formation areas are localized in the North Atlantic (L, N) and around Antarctica (R, W). Blue, purple, and red lines depict the deep, bottom and surface flows, respectively. Deep waters are brought back to the surface by mixing or wind-driven processes. Figure 1 from *Kuhlbrodt et al. (2007)*.

Ocean's role in climate

The oceans store heat and regulate its transport on the Earth surface (*Bengtsson, 1997*). Oceans absorb more radiation than would be expected from their relative coverage of the Earth surface. Indeed the net gain for the oceans is about 77% of the total of energy absorbed at the surface, making the oceans the Earth's principal reservoir of thermal energy and moisture (*Bradley, 1999*). Several reasons explain why the oceans take up such an important fraction of incoming radiation. First, seawater has a much lower albedo than land surface, second, the transparency of water lets the radiation penetrate to greater depth

than it would in soils, and third, the turbulent mixing in the upper ocean layer is much more efficient in distributing heat than thermal conductivity (*Frakes, 1979; Niiler, 1992*). The high heat capacity of the oceans allows them to store heat and to redistribute it on timescales of years to centuries. Most of the energy gained by the ocean is used in the evaporation processes evidencing their role in the planetary water cycle and radiative balance (*Bengtsson, 1997*). Further they control atmospheric CO₂ levels on time scales ranging from decades to millenia (*Siegenthaler, 1986; Archer et al., 2000; Jansen et al., 2007*).

Transport in the ocean is accomplished through the wind-driven surface circulation and the thermohaline overturning, the latter resulting from vertical density imbalance created by evaporation, cooling by cold winds, or sea ice formation. Both wind-driven and thermohaline circulations play an equivalent role in the global heat transport (*Talley, 1999*). In the context of our study we will mainly focus on the circulation of deep ocean water masses, hence on the second type of flow. However the two types of circulation are interrelated and it is impossible to dissociate them. In fact, winds provide some of the mixing energy needed to sustain the flow based on thermohaline processes (*Munk and Wunsch, 1998; Kuhlbrodt et al., 2007*). We will then refer to the flow at the largest scale as the global overturning circulation, or the global ocean circulation, indifferently. This flow pattern is depicted in Figure 1.1. It is characterized by very localized areas of deep water formation but widespread distribution of the return flow to the surface.

Global carbon cycle

Greenhouse gases are naturally present in the Earth atmosphere. Without their radiative effect the global mean Earth surface¹ temperature would be about 33°C lower (*Berger and Tricot, 1992*). CO₂ is the second most important greenhouse gas after water vapor; under clear sky conditions it contributes 26% of the radiative forcing (*Kiehl and Trenberth, 1997*).

Carbon, in organic and inorganic forms, is ubiquitous on Earth. Processes controlling the atmospheric CO₂ may be split into two categories on the basis of their respective characteristic timescales (*Berner, 1998*). A first biogeochemical cycle consisting in the exchange of carbon between the superficial reservoirs (the atmosphere, the ocean, the terrestrial biosphere and soils) controls CO₂ on timescales of thousands of years. On longer timescales (multimillion years) the transfer of carbon between rocks and the superficial reservoirs imposes its pace. In the second group the erosion of Ca and Mg silicate and carbonate minerals and the burial of organic matter in marine sediments provide sinks for atmospheric CO₂; while metamorphism, diagenesis, and weathering of ancient organic matter represent sources of atmospheric CO₂. Figure 1.2 illustrates the fastest of

¹i. e., at ground or sea level.

these two cycles with values relevant for the end of the 20th century. Among the reservoirs that rapidly exchange carbon with the atmosphere, the ocean is the largest. The oceans' inventory being 50 to 60 times that of the atmosphere, small changes in their content may significantly affect atmospheric CO₂.

From the fluxes provided in Figure 1.2, we may derive a turnover time (i.e., the inventory divided by the gross flux into or out of the reservoir (*Bolin and Rodhe, 1973*) of slightly more than 3 years for CO₂ in the pre-industrial atmosphere. This *turnover time* must not be confused with the *adjustment time* of atmospheric CO₂ to a perturbation. The latter reflects the equilibration time with both the continental biosphere and the upper ocean. The effective adjustment time for the atmospheric CO₂ is much longer. It is actually set by the rate at which deep ocean water masses replace those in contact with the atmosphere (*Broecker and Peng, 1982; Siegenthaler, 1986*). This rate explains the slow response predicted for the next centuries (Figure 1.3).

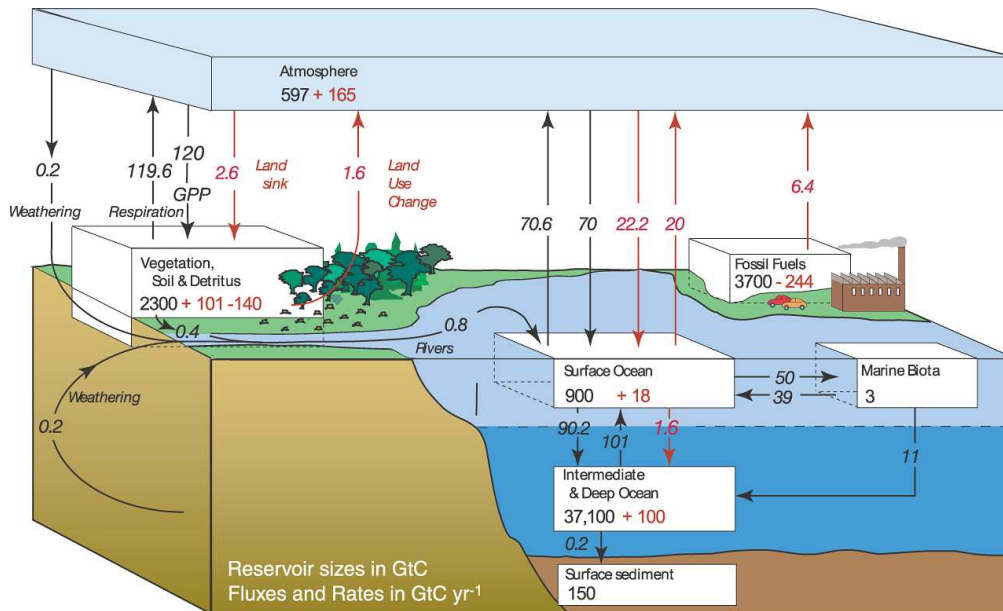


Figure 1.2: The global carbon cycle in the mid 1990s. Units are gigatons of carbon (GtC) in reservoirs and GtC yr⁻¹ for fluxes. Pre-industrial quantities are in black. The anthropogenic modification of these reservoirs and fluxes is given in red. Figure 7.3 from *Denman et al. (2007)*.

It should be kept in mind that Figure 1.2 provides only a frozen representation of the global carbon cycle. The carbon cycle is actually highly dynamic and exhibits significant variability on multiple timescales, from seasons to millenia.

Figure 1.2 also illustrates how the industrial revolution, by accelerating the

erosion of ancient organic matter, has raised the human impact on the environment to the level of geological forcings (*Houghton et al.*, 1996).

During the 1990s the anthropogenic emissions (fossil fuel + cement) amounted to 6.4 ± 0.4 GtC/yr. Over the same period the net fluxes to the ocean and to the land were equal to 2.2 ± 0.4 GtC/yr and 1.0 ± 0.6 GtC/yr, respectively, and the atmospheric reservoir increased on average by 3.2 ± 0.1 GtC/yr (*Denman et al.*, 2007). Hence during that decade the ocean absorbed about 34% of the perturbation, while 50% remained in the atmosphere.

Addressing the global and ocean carbon cycles

Several tools may be of use in the framework of global (or ocean) carbon cycle studies. However, their realms differ significantly. Field measurements though providing more and more information about the present-day carbon cycle, are more limited when information about the historical period or the more distant past is needed.

Numerical models (forward, inverse,...) allow to apprehend at once the spatial and temporal complexities inherent to natural phenomena. They may also complement other methods such as those based on proxy reconstructions or on field data, by making up for uncomplete data coverage. They may also allow the assessment of past climate changes as reconstructed with paleo-proxies. Forward modelling is the only way by which we may address future climate changes.

However, no tool is perfect. The different numerical models currently available often display a wide range of results when addressing the very same problem. The two following themes and the currently available results illustrate this topic.

Future atmospheric levels

Several Earth system models of intermediate complexity (EMIC) with active carbon cycle have been used for climate predictions over the next millenium (Figure 1.3). These models fully account for carbon-climate feedbacks in future projections. The model forcing was provided by a scenario where it is assumed that CO₂ emissions continue to increase until the year 2100 and that they cease afterwards (see top left panel). For the active CO₂ emission phase, all models predict an increase in the fraction of total emissions that remains in the atmosphere (third row, right-hand panel) together with a decline in the fraction absorbed by the ocean (lower right panel). The decrease of the buffer capacity is responsible for this decrease in the ocean uptake rate (*Maier-Reimer et al.*, 1995; *Friedlingstein et al.*, 2006; *Plattner et al.*, 2008). Once emissions cease, atmospheric CO₂ concentrations decline (upper right panel). The relative role of the continental biosphere decreases in response to diminishing atmospheric CO₂

concentrations, while the ocean uptake fraction becomes larger. Some fraction of the anthropogenic perturbation will nevertheless remain airborne in these model experiments since neutralization by reaction with carbonates and igneous rock is not considered. On time scales of the order of centuries to millenia it is the ocean ventilation rate that determines the adjustment time of the atmospheric perturbation. The characteristic time scales for the atmosphere and the ocean (upper right and bottom left panels, respectively) are, however, model-dependent.

Natural and anthropogenic CO₂ in the ocean

The oceans are currently an important sink for anthropogenic CO₂. As a result of this perturbation, the present-day marine chemistry has already been modified since pre-industrial times. A test of the ability of models at reproducing the role of the ocean in the carbon cycle at the climate time scale is provided by the exercise of separating the anthropogenic perturbation from the natural cycle.

Model- and field-based reconstructions differ significantly with respect to the magnitude of CO₂ fluxes in the Southern Ocean (Figure 1.4; *Gruber et al.*, 2009). Models furthermore differ widely in the predicted global carbon anthropogenic uptake (*Orr et al.*, 2001; *Matsumoto et al.*, 2004). Most of the differences seem also to be attributable to model differences in the Southern Ocean fluxes (*Orr et al.*, 2001). *Orr et al.* (2001) and *Doney et al.* (2004) invoke differences in mixing and advection schemes as the cause for such differences among models.

Failure in reproducing the contemporary air-sea CO₂ fluxes unfortunately lowers the confidence level in projections of future climate changes.

Another question that still remains elusive relates to the mechanisms that drive the large glacial to interglacial atmospheric CO₂ change of about 100 ppm (*Archer et al.*, 2000; *Kohfeld et al.*, 2005; *Jansen et al.*, 2007). An inadequate representation of the ocean mixing which results in a lack of model sensitivity could be one reason why models do not succeed at reproducing this past transition (*Archer et al.*, 2000).

Contents

This work focuses largely on the study of ocean ventilation as reproduced by Ocean General Circulation Models (OGCMs) and Ocean Carbon Cycle Models (OCCMs). Both artificial or real ocean tracers are of help for this purpose. A full ocean carbon cycle was developed and used to address both ventilation problems and climate studies. Climate studies we contributed to with this model are presented elsewhere (*Menviel et al.*, 2008a; *Plattner et al.*, 2008; *Okazaki et al.*, 2010; *Menviel et al.*, 2011a). Here we focus on the aspects related to the ocean ventilation.

The present manuscript is structured as follows. Chapter 2 is devoted to ocean ventilation as reproduced by OGCMs. It is shown how idealized tools may be of help in extracting the most relevant information from the complex three-dimensional circulation. The ocean carbon cycle and its modelling are the main topic of Chapter 3 which contains a description of LOCH, the ocean carbon cycle model we developed. Sensitivity studies of the marine carbon cycle and performance of LOCH are shortly addressed. The issue of ocean ventilation is again put forward in Chapter 4 which focuses on carbon isotopes and the bomb radiocarbon uptake by the ocean. We will close this thesis with general conclusions and present some perspectives for future work in Chapter 5.

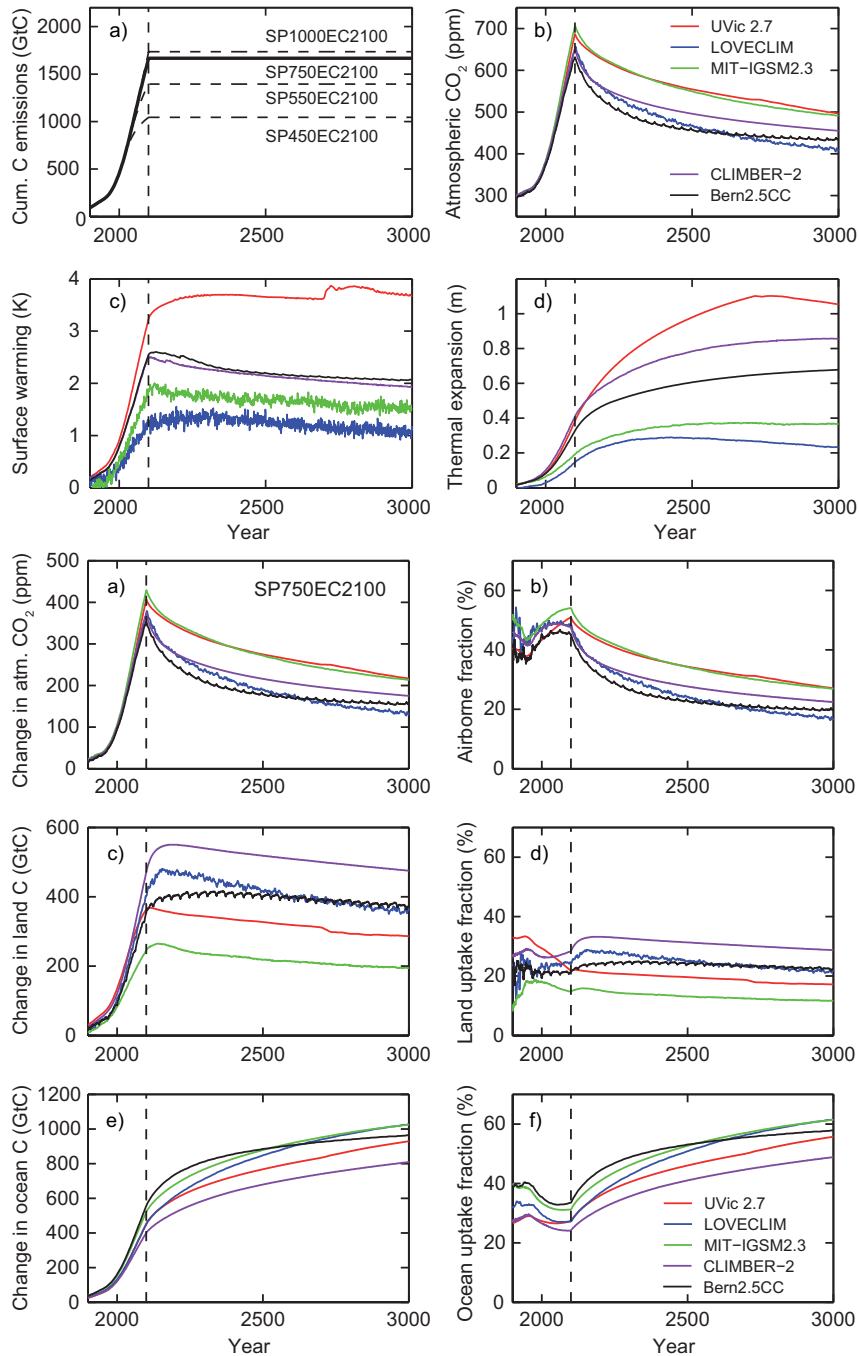


Figure 1.3: Projections over the third millennium obtained with five EMICs. The top four panels illustrate the evolution of cumulated emissions (top left), prognostic atmospheric CO₂ (top right), surface temperature increase and ocean thermal expansion (row 2, left and right, resp.). The lower six panels present results for the three carbon reservoirs, the ocean, the continental biosphere, and the atmosphere, from bottom to top, respectively. The left row contains the inventory changes, and the right row the evolution of the relative fraction of the emissions taken up by the corresponding reservoir. This figure is based upon Figures 5 and 6 from *Plattner et al. (2008)*.

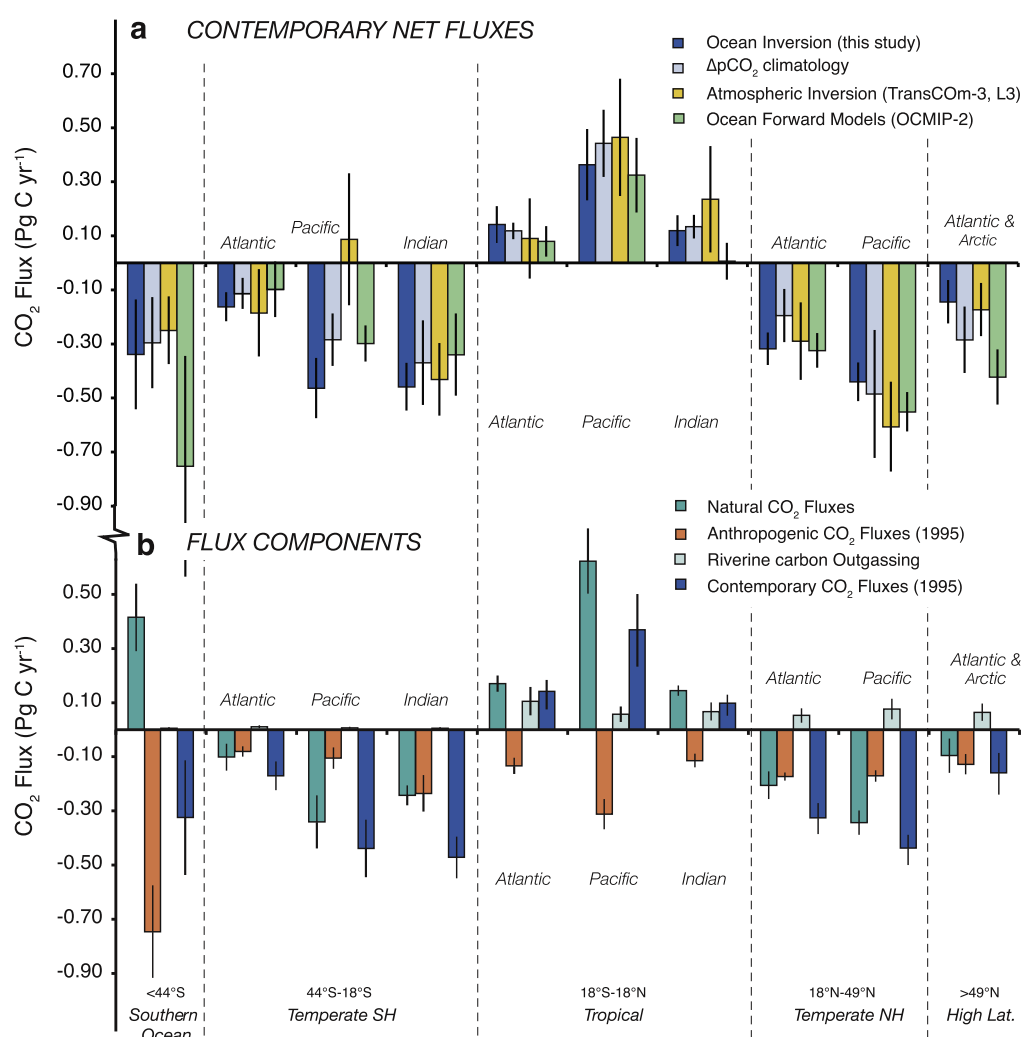


Figure 1.4: **a** Net air to sea CO₂ fluxes partitioned between ocean regions (Southern Ocean, Southern Hemisphere temperate, Tropical, Northern Hemisphere temperate, and High Latitudes). In the three temperate and tropical latitude bands the fluxes are further distributed among oceans (Atlantic, Pacific, Indian). Data-based estimates correspond to the yellow bars, forward model studies to the green bars. In **b** the fluxes estimated with the ocean inverse method in **a** (blue) are further decomposed into natural (green), anthropogenic (pink), and riverine (light blue) contributions. In both panels positive values correspond to fluxes toward the atmosphere. Figure 1 from Gruber *et al.* (2009).

Chapter 2

Assessing ocean ventilation

... mais comment mesurer
L'âge de l'eau? L'âge de l'arbre
Se compte aux anneaux qui entourent
L'aubier, mais le coeur d'un liquide
Est dans sa transparence, c'est le
Reffet qu'on y projette qui
Vieillit,...

J. Darras

The global ocean circulation exerts a strong control on atmospheric CO₂ levels as well as on Earth's surface temperature. Ocean carbon uptake constitutes the rate limiting process for eliminating the anthropogenic atmospheric CO₂ perturbation; the characteristic timescale being of the order of several centuries (*Broecker and Peng, 1974; Siegenthaler, 1986; Maier-Reimer and Hasselmann, 1987; Maier-Reimer et al., 1995; Plattner et al., 2008*). A weakening of the Atlantic Meridional Overturning Circulation (AMOC) is usually associated with Northern Hemisphere cooling (*Boyle and Keigwin, 1987; Mikolajewicz et al., 1997*). Furthermore, surface warming in CO₂ doubling model experiments appears to be related to the efficiency of ocean heat uptake (*Raper et al., 2002; Schmittner et al., 2009*).

The rate at which the ocean can sequester excess heat and carbon from the atmosphere is determined by its ventilation. Ocean ventilation is defined as the renewal of interior waters by seawater that has been in contact with the atmosphere (*England, 1995; Broecker et al., 1999; England and Maier-Reimer, 2001*). This renewal which results in the downward mixing of various properties occurs via several vertical transport mechanisms: subduction, convection, advection or mixing.

In this chapter we address tools and methods aimed at a better understanding of ocean ventilation. We introduce relevant concepts in section 2.1. Section 2.2

describes a 1-D model representation of the global ocean, which may suggest an appropriate scaling of the water age or ocean ventilation. That section is divided into four parts. Section 2.2.1 presents at length this simplified tool, further developments are given in section 2.2.2, followed by section 2.2.3 which shows how this 1-D model may be of use for 3-D OGCMs evaluation and conclusions in section 2.2.4. Eventually in Section 2.3 we analyze age biases with the help of another simple 1-D model. By providing information at basin-scales, it allows to get further understanding of the ocean interior circulation as reproduced in OGCMs.

2.1 Diagnosing ocean ventilation: age tracers

According to *England* (1995) the “World Ocean circulation at its largest scale can be thought of as a gradual renewal or ventilation of the deep ocean by water that was once at the sea surface”. A measure of the ventilation rate is therefore given by the time elapsed since a water mass or a seawater constituent left the surface mixed layer. This time is defined as the *age* of the water mass or seawater constituent. Water in contact with the atmosphere (i.e. residing in the mixed layer) is considered to have an age equal to zero (*England and Maier-Reimer*, 2001).

With such a definition of the age advantage can be taken of any constituent whose sole source is the atmosphere in order to assess ventilation timescales from field measurements. While the use of radiocarbon dates back several decades (e.g., *Kulp et al.*, 1952; *Craig*, 1957), the use of age tracers (radioactive or not) is still in full expansion. ^3H to ^3He ratio, CFCs ratio, and others are at the basis of techniques for inferring water mass ventilation times and deriving quantities such as anthropogenic carbon ocean uptake or oxygen utilization rates (*Jenkins and Goldman*, 1985; *Jenkins*, 1987; *Karstensen and Tomczak*, 1998; *Thomas and Ittekkot*, 2001).

In modelling studies a popular tool is the “ventilation age tracer” or water age (*Stommel and Arons*, 1960a,b; *Thiele and Sarmiento*, 1990; *Takeoka*, 1991; *England*, 1995; *Deleersnijder et al.*, 2001; *Hall and Haine*, 2002) This tool, which has no natural equivalent, provides an accurate measure of the ventilation rate. Indeed, as will be discussed shortly later on, age estimates based on chemical tracers in modeling or field studies suffer from several errors and limitations.

2.1.1 Constituent-oriented Age and Residence time Theory

The ages definitions used in the present work are those established under the Constituent-oriented Age and Residence time Theory (CART; *Delhez et al.*, 1999;

Deleersnijder et al., 2001, 2002; *Delhez et al.*, 2003). CART is based on mass budget considerations and yields the equations, in flux form, governing the evolution of the concentration and the age concentration from which the mean age of the constituent under study is derived. The complete mathematical developments as well as a description of CART may be found in the above mentioned references. We present here the basic concept of CART together with some properties of the various age concepts and their application to ocean ventilation studies.

Seawater is a mixture of several constituents, i.e. water, dissolved salts, plankton, etc. Let us consider that every constituent is concentrated in pointwise particles. CART then relies on the following assumption (*Deleersnijder et al.*, 2001):

The mean age of a particle ensemble is the mass-weighted, arithmetic average of the ages of the particles considered; this is valid for particles of the same constituents or for particles of different constituents.

In order to establish the age equations we need to consider the concentration distribution function $c_k(t, \mathbf{x}, \tau)$ which for a tracer k describes the distribution of the concentration of this tracer in the age space (*Delhez et al.*, 1999; *Deleersnijder et al.*, 2001). That is $c_k(t, \mathbf{x}, \tau)d\tau$ measures the contribution of the material with an age between τ and $\tau + d\tau$ to the total concentration¹ $C_k(t, \mathbf{x})$ of the tracer k at time t and position \mathbf{x} :

$$C_k(t, \mathbf{x}) = \int_0^\infty c_k(t, \mathbf{x}, \tau)d\tau. \quad (2.1)$$

In accordance with the definition of the distribution function, the mean age of the tracer is

$$a_k(t, \mathbf{x}) = \frac{1}{C_k(t, \mathbf{x})} \int_0^\infty \tau c_k(t, \mathbf{x}, \tau)d\tau. \quad (2.2)$$

This last expression leads to the concept of the age concentration

$$\alpha_k(t, \mathbf{x}) = C_k(t, \mathbf{x}) a_k(t, \mathbf{x}) = \int_0^\infty \tau c_k(t, \mathbf{x}, \tau)d\tau. \quad (2.3)$$

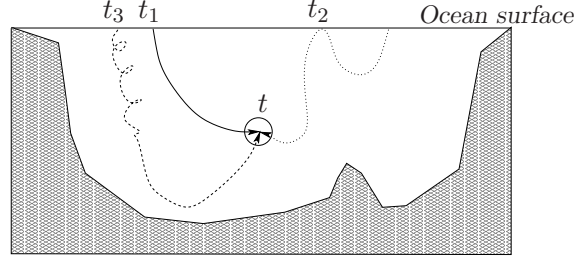
The age concentration α_k represents the relative contribution of the k -th constituent to the total age content of a sample containing different constituents. A simple case presented on page 14 helps to more easily grasp the concepts of age averaging and age concentration in the context of ocean ventilation.

CART allows to establish the governing equations for α_k in a fully coherent way with that governing C_k . The prognostic equations for C_k and α_k are of the

¹ C_k represents a mass fraction, i.e. the ratio of the total mass of the constituent in the sample to the total mass of the sample.

Box 1 Age averaging and age concentration concepts

Let us consider a fluid parcel containing \mathcal{N} particles of several constituents sampled at time t at an arbitrary location in the ocean (such a situation is illustrated in the figure below with $\mathcal{N} = 3$).



The particles followed different trajectories since they last touched the ocean surface at time t_i ($i = 1 \dots \mathcal{N}$). With a_i the individual age of the i -th particle ($a_i = t - t_i$) and m_i its mass, the total age content of the fluid parcel under consideration is

$$A_T = \sum_{i=1}^{\mathcal{N}} m_i a_i.$$

Suppose now that the number of different constituents in that seawater sample is \mathcal{M} with n_k the number of particles of the same constituent, each constituent being identified with the subscript k ($k = 1 \dots \mathcal{M}$).

The number of particles of each constituent n_k must satisfy $\sum_{k=1}^{\mathcal{M}} n_k = \mathcal{N}$, and the

$$\text{mean age associated to the } k\text{-th constituent is } a_k = \frac{\sum_{j=1}^{n_k} m_j a_j}{\sum_{j=1}^{n_k} m_j}.$$

It is readily seen that A_T may also be written as $A_T = \sum_{k=1}^{\mathcal{M}} m_k a_k$, in which m_k is

$$\text{the total mass of the } k\text{-th constituent, } m_k = \sum_{j=1}^{n_k} m_j.$$

If ΔV represents the volume of the water parcel and ρ is a reference density for seawater this expression may be transformed into

$$A_T \simeq \rho \Delta V \sum_{k=1}^{\mathcal{M}} C_k a_k, \quad (2.4)$$

where C_k is the dimensionless mass fraction $C_k = m_k / (\rho \Delta V)$. The definition of the age concentration to be associated to the k -th constituent naturally stems from (2.4): $\alpha_k = C_k a_k$.

Hence α_k the age concentration of constituent k represents the relative contribution of the k -th constituent to the total age content A_T of the seawater sample under consideration.

same form (and hence contain the same physics) as those used for scalars in the model (Chapter 3, Eq. (3.16); *Deleersnijder et al.*, 2001):

$$\frac{\partial C_k}{\partial t} = -\nabla \bullet (\mathbf{u}C_k - \mathbf{K} \bullet \nabla C_k) + \mathcal{P}_k, \quad (2.5)$$

$$\frac{\partial \alpha_k}{\partial t} = -\nabla \bullet (\mathbf{u}\alpha_k - \mathbf{K} \bullet \nabla \alpha_k) + \Pi_k + C_k. \quad (2.6)$$

The last term on the right hand side of (2.6) constitutes a source for α_k and is associated with the ageing of the constituent. The source (or sink) terms \mathcal{P}_k and Π_k are given by (*Deleersnijder et al.*, 2001):

$$\mathcal{P}_k(t, \mathbf{x}) = \int_0^\infty p_k(t, \mathbf{x}, \tau) d\tau \quad \text{and} \quad \Pi_k(t, \mathbf{x}) = \int_0^\infty \tau p_k(t, \mathbf{x}, \tau) d\tau, \quad (2.7)$$

where p_k is the rate of production or destruction of the fraction of constituent k with age τ . These equations apply to any tracer in the marine environment, even those subject to complex production and destruction processes.

Whenever the source and sink terms in (2.7) may be represented by simple expressions, the computation of the age of any tracer is straightforward. Indeed it is then sufficient to include in the model the pair of equations (2.5) and (2.6) with the appropriate source/sink terms and boundary conditions. Since we deal with ocean ventilation, we define the age of a such a particle as the time elapsed since it last touched the ocean surface. This is taken care of through the surface boundary condition term.

In the following we restrict our study to tracers which are either passive or subject to radioactive decay exclusively. Let C_λ and α_λ denote the concentration and age concentration of a constituent with radioactive decay rate λ (s^{-1}) or half-life equal to $\ln 2/\lambda$. Since elements of all ages have exactly the same probability to decay, equations (2.5) and (2.6) for this tracer become

$$\frac{\partial C_\lambda}{\partial t} = -\nabla \bullet (\mathbf{u}C_\lambda - \mathbf{K} \bullet \nabla C_\lambda) - \lambda C_\lambda, \quad (2.8)$$

$$\frac{\partial \alpha_\lambda}{\partial t} = -\nabla \bullet (\mathbf{u}\alpha_\lambda - \mathbf{K} \bullet \nabla \alpha_\lambda) - \lambda \alpha_\lambda + C_\lambda. \quad (2.9)$$

The radioactive tracer age a_λ is computed from the ratio of α_λ to C_λ . The age of a conservative tracer is simply obtained by setting $\lambda = 0$ in the above equations.

It must be stressed that CART makes a clear distinction between the age of a water mass and the ages of the tracers carried by this water. Seawater is a mixture of several constituents, i.e. water, dissolved salts, plankton, etc. Under the influence of mixing and diffusion naturally occurring in the ocean, a seawater parcel is likely to contain particles of constituents having different ages, even when no chemical or physical degradation occurs. Diffusive flow are indeed not

characterized by a single time scale but rather by an age spectrum (e.g. *Khatiwala et al.*, 2001; *Hall et al.*, 2002; *Delhez et al.*, 2003).

Several studies imply that water may be treated as a conservative tracer (*Delhez et al.*, 1999; *Deleersnijder et al.*, 2001, 2002). Since the concentration of water $C_w(t, \mathbf{x})$ is unity, it is readily obtained that the age of the water $a_w(t, \mathbf{x})$ satisfies

$$\frac{\partial a_w}{\partial t} = 1 - \nabla \bullet (\mathbf{u}a_w - \mathbf{K} \bullet \nabla a_w) \quad (2.10)$$

It has been shown (*Deleersnijder et al.*, 2001, 2002) that at steady state, and under appropriate boundary conditions, a_w is equivalent to the ventilation timescale or the ventilation age tracer used as diagnostic of OGCMs (e.g. *Thiele and Sarmiento*, 1990; *Takeoka*, 1991; *England*, 1995).

The classical radioage \tilde{a}_λ is simply obtained from

$$\tilde{a}_\lambda(t, \mathbf{x}) = \frac{1}{\lambda} \ln \frac{C_0(t, \mathbf{x})}{C_\lambda(t, \mathbf{x})} \quad (2.11)$$

where C_0 is the concentration of the associated conservative tracer.

We address radioages, more specifically radiocarbon-derived ages, in the context of ocean ventilation studies in section 4.1. In the rest of this section we review some properties of the age tracers and point to some limitations in their use.

2.1.2 Timescales of use in ventilation studies and their relationship

Several limitations occur when wishing to obtain ventilation rate estimates from field studies. First, the water age, having no natural equivalent, is not a measurable quantity. It may only be obtained by indirect methods (radioages, tracer ratio, oxygen utilisation, water budget...). As presented further in the text those indirect methods suffer from systematic biases. Second, data sparsity and scarcity still constitute today strong limitations in the use of field measurements for ventilation studies. This is why ventilation estimates are more than often based on budget considerations.

A time constant commonly used to characterize a reservoir is the *turnover time*² \mathcal{T}_o . This time is given by the ratio between the inventory of a material in a reservoir Q and the total flux \mathcal{F} out of it (*Bolin and Rodhe*, 1973):

$$\mathcal{T}_o = \frac{Q}{\mathcal{F}}.$$

²This timescale is sometimes named the *flushing* time or the *renewal* time.

The turnover time is an useful concept since in many cases it may provide a first order estimate of the *response* time, i.e., the time needed for adjustment following a sudden change (Rodhe, 1992).

Let us consider two other timescales characterizing a reservoir. The *average transit time*³ \mathcal{T}_t represents the average time spent by particles in the reservoir and $\langle a \rangle$ is the average age of particles within the reservoir.

While it has been demonstrated (Bolin and Rodhe, 1973) that at steady state $\mathcal{T}_t = \mathcal{T}_o$, there is no simple relationship between $\langle a \rangle$ and \mathcal{T}_t (or \mathcal{T}_o) even in equilibrium situations. Considerations based on the age and transit time distribution functions (Bolin and Rodhe, 1973) nevertheless allow to distinguish among three situations.

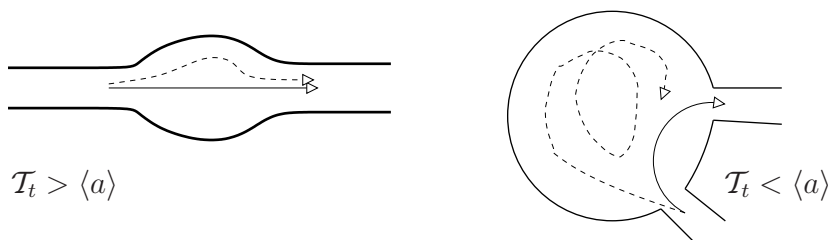


Figure 2.1: The global mean age $\langle a \rangle$ is smaller than the transit time \mathcal{T}_t for the estuary-like case (left). The opposite relationship is obtained when considering a bay or a lagoon (right). After Takeoka (1991).

When the inlet and outlet of a reservoir are close to each other (Fig. 2.1) younger particles more easily escape the domain, hence $\langle a \rangle > \mathcal{T}_t = \mathcal{T}_o$. On the other hand $\langle a \rangle < \mathcal{T}_t = \mathcal{T}_o$ when the removal process mostly affects older particles such in a river or, as will be shown further in this chapter, in the global ocean. In a well-mixed reservoir, or in the presence of a first order removal process ($\mathcal{F} = -\kappa\mathcal{Q}$, with κ constant), all particles have the same probability of being removed. In such situations $\langle a \rangle = \mathcal{T}_t = \mathcal{T}_o$.

It is clear from the preceding discussion that \mathcal{T}_o does not necessarily provide an accurate measure of the ventilation timescale. However, for reasons exposed earlier, in oceanographic field studies, estimates of deep ocean ventilation rates are sometimes based on turnover time (e.g., Broecker *et al.*, 1999). The only available alternative is the use of tracers, radioactive or not, whose dominant source is located in the atmosphere.

The main problem with the age derived from natural tracers is the bias toward smaller values than the actual water age or ventilation time (Stuiver *et al.*, 1983;

³This timescale is sometimes referred to as the *residence* time. This naming however contradicts the definition of the *residence* time which is the time required to leave the domain (Takeoka, 1984).

Jenkins, 1987; Karstensen and Tomczak, 1998; Deleersnijder et al., 2001; Khatiwala et al., 2001; Delhez et al., 2003). The reason for such a behavior stems from mixing processes as is easily understood by examining the transport equation for the mean age of a radioactive tracer which is obtained by combining (2.8) and (2.9):

$$\frac{\partial a_\lambda}{\partial t} = 1 - \nabla \cdot (\mathbf{u} a_\lambda - \mathbf{K} \cdot \nabla a_\lambda) + \frac{2}{C_\lambda} \nabla a_\lambda \cdot \mathbf{K} \cdot \nabla C_\lambda. \quad (2.12)$$

The right-hand side of this equation contains an additional term when compared to that for seawater, Eq. (2.10). The role of this term may intuitively be understood from the following consideration. As the distance from the source increases, the concentration of the decaying tracer decreases while the age increases. \mathbf{K} being positive, this additional term is negative and constitutes hence a sink for a_λ (*Jenkins, 1987; Khatiwala et al., 2001*). This has the effect of biasing the age deduced from radioactive tracers towards younger values (a similar result holds for \tilde{a}_λ ; *Jenkins (1987)*). This bias increases with increasing mixing or with increasing decay rate.

From considerations involving the Green function it can rigorously be shown (*Deleersnijder et al., 2001; Delhez et al., 2003*) that the following relationship holds for any λ

$$a_\lambda(\mathbf{x}, t) \leq \tilde{a}_\lambda(\mathbf{x}, t) \leq a_w(\mathbf{x}, t),$$

under the condition that similar boundary conditions apply to the radioactive tracer and the conservative tracer or water. As illustrated in Figure 2.2 both the radioage and the radioactive tracer mean age tend to the mean age of the conservative tracer for $\lambda \rightarrow 0$ while decreasing asymptotically toward zero for increasing values of λ (*Delhez et al., 2003*).

It follows that while radiocarbon may provide an accurate estimate of the ocean ventilation rate, tracers with larger decay rate (e.g. ^3H) or non-linear atmospheric time history (e.g. CFCs) underestimate it. This bias does not solely affect evaluation of processes on long time scales but also on the decadal to centennial time scales in the upper ocean. An example is provided by the overestimate of anthropogenic carbon in relatively young waters as computed with the δC^* method (*Hall et al., 2004; Matsumoto and Gruber, 2005*). An additional difficulty arises from the heterogeneity and the non-stationarity of air-sea fluxes; a reduced rate of tracer uptake at the surface results in an apparent ageing of water (e.g., *Adkins and Boyle, 1997; Campin et al., 1999*).

2.2 A simple analog – the leaky funnel model

In order to study ocean ventilation rate and its properties one may take advantage of numerical simulations and field measurements of appropriate tracer

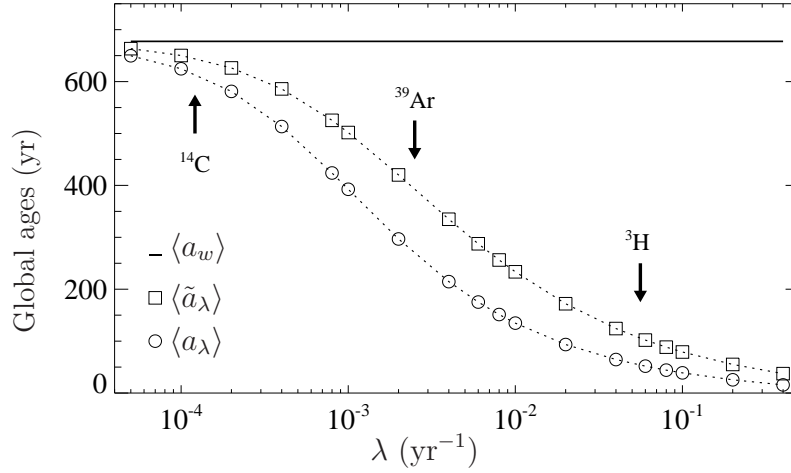


Figure 2.2: Domain averaged mean ages as function of the radioactive decay rate λ which is presented on a logarithmic scale. The solid line corresponds to the water age a_w , squares and circles to the radioage \tilde{a}_λ and radioactive tracer age a_λ , respectively. The arrows help identify ^{14}C , ^{39}Ar and ^3H . Results obtained with the UL-OM model, version LC (Appendix A). Modified from *Delhez et al.* (2003)

concentrations. However the intrinsic complexity of water masses circulation and the huge amount of information provided by OGCMs make it difficult to extract the most relevant information on spatial and temporal scales characterising ventilation.

In *Mouchet and Deleersnijder* (2008), Section 2.2.1, we show that an idealised model may suggest an appropriate scaling of the water age. A 1-D advection-diffusion model is proposed in which the deep ocean is represented as a leaky pipe with decreasing section (i.e. a leaky funnel) - allowing recirculation of water and tracers toward the surface. The analytical solutions to the steady-state problem are readily obtained and yield expressions of the domain averaged-ages as functions of three independent numbers which determine the flow characteristic scales. A suite of experiences with a 3-D OGCM allow us to calibrate and validate the leaky funnel representation. The agreement between the domain-averaged ages (water and radiocarbon) as obtained with the OGCM and with the leaky funnel is excellent. Furthermore, the parameters derived from this exercise have a clear physical meaning; the turnover time, the length scale of trajectories, and the diffusivity scale being consistent with our current knowledge of the World Ocean circulation.

The reasons for the excellent agreement between the 1-D representation and the 3-D OGCM remained rather elusive. Additional developments based on the

age distribution function now offer the opportunity to revisit the leaky funnel model and reach a better understanding of the process leading to such an agreement (*Mouchet et al.*, 2011). These new developments provide a supplementary and fully consistent validation of the leaky funnel representation. Eventually the age distribution suggests some interpretation of the deep ocean ventilation properties which could explain the excellent correspondence between 3-D and 1-D domain-averaged ages. This is the subject of Section 2.2.2.

This simple analog has a potential for applications in modelling studies. It may help in evaluating the relative importance, at the largest scales of motion, of advection and diffusion in 3-D models. It also offers the opportunity to get an estimate of the numerical diffusivity even in the case of complex numerical schemes. These matters are addressed in Section 2.2.3 which ends with a brief discussion of the strengths and limitations of this simple representation of the deep global ocean.

2.2.1 The leaky funnel model, a metaphor of the ventilation of the World Ocean as simulated in an OGCM

This work published as *Mouchet and Deleersnijder* (2008), hereafter referred to as **MD08**, is included in pages 21 to 34.

2.2.2 The leaky funnel revisited

This work submitted as *Mouchet et al.* (2011), hereafter referred to as **MA11**, is included in pages 35 to 57.

The leaky funnel model, a metaphor of the ventilation of the World Ocean as simulated in an OGCM

By ANNE MOUCHET^{1*} and ERIC DELEERSNIJDER², ¹Université de Liège, Astrophysics, Geophysics and Oceanography Department, 17 Allée du Six-Août, 4000 Liège, Belgium; ²Université catholique de Louvain, Louvain School of Engineering, Centre for Systems Engineering and Applied Mechanics (CESAME), 4 Avenue Georges Lemaître, 1348 Louvain-la-Neuve, Belgium

(Manuscript received 11 January 2007; in final form 24 January 2008)

ABSTRACT

It is seen that an idealized model may suggest an appropriate scaling of the water age in the World Ocean, which is a measure of the ventilation rate. We use a 1-D advection–diffusion model in which the deep ocean is represented as a leaky funnel, allowing recirculation towards the surface. The analytical solutions to the steady-state problem are readily obtained. The three parameters of the leaky funnel model are estimated in such a way that the behaviour of the domain-averaged water age be as similar as possible to that derived from a 3-D model in a series of sensitivity runs. The agreement between both sets of mean ages is excellent, with a linear correlation coefficient very close to unity. A good agreement is also found for the age of radioactive tracers and the associated radioages. The parameters of the leaky funnel model have a clear physical meaning, that is, the order of magnitude of the horizontal velocity, the mean length of water parcel trajectories in the deep ocean, and a horizontal diffusivity scale. The values of all of them turn out to be consistent with our current knowledge of the World Ocean circulation.

1. Introduction

The large-scale ocean circulation exerts a strong control on the Earth climate: it plays a significant role in heat and water transport as well as in the exchange of greenhouse gases with the atmosphere. It is then of primary importance for Earth system studies to improve our understanding of the temporal and spatial scales of the global circulation and the renewal rate of ocean water masses.

The scales of interest can be derived either from field measurements of appropriate tracer concentrations or from ocean general circulation models (OGCMs) (e.g. England and Maier-Reimer, 2001). However, the intrinsic complexity of water masses circulation and the huge amount of information provided by OGCMs make it difficult to extract the most relevant information in a concise way. An illustration of the latter point is provided by model intercomparison studies: very often different behaviours are evidenced but in-depth explanations thereof are yet to be found (e.g. Broecker et al., 1999a; Archer et al., 2003; Dutay et al., 2004). Therefore there is a need for accompanying the necessary improvement and development of 3-D models with the build-up

of elementary tools and simple experiments. Ideally such tools should provide easily dealt with mathematical formulations in order to help clearly identify the main driving processes together with their relevant spatial and temporal timescales.

In this paper, we suggest such a tool which could help in summarizing or comparing complex 3-D OGCMs results. The intent underlying such a step is to understand processes rather than to simulate nature. This approach is in line with other simple formulations already successfully applied in ocean circulation studies (e.g. Maier-Reimer, 1993; Doney and Jenkins, 1994; Huang, 1999)

A widely used simplified tool consists in the 1-D advection–diffusion model. Analytical solutions are readily obtained from which characteristic scales may be derived. Using different assumptions (e.g. finite or infinite domain, negligible diffusion, etc.) this model may be applied to a range of situations.

Analyses of the ocean inventory of anthropogenic carbon (Gruber, 1998; Thomas and Ittekkot, 2001) or of the ventilation rate of the thermocline (Jenkins, 1998; Robbins et al., 2000) implicitly or explicitly rely on the assumption that mixing is negligible. This is equivalent to considering a purely advective transport in an infinite pipe (Hall et al., 2002). Maier-Reimer (1993) interpreted the distribution of ¹⁴C versus ³⁹Ar in his 3-D model with the help of analytical solutions to the purely advective and purely diffusive problems in a 1-D infinite pipe.

*Corresponding author.

e-mail: a.mouchet@ulg.ac.be

DOI: 10.1111/j.1600-0870.2008.00322.x

Munk (1966) inferred the deep ocean mixing rate from a vertical advection–diffusion balance model applied to a finite domain. When adjusted to density and radiocarbon data for the Pacific Ocean this model led to values of the vertical velocity and the diffusion coefficient of the order of 10^{-7} and $10^{-4} \text{ m}^2 \text{ s}^{-1}$, respectively. Munk and Wunsch (1998) applied a modified version of this model to the global ocean and obtained results agreeing well with the previous work of Munk (1966). Munk's model was also used to understand the relationship between the distributions of ^{39}Ar and ^{14}C in the deep ocean (Broecker and Peng, 2000) or to assess the oxygen consumption rate in the deep Pacific Ocean (Craig, 1971).

A leaky pipe model was applied to study the distribution of tracers in the tropical atmosphere (Neu and Plumb, 1999). This model differs from those cited above in that the wall of the pipe is permeable, allowing for lateral (cross-flow) diffusive exchange with adjacent air masses (Plumb, 1996; Neu and Plumb, 1999). A similar model is applied in the study of the propagation of tracers along a deep western boundary current (DWBC) (Doney and Jenkins, 1994; Waugh and Hall, 2005). In that case, the DWBC is modelled as a 1-D purely advective flow exchanging material with an interior region through lateral mixing.

Despite their wide use the various versions of the 1-D model suffer from serious limitations when applied to ocean ventilation. The 1-D pipe model with pure bulk advection is often used to derive ventilation times from tracer measurements but neglecting diffusion results in a significant bias affecting ventilation times (Hall et al., 2002; Delhez et al., 2003). Technical difficulties are also inherent to any formulation. In the infinite pipe configuration it is not always possible to obtain domain-averaged quantities. Analytical solutions for the general case of radioactive tracers in the model of Munk (1966) are difficult to handle. However, the main reason why these 1-D models are not fully adequate to study the large-scale ventilation of the ocean lies in their rudimentary representation of the return flow to the ocean surface. The infinite domain version does not account for that process while the finite domain version of Munk forces the water to follow a unique track.

Water mass formation is confined within restricted areas (Broecker, 1991; Broecker et al., 1998; Talley, 1999) but this may not be the case for the upwelling of abyssal water which balances the production of deep water at high latitudes. Stommel and Arons (1960) considered a spatially uniform vertical velocity. However, recent works (Polzin et al., 1997; Kunze et al., 2006; St. Laurent and Simmons, 2006) evidenced that vertical mixing in the deep is highly heterogeneous and that the actual abyssal circulation patterns are far more complex than described in Stommel and Arons (1960). Nevertheless, the general concept of a clear separation between very localized deep water formation and widely distributed return flow has remained unchallenged until now.

Here, we suggest a simple model which allows recirculation towards the surface to occur progressively. In this model the deep

ocean is represented as a leaky pipe with decreasing section, that is, a leaky funnel. Under the hypothesis of homogeneous properties across the pipe section the problem reduces to the solution of a 1-D advection–diffusion equation. With the definition of the age of a tracer as the time elapsed since it left the surface mixed layer, analytical solutions to the steady-state problem are readily obtained. Moreover domain-averaged quantities are easily derived. Though this model shares similarities with the leaky pipe of Neu and Plumb (1999), it is different in the underlying concept of a changing geometry which allow tracers to progressively leave the domain of interest.

This paper is organized as follows. After a brief review of age definitions and concepts (Section 2) we present the 1-D leaky funnel in Section 3 and derive the relevant analytical solutions. The domain-averaged ages are simple functions of two independent parameters related to the flow characteristic scales. Sensitivity studies are then performed with a 3-D OGCM. The domain-averaged ages of the water and of radioactive tracers are computed for various sets of velocities and diffusivities (Section 4). These ages are compared to those predicted by the leaky funnel in Section 5. The meaning of the characteristic scales is then discussed in Section 6.

2. Ages

All age definitions are based on the Constituent-oriented Age and Residence time Theory (CART) (<http://www.climate.be/CART> Delhez et al., 1999; Deleersnijder et al., 2001, 2002; Delhez et al., 2003). CART allows for a clear distinction to be made between the age of a water mass and the ages of the radioactive tracers carried by this water. Three different ages may hence be derived in modelling studies: the age of a radioactive tracer, the age of a conservative tracer or the water age, and eventually the classical radioage. For conservative or radioactive tracers, CART's ages are exactly equivalent to those obtained from Green's function-based approaches (e.g. Holzer and Hall, 2000; Haine and Hall, 2002), as suggested in Delhez et al. (2003).

2.1. Age of a radioactive tracer

Let $C_\lambda(t, \mathbf{x})$ denote the concentration at time t and position $\mathbf{x} = (x, y, z)$ of a radioactive tracer with decay rate λ or half-life equal to $\ln 2\lambda^{-1}$. Then $C_\lambda(t, \mathbf{x})$ obeys the following transport equation

$$\frac{\partial C_\lambda}{\partial t} = -\nabla \bullet (\mathbf{u}C_\lambda - \mathbf{K} \bullet \nabla C_\lambda) - \lambda C_\lambda, \quad (1)$$

with \mathbf{u} the velocity vector and \mathbf{K} the diffusivity tensor which is assumed to be symmetric and positive definite (Deleersnijder et al., 2001).

Delhez et al. (1999) define the age concentration α_λ associated to such a tracer as the product of the concentration $C_\lambda(t, \mathbf{x})$ and the age $a_\lambda(t, \mathbf{x})$ of the radioactive tracer:

$$\alpha_\lambda(t, \mathbf{x}) = C_\lambda(t, \mathbf{x}) a_\lambda(t, \mathbf{x}). \quad (2)$$

Delhez et al. (1999) and Deleersnijder et al. (2001) established that $\alpha_\lambda(t, \mathbf{x})$ satisfies the following equation

$$\frac{\partial \alpha_\lambda}{\partial t} = -\nabla \bullet (\mathbf{u}\alpha_\lambda - \mathbf{K} \bullet \nabla \alpha_\lambda) - \lambda \alpha_\lambda + C_\lambda. \quad (3)$$

The last term on the right-hand side of (3) constitutes a source for α_λ and is associated with the ageing of the constituent (Delhez et al., 1999). The contribution of this term is fully understood by considering the transport equation for $a_\lambda(t, \mathbf{x})$:

$$\frac{\partial a_\lambda}{\partial t} = -\nabla \bullet (\mathbf{u}a_\lambda - \mathbf{K} \bullet \nabla a_\lambda) + 2 \frac{\nabla a_\lambda \bullet \mathbf{K} \bullet \nabla C_\lambda}{C_\lambda} + 1. \quad (4)$$

The last term on the right-hand side of (4) corresponds to the source term in (3) and expresses the increase of age with time.

Due to the existence of non-linearities in the diffusive transport, eq. (4) differs greatly from eq. (1) and would call for a specific numerical scheme in order to solve it. On the other hand a similar numerical scheme may be used to solve (1) and (3). Therefore, the method adopted herein guarantees that subgrid-scale parametrizations in eqs (1) and (3) are consistent with each other (Delhez et al., 1999). Once the concentration and the age concentration are obtained, the age a_λ is computed from the ratio of α_λ to C_λ .

2.2. Water age

The age of the water is equivalent to the age of a conservative tracer (i.e. a tracer for which $\lambda = 0$) with appropriate boundary conditions (Delhez et al., 1999; Deleersnijder et al., 2001, 2002). With C_w and α_w the concentration and the age concentration of this conservative tracer, respectively, the associated age is then

$$a_w(t, \mathbf{x}) = \frac{\alpha_w(t, \mathbf{x})}{C_w(t, \mathbf{x})}. \quad (5)$$

C_w and α_w are, respectively obtained with the help of eqs (1) and (3) in which one imposes $\lambda = 0$.

Since we are to investigate ocean ventilation the source region is taken to be the ocean surface S . Therefore, the following boundary conditions apply on S

$$\alpha_w(t, \mathbf{x}) = 0 \quad \text{and} \quad C_w(t, \mathbf{x}) = 1 \quad \text{for} \quad \mathbf{x} \in S. \quad (6)$$

In this particular case the age concentration α_w and the concentration C_w represent those of the surface water as defined by Deleersnijder et al. (2002). It has been shown (Deleersnijder et al., 2001, 2002) that for steady-state (or $t \rightarrow \infty$) the associated age a_w tends towards the age of the water or the ventilation time, which represents the time it takes for a parcel of water to travel from the surface to the location \mathbf{x} . Conservative water mass tracers provide a diagnostic of the transport and have been extensively used in modelling studies (Thiele and Sarmiento, 1990; Takeoka, 1991; Haidvogel and Bryan, 1992; England, 1995; Hirst, 1999) in order to estimate oceanic ventilation timescales. As we deal with steady state the tracer age a_w is called the *water age* (this tracer is sometimes referred to as the *perfect age tracer*, Wunsch, 2002).

2.3. Radioage

The classical radioage τ_λ is evaluated from the ratio of the concentration of a conservative tracer C_0 to the concentration of a radioactive tracer with C_0 and C_λ subject to identical boundary conditions,

$$\tau_\lambda(t, \mathbf{x}) = \frac{1}{\lambda} \ln \frac{C_0(t, \mathbf{x})}{C_\lambda(t, \mathbf{x})}. \quad (7)$$

Tritium ages, for example, are obtained with the help of (7) from the distributions of ^3H and ^3He (Jenkins, 1987). In that case C_λ represents the concentration of ^3H and C_0 is the sum of ^3H and ^3He concentrations. Table 1 presents an overview of the different concepts presented in this section.

Table 1. Summary of the different variables intervening in the age computation. For each variable (column 1) a meaning or definition is given in column 2, together with the relevant equation from the main text (column 4). The third column suggests oceanographic examples when available

Variable	Meaning or definition	Oceanographic example	Equation in text
C_λ	Radioactive ^a tracer concentration	^3H , $^{14}\text{C}^b$	(1)
a_λ	Age of the radioactive tracer	–	(4)
α_λ	Age concentration, $\alpha_\lambda = C_\lambda a_\lambda$	–	(3)
C_0	Conservative tracer concentration	Na, $^3\text{H}+^3\text{He}$, $^{12}\text{C}^b$. . .	(1) with $\lambda = 0$
τ_λ	Radioage, $\tau_\lambda = \frac{1}{\lambda} \ln \frac{C_0}{C_\lambda}$	Radiocarbon age, Tritium age. . .	(7)
C_w	Water concentration	Water	(1) with $\lambda = 0$
α_w	Water age concentration, $\alpha_w = C_w a_w$	–	(3) with $\lambda = 0$
a_w	Water age	No oceanographic example, widely used in modelling studies (e.g. Thiele and Sarmiento, 1990; England, 1995; Deleersnijder et al., 2002)	(4)

^a $1/\lambda$ is the mean life of the radioactive tracer.

^bThe real carbon cycle is more complex than the processes considered in this study; but the concepts of CART also apply to the radiocarbon ages as derived from field studies.

CART formalism, which is adopted herein, is an easy way of evaluating the age of every constituent of seawater or group of constituents, including seawater itself. The ages of any number of tracers are easily computed from the outputs of a numerical model. For each tracer under consideration it is indeed sufficient to include in the model a pair of eqs (1)–(3) with the appropriate boundary conditions.

3. The leaky funnel model

The ocean has a fully 3-D and time-varying circulation whose complexity is hardly met by lower dimension and steady-state descriptions. However, low order representations may help to capture some essential features. According to H. Stommel (Stommel, 1958; Stommel and Arons, 1960) ‘the horizontal circulation in the actual ocean may be thought to be a consequence of localized sinking and generalized upwelling’ (Warren, 1981). Our model is based on this simple description.

The deep ocean is idealized as a pipe whose cross-sectional area decreases alongflow. The pipe has porous walls which allow water and tracers to irreversibly leave the domain. This loss of water or matter through leakage may be interpreted as a way of allowing recirculation towards the surface as in the real ocean. This leaky funnel is schematically depicted in Fig. 1. Subduction or entrainment of surface waters feed the leaky funnel at the opening; no water is allowed to enter the funnel at any other location.

Though sharing similarities with existing 1-D models characterized by porous walls (Doney and Jenkins, 1994; Plumb, 1996; Neu and Plumb, 1999; Waugh and Hall, 2005) our model differs from these in several aspects. None of these models considers an alongflow decrease of the cross-sectional area of the pipe; when lateral, cross-flow exchange of tracer with an external region is allowed, it is represented with the help of a mixing term. Doney and Jenkins (1994), Plumb (1996) as well as Waugh and Hall (2005) consider purely advective flow within their 1-D model.

In our model water and tracers escape the domain as they are transported downstream. Both advection and diffusion processes are considered as in Neu and Plumb (1999). As represented in Fig. 1, the cross-sectional area (or section) of the funnel $S(x)$ is a function of x , the downstream coordinate ($0 \leq x < \infty$). The entrainment out of the funnel takes the form of an advective flux. There is no diffusive flux of concentrations across the funnel wall, that is,

$$(\mathbf{K} \bullet \nabla C_\lambda) \bullet \mathbf{n} = 0 = (\mathbf{K} \bullet \nabla \alpha_\lambda) \bullet \mathbf{n}, \tag{8}$$

where \mathbf{n} is an outward unit vector normal to the external envelope of the funnel. We further assume that all variables and properties are homogeneously distributed over S , hence they solely depend on x and t . Integrating eqs (1) and (3) over $S(x)$ yields a 1-D problem.

Then, the concentration $C_\lambda(t, x)$ and the age concentration $\alpha_\lambda(t, x)$ of a radioactive tracer with decay rate λ satisfy the fol-

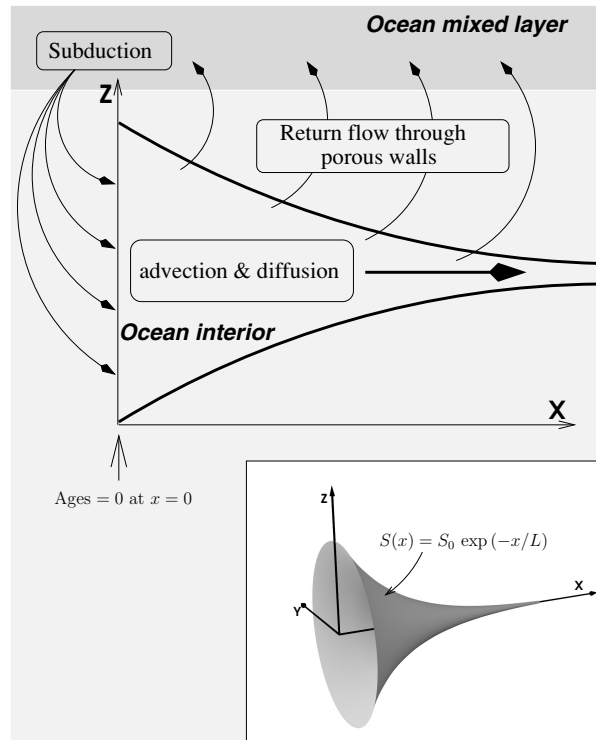


Fig. 1. Schematic representation of the leaky funnel model. A 3-D view is given in the inset while the main figure consists of a projection onto the x - z plane. The leaky funnel extends from $x = 0$ to $x = \infty$ with a decreasing section. The entrance of the funnel is fuelled with water subducted from the ocean surface. The porous walls allow water to escape the funnel. Advection and diffusion control the tracer transport within the funnel. At the entrance (boundary at $x = 0$) concentrations are set to unity and ages to zero.

lowing transport equations

$$S \frac{\partial C_\lambda}{\partial t} + \frac{\partial (SUC_\lambda)}{\partial x} = UC_\lambda \frac{\partial S}{\partial x} + \frac{\partial}{\partial x} \left(SK \frac{\partial C_\lambda}{\partial x} \right) - \lambda SC_\lambda, \tag{9}$$

$$S \frac{\partial \alpha_\lambda}{\partial t} + \frac{\partial (SUA_\lambda)}{\partial x} = UA_\lambda \frac{\partial S}{\partial x} + \frac{\partial}{\partial x} \left(SK \frac{\partial \alpha_\lambda}{\partial x} \right) - \lambda S\alpha_\lambda + SC_\lambda, \tag{10}$$

where U and K represent, respectively, the velocity and the diffusivity in the funnel.

With S decreasing alongflow, the first term to the right in eqs (9) and (10) represents a sink. Indeed the divergence of the flux through any section of the funnel is compensated for by the loss of water—and tracer—through the porous walls.

In order to get analytical solutions to the above equations further simplifications are necessary. First, we assume that the funnel section decreases exponentially with a constant length scale L : $S(x) = S_0 \exp(-x/L)$. Second, we take U and K as positive constants and assume steady-state. Under these assumptions, the

transport eqs (9)–(10) become

$$\frac{d^2 C_\lambda}{dx^2} - \frac{U'}{K} \frac{dC_\lambda}{dx} - \frac{\lambda}{K} C_\lambda = 0 \quad (11)$$

$$\frac{d^2 \alpha_\lambda}{dx^2} - \frac{U'}{K} \frac{d\alpha_\lambda}{dx} - \frac{\lambda}{K} \alpha_\lambda = -\frac{1}{K} C_\lambda. \quad (12)$$

The modified velocity $U' = U + K/L$ arises from the varying section $S(x)$ in the diffusive terms of (9) and (10). It is readily seen that the set of eqs (11) and (12) is equivalent to that obtained for the 1-D advection–diffusion problem in a constant-section pipe with constant velocity U' and diffusivity K .

At this stage it is useful to introduce the following dimensionless numbers

$$Pe = \frac{UL}{K} \quad \text{Peclet number,} \quad (13)$$

$$Je = \frac{U^2}{K\lambda} \quad \text{Jenkins number.} \quad (14)$$

The Jenkins number¹ Je is equivalent to a Peclet number in which the length scale would be $U\lambda^{-1}$ (Jenkins, 1987). This length scale measures the distance travelled by the radioactive tracer during its mean lifetime in the case of a purely advective flow. In addition, we define the modified Jenkins number based on the modified velocity U' :

$$Je' = \frac{(U')^2}{K\lambda} = Je \left(\frac{1+Pe}{Pe} \right)^2. \quad (15)$$

We then apply the boundary conditions equivalent to a zero age at the entrance of the funnel, $x = 0$, as defined in (6), that is,

$$C_\lambda(x=0) = 1,$$

$$\alpha_\lambda(x=0) = 0.$$

For $x \rightarrow \infty$ we impose that the tracer concentration is bounded and that the age concentration does not increase exponentially.

Under these conditions the solutions to (11) and (12) read

$$C_\lambda(x) = \exp \left[-\frac{U'x}{2K} \left(\sqrt{1 + \frac{4}{Je'}} - 1 \right) \right] \quad (16)$$

$$\alpha_\lambda(x) = \frac{x}{U' \sqrt{1 + \frac{4}{Je'}}} \exp \left[-\frac{U'x}{2K} \left(\sqrt{1 + \frac{4}{Je'}} - 1 \right) \right], \quad (17)$$

and the age of a radioactive tracer is

$$a_\lambda(x) = \frac{\alpha_\lambda(x)}{C_\lambda(x)} = \frac{x}{U'} \sqrt{\frac{Je'}{4 + Je'}}. \quad (18)$$

The age of the water or a passive tracer is obtained by taking the limit $\lambda \rightarrow 0$, that is,

$$C_w(x) = \lim_{\lambda \rightarrow 0} C_\lambda(x) = 1,$$

$$a_w(x) = \lim_{\lambda \rightarrow 0} a_\lambda(x) = \frac{x}{U'},$$

implying that

$$a_w(x) = \frac{x}{U'} = \frac{x}{U} \frac{Pe}{1 + Pe}. \quad (19)$$

The radioage is also easily derived

$$\tau_\lambda(x) = \frac{-1}{\lambda} \ln \left(\frac{C_\lambda(x)}{C_w(x)} \right) = \frac{x}{U'} \frac{2\sqrt{Je'}}{\sqrt{4 + Je'} + \sqrt{Je'}}. \quad (20)$$

The funnel domain is infinite but its volume is finite. The latter is readily seen to be

$$\Omega = \int_0^\infty S(x) dx = S_0 L.$$

Hence it is possible to derive domain-averaged quantities, which we define as

$$\langle y \rangle = \Omega^{-1} \int_0^\infty y(x) S(x) dx.$$

Then the domain-averaged ages read

$$\langle a_w \rangle = \frac{L}{U} \frac{Pe}{1 + Pe}, \quad (21)$$

$$\langle \tau_\lambda \rangle = \langle a_w \rangle \frac{2\sqrt{Je'}}{\sqrt{4 + Je'} + \sqrt{Je'}}, \quad (22)$$

$$\langle a_\lambda \rangle = \langle a_w \rangle \sqrt{\frac{Je'}{4 + Je'}}. \quad (23)$$

The domain-averaged age of water $\langle a_w \rangle$ depends on the Peclet number and scales as $A_0 = L/U$, which is an advective timescale. Equation (21) may also be written as

$$\frac{1}{\langle a_w \rangle} = \frac{K}{L^2} + \frac{U}{L} = \frac{1}{A_D} + \frac{1}{A_0} \quad (24)$$

in which $A_D = L^2/K$ represents a characteristic timescale for diffusion.

The relative magnitude of the terms in (24) determines which process (advection or diffusion) controls the flow timescale. The boundary between the two regimes is clearly delineated by Pe and eq. (21) logically exhibits the following asymptotic behaviour

$$\langle a_w \rangle \sim A_0 Pe = A_D \quad \text{for } Pe \rightarrow 0,$$

$$\langle a_w \rangle \sim A_0 \left(1 - \frac{1}{Pe} \right) = A_0 \left(1 - \frac{A_0}{A_D} \right) \quad \text{for } Pe \rightarrow \infty.$$

From (22) and (23) it can be seen that the age of a radioactive tracer a_λ and the radioage τ_λ both underestimate the water age and that the bias is a function of λ (Delhez et al., 2003). These

¹We suggest this number be known as the ‘Jenkins number’ because, to the best of our knowledge, it is William Jenkins who first introduced it in ocean ventilation rate studies (e.g. Jenkins, 1987).

equations admit the following asymptotic expansions

$$\frac{\langle a_\lambda \rangle}{\langle a_w \rangle} \sim 1 - \frac{2}{Je'} \quad \text{for } Je' \rightarrow \infty,$$

$$\frac{\langle \tau_\lambda \rangle}{\langle a_w \rangle} \sim 1 - \frac{1}{Je'} \quad \text{for } Je' \rightarrow \infty,$$

and

$$\frac{\langle a_\lambda \rangle}{\langle a_w \rangle} \sim \frac{Je'^{1/2}}{2} \quad \text{for } Je' \rightarrow 0,$$

$$\frac{\langle \tau_\lambda \rangle}{\langle a_w \rangle} \sim Je'^{1/2} \quad \text{for } Je' \rightarrow 0.$$

These asymptotic expressions are consistent with those of Delhez et al. (2003). At small λ (high Je') the age bias is a linear function of the decay rate. On the other hand, for a large decay rate both the radioage τ_λ and the radioactive tracer age a_λ tend towards zero as $\lambda^{-1/2}$.

The parameters of the leaky funnel (L , U , K) are to be determined in such a way that the behaviour of the mean age predicted by this simple model be as close as possible to that computed by an OGCM. This is explained below.

4. 3-D OGCM experiments

The leaky funnel concept could be tested against field data (e.g. ^{14}C) but this would call for complex boundary condition formulations at the surface which are not easily dealt with analytically. However, our aim is to provide a tool which could help in summarizing or comparing complex 3-D OGCMs results. We henceforth evaluate the performance of the leaky funnel against results from a 3-D ocean model. This approach is in line with other simple formulations already successfully applied in ocean circulation studies (e.g. Maier-Reimer, 1993; Huang, 1999).

4.1. 3-D model description

We take the annual mean circulation from the Louvain-la-Neuve OGCM (Deleersnijder and Campin, 1995; Campin and Goosse, 1999). The latter is a primitive-equation, free-surface OGCM resting on the usual set of assumptions, that is, the hydrostatic equilibrium and the Boussinesq approximation. The horizontal resolution is $3^\circ \times 3^\circ$. The so-called 'z-coordinate' underlies a vertical discretization with 15 levels ranging in thickness from 20 m at the surface to 700 m in the deep ocean. A realistic bathymetry is used. The parametrization of vertical mixing is based on the Pacanowski and Philander (1981) formulation. Wherever the vertical density profile is unstable, the vertical diffusivity (Marotzke, 1991) is increased to $10 \text{ m}^2 \text{ s}^{-1}$. The parametrization of dense water flow down topographic features of Campin and Goosse (1999) is applied in the model. The experimental set up for the OGCM circulation corresponds to the control run described in Campin et al. (1999). The OGCM was assessed against the global distributions of temperatures, salinities as well as the estimated values of water transport in different

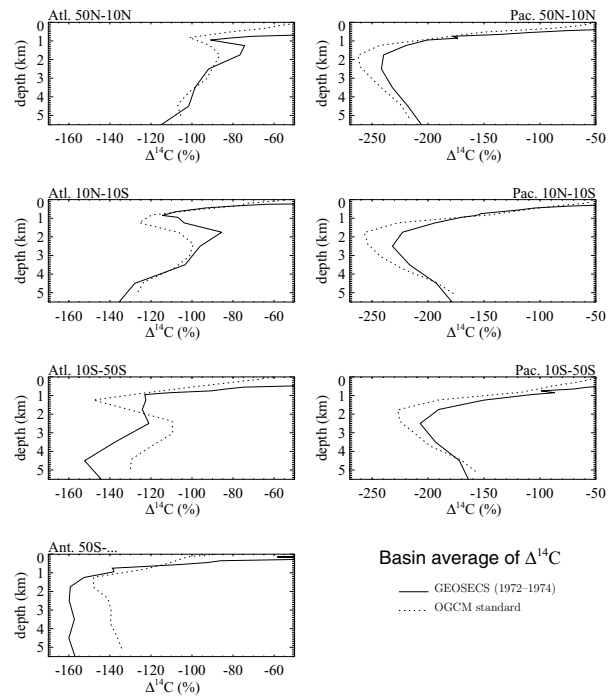


Fig. 2. Mean $\Delta^{14}\text{C}$ vertical profiles in several oceanic basins from GEOSECS data (solid) and from the OGCM standard version (dotted). The values in the North, Equatorial and Southern Atlantic and Pacific Oceans are reproduced, respectively, in the upper left and right three panels, with the bottom panel representing the Southern Ocean (south of 50°S). The pre-industrial OGCM $\Delta^{14}\text{C}$ is computed with the simplified method of Toggweiler et al. (1989). The discrepancy between model and data in the upper ocean partly results from the penetration of bomb ^{14}C that is not considered in this model experiment.

locations (North Atlantic, Drake passage...). Without any further tuning we then simulate the $\Delta^{14}\text{C}$ distribution following the approach of Toggweiler et al. (1989). The circulation reasonably reproduces the pre-bomb $\Delta^{14}\text{C}$ distribution in the deep ocean (Fig. 2).

The model simulates the distribution of the concentrations and age concentrations of water together with those of three radioactive tracers: ^{14}C ($\lambda = 1.2 \times 10^{-4} \text{ yr}^{-1}$), ^{39}Ar ($\lambda = 2.5 \times 10^{-3} \text{ yr}^{-1}$) and ^3H ($\lambda = 5.6 \times 10^{-2} \text{ yr}^{-1}$). These modelled radioactive tracers are idealized versions of the natural tracers. For example, we do not take into account the complex boundary conditions arising from the heterogeneity of air-sea fluxes in the real ocean, nor do we consider the dependency of ^{14}C air-sea fluxes on carbonate chemistry.

The boundary conditions at the surface for α_λ , C_λ , a_w and C_w correspond to a restoring of surface values to fixed values (concentrations = 1, ages = 0) using a very small restoring time constant ($\approx 1/3$ d). On the other hand, advective and diffusive fluxes across the ocean floor and lateral boundaries are set to zero.

4.2. Experimental setup

The leaky funnel yields an expression of the domain-averaged water age containing the parameters A_0 and Pe (Eq. 23). As will be seen later, the 3-D numerics calls for an additional parameter to be determined. In order to estimate these parameters from the domain-averaged 3-D OGCM water age we need several solutions to the OGCM transport process. For this purpose we performed a number of numerical experiments in which the velocity and the diffusivity tensor of the standard run, hereafter denoted \mathbf{u}_S and \mathbf{K}_S , were homogeneously multiplied by constant factors. These modifications were achieved by running the tracer model off-line, which solely affects the distribution of the non-dynamically active tracers.

Artificial modification of the velocity field in a 3-D transport model has previously been performed in ventilation studies (e.g. Heinze et al., 1991). While such artificial changes are not the consequence of any physical mechanism they help answering the not so trivial question ‘what tracer distributions, what timescales, would be relevant if the circulation was more sluggish or more rapid?’.

It should be stressed that the modified velocities and diffusivities applied in the off-line tracer model do not correspond to dynamically consistent states. Only the reference state is dynamically consistent (momentum and buoyancy equations) and in agreement with the boundary conditions at the ocean surface. The other states may be viewed as artefacts that are necessary for the values Pe and A_0 to be determined. Modifying independently the velocity and the diffusivity contradicts the momentum equation and the dynamical balances of the model. However it is easily seen that the continuity equation remains verified. Hence mass is conserved for all of the sensitivity experiments. The condition of no flux through ocean boundaries and the finite volume method which is used for discretizing the transport equations further guarantee that the system is mass-conserving. Nevertheless, no attempt is made here to generate dynamically consistent states from the OGCM, since the objective of the present study solely consists in establishing the order of magnitude of the timescales related to the transport processes.

With M the total number of experiments, the velocity and explicit diffusivity for experiment i ($i = 1, \dots, M$) are then

$$\mathbf{u}_i = \gamma_i \mathbf{u}_S \quad \text{and} \quad \mathbf{K}_i = \beta_i \mathbf{K}_S. \quad (25)$$

In other words, the transport operator in experiment i is of the form

$$\nabla \bullet (\mathbf{u}_i \xi - \mathbf{K}_i \bullet \nabla \xi) = \nabla \bullet (\gamma_i \mathbf{u}_S \xi - \beta_i \mathbf{K}_S \bullet \nabla \xi), \quad (26)$$

where $\xi \in \{C_w, \alpha_w, C_\lambda, \alpha_\lambda\}$. $M = 26$ experiments are performed with γ_i comprised between 0.125 and 2.0 and β_i between 1 and 6 (Table 2). The model is integrated over several thousand years (up to 30×10^3 yr for small γ_i) in order to achieve a steady-state of the tracer concentration and age concentration fields.

Let U_S and K_S denote the values of velocity and diffusivity in the leaky funnel corresponding to the flow conditions of the standard run of the OGCM. The velocity corresponding to experiment i is then

$$U_i = \gamma_i U_S. \quad (27)$$

However, the associated diffusivity is not $\beta_i K_S$, for the impact of numerical diffusion must be taken into account. As the latter is proportional to the velocity (Roache, 1972), the leaky funnel diffusivity actually is

$$K_i = \beta_i K_S^E + \gamma_i K_S^N. \quad (28)$$

where K_S^E and K_S^N represent the contributions from explicit and numerical diffusivities, associated with the standard version of the 3-D transport model. Obviously, the total diffusivity of the leaky funnel model that is associated with the 3-D model standard run is $K_S = K_S^E + K_S^N$.

It follows that the global Peclet number associated with experiment i is given by

$$\frac{1}{Pe_i} = \frac{\beta_i K_S^E + \gamma_i K_S^N}{\gamma_i U_S L} = \frac{\beta_i}{\gamma_i} \frac{1}{Pe^E} + \frac{1}{Pe^N}, \quad (29)$$

where $Pe^E = U_S L / K_S^E$ and $Pe^N = U_S L / K_S^N$ represent the Peclet numbers associated with the explicit and numerical diffusion, respectively.

If the leaky funnel model describes properly the ventilation of the deep ocean in the 3-D model, then the 3-D domain-averaged water ages ($\langle a_w \rangle$) from the M experiments would follow (21) with U and K replaced by expressions (27) and (28). Hence the predicted domain-averaged water age for experiment i , $\langle \hat{a}_w \rangle_i$, is given by

$$\langle \hat{a}_w \rangle_i = \frac{L}{U_i} \frac{Pe_i}{1 + Pe_i} = \frac{A_0}{\gamma_i} \frac{1}{1 + \frac{\beta_i}{\gamma_i} \frac{1}{Pe^E} + \frac{1}{Pe^N}}. \quad (30)$$

The predicted ages, that is, the ages derived from the leaky funnel model, depend on three unknown parameters (A_0 , Pe^E and Pe^N), the dependencies on Pe^E and Pe^N being non-linear. As the number of experiments M is much larger than three, the system defined by (30) is overdetermined. The values of the three unknown parameters are determined by an optimization procedure. They are adjusted so as to achieve the minimum of the quadratic expression

$$\sum_{i=1}^M (\langle \hat{a}_w \rangle_i - \langle a_w \rangle_i)^2,$$

where $\langle a_w \rangle_i$ is the OGCM domain-averaged water age obtained with experiment i . The Levenberg–Marquardt non-linear least-squares algorithm (Press et al., 1988) is used to determine A_0 , Pe^E and Pe^N from the water ages obtained with the 3-D model (Table 2).

Table 2. Domain-averaged ages obtained for the $M = 26$ experiments with the 3-D OGCM: water age (column 4) followed by the radioactive age and the radioage of ^{14}C (columns 5 & 6), ^{39}Ar (columns 7 & 8) and ^3H (columns 9 & 10). The values for γ_i and β_i corresponding to each experiment i are given in the second and third columns

i	γ_i	β_i	Water	^{14}C		^{39}Ar		^3H	
			$\langle a_w \rangle_i$ (yr)	$\langle \tau_\lambda \rangle_i$ (yr)	$\langle a_\lambda \rangle_i$ (yr)	$\langle \tau_\lambda \rangle_i$ (yr)	$\langle a_\lambda \rangle_i$ (yr)	$\langle \tau_\lambda \rangle_i$ (yr)	$\langle a_\lambda \rangle_i$ (yr)
1	2	1	412.83	392.64	402.30	223.86	292.04	54.21	78.09
2	1	1	763.71	692.73	726.81	304.63	443.53	76.65	105.57
3	1/2	1	1355.90	1139.32	1240.81	386.01	624.54	73.05	135.38
4	1/3	1	1832.97	1460.61	1632.16	429.48	737.07	81.96	152.80
5	1/4	1	2230.32	1698.62	1938.20	457.58	814.33	113.88	164.40
6	1/5	1	2561.77	1883.25	2183.78	477.39	871.09	74.37	172.46
7	1/6	1	2831.90	2028.70	2381.51	491.92	913.87	79.49	177.97
8	1/7	1	3071.00	2147.31	2548.51	503.22	948.04	75.76	182.14
9	1/8	1	3268.69	2244.41	2687.65	511.91	975.42	77.36	185.42
10	2	2	395.72	375.77	385.34	209.91	277.02	44.77	81.09
11	1	2	698.63	635.61	665.92	278.48	407.77	55.29	104.48
12	1/2	2	1143.68	981.10	1057.58	340.74	550.11	65.44	125.00
13	1/3	2	1455.77	1202.98	1320.16	370.26	628.82	61.55	135.20
14	1/4	2	1685.30	1354.90	1506.09	387.14	677.95	61.89	140.88
15	1/5	2	1860.32	1465.71	1644.71	398.20	711.61	62.76	144.69
16	1/6	2	1995.64	1548.62	1750.22	405.98	735.76	64.99	147.54
17	1/7	2	2106.54	1614.38	1835.21	411.92	754.38	64.13	149.64
18	1/8	2	2197.14	1666.99	1903.98	416.55	768.98	63.75	151.19
19	2	4	360.60	343.08	351.57	192.77	254.29	37.57	75.88
20	1	4	588.32	541.89	564.34	247.39	357.62	44.45	91.64
21	1/2	4	864.73	767.47	813.83	289.36	455.01	48.53	104.46
22	1/3	4	1026.21	891.97	955.45	306.14	501.44	50.33	110.30
23	1/4	4	1202.26	1021.67	1106.38	320.65	545.36	52.34	115.47
24	2	6	329.23	314.31	321.59	180.38	236.00	36.97	70.55
25	1	6	506.79	471.81	488.81	225.71	320.67	39.98	82.88
26	1/2	6	695.85	631.30	662.37	257.10	392.88	43.02	92.15

5. Results

The least-squares fit of eq. (30) to the M domain-averaged water ages from the 3-D model leads to the estimates of A_0 , Pe^E and Pe^N given in Table 3. With these values one may now compute the predicted (leaky funnel) ages corresponding to each experiment. The predicted water ages are given by (30) while the predicted radioages and radioactive tracer ages are obtained

Table 3. Parameters of the leaky funnel model as obtained from a least squares fit to the 3-D model results (domain-averaged water ages for all experiments). The last column gives the Peclet number computed from eq. (29) with $\beta_i = \gamma_i = 1$

A_0	Pe^E	Pe^N	Pe
1010.36 yr	6.41	6.98	3.34

from

$$\langle \hat{\tau}_\lambda \rangle_i = \langle \hat{a}_w \rangle_i \frac{2\sqrt{Je'_i}}{\sqrt{4 + Je'_i} + \sqrt{Je'_i}}, \quad (31)$$

$$\langle \hat{a}_\lambda \rangle_i = \langle \hat{a}_w \rangle_i \frac{\sqrt{Je'_i}}{\sqrt{4 + Je'_i}}, \quad (32)$$

which derive from (22) and (23). The modified Jenkins number Je'_i in the above expressions is

$$Je'_i = \frac{1}{\lambda} \frac{\gamma_i Pe_i}{A_0} \left(\frac{1 + Pe_i}{Pe_i} \right)^2, \quad (33)$$

where Pe_i is given by eq. (29). Table 4 lists the leaky funnel and OGCM domain-averaged ages for the standard case ($\gamma_i = 1$ and $\beta_i = 1$). The leaky funnel ages are presented versus OGCM ages in Figs. 3 and 4. The domain-averaged ages predicted by the leaky funnel and those obtained from the 3-D model are in excellent agreement. The linear correlation coefficients (column 4, Table 4) for $\langle a_w \rangle$ and $\langle a_{^{14}\text{C}} \rangle$ are very close to 1 and the

Table 4. Assessment of the leaky funnel domain-averaged ages for the four tracers considered. The ages for the standard 3-D run are given in column 2. With $\gamma_i = 1$ and $\beta_i = 1$ we obtain the leaky funnel ages in column 3 from eqs (30), (31)–(32), expressions (29) and (33) and the values in Table 3. Column 4 contains the linear correlation coefficient r between leaky funnel (1-D) and 3-D model domain-averaged ages. The rms difference between leaky funnel and 3-D model ages ζ is given in column 5

	3-D OGCM	Leaky Funnel	r	ζ
	$\gamma_i = 1, \beta_i = 1$			
$\langle a_w \rangle$	763.71 yr	777.72 yr	0.9998	40.86 yr
$\langle \tau_{^{14}\text{C}} \rangle$	726.81 yr	761.56 yr	0.9989	65.69 yr
$\langle a_{^{14}\text{C}} \rangle$	692.73 yr	746.06 yr	0.9969	92.03 yr
$\langle \tau_{^{39}\text{Ar}} \rangle$	443.53 yr	582.45 yr	0.9867	142.58 yr
$\langle a_{^{39}\text{Ar}} \rangle$	304.63 yr	465.55 yr	0.9765	145.49 yr
$\langle \tau_{^3\text{H}} \rangle$	105.57 yr	209.86 yr	0.9479	82.27 yr
$\langle a_{^3\text{H}} \rangle$	76.65 yr	121.29 yr	0.8957	51.56 yr

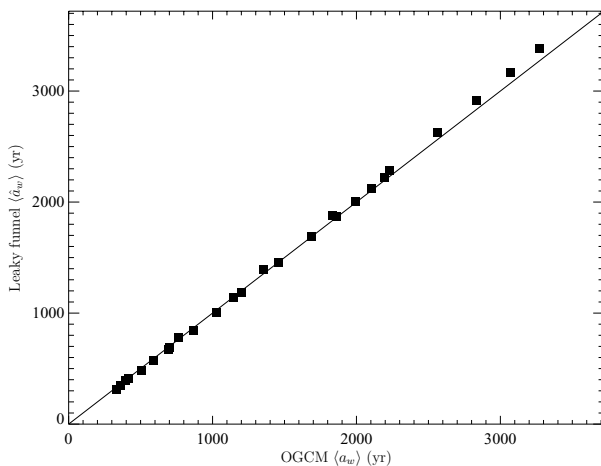


Fig. 3. Scatter plot of the predicted domain-averaged water ages versus those computed from the 3-D model. The leaky funnel ages are computed by means of eq. (30) and the parameters in Table 3. The linear correlation coefficient is equal to 0.9998 and the rms difference 40.87 yr (Table 4).

corresponding rms differences (column 5, Table 4) are relatively small.

It should be noted that radioages are not completely independent from the water ages. Indeed, they derive from the same advection–diffusion Green’s function (e.g. Haine and Hall, 2002; Delhez et al., 2003). However, the parameters of the funnel were estimated with the help of the domain-averaged water ages. Non-linearities arising from cross-products result in additional contributions intervening in the domain-averaged radioages and radioactive tracer ages. Hence the latter provide supplementary information and additional means for assessing the quality of the fit.

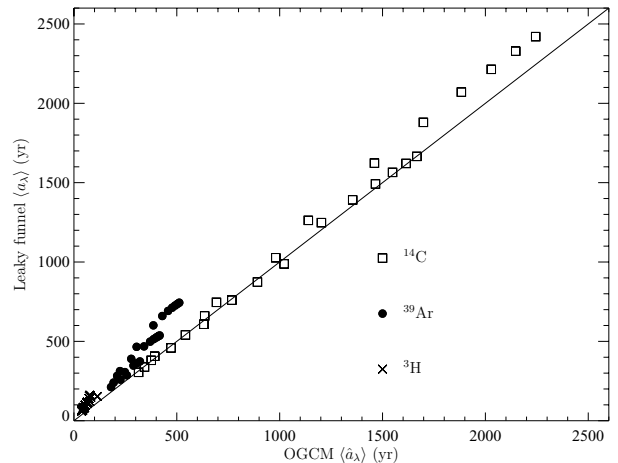
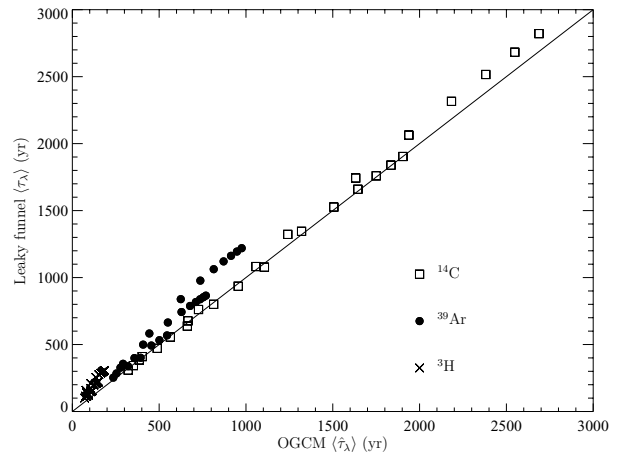


Fig. 4. Scatter plot of the predicted domain-averaged radioages (top) and radioactive tracer ages (bottom) versus those computed from the 3-D model. The leaky funnel ages are computed by means of eqs (31)–(32) and the parameters in Table 3. The linear correlation coefficients and rms differences corresponding to the fit for each of the radioactive tracer are given in Table 4.

The agreement for the radioelement ages is excellent for ^{14}C but deteriorates as λ increases: the leaky funnel predicted ages are systematically larger (older) than the 3-D model values (Fig. 4). The reasons thereof are to be found in the heterogeneity of the 3-D circulation and the fact that distinct water masses fill the deep ocean in the OGCM experiments. The changes in γ_i and β_i do not only affect the deep interior circulation but also the exchanges with the surface through changes in subduction and convection rates. In the leaky funnel representation the age is set to zero at the funnel boundary directly feeding from the ocean surface. In the 3-D OGCM the age is set to zero at the ocean surface but due to the existence of multiple pathways between the surface and the deep ocean, the water starting its journey through the deep ocean does not necessarily have a zero age. Since the

largest values of velocity and of explicit diffusion occur in the upper ocean layers and in convection regions the initial ages of the individual water masses filling the deep ocean differ among experiments. We allow for these differences by associating an error estimate to each of the 3-D average water ages in the fitting procedure. We impose that the error increases with $\langle a_w \rangle_i$ in order to reflect the larger value of the age tagging water entering the deep ocean in the case of a slower circulation. A close look at the age distributions obtained for the M experiments together with the analysis of the statistics of fit allow us to conclude that the error represents 2–3% of $\langle a_w \rangle_i$. The estimates of the parameters are not sensitive to the percentage assigned to this error but may change by a few percent for different uncertainty formulations. However, these changes do not impact significantly the order of magnitude of the derived scales presented in the next section. We also examined the robustness of the estimates by using a different procedure. The built-in IDL function *CURVEFIT* (Research Systems Inc., 1999) based on a gradient-expansion algorithm resulted in parameters values very close to those obtained with the Levenberg–Marquardt algorithm (relative differences of 0.1 and 0.6% for A_0 and Pe , respectively).

The systematic bias of the age of radioactive tracers is explained by the differences in pathways and transit time towards the deep ocean. It is well known (Jenkins, 1987; Khaliwala et al., 2001; Delhez et al., 2003) that mixing processes create a bias towards younger ages and that this bias increases with increasing mixing or with increasing radioactive decay constant. The larger mixing, of both explicit and numerical types, experienced by the radioactive tracers before reaching the deep ocean results in lower ages in the 3-D experiments. As expected the discrepancy increases with λ and results for ^3H are of a poorer quality than those obtained for tracers having a slower decay rate (Fig. 4).

In a sensitivity test we assumed that numerical diffusion does not contribute to the age distributions in the 3-D OGCM. In that case, the purely advective age scales A_0 decreases to 883.78 yr while Pe^E increases to 7.33. Under this hypothesis the lack of contribution from Pe^N in the denominator of (30) is compensated for by an increase in Pe^E and a decrease in A_0 . When numerical diffusion is neglected, the rms differences between the leaky funnel and the OGCM radioactive tracer ages increase while those for water ages do not change. Again this is due to the larger sensitivity of radioactive tracer ages to mixing. This sensitivity test illustrates the role played by numerical diffusion in coarse grid OGCMs (Oschlies, 2000; Doney et al., 2004).

The leaky funnel and 3-D models also generally agree for the volume distribution of water ages. In the leaky funnel this distribution is given by:

$$\phi(a_w) = \frac{e^{-a_w/\langle a_w \rangle}}{\langle a_w \rangle}, \quad (34)$$

where $\phi(a_w)\delta a_w$ represents the fraction of the volume occupied by water with ages comprised in the interval $[a_w, a_w + \delta a_w]$ (see Appendix A for a derivation). This volume fraction decreases

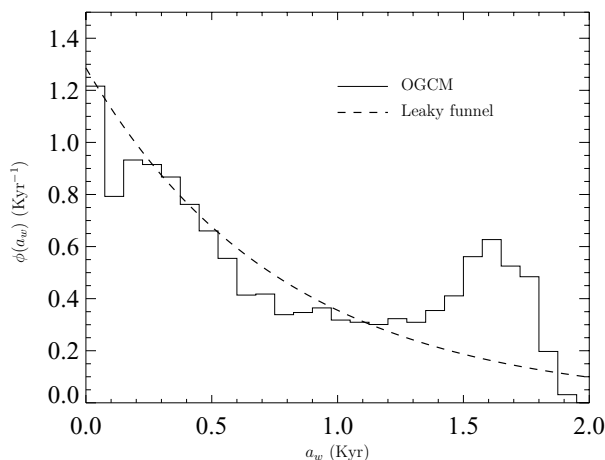


Fig. 5. Volume density distribution of water age for the standard case ($\gamma_i = 1$ and $\beta_i = 1$). The dashed curve represents the distribution for the leaky funnel (eq. 34) with parameters from Table 3. The volumes from the 3-D experiment (solid) were grouped into 75 yr bins.

exponentially as age increases (Fig. 5). The solid line in the same figure is the distribution of the 3-D model ages. In order to derive the latter curve, we computed the volume density corresponding to 75 yr age intervals. There is a general agreement between both distributions. The local maximum in the 3-D model curve at large ages apparently results from a recirculation cell in the deep Pacific Ocean.

Such a close match between a very simple 1-D model and a complex 3-D ocean circulation model with its multiple ventilation pathways is unexpected. We devoted many efforts to find hidden dependencies among the parameters as well as to examine every aspects of our method. However we did not find any bias in our reasoning. Hence we assume that the close correspondence is not a methodological artefact.

6. Discussion

In what follows we examine the physical relevance of the values in Table 3 and derive the characteristic circulation scales. From the leaky funnel we obtain a timescale and a dimensionless parameter related to the circulation in the global ocean: $A_0 = \frac{L}{U} = 1010.36\text{yr}$ and $Pe = \frac{UL}{K} = 3.34$ (Table 3). A_0 is a measure of the average ventilation time in the absence of diffusion processes. From (21) it is easily seen that $\langle a_w \rangle \leq A_0$ for any Pe . Hence A_0 provides an upper limit of the actual ventilation timescale.

Most observational estimates of deep ocean ventilation timescales actually measure the turnover (or flushing) times as they are usually based on the knowledge of a reservoir size and its budget (e.g. Broecker and Peng, 1982; Stuiver et al., 1983; Broecker et al., 1999b). However, the mean age and the flushing

time represent conceptually different timescales which, in most cases, have different values (Bolin and Rodhe, 1973).

In the leaky funnel, A_0 measures the turnover time of water while the turnover time of a radioactive tracer is $\theta(C_\lambda) = A_0/(A_0 \lambda + 1)$ (see Appendix B for a full derivation). Hence the turnover time for radiocarbon in the leaky funnel is $\theta(^{14}\text{C}) \simeq 901$ yr ($\lambda = 1.2 \times 10^{-4} \text{ yr}^{-1}$). Broecker et al. (1999b) obtained a value of 850 yr for the turnover time of the deep ocean based on the production rate of new deep water.² Several authors estimated the flushing time of the deep ocean from radiocarbon inventories to be comprised between 500 and 1000 yr (Stuiver et al., 1983; Broecker and Peng, 1982). Given the many uncertainties these values compare rather favourably with the timescales derived from the leaky funnel.

For a reservoir at steady-state, a turnover time larger than the domain-averaged water age indicates a situation in which the source and sink areas are away from each other (Bolin and Rodhe, 1973). This corresponds well with the deep sea reservoir whose sources are located in polar areas and sinks distributed among the main ocean basins.

There are not many global estimates of oceanic Pe . Based on literature sources it seems that the characteristic Peclet number for global horizontal ocean circulation is comprised between 1 and 10. Takeoka (1991) used a 2-D model to reproduce the vertical distribution of observed radiocarbon ages in the Pacific Ocean; he obtained the best agreement for $Pe = 5$. Larger values are usually assumed close to the surface ocean. For example, Colin de Verdière (1993) derives a Peclet number of 10 from typical surface velocities and motion length scale.

Scaling arguments for the steady overturning circulation in a simplified basin point to a link between the horizontal circulation and the vertical diffusion (Bryan, 1987; Huang, 1999). Mass balance and a vertical advective-diffusive balance of the density lead to the following scaling laws

$$U_h L_v \sim W L_h \quad \text{and} \quad L_v \sim K_v / W, \quad (35)$$

where L_h , L_v , U_h , W and K_v are appropriate scales for the horizontal and vertical motion, the horizontal and vertical velocities and the vertical diffusion, respectively. From (35) we obtain

$$A_0 = \frac{L}{U} \equiv \frac{L_h}{U_h} \sim \frac{L_v^2}{K_v}. \quad (36)$$

With A_0 from Table 3 and $L_v \sim 2 \times 10^3$ m we obtain $K_v \sim 1.3 \times 10^{-4} \text{ m}^2 \text{ s}^{-1}$. This diffusivity level agrees well with several estimates of subthermocline mixing (Munk, 1966; Munk and Wunsch, 1998; Toole and McDougall, 2001).

A_0 and Pe are based on three characteristic scales of the flow: L , U and K . As the model does not provide a third relationship linking these three scales, one scale needs to be imposed in order to derive the two others. The velocity scale U is estimated as the

average velocity amplitude over the deep ocean. The deep ocean in the 3-D model may be defined to be the water that is at least 1000 m below the surface (Fig. 2). For depths larger than 1 km the mean horizontal velocity U in the 3-D model is $\sim 3 \times 10^{-3} \text{ m s}^{-1}$. With this value, the spatial scale and the diffusivity are easily derived, that is, $L = 9.6 \times 10^4 \text{ km}$ and $K = 8.6 \times 10^4 \text{ m}^2 \text{ s}^{-1}$.

L is the e-folding length of the leaky funnel section but it also represents the average distance travelled by water parcels in the leaky funnel model (Appendix A). The length scale derived from the leaky funnel representation seems to be coherent with the large-scale tracer and nutrient distributions in the ocean (Broecker, 1991).

The scaling for K may be examined in the light of the study of Okubo (1971) who provided upper and lower bounds for the horizontal diffusivity as a function of the length scale of motion in the sea. The upper and lower bounds for diffusivity proposed by Okubo (1971) are represented by the black lines in Fig. 6. From that figure we may derive the length scales associated with the diffusivity obtained from the leaky funnel model (dotted lines in Fig. 6). These length scales are in the interval 2.0×10^3 – 2.1×10^4 km. Such length scales are comparable to those of basin-scales processes. It must be stressed that these characteristic lengths are not of the same nature as the length scale L , the former being related to the largest scales of motion in the World Ocean while the latter represents the mean distance travelled by water parcels in the deep ocean. This is why the orders of magnitude of these length scales are different.

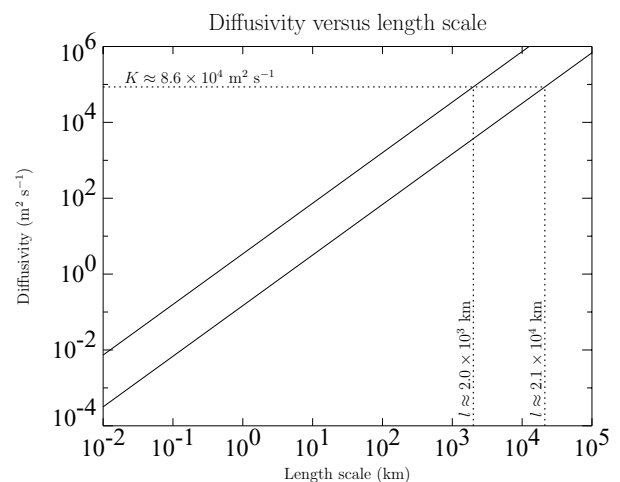


Fig. 6. Relationship between horizontal diffusivity and length scale in the ocean (from Okubo, 1971). On these logarithmic scales the two solid lines have a slope of 4/3 and represent the upper and lower bounds for the diffusivity associated with a particular length scale. As indicated by the dotted lines, the value of the diffusivity K associated with the leaky funnel corresponds to length scales between 2.0×10^3 and 2.1×10^4 km.

² Assuming that the deep ocean occupies 60% of the total ocean volume and that the rate of deep water formation is 30 Sv.

7. Conclusions and perspectives

The leaky funnel model presented in this study appears to provide an adequate description of some transport properties of a 3-D model of the large-scale ocean circulation. The scales suggested by this conceptual model have a clear physical meaning and are consistent with our current perception of the World Ocean circulation.

Several questions are raised in this work. The excellent agreement between the ages predicted by the 1-D funnel model and those obtained in the 3-D simulations appears robust. The volume distribution of water age of the leaky funnel and that of the OGCM reference state, which is not a direct product of the sensitivity analysis, compare favourably. Further, the parameters suggested from the leaky funnel model, that is A_0 and Pe , for water ages, are clearly independent. We do not have any satisfactory explanation for such a close agreement, which was unexpected at first. Presently, we are examining the reasons leading to this behaviour and are working on the possible interpretations.

The scales A_0 and Pe derived from the leaky funnel are based on OGCM domain-averaged water ages, the OGCM being calibrated against other field data or climatology (T, S, ...). It should be stressed that these scales reflect the OGCM internal transport and the relative role of advection and diffusion in reproducing the observed tracer distributions. The method we adopted has some questionable aspects since the flow fields considered here are not dynamically consistent, but this method seems relevant as it allows the measure of the scales of the ventilation time with respect to velocity and/or diffusivity changes.

The derived Peclet number, $Pe \sim 3$, appears at first to be small. This value is in line with the results of a recent analysis of the large-scale ocean ventilation (Holzer and Primeau, 2006) which points to a somewhat diffusive large-scale ocean transport. However, we could also question the transport in our OGCM as models from this generation are known to be quite diffusive (Oschlies, 2000; Doney et al., 2004).

The leaky funnel also has limitations due to its simple representation of the 'return' flow. The agreement would also need to be tested against 3-D model with more detailed or 'realistic' vertical mixing as this process is highly heterogeneous (Polzin et al., 1997; St. Laurent et al., 2001).

The simple physical analogue provided by the leaky funnel model could be a useful tool in model intercomparison studies. Extracting the scales A_0 and Pe by means of the method presented herein could help in evidencing the large-scale circulation characteristics in OGCMs. Indeed, similar distributions of mean water ages could potentially be obtained from OGCMs with different dynamics. More (or less) advection together with less (or more) diffusion would then result in a larger (smaller) A_0 together with a smaller (larger) Pe . Preliminary tests with another OGCM (the Hamburg LSG OGCM, Maier-Reimer et al., 1993), seem promising and the derived values are fully consis-

tent with the observed differences between the respective 3-D tracer distributions.

8. Acknowledgments

The authors thank Jean-Michel Campin and Jean-Marie Beckers for fruitful discussions and an anonymous reviewer for very constructive comments which helped much in improving the manuscript. A. Mouchet thanks the Belgian Federal Science Policy (BELSPO) for support through the ASTER project (SD/CS/01A). Eric Deleersnijder is a Research Associate with the Belgian National Fund for Scientific Research (FNRS); he is indebted to Professor Tom W.N. Haine for useful discussions during the first stage of the design of the leaky funnel model.

9. Appendix A: Volume distribution and average trajectory length

The volume distribution function of water age is defined in such a way that $\phi(a_w) \delta a_w$ represents the fraction of volume in which the water age lies in the interval $[a_w, a_w + \delta a_w]$. In the leaky funnel, this volume fraction is

$$\phi(a_w) \delta a_w = \frac{S(x) \delta x}{L S_0}$$

with $S(x) = S_0 \exp(-x/L)$. Expression (21) may be transformed to

$$a_w(x) = \frac{x}{L} \langle a_w \rangle$$

implying that $\delta a_w = (\langle a_w \rangle / L) \delta x$. Combining all of the above equations leads to

$$\phi(a_w) = \frac{a_w}{\langle a_w \rangle} e^{-a_w / \langle a_w \rangle}$$

A fraction $(S(x) - S(x + \Delta x)) / S_0$ of the fluid parcels leaves the funnel in the interval $[x, x + \Delta x]$ after having travelled a distance that tends towards x as $\Delta x / L \rightarrow 0$. Since

$$\frac{S(x) - S(x + \Delta x)}{S_0} \rightarrow \frac{-1}{S_0} \frac{dS}{dx} \Delta x, \quad \text{for} \quad \frac{\Delta x}{L} \rightarrow 0$$

the mean trajectory length is then given by the e-folding scale of the section,

$$\int_0^\infty x \frac{-1}{S_0} \frac{dS}{dx} dx = \frac{1}{L} \int_0^\infty x e^{-x/L} dx = L$$

10. Appendix B: Turnover time

The turnover time is defined as the ratio of the content of a reservoir to the sum of its sinks (Bolin and Rodhe, 1973). At steady-state the sinks must balance the sources. The source term is provided by the inflow of new material at $x = 0$. This flux is

given by

$$F_{\lambda}(0) = S_0 \left\{ UC_{\lambda}(0) - K \left[\frac{\partial C_{\lambda}(x)}{\partial x} \right]_{\text{at } x=0} \right\}$$

With the help of (16) and the definition of U' ($U' = U + K/L$) this flux is

$$\begin{aligned} F_{\lambda}(0) &= S_0 \left[U + \frac{U'}{2} \left(\sqrt{1 + \frac{4}{Je'}} - 1 \right) \right] \\ &= \frac{S_0 K}{L} \left[\frac{U'L}{2K} \left(\sqrt{1 + \frac{4}{Je'}} + 1 \right) - 1 \right] \end{aligned}$$

The inventory of a tracer with concentration C_{λ} in the leaky funnel is

$$\begin{aligned} Q_{\lambda} &= \int_0^{\infty} S(x) C_{\lambda}(x) dx \\ &= S_0 \int_0^{\infty} \exp \left[-\frac{x}{L} - \frac{U'x}{2K} \left(\sqrt{1 + \frac{4}{Je'}} - 1 \right) \right] dx \\ &= \frac{S_0 L}{1 + \frac{U'L}{2K} \left(\sqrt{1 + \frac{4}{Je'}} - 1 \right)} \end{aligned}$$

Hence

$$\theta(C_{\lambda}) = \frac{Q_{\lambda}}{F_{\lambda}(0)} = \frac{L}{U} \frac{1}{\lambda(L/U) + 1} = \frac{A_0}{\lambda A_0 + 1}.$$

The turnover time for water or a passive constituent ($\lambda = 0$) is then given by A_0 . This timescale provides an upper limit for the turnover time of any radioactive tracer.

References

- Archer, D., Martin, P., Milovich, J., Brovkin, V., Plattner, G.-K. and co-authors. 2003. Model sensitivity in the effect of Antarctic sea ice and stratification on atmospheric pCO₂. *Palaeoceanography* **18**, 1012, doi:10.1029/2002PA000760.
- Bolin, B. and Rodhe, H. 1973. A note on the concepts of age distribution and transit time in natural reservoirs. *Tellus* **25**, 58–62.
- Broecker, W. S. 1991. The great ocean conveyor. *Oceanography* **4**, 79–89.
- Broecker, W. S. and Peng, T.-H. 1982. *Tracers in the Sea*. Lamont Doherty Geological Observatory, Columbia University, New York, 690 p.
- Broecker, W. S. and Peng, T.-H. 2000. Comparison of ³⁹Ar and ¹⁴C ages for waters in the deep ocean. *Nucl. Instrum. Methods Phys. Res. Sect. B* **172**, 473–478.
- Broecker, W. S., Lynch-Stieglitz, J., Archer, D., Hoffmann, M., Maier-Reimer, E. and co-authors. 1999a. How strong is the Harvardton-Bear constraint? *Glob. Biogeochem. Cycle* **13**, 817–820.
- Broecker, W. S., Sutherland, S. and Peng, T. 1999b. A possible 20th-century slowdown of Southern Ocean deep water formation. *Science* **286**, 1132–1135.
- Broecker, W. S., Peacock, S., Walker, S., Weiss, R., Fahrbach, E. and co-authors. 1998. How much deep water is formed in the Southern Ocean? *J. Geophys. Res.* **103**, 15833–15844.
- Bryan, F. 1987. Parameter sensitivity of primitive equation OGCMs. *J. Phys. Oceanogr.* **17**, 970–985.
- Campin, J.-M., Fichet, T. and Duplessy, J.-C. 1999. Problems with using radiocarbon to infer ocean ventilation rates for past and present climates. *Earth Planet. Sci. Lett.* **165**, 17–24.
- Campin, J.-M. and Goosse, H. 1999. Parameterization of density-driven downsloping flow for a coarse-resolution ocean model in z-coordinate. *Tellus* **51**, 412–430.
- Colin de Verdière, A. 1993. On the oceanic thermohaline circulation. In: *Modelling the Ocean-Climate Interactions* (eds J. Willebrand and D. L. T. Anderson), Springer Verlag, Heidelberg, 151–183.
- Craig, H. 1971. The deep metabolism: oxygen consumption in abyssal ocean water. *J. Geophys. Res.* **76**, 5078–5086.
- Deleersnijder, E. and Campin, J.-M. 1995. On the computation of the barotropic mode of a free-surface world ocean model. *Ann. Geophys.* **13**, 675–688.
- Deleersnijder, E., Campin, J.-M. and Delhez, E. 2001. The concept of age in marine modelling. I. Theory and preliminary model results. *J. Mar. Syst.* **28**, 229–267.
- Deleersnijder, E., Mouchet, A., Delhez, E. and Beckers, J.-M. 2002. On the transient behaviour of water ages in the world ocean. *Math. Comput. Model.* **36**, 121–127.
- Delhez, E., Campin, J.-M., Hirst, A. C. and Deleersnijder, E. 1999. Toward a general theory of the age in ocean modelling. *Ocean Model.* **1**, 17–27.
- Delhez, E., Deleersnijder, E., Mouchet, A. and Beckers, J.-M. 2003. A note on the age of radioactive tracers. *J. Mar. Syst.* **38**, 277–286.
- Doney, S. C. and Jenkins, W. J. 1994. Ventilation of the deep western boundary current and abyssal western North Atlantic: estimates from tritium and ³He distributions. *J. Phys. Oceanogr.* **24**, 638–659.
- Doney, S. C., Lindsay, K., Caldeira, K., Campin, J.-M., Drange, H. and co-authors. 2004. Evaluating global ocean carbon models: The importance of realistic physics. *Glob. Biogeochem. Cycle* **18**, GB3017, doi:10.1029/2003GB00215.
- Dutay, J.-C., Jean-Baptiste, P., Campin, J.-M., Ishida, A., Maier-Reimer, E. and co-authors. 2004. Evaluation of OCMIP-2 ocean models' deep circulation with mantle helium-3. *J. Mar. Syst.* **48**, 15–36, doi:10.1016/j.jmarsys.2003.05.010.
- England, M. H. 1995. The age of water and ventilation timescales in a global ocean model. *J. Phys. Oceanogr.* **25**, 2756–2777.
- England, M. H. and Maier-Reimer, E. 2001. Using chemical tracers to assess ocean models. *Rev. Geophys.* **39**, 29–70.
- Gruber, N. 1998. Anthropogenic CO₂ in the Atlantic Ocean. *Glob. Biogeochem. Cycle* **12**, 165–191.
- Haidvogel, D. and Bryan, F. 1992. Ocean general circulation modeling. In: *Climate System Modeling* (ed. K. E. Trenberth), Cambridge University Press, USA, chap. 11, 371–412.
- Haine, T. W. N. and Hall, T. M. 2002. A generalized transport theory: water-mass composition and age. *J. Phys. Oceanogr.* **32**, 1932–1946.
- Hall, T., Haine, T. and Waugh, D. 2002. Inferring the concentration of anthropogenic carbon in the ocean from tracers. *Glob. Biogeochem. Cycle* **16**, 1131–273, doi:10.1029/2001GB001835.
- Heinze, C., Maier-Reimer, E. and Winn, K. 1991. Glacial pCO₂ reduction by the world ocean: experiments with the Hamburg carbon cycle model. *Palaeoceanography* **6**, 395–430.

- Hirst, A. C. 1999. Determination of water component age in ocean models: application to the fate of north atlantic deep water. *Ocean Model.* **1**, 81–94.
- Holzer, M. and Hall, T. M. 2000. Transit-time and tracer-age distributions in geophysical flows. *J. Atmos. Sci.* **57**, 3539–3558.
- Holzer, M. and Primeau, F. W. 2006. The diffusive ocean conveyor. *Geophys. Res. Lett.* **33**, L14, 618, doi:10.1029/2006GL026232.
- Huang, R. X. 1999. Mixing and energetics of the oceanic thermohaline circulation. *J. Phys. Oceanogr.* **29**, 727–746.
- Jenkins, W. J. 1987. ^3H and ^3He in the Beta Triangle: observations of gyre ventilation and oxygen utilization rates. *J. Phys. Oceanogr.* **17**, 763–783.
- Jenkins, W. J. 1998. Studying subtropical thermocline ventilation and circulation using tritium and ^3He . *J. Geophys. Res.* **103**, 15 817–15 831.
- Khatiwal, S., Visbeck, M. and Schlosser, P. 2001. Age tracers in an ocean GCM. *Deep-Sea Res.* **48**, 1423–1441.
- Kunze, E., Firing, E., Hummon, J. M., Chereskin, T. K. and Thurnherr, A. M. 2006. Global abyssal mixing inferred from lowered ADCP shear and CTD strain profiles. *J. Phys. Oceanogr.* **36**, 1553–1576 (Corrigendum pp 2350–2352).
- Maier-Reimer, E. 1993. Geochemical cycles in an ocean general circulation model. Preindustrial tracer distributions. *Glob. Biogeochem. Cycle* **7**, 645–677.
- Maier-Reimer, E., Mikolajewicz, U. and Hasselmann, K. 1993. Mean circulation of the Hamburg LSG OGCM and its sensitivity to the thermohaline surface forcing. *J. Phys. Oceanogr.* **23**, 731–757.
- Marotzke, J. 1991. Influence of convective adjustment on the stability of the thermohaline circulation. *J. Phys. Oceanogr.* **21**, 903–907.
- Munk, W. 1966. Abyssal recipes. *Deep-Sea Res.* **13**, 707–730.
- Munk, W. and Wunsch, C. 1998. Abyssal recipes II: energetics of tidal and wind mixing. *Deep-Sea Res.* **45**, 1977–2010.
- Neu, J. L. and Plumb, R. A. 1999. Age of air in a “leaky pipe” model of stratospheric transport. *J. Geophys. Res.* **104**, 19 243–19 255.
- Okubo, A. 1971. Oceanic diffusion diagrams. *Deep-Sea Res.* **18**, 789–802.
- Oschlies, A. 2000. Equatorial nutrient trapping in biogeochemical ocean models: the role of advection numerics. *Glob. Biogeochem. Cycle* **14**, 655–667.
- Pacanowski, R. C. and Philander, S. G. H. 1981. Parameterization of vertical mixing in numerical models of tropical oceans. *J. Phys. Oceanogr.* **11**, 1443–1451.
- Plumb, R. A. 1996. A “tropical pipe” model of atmospheric transport. *J. Geophys. Res.* **101**, 3957–3972.
- Polzin, K. L., Toole, J. M., Ledwell, J. R. and Schmitt, R. W. 1997. Spatial variability of turbulent mixing in the Abyssal Ocean. *Science* **276**, 93–96.
- Press, W., Flannery, B., Teukolsky, S. and Vetterling, W. 1988. *Numerical Recipes*. Cambridge University Press, Cambridge.
- Research Systems Inc. 1999. IDL software, version 5.3.
- Roache, P. 1972. On artificial viscosity. *J. Comput. Phys.* **10**, 169–184.
- Robbins, P., Price, J., Owens, W. and Jenkins, W. 2000. The importance of lateral diffusion for the ventilation of the lower thermocline in the subtropical north atlantic. *J. Phys. Oceanogr.* **30**, 67–89.
- St. Laurent, L. et al 2001. Buoyancy forcing by turbulence above rough topography in the abyssal Brazil Basin. *J. Phys. Oceanogr.* **31**, 3476–3495.
- St. Laurent, L. and Simmons, H. 2006. Estimates of power consumed by mixing in the ocean interior. *J. Climate* **19**, 4877–4890.
- Stommel, H. 1958. The abyssal circulation. *Deep-Sea Res.* **5**, 80–82.
- Stommel, H. and Arons, A. 1960. On the abyssal circulation of the world ocean—I. Stationary planetary flow patterns on a sphere. *Deep-Sea Res.* **6**, 140–154.
- Stuiver, M., Quay, P. and Östlund, H. G. 1983. Abyssal water carbon-14 distribution and the age of the world oceans. *Science* **219**, 849–851.
- Takeoka, H. 1991. Effects of the deep ocean circulation on the reservoir characteristics of the ocean. *J. Oceanogr. Soc. Japan* **47**, 27–32.
- Talley, L. D. 1999. Some aspects of ocean heat transport by the shallow, intermediate and deep overturning circulations. In: *Mechanisms of Global Climate Change at Millennial Time Scales, Geophys. Monogr. Ser.*, Volume 112 (eds P. U. Clark, R. S. Webb and L. D. Keigwin), AGU, Washington, DC, 1–22.
- Thiele, G. and Sarmiento, J. 1990. Tracer dating and ocean ventilation. *J. Geophys. Res.* **95**, 9377–9391.
- Thomas, H. and Ittekkot, V. 2001. Determination of anthropogenic CO_2 in the North Atlantic Ocean using water mass ages and CO_2 equilibrium chemistry. *J. Mar. Syst.* **27**, 325–336.
- Toggweiler, J. R., Dixon, K. and Bryan, K. 1989. Simulations of radiocarbon in a coarse-resolution world ocean model. 1. Steady state prebomb distributions. *J. Geophys. Res.* **94**, 8217–8242.
- Toole, J. and McDougall, T. 2001. Mixing and stirring in the ocean interior. In: *Ocean Circulation and Climate. Observing and Modelling the Global Ocean*, Chap. 5.2 (eds G. Siedler, J. Church and J. Gould), Academic Press, San Diego, USA, 337–356.
- Warren, B. 1981. Deep circulation of the world ocean. In: *Evolution of Physical Oceanography* (eds B. Warren and C. Wunsch), MIT Press, Cambridge, MA, 6–41.
- Waugh, D. W. and Hall, T. M. 2005. Propagation of tracer signals in boundary currents. *J. Phys. Oceanogr.* **35**, 1538–1552.
- Wunsch, C. 2002. Oceanic age and transient tracers: analytical and numerical solutions. *J. Geophys. Res.* **107**, 3048, doi:10.1029/2001JC000797.

The leaky funnel model revisited

Anne MOUCHET*, Eric DELEERSNIJDER^{†‡}
and François PRIMEAU[§]

Submitted to Tellus, May 19, 2011

Abstract

Mouchet and Deleersnijder (2008) proposed an idealized view of the global ocean ventilation. They considered the flow as occurring in a porous pipe with decreasing section (a leaky funnel). The agreement between the domain-averaged ages as obtained with a coarse-grid 3D OGCM and the leaky funnel is excellent. Further, it allows to infer characteristic scales which are consistent with the current knowledge of the ocean ventilation. However, the calibration and validation method, based on numerical experiments in which the circulation fields of the OGCM were artificially modified, is in contradiction with the OGCM internal dynamics. In this note we revisit the leaky funnel and base our study on the global water age distribution $\varphi(\tau)$, where $\varphi(\tau)\Delta\tau$ is the ocean volume fraction whose age lies in the interval $[\tau, \tau + \Delta\tau]$. The steady-state analytical solution for this distribution is seen to be in excellent agreement with the numerical results from two coarse grid OGCMs. This outcome helps to eliminate any concern about possible biases stemming from the calibration method of Mouchet and Deleersnijder (2008). Furthermore it provides a possible interpretation of the deep ocean ventilation properties. It suggests that for large ages, water parcels have the same life expectancy, whatever their age.

*Corresponding author;

A.Mouchet@ulg.ac.be, Université de Liège, Astrophysics, Geophysics and Oceanology Department, 17 Allée du Six-Août, 4000 Liège, Belgium

[†]Université catholique de Louvain, Institute of Mechanics, Materials and Civil Engineering (iMMC), 4 Avenue G. Lemaître, 1348 Louvain-la-Neuve, Belgium

[‡]Université catholique de Louvain, Earth and Life Institute (ELI), Georges Lemaître Centre for Earth and Climate Research (TECLIM), 2 chemin du Cyclotron, 1348 Louvain-la-Neuve, Belgium

[§]Department of Earth System Science, University of California at Irvine, Rowland Hall, Irvine, CA 92697, USA

1 Introduction

The rate at which the ocean can sequester excess heat and carbon from the atmosphere is determined by its ventilation, i.e. the renewal of interior waters by seawater that has been in contact with the atmosphere. In the context of climate and environmental studies it is of importance to better assess ocean ventilation rate and its properties. The age, which measures the time needed for water parcels to travel from the ocean surface to the interior, is the appropriate tool for this purpose. Of use are numerical simulations and field measurements of appropriate tracer concentrations. However, the intrinsic complexity of water masses circulation and the huge amount of information provided by OGCMs make it difficult to extract the most relevant information on spatial and temporal scales characterising ventilation. On the other hand, low-order representations of the world ocean circulation, despite their simplifying hypotheses, very often supply the means allowing one to gain some insight into the main flow characteristics (e.g., *Munk, 1966; Craig, 1971; Jenkins, 1998; Maier-Reimer, 1993; Munk and Wunsch, 1998; Broecker and Peng, 2000*).

Along this line *Mouchet and Deleersnijder (2008)* (hereinafter referred to as MD08) suggested an idealised model which provides a scaling of the water age. A 1D advection-diffusion model is proposed in which the interior ocean is represented as a leaky pipe with decreasing section (i.e. a leaky funnel) - allowing recirculation of water and tracers toward the surface (Fig. 1). The analytical solutions to the steady-state problem are readily obtained and yield expressions of the domain averaged-ages as functions of three independent parameters which determine the flow characteristic scales.

A series of experiments with a 3D OGCM allow for the calibration and validation of the leaky funnel representation. The agreement between the domain-averaged ages (water and radiocarbon) as obtained with the OGCM and with the leaky funnel is excellent. Moreover the parameters derived from this exercise have a clear physical meaning; the turnover time, the mean length of trajectories, and the diffusivity scale being consistent with our current knowledge of the World Ocean circulation.

Despite the amount of converging results some concerns were raised about the calibration and validation method of MD08. Specifically they pointed to the fact that their method disregards the OGCM internal dynamics.

MD08 generated a set of dynamical fields by multiplying by spatially uniform values the reference velocity and diffusivity fields from the OGCM. These artificial solutions do not represent possible oceanic circulation states. Only the reference state is entirely physically relevant. The perturbed states were designed with the sole objective of answering the question “What would

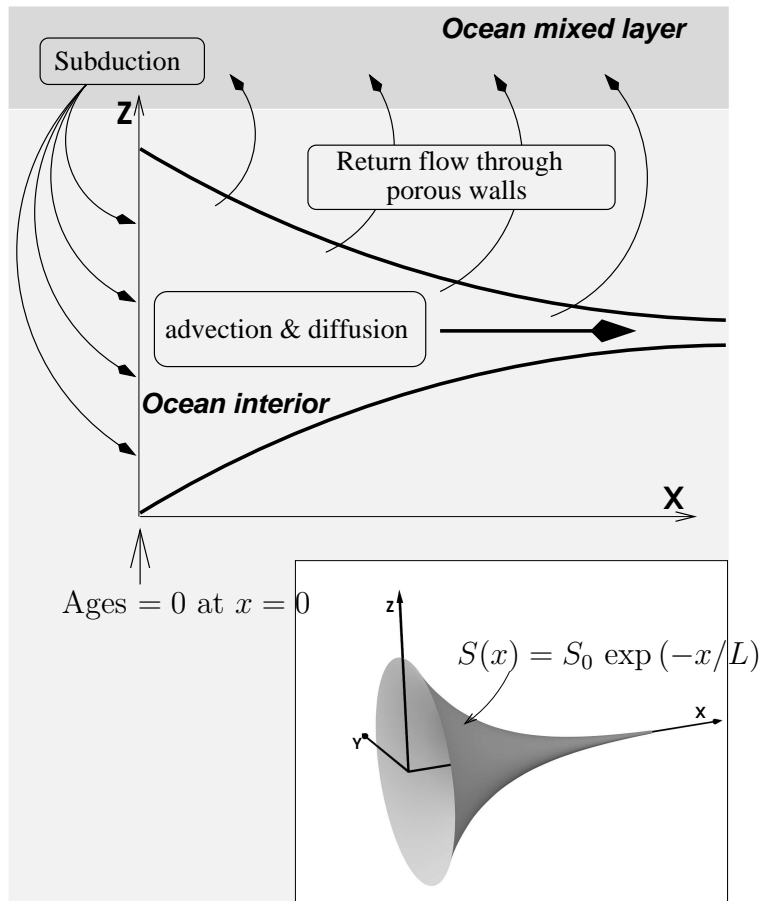


Figure 1: Schematic representation of the leaky funnel model. A 3D view is given in the inset while the main figure consists of a projection onto the x - z plane. The leaky funnel extends from $x = 0$ to $x = \infty$ with a decreasing section. The entrance of the funnel is fueled with water subducted from the ocean surface. The porous walls allow water to escape the funnel. Advection and diffusion control the transport within the funnel. At the entrance (boundary at $x = 0$) concentrations are set to unity and ages to zero.

be the ventilation (or age distribution) under different conditions of velocity and diffusivity?”. This question arises from the need to evaluate the parameters of the leaky funnel representation. A similar approach was previously used by *Heinze et al.* (1991) in the search for the causes of the glacial–interglacial atmospheric CO₂ variations. Such artificial modifications are aimed at evaluating the consequences of a circulation change on tracer distributions. However they are rather questionable.

Performing experiments in which the diffusivity and the velocity fields are independently multiplied by spatially-homogeneous values is in contradiction with the OGCM internal dynamics (buoyancy, momentum, surface forcing...) and satisfy none of the finite-difference approximations of the OGCM, except the continuity equation. Another disadvantage of the method of MD08 stems from the fact that a significant number of long-duration numerical experiments are necessary in order to calibrate the parameters of the simplified model.

Further developments based on the water age distribution (a generalisation of the age distribution function of *Bolin and Rodhe* (1973)) offer now the opportunity to revisit the leaky funnel model and eliminate any concern about possible biases stemming from the calibration method of MD08. These new developments yield a supplementary and fully coherent validation of the leaky funnel representation. Indeed the water age distribution function is obtained from the 3D OGCM reference state - hence concerns about the validity of results obtained with the 3D OGCM artificial states are eliminated. Eventually the water age distribution function suggests interpretations of the deep ocean ventilation properties which result in the excellent correspondence between 3D and 1D domain-averaged ages. Besides, in contrast to MD08 only one numerical experiment is sufficient for estimating the leaky funnel parameters from which characteristic flow scales may be drawn.

This simple analog has a potential for applications in modelling studies. It may help in evaluating the relative importance, at the largest scales of motion, of advection and diffusion in 3D models.

The paper is organised as follows. After presenting the water age distribution function in section 2 the analytical solutions for the leaky funnel are established in 3. The results from the 3D OGCMs are presented and examined in section 4 which is followed by a discussion of the results (section 5). Conclusions are presented in section 6

2 Global water age distribution

The aim of this work being the assessment of ocean ventilation timescales, we focus on water age distribution. This distribution naturally stems from the definition of the concentration distribution function (*Deleersnijder et al.*, 2001; *Delhez and Deleersnijder*, 2002; *Delhez et al.*, 2003) expressed for seawater. The concentration distribution function $c(t, \mathbf{x}, \tau)$ is defined so that $c(t, \mathbf{x}, \tau) \Delta\tau$, for $\Delta\tau \rightarrow 0$, represents the contribution of the material with an age comprised between τ and $\tau + \Delta\tau$ to the total concentration¹ $C(t, \mathbf{x})$ at time t and position \mathbf{x} . $C(t, \mathbf{x})$ is then obtained from the integration of c in the age space. Since seawater is the aggregate of every constituents composing it, its concentration is equal to unity, and its concentration distribution function obeys

$$C(t, \mathbf{x}) = \int_0^\infty c(t, \mathbf{x}, \tau) d\tau = 1 \quad (1)$$

The *mean water age* a is obtained from the first-order moment of the concentration distribution function (*Delhez et al.*, 1999; *Deleersnijder et al.*, 2001):

$$a(t, \mathbf{x}) = \frac{1}{C(t, \mathbf{x})} \int_0^\infty \tau c(t, \mathbf{x}, \tau) d\tau = \int_0^\infty \tau c(t, \mathbf{x}, \tau) d\tau. \quad (2)$$

Hence $c(t, \mathbf{x}, \tau)$ is the distribution function for water age and will from now on be referred to as the *water age distribution*.

The *global water age distribution* results from the integration of $c(t, \mathbf{x}, \tau)$ over the volume Ω of the domain of interest

$$\varphi(t, \tau) = \frac{1}{\Omega} \int_\Omega c(t, \mathbf{x}, \tau) d\Omega. \quad (3)$$

For $\Delta\tau \rightarrow 0$, $\Omega \varphi(\tau) \Delta\tau$ represents the volume of water with an age comprised in the interval $[\tau, \tau + \Delta\tau]$. Expressions (3) and (1) lead to the following normalisation condition on φ

$$\int_0^\infty \varphi(t, \tau) d\tau = 1. \quad (4)$$

The global water age distribution as given by (3) is a generalisation of the age distribution function of *Bolin and Rodhe* (1973) who restricted their study to steady-state problems. Furthermore, the global water age distribution is closely related to the *cumulative ventilation rate distribution* $\Phi(\tau)$

¹ C represents a mass fraction, i.e. the ratio of the total mass of the constituent in the sample to the total mass of the sample.

introduced in *Primeau and Holzer (2006)*. In the case of a steady flow $M\varphi(\tau) = \Phi(\tau)$ where M is the total mass of the fluid. The quantity $\Phi(\tau)$ having units of mass/time can be interpreted as the entering mass flux of surface waters that will reside in the interior for a time τ or longer before exiting (*Primeau and Holzer, 2006; Hall et al., 2007*).

On the other hand, $\varphi(\tau)$ is conceptually different from the *global distribution of mean water age* $\phi(a)$ examined in MD08. Computed directly with the help of mean water ages $\phi(a)\Delta a$ represents the fraction of the volume occupied by water with mean ages comprised in the interval $[a, a + \Delta a]$. It takes the following form

$$\phi(t, a) = \lim_{\Delta a \rightarrow 0} \frac{1}{\Omega \Delta a} \int_{\Omega} \square_{a, a+\Delta a}(a'(\mathbf{x})) d\Omega, \quad (5)$$

in which \square is the rectangular function:

$$\square_{a, a+\Delta a}(a') = \begin{cases} 1 & \text{if } a \leq a' \leq a + \Delta a, \\ 0 & \text{otherwise.} \end{cases} \quad (6)$$

Since the presence of diffusion generates differences in pathways toward the final location, a water parcel is characterized by a range of ages, rather than a single age. Therefore, $\phi(a)$ the global distribution of mean water age does not adequately represent the age distribution in the domain. On the other hand $\varphi(\tau)$ which is based on the individual ages provides a correct domain age distribution. Only in the case of a purely advective flow would both functions be identical.

The domain-averaged water age or *global mean water age* is obviously related to φ by

$$\langle a(t) \rangle = \frac{1}{\Omega} \int_{\Omega} a(t, \mathbf{x}) d\Omega = \frac{1}{\Omega} \int_{\Omega} \int_0^{\infty} \tau c(t, \mathbf{x}, \tau) d\tau d\Omega = \int_0^{\infty} \tau \varphi(t, \tau) d\tau. \quad (7)$$

The global water age distribution is obtained by computing $c(t, \mathbf{x}, \tau)$ for the problem at stake and then integrating it over the domain. The equation governing the evolution of $c(t, \mathbf{x}, \tau)$ is (*Delhez et al., 1999; Deleersnijder et al., 2001; Delhez and Deleersnijder, 2002*):

$$\frac{\partial c}{\partial t} = -\nabla \bullet (\mathbf{u}c - \mathbf{K} \bullet \nabla c) - \frac{\partial c}{\partial \tau}, \quad (8)$$

with \mathbf{u} the velocity vector and \mathbf{K} the diffusivity tensor which must be symmetric and positive definite (*Deleersnijder et al., 2001*).

In the context of ocean ventilation studies, solutions to (8) are sought by tagging water masses that were once exposed to the surface where the

concentration and the age are set to 1 and 0, respectively. This is achieved through imposing that at the ocean surface S

$$c(t, \mathbf{x}, \tau) = \delta(\tau), \text{ for } \mathbf{x} \in S. \quad (9)$$

with δ the Dirac function.

3 Leaky funnel solutions

In this text we restrict the description of the leaky funnel to its key aspects. The interested reader will find a detailed description of this model together with the mathematical expressions and derivations of analytical solutions in MD08.

The leaky funnel (Fig. 1) is a semi-infinite pipe characterized by a cross-sectional area $S(x)$ which is a decreasing function of x , the downstream coordinate ($0 \leq x < \infty$). Both advection and diffusion processes contribute to the transport in the funnel. The porous outer envelope allows water to escape the domain while being transported downstream. Assuming further that all variables and properties are homogeneously distributed over S , i.e., they solely depend on x and t , yields a one dimensional problem.

In this configuration the evolution of the water age distribution $c(t, x, \tau)$ in the leaky funnel obeys

$$S \frac{\partial c}{\partial t} + \frac{\partial(SUc)}{\partial x} = -Qc + \frac{\partial}{\partial x} \left(SK \frac{\partial c}{\partial x} \right) + S \frac{\partial c}{\partial \tau}, \quad (10)$$

with U and K the velocity and the diffusivity, respectively, and where $Q(t, x)$ represents the water flux leaving the funnel through the porous lateral boundary. This flux is obtained from the continuity equation which reads

$$\frac{\partial(SU)}{\partial x} = -Q. \quad (11)$$

In order to obtain analytical solutions we take U and K as positive constants and assume that all variables are at a steady state. We also impose that the funnel section decreases exponentially with a constant length scale L : $S(x) = S_0 \exp(-x/L)$.

Under these assumptions (10) reduces to the classical one dimensional problem of advection and diffusion in a semi-infinite pipe with a constant section:

$$\frac{\partial c}{\partial \tau} = -U' \frac{\partial c}{\partial x} + K \frac{\partial^2 c}{\partial x^2}. \quad (12)$$

The modified velocity $U' = U + K/L$ arises from the section change with x .

We solve equation (12) by imposing condition (9) at the funnel entrance, $c(x = 0, \tau) = \delta(\tau)$, together with the additional constraints

$$c(x, \tau = 0) = 0, \text{ and } c(x = \infty, \tau) = 0. \quad (13)$$

The solution to (12) under such conditions is found to be (e.g., *Hall and Haine, 2002; Delhez et al., 2003*):

$$c(x, \tau) = \frac{x}{\sqrt{4\pi K \tau^3}} \exp \left[-\frac{(x - U'\tau)^2}{4K\tau} \right]. \quad (14)$$

The leaky funnel domain is semi-infinite but its volume is finite ($\Omega = \int_0^\infty S(x)dx = S_0 L$), therefore domain-averaged quantities may be computed.

The global water age distribution, obtained by integrating (14) over Ω , is given by the following expression:

$$\begin{aligned} \varphi(\tau) &= \frac{1}{L} \int_{\Omega} e^{-x/L} c(x, \tau) dx \\ &= \sqrt{\frac{K}{\pi L^2 \tau}} \exp \left(-\frac{U'^2}{4K} \tau \right) + \frac{1}{\theta} \left[1 + \operatorname{erf} \left(\frac{1}{\theta} \sqrt{\frac{L^2}{K}} \tau \right) \right] \exp \left(-\frac{U}{L} \tau \right), \end{aligned} \quad (15)$$

in which

$$\frac{1}{\theta} = \frac{1}{2} \left(\frac{U}{L} - \frac{K}{L^2} \right), \text{ and } \operatorname{erf}(y) = \frac{2}{\sqrt{\pi}} \int_0^y e^{-\xi^2} d\xi.$$

To get the global water age distribution (15) as well as forthcoming expression (16), integrals involving the water age distribution have to be performed, a task that may be achieved with the help of *Gradshteyn and Ryzhik* (2000) or a symbolic calculation software.

The normalisation condition (4) for $\varphi(\tau)$ holds true, as is demonstrated in Annex Appendix A (page 16).

The mean water age is found to be

$$a(x) = \int_0^\infty \tau c(x, \tau) d\tau = \frac{x}{U'}. \quad (16)$$

The global mean water age or domain-averaged water age $\langle a \rangle$ is given by the timescale L/U' :

$$\langle a \rangle = \Omega^{-1} \int_0^\infty a(x) S(x) dx = \int_0^\infty \tau \varphi(\tau) d\tau = \frac{L}{U'}. \quad (17)$$

4 3D OGCM experiments

In order to test the leaky funnel representation we perform numerical experiments with the help of two Ocean General Circulation Models (OGCM). Besides the annual mean circulation from the Louvain-la-Neuve OGCM (*Deleersnijder and Campin, 1995; Campin and Goosse, 1999*), which we utilized in MD08, we also take three-dimensional fields provided by the dynamical Large-Scale Geostrophic Ocean General Circulation Model (*Maier-Reimer et al., 1993*) in its annually averaged version (*Winguth et al., 1999; Heinze et al., 2003*). A description of the main characteristics of these OGCMs is given in appendix Appendix B.

At a steady state (8) reduces to the usual equation describing the evolution of concentration in which time is replaced by τ :

$$\frac{\partial c}{\partial \tau} = -\nabla \bullet (\mathbf{u}c - \mathbf{K} \bullet \nabla c). \quad (18)$$

The steady-state water age distribution can, thus, be obtained as the transient solution of a classical advection–diffusion problem (*Beckers et al., 2001; Delhez and Deleersnijder, 2002*).

Equation (18) is solved numerically with the same transport scheme as that used for tracers in the 3D model. Advective and diffusive fluxes across the ocean floor and lateral boundaries are set to zero. We impose homogeneous initial conditions: $c(\mathbf{x}, \tau = 0) = 0$ for \mathbf{x} belonging to the ocean domain.

At the ocean surface S the boundary condition should be given by (9) rewritten for steady state

$$c(\mathbf{x}, \tau) = \delta(\tau), \text{ for } \mathbf{x} \in S, \quad (19)$$

For a stationary problem c is therefore provided by the impulse response or Green’s function (*Beckers et al., 2001*).

There are technical difficulties linked to the use of a Dirac impulse as boundary condition. In order to circumvent these we take advantage of the fact that the impulse response may be obtained from the derivative of the step response. Indeed the delta function can be viewed as the derivative of the unit or Heaviside step function, $dH(\tau)/d\tau = \delta(\tau)$ ($H(\tau) = 1$ for $\tau \geq 0$ and $H(\tau) = 0$ for $\tau < 0$). We then numerically solve (18) for a function which we denote c^* . This solution is obtained under the same constraints as applied to c of homogeneous initial conditions and of no flux across the boundaries but the boundary condition for c^* at the ocean surface is

$$c^*(S, \tau) = H(\tau). \quad (20)$$

The derivative with respect to τ of c^* yields the water age distribution in the 3D model. One finally obtains the global water age distribution (Figure 2) by computing the domain-average of $c(\mathbf{x}, \tau)$ at each time step.

5 Results and Discussion

5.1 Characteristic scales

The parameters needed to fully determine the leaky funnel distribution (15) may be deduced by fitting this expression to the data resulting from the 3D OGCM experiments. For this purpose, it is necessary to identify independent parameters. Two distinct timescales stem from a close examination of the parameters intervening in (15): $A_0 = L/U$ and $A_D = L^2/K$, the advection and diffusion timescales characterizing the flow. Re-expressing (15) by means of the definitions for A_0 and A_D leads to

$$\begin{aligned} \varphi(\tau) = & \sqrt{\frac{1}{\pi A_D \tau}} \exp \left[-\frac{1}{4A_D} \left(1 + \frac{A_D}{A_0} \right)^2 \tau \right] \\ & + \frac{1}{\theta} \left[1 + \operatorname{erf} \left(\frac{1}{\theta} \sqrt{A_D \tau} \right) \right] \exp \left(-\frac{\tau}{A_0} \right), \end{aligned} \quad (21)$$

and

$$\frac{1}{\theta} = \frac{1}{2} \left(\frac{1}{A_0} - \frac{1}{A_D} \right).$$

We are hence left with two parameters to be determined, A_0 , and A_D .

The non-linear least squares fitting procedure in IDL MPFIT (*Markwardt*, 2009) based on the Levenberg-Marquardt algorithm (*Moré*, 1978) is used to evaluate those two parameters from the OGCM global water age distribution. In order to prevent large values at very low ages to dominate the solution we specify weights to the OGCM results inversely proportional to the function values². The OGCM responses were computed for over twenty thousand years.

Table (1) presents the values of A_0 and A_D obtained with this method,

²We tested this method by also considering weights linearly increasing with τ or by using the square root of the function. Those methods produce results which are extremely close to those presented herein.

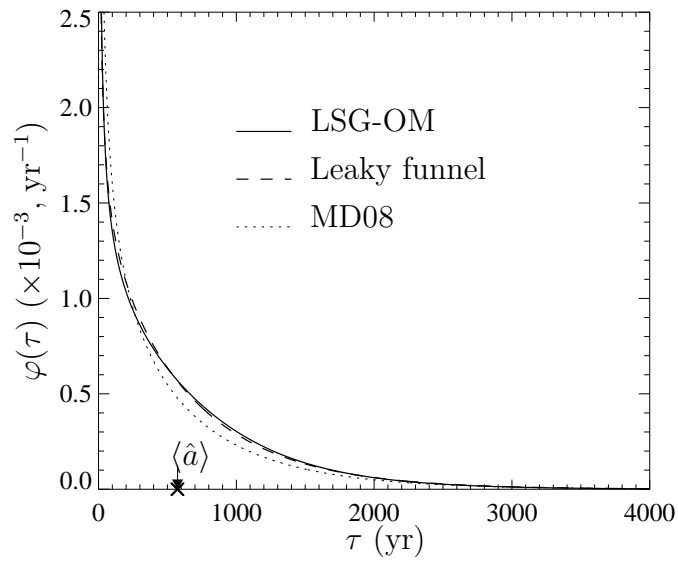
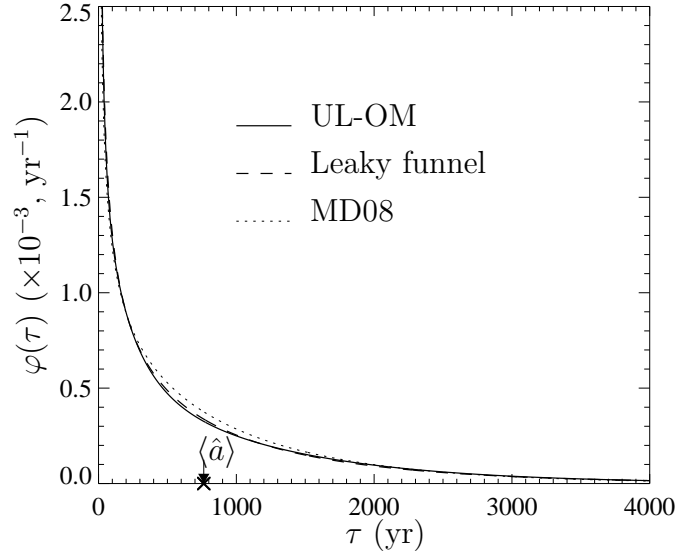


Figure 2: Global water age distribution (solid line) versus age in two 3D OGCMs (of which a description may be found in Appendix Appendix B), UL-OM (top) and LSG-OM (bottom), compared to that predicted by the leaky funnel (dotted line). The leaky funnel curve in each panel is obtained with the parameters appropriate to the corresponding OGCM from Table 1. The curve obtained with the method of MD08 is also represented (dash). The arrow points to the estimate of the global mean water age $\langle \hat{a} \rangle$ while the \times on the τ axis corresponds to the actual global mean water age $\langle a \rangle$ obtained with each OGCM.

Table 1: Parameters A_0 and A_D of the leaky funnel model as obtained from a least squares fit to the 3D model results. The estimated Pe number and global mean water age are given in columns four and five, respectively. The last column contains the actual global mean water age from the 3D OGCM experiment.

OGCM	A_0	A_D	Pe	$\langle \hat{a} \rangle$	$\langle a \rangle$
	yr	yr		yr	yr
UL-OM	1243	1982	1.6	764	764
LSG-OM	644	5249	8.1	574	573

together with the estimated Peclet number and global mean water age $\langle \hat{a} \rangle$:

$$Pe = \frac{UL}{K} = \frac{A_D}{A_0}, \quad (22)$$

$$\langle \hat{a} \rangle = \frac{L}{U'} = \left(\frac{1}{A_0} + \frac{1}{A_D} \right)^{-1}. \quad (23)$$

As can be seen the concordance between estimated and actual OGCM global mean water ages is excellent and there is a fair agreement between the experimental (OGCM) and theoretical (leaky funnel) curves (Figure 2). Figure 2 also contains the distribution given by equation (21) but in which we imposed the parameters as obtained with the MD08 method. The distributions obtained with the method of MD08 are consistent with those arising from the present work. This allows to lift any concern about the conclusions of MD08. The differences between the curves resulting from the present work and that produced by the MD08 method may be explained by the fact that the latter relies on global water ages which principally reflect the deep ocean properties (since it occupies the largest volume). In addition, the upper layers, with smaller relative volume contribution to the mean, are characterized by very small ages. On the contrary, the global water age distribution provides information for all ages, and, hence, it is more impacted by the response of the upper layers of the ocean.

It should not be concluded from the values in Table 1 that the transport in LSG-OM is less diffusive than in UL-OM. Numerical diffusion, which is not accounted for in the present study, is congruent with the upstream scheme used for resolving advection in LSG-OM. As commented on in MD08, ignoring the role played by numerical diffusivity results in an overestimate of A_D and, since (23) holds, in an underestimate of A_0 . A study of the LSG-OM ages with the method of MD08, which allows to take into account both the

explicit and the numerical diffusivities, leads to the conclusion that the effective Pe of both models is of the same order of magnitude ($Pe \sim 2 - 3$; *Mouchet, 2011*). The two models however differ drastically with respect to their A_0 scales, UL-OM being characterized by the largest value. This reflects the more sluggish circulation in the Pacific Ocean predicted by UL-OM. The Peclet numbers associated to the interior circulation appear to be rather low. Other studies also pointed to the possibility that the large scale transport in the ocean might be more dominated by diffusion than previously thought (*Deleersnijder et al., 2002; Holzer and Primeau, 2006*). However these conclusions result from experiments with coarse grids OGCMs. Reassessing them by means of eddy-resolving models would be necessary.

5.2 Asymptotic analysis

The asymptotic properties of the global distribution may provide some insight into ocean processes as reproduced by OGCMs. Two regimes are identified considering the behavior of φ at low or large ages.

For $\tau \rightarrow 0$ solution (21) behaves like

$$\varphi(\tau) \sim \frac{1}{\sqrt{\pi A_D \tau}}, \quad (24)$$

an expression which does not involve advection. Diffusion is the main process controlling the distribution for $\tau \rightarrow 0$. As opposed to advection, which has a finite propagation speed, the parabolic nature of diffusion transmits the initial perturbation at once to areas far from the boundary. Hence in the early stages regions rapidly exchanging with the surface dominate the solution. This feature is made clear in Figure 3 where it is seen that the global water age distribution closely follows (24) for ages that are typical of newly formed water masses.

The $\tau^{-1/2}$ singularity of $\varphi(\tau)$ at $\tau = 0$ is a physical consequence of diffusion (*Primeau and Holzer, 2006; Hall et al., 2007*). This singularity reflects the fact that the gross (one-way) flux into the interior is infinite as it is dominated by fluid elements that reside in the interior for infinitesimally short times before they make contact with the surface and exit the domain. A simple random walk model is presented in *Hall and Holzer (2003)* to illustrate the phenomenon.

The role of diffusion also explains the discrepancy between the global distribution of mean age ϕ and φ (Figure 3). For the leaky funnel, as established in MD08, ϕ takes the form:

$$\phi(a) = \frac{e^{-a/\langle \hat{a} \rangle}}{\langle \hat{a} \rangle}. \quad (25)$$

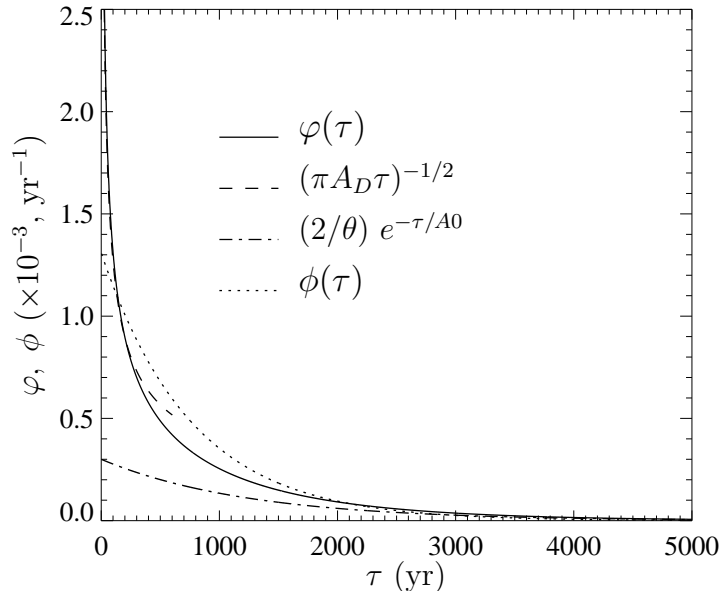


Figure 3: Global water age distribution $\varphi(\tau)$ in the leaky funnel (solid line) versus age. The two asymptotes when $\tau \rightarrow 0$ and $\tau \rightarrow \infty$ are represented by the dashed and dot-dash lines, respectively. Also illustrated is the global distribution of mean water age $\phi(\tau)$ (dotted line). We build these curves with the help of the A_0 and A_D values obtained with the UL-OM model.

ϕ is computed with the help of the global mean water age, that is an equilibrium age reflecting mostly the deep ocean properties. Only in the case of negligible diffusion does ϕ correctly approximate φ . Indeed, if $K \rightarrow 0$, then φ reduces to

$$\varphi(\tau) \sim \frac{e^{-\tau/A_0}}{A_0}, \quad (26)$$

which is equivalent to (25) since $\langle a \rangle \rightarrow A_0$ when $K \rightarrow 0$.

For large ages φ may be approximated by

$$\varphi(\tau) \sim (2/\theta)e^{-\tau/A_0}, \text{ for } \tau \rightarrow \infty. \quad (27)$$

This distribution is identical to that characterizing a first-order removal process (*Bolin and Rodhe, 1973*) with an e-folding decay given by the advection time scale A_0 . This behavior means that, above some age, the probability to escape the main flow is identical for all particles, whatever their age.

The fact that both the leaky funnel and the OGCMs behave as first-order removal processes for $\tau \rightarrow \infty$ is a consequence of the finite volume of their domains which ensures that the advection-diffusion transport operators have discrete eigenmode expansions. In the limit as $\tau \rightarrow \infty$, solutions are dominated by the most slowly decaying eigenmode (*Primeau and Holzer, 2006; Primeau and Deleersnijder, 2009*). The least-squares fit of the leaky funnel model parameters to the OGCMs' global water age distribution for ages ranging from zero to more than twenty thousand years ensured a close correspondence of the most slowly decaying eigenvalues for the OGCMs and the leaky funnel model. Indeed, if the least-squares fit had been performed over an infinite age interval the dominance of the solution by the most slowly decaying eigenmode for large ages would have ensured exact equality between the advective timescale A_0 for the leaky funnel model and the reciprocal of the most slowly decaying eigenmode of the OGCMs' advection-diffusion transport operator subject to Dirichlet boundary conditions.

The age distribution as computed here also provides information on the adjustment after a sudden change in the system. The analysis of the leaky funnel approximation suggests the existence of two regimes in the response of ocean water masses. The amount of very young particles is very large, indicating a fast exchange with the boundary. This results in the rapid initial decrease in the adjustment. As age (or time) progresses a longer time scale controls the distribution and the response. Away from areas of water masses renewal, in the interior, the adjustment rate is given by the advective time scale, which also represents the turnover time of the leaky funnel. The response time of the interior ocean as a whole is then given by A_0 , the eigenmode with smallest absolute value, corresponding to the slowest change with time.

6 Conclusion

The leaky funnel representation seems able not only to capture the mean water ages (*Mouchet and Deleersnijder, 2008*) but also, as demonstrated in this work, the global water age distribution predicted by two different OGCMs. Some intrinsic process of the ocean circulation such as reproduced by OGCMs must then have been captured by this simple 1D model. One conclusion of this work is that the deep ocean seems to behave like a first-order system.

The good correlation between the age distributions in the leaky funnel and in the OGCMs provides a further validation for this representation and allows any concern about the method of MD08 to be lifted. The MD08

method allows to separate for the respective contributions of explicit and numerical diffusivities in determining the circulation. The global water age distribution does not offer the possibility for such a distinction to be made. On the other hand, it is sufficient to perform only one numerical experiment in order to obtain φ and calibrating the 1D model parameters, while the MD08 method calls for a rather large number of numerical experiments, some of them needing to be performed over more than 20 kyr in order to achieve steady state. Apart from the information on the numerical diffusion present in OGCMs the method based on the global water age distribution provides additional information which is not offered by global mean ages.

Both the global mean water age and global water age distribution predicted by the 1D leaky funnel representation agree closely with those given by the more complex 3D OGCMs. At this stage we are still lacking a complete explanation for such similitude. However, it must be stressed that there are many examples of reduced-dimension models that proved highly successful at representing the state of much more complex models (e.g., *Deleersnijder et al., 1997; Tartinville et al., 1997; Deleersnijder et al., 1998*).

7 Acknowledgement

We are grateful to Arne Winguth, Ernst Maier-Reimer, and Jean-Michel Campin for kindly providing the 3D OGCM transport fields. Eric Deleersnijder is a Research Associate with the Belgian Fund for Scientific Research (F.R.S. - FNRS). François Primeau was supported by NSF grant OCE-0726871.

Appendix A

Proof that $\varphi(\tau)$ as given by (15) verifies the normalisation condition (4)

The integration of (15) is made easier by first rewriting it as follows

$$\begin{aligned} \varphi(\tau) = & \sqrt{\frac{K}{\pi L^2 \tau}} \exp\left(-\frac{U'^2 \tau}{4K}\right) + \frac{1}{\theta} \exp\left(-\frac{U\tau}{L}\right) \\ & + \frac{1}{\theta} \operatorname{erf}\left(\frac{1}{\theta} \sqrt{\frac{L^2 \tau}{K}}\right) \exp\left(-\frac{U\tau}{L}\right) \end{aligned} \quad (28)$$

We treat separately the integration of each of the three terms on the right handside of (28).

The integration of the first term is performed with the help of

$$\int_0^\infty y^n \exp(-ay) dy = \frac{\Gamma(n+1)}{a^{n+1}},$$

(Abramowitz and Stegun, 1972) in which we set $n = -1/2$ and $a = U'^2/(4K)$. Since $\Gamma(1/2) = \sqrt{\pi}$ we get

$$\sqrt{\frac{K}{\pi L^2}} \int_0^\infty \tau^{-1/2} \exp\left(-\frac{U'^2 \tau}{4K}\right) d\tau = \frac{2K}{LU'} \quad (29)$$

The integration of the second term is straightforward

$$\int_0^\infty \frac{1}{\theta} \exp\left(-\frac{U\tau}{L}\right) d\tau = \frac{L}{U\theta} \quad (30)$$

For the treatment of the last term we take advantage of the following properties of the error function:

$$\frac{d}{dy} \operatorname{erf}(y) = \frac{2}{\sqrt{\pi}} \exp(-y^2), \quad \operatorname{erf}(0) = 0, \quad \text{and} \quad \operatorname{erf}(\infty) = 1.$$

We then make use of the integration by parts relationship

$$\int f(\tau) g'(\tau) d\tau = f(\tau) g(\tau) - \int f'(\tau) g(\tau) d\tau.$$

Setting

$$f = \operatorname{erf}\left(\frac{1}{\theta} \sqrt{\frac{L^2 \tau}{K}}\right), \quad \text{and} \quad g' = \exp\left(-\frac{U\tau}{L}\right),$$

it follows

$$f' = \frac{1}{\theta} \sqrt{\frac{L^2}{K\pi}} \tau^{-1/2} \exp\left(-\frac{L^2 \tau}{K\theta^2}\right), \quad \text{and} \quad g = -\frac{L}{U} \exp\left(-\frac{U\tau}{L}\right).$$

The integral then becomes

$$\begin{aligned} & \int_0^\infty \frac{1}{\theta} \operatorname{erf}\left(\frac{1}{\theta} \sqrt{\frac{L^2 \tau}{K}}\right) \exp\left(-\frac{U\tau}{L}\right) d\tau \\ &= -\frac{L}{\theta U} \left[\operatorname{erf}\left(\frac{1}{\theta} \sqrt{\frac{L^2 \tau}{K}}\right) \exp\left(-\frac{U\tau}{L}\right) \right]_0^\infty \\ & \quad + \frac{L^2}{U\theta^2 \sqrt{K\pi}} \int_0^\infty \tau^{-1/2} \exp\left(-\left(\frac{U}{L} + \frac{L^2}{K\theta^2}\right)\tau\right) d\tau \\ &= \frac{L^2}{U\theta^2} \frac{\Gamma(1/2)}{\sqrt{K\pi}} \frac{1}{\sqrt{\frac{U}{L} + \frac{L^2}{K\theta^2}}} = \frac{L^2}{U\theta^2} \frac{1}{\sqrt{\frac{UK}{L} + \frac{L^2}{\theta^2}}}. \end{aligned} \quad (31)$$

Adding together (29), (30), and (31) one easily gets that (15) verifies condition (4).

Appendix B

Main features of the OGCMs used in this study

The transport model is driven by three-dimensional fields of velocity components, potential temperature, salinity, and convective mixing from two OGCMs in their annually averaged versions. The numerical scheme of the off-line transport model is adapted according to the OGCM fields driving it so that the physics determining the distribution of tracers is as close as possible to that determining the distribution of active variables in the dynamical model. Both these models belong to the coarse-grid OGCM class as none of them is eddy-resolving. They nevertheless capture the essential of deep ocean circulation. A short description of both OGCMs follows.

- UL-OM: Louvain-la-Neuve OGCM (*Deleersnijder and Campin, 1995; Campin and Goosse, 1999*).

UL-OM is a primitive-equation, free-surface OGCM resting on the usual set of assumptions, i.e., the hydrostatic equilibrium and the Boussinesq approximation. The horizontal resolution is $3^\circ \times 3^\circ$. The so-called “z-coordinate” underlies a vertical discretization with 15 levels ranging in thickness from 20 m at the surface to 700 m in the deep ocean. A realistic bathymetry is used. The parameterization of vertical mixing is based on the *Pacanowski and Philander (1981)* formulation. Wherever the vertical density profile is unstable, the vertical diffusivity (*Marotzke, 1991*) is increased to $10 \text{ m}^2 \text{ s}^{-1}$. The parameterization of dense water flow down topographic features of *Campin and Goosse (1999)* is applied in the model. The experimental set up for the OGCM circulation corresponds to the control run described in *Campin et al. (1999)*. This OGCM was assessed against the global distributions of temperatures, salinities as well as the estimated values of water transport in different locations (North Atlantic, Drake passage...). The circulation of this OGCM reasonably reproduces the pre-bomb $\Delta^{14}\text{C}$ distribution in the deep ocean (*Mouchet and Deleersnijder, 2008*).

- LSG-OM: Large-Scale Geostrophic Ocean General Circulation Model (*Maier-Reimer et al., 1993; Mikolajewicz et al., 1993*).

The Hamburg large-scale geostrophic model (LSG) has been used in a number of climate and ocean tracer studies (e.g., *Mikolajewicz et al., 1997; Winguth et al., 1999; Heinze et al., 2003; Dutay et al., 2004*). It is

based on the conservation laws for heat, salt, and momentum, the full equations of state, the hydrostatic approximation and the Boussinesq approximation. The circulation is divided into a barotropic and a baroclinic components, allowing for free surface elevation changes. It also includes a simple sea ice model to account for brine release during freezing. The formulation of the model is fully implicit. It has a horizontal resolution of $3.5^\circ \times 3.5^\circ$ on a E-grid (*Arakawa and Lamb, 1977*). The water column is subdivided into 11 layers. This model has a smoothed realistic topography. Advection of tracers is solved with the help of an upstream scheme both horizontally and vertically. A horizontal diffusion term ($200 \text{ m}^2 \text{ s}^{-1}$) suppresses mode divergence resulting from the use of a staggered E-grid. Our off-line transport model formulation is very close to that of *Heinze et al. (2003)*. The only difference lies in the treatment of open-ocean convection process, which in our model version takes the form of an explicit diffusion term. As in *Heinze and Dittert (2005)* the annually averaged fields needed to drive the model represent the pre-industrial ocean state and are obtained from a LSG run resolving the seasonal cycle (*Winguth et al., 1999*).

Appendix C

Erratum for MD08

It appears that typing errors affected several equations in MD08. The correct versions follow.

Equations (9) and (10) of MD08 should read:

$$\begin{aligned}
 S \frac{\partial C_\lambda}{\partial t} + \frac{\partial (SUC_\lambda)}{\partial x} &= C_\lambda \frac{\partial (US)}{\partial x} + \frac{\partial}{\partial x} \left(SK \frac{\partial C_\lambda}{\partial x} \right) \\
 &\quad - \lambda SC_\lambda, \\
 S \frac{\partial \alpha_\lambda}{\partial t} + \frac{\partial (SU\alpha_\lambda)}{\partial x} &= \alpha_\lambda \frac{\partial (US)}{\partial x} + \frac{\partial}{\partial x} \left(SK \frac{\partial \alpha_\lambda}{\partial x} \right) \\
 &\quad - \lambda S\alpha_\lambda + SC_\lambda.
 \end{aligned}$$

The correct expression for the volume distribution of water age (3d equation in Appendix A) is

$$\phi(a_w) = \frac{e^{-a_w / \langle a_w \rangle}}{\langle a_w \rangle}.$$

References

- Abramowitz, M., and I. Stegun, *Handbook of mathematical functions*, ninth ed., Dover Publications, New-York, 1972, 1030p.
- Arakawa, A., and V. R. Lamb, Computational design of the basic dynamical process of the UCLA general circulation model, *Methods of Computational Physics*, *17*, 173–265, 1977.
- Beckers, J.-M., E. J. M. Delhez, and E. Deleersnijder, Some properties of generalized age-distribution equations in fluid dynamics, *SIAM J. Appl. Math.*, *61*, 1526–1544, 2001.
- Bolin, B., and H. Rodhe, A note on the concepts of age distribution and transit time in natural reservoirs, *Tellus*, *25*, 58–62, 1973.
- Broecker, W. S., and T.-H. Peng, Comparison of ^{39}Ar and ^{14}C ages for waters in the deep ocean, *Nuclear Instruments and Methods in Physics Research Section B*, *172*, 473–478, 2000.
- Campin, J.-M., and H. Goosse, Parameterization of density-driven downsloping flow for a coarse-resolution ocean model in z-coordinate, *Tellus*, *51*, 412–430, 1999.
- Campin, J.-M., T. Fichefet, and J.-C. Duplessy, Problems with using radiocarbon to infer ocean ventilation rates for past and present climates, *Earth and Planetary Science Letters*, *165*, 17–24, 1999.
- Craig, H., The deep metabolism: oxygen consumption in abyssal ocean water, *Journal of Geophysical Research*, *76*, 5078–5086, 1971.
- Deleersnijder, E., and J.-M. Campin, On the computation of the barotropic mode of a free-surface world ocean model, *Annales Geophysicae*, *13*, 675–688, 1995.
- Deleersnijder, E., J.-M. Beckers, J.-M. Campin, M. El Mohajir, T. Fichefet, and P. Luyten, Some mathematical problems associated with the development and use of marine models, in *The Mathematics of Models for Climatology and Environment*, edited by J. I. Díaz, vol. I48 of *NATO ASI Series*, pp. 39–86, Springer Verlag, Berlin Heidelberg, 1997.
- Deleersnijder, E., J. Wang, and C. N. K. Mooers, A two-compartment model for understanding the simulated three-dimensional circulation in Prince William Sound, Alaska, *Continental Shelf Research*, *18*, 279–287, 1998.

- Deleersnijder, E., J.-M. Campin, and E. Delhez, The concept of age in marine modelling. I. Theory and preliminary model results, *Journal of Marine Systems*, 28, 229–267, 2001.
- Deleersnijder, E., A. Mouchet, E. Delhez, and J.-M. Beckers, On the transient behaviour of water ages in the world ocean, *Mathematical and Computer Modelling*, 36, 121–127, 2002.
- Delhez, E., and E. Deleersnijder, The concept of age in marine modelling: II. Concentration distribution function in the English Channel and the North Sea, *Journal of Marine Systems*, 31, 279–297, 2002.
- Delhez, E., J.-M. Campin, A. C. Hirst, and E. Deleersnijder, Toward a general theory of the age in ocean modelling, *Ocean Modelling*, 1, 17–27, 1999.
- Delhez, E., E. Deleersnijder, A. Mouchet, and J.-M. Beckers, A note on the age of radioactive tracers, *Journal of Marine Systems*, 38, 277–286, 2003.
- Dutay, J.-C., et al., Evaluation of OCMIP-2 ocean models’ deep circulation with mantle helium-3, *Journal of Marine Systems*, 48, 15–36, 2004.
- Gradshteyn, I., and I. Ryzhik, *Tables of Integrals, Series, and Products*, sixth ed., Academic Press, San Diego, 2000.
- Hall, T. M., and T. W. N. Haine, On ocean transport diagnostics: The idealized age tracer and the age spectrum, *Journal of Physical Oceanography*, 32, 1987–1991, 2002.
- Hall, T. M., and M. Holzer, Advective-diffusive mass flux and implications for stratosphere-troposphere exchange, *Geophysical Research Letters*, 30, 1222, 2003.
- Hall, T. M., T. W. N. Haine, M. Holzer, D. A. Lebel, F. Terenzi, and D. W. Waugh, Ventilation rates estimated from tracers in the presence of mixing, *Journal of Physical Oceanography*, 37, 2599–2611, 2007.
- Heinze, C., and N. Dittert, Impact of paleocirculations on the silicon redistribution in the world ocean, *Marine Geology*, 214, 201–213, 2005.
- Heinze, C., E. Maier-Reimer, and K. Winn, Glacial pCO₂ reduction by the world ocean: experiments with the Hamburg carbon cycle model, *Palaeoceanography*, 6, 395–430, 1991.

- Heinze, C., A. Hupe, E. Maier-Reimer, N. Dittert, and O. Ragueneau, Sensitivity of the marine biospheric Si cycle for biogeochemical parameter variations, *Global Biogeochemical Cycles*, *17*, 1086, 2003.
- Holzer, M., and F. W. Primeau, The diffusive ocean conveyor, *Geophysical Research Letters*, *33*, L14,618, 2006.
- Jenkins, W. J., Studying subtropical thermocline ventilation and circulation using tritium and ^3He , *Journal of Geophysical Research*, *103*, 15,817–15,831, 1998.
- Maier-Reimer, E., Geochemical cycles in an ocean general circulation model. Preindustrial tracer distributions, *Global Biogeochemical Cycles*, *7*, 645–677, 1993.
- Maier-Reimer, E., U. Mikolajewicz, and K. Hasselmann, Mean circulation of the Hamburg LSG OGCM and its sensitivity to the thermohaline surface forcing, *Journal of Physical Oceanography*, *23*, 731–757, 1993.
- Markwardt, C. B., Non-linear least-squares fitting in idl with mpfit, in *Astronomical Society of the Pacific Conference Series*, edited by D. A. Bohlander, D. Durand, and P. Dowler, vol. 411 of *Astronomical Society of the Pacific Conference Series*, pp. 251–254, 2009, <http://purl.com/net/mpfit>.
- Marotzke, J., Influence of convective adjustment on the stability of the thermohaline circulation, *Journal of Physical Oceanography*, *21*, 903–907, 1991.
- Mikolajewicz, U., E. Maier-Reimer, T. J. Crowley, and K. Kim, Effect of Drake and Panamanian Gateways on the circulation of an ocean model, *Palaeoceanography*, *8*, 4, 1993.
- Mikolajewicz, U., T. J. Crowley, A. Schiller, and R. Voss, Modeling North Atlantic/North Pacific teleconnections during the Younger Dryas, *Nature*, *387*, 384–387, 1997.
- Moré, J., The Levenberg-Marquardt algorithm: Implementation and theory, *Numerical Analysis*, *630*, 105, 1978.
- Mouchet, A., A 3D model of ocean biogeochemical cycles and climate sensitivity studies, Ph.D. thesis, Université de Liège, Liège, Belgium, 2011.
- Mouchet, A., and E. Deleersnijder, The leaky funnel model, a metaphor of the ventilation of the World Ocean as simulated in an OGCM, *Tellus*, *60A*, 761–774, 2008.

- Munk, W., Abyssal recipes, *Deep-Sea Research*, *13*, 707–730, 1966.
- Munk, W., and C. Wunsch, Abyssal recipes II: energetics of tidal and wind mixing, *Deep-Sea Research*, *45*, 1977–2010, 1998.
- Pacanowski, R. C., and S. G. H. Philander, Parameterization of vertical mixing in numerical models of tropical oceans, *Journal of Physical Oceanography*, *11*, 1443–1451, 1981.
- Primeau, F., and E. Deleersnijder, On the time to tracer equilibrium in the global ocean, *Ocean Science*, *5*, 13–28, 2009, www.ocean-sci.net/5/13/2009/.
- Primeau, F. W., and M. Holzer, The oceans memory of the atmosphere: Residence-time and ventilation-rate distributions of water masses, *Journal of Physical Oceanography*, *36*, 1439–1456, 2006.
- Tartinville, B., E. Deleersnijder, and J. Rancher, The water residence time in the Mururoa atoll lagoon: a three-dimensional model sensitivity analysis, *Coral Reefs*, *6*, 193–203, 1997.
- Winguth, A. M. E., D. Archer, J.-C. Duplessy, E. Maier-Reimer, and U. Mikolajewicz, Sensitivity of paleonutrient tracer distributions and deep-sea circulation to glacial boundary conditions, *Palaeoceanography*, *14*, 304–323, 1999.

2.2.3 On the role of numerical diffusivity and its assessment

Mixing is an essential mechanism in the ocean overturning circulation (*Stommel and Arons*, 1960a,b; *Munk and Wunsch*, 1998). Vertical mixing sustains the deep circulation by pulling the water from the deep ocean up toward the surface working against the density gradient. In most of the ocean interior the vertical mixing is weak $\sim 10^{-5}\text{m}^2\text{s}^{-1}$ (*Ledwell et al.*, 1993; *Toole and McDougall*, 2001) but larger diapycnal diffusivities, up to $10^{-3}\text{m}^2\text{s}^{-1}$, occur in very localized areas where tides and currents interact with the rough bottom topography (*Polzin et al.*, 1997; *Webb and Sugimotohara*, 2001; *Kunze et al.*, 2006; *St. Laurent and Simmons*, 2006).

In OGCMs diapycnal diffusivity plays an important role in determining the stability of the overturning circulation (*Zhang et al.*, 1999; *Schmittner and Weaver*, 2001). An inadequate representation of the mixing processes in models may result in an unrealistic balance between the driving mechanisms of the deep ocean circulation and, consequently, to a possibly false assessment of the climatic feedbacks (*Kuhlbrodt et al.*, 2007). According to *Schmittner et al.* (2009) the range in vertical mixing between models is a contributing factor to the large ranges in transient climate sensitivity and climate–carbon cycle feedbacks.

Hence it is of importance to assess the mixing effectively taking place in models, i.e., including both numerical and explicit diffusivities. Explicit diffusion has a clear physical meaning. It is meant to take into account unresolved subgridscale physical processes. On the contrary numerical diffusion, associated to the advection scheme, is a consequence of the finite difference method, and does not bear any physical significance. However its effects should not be overlooked. Indeed it seems that in ocean models the numerical diffusivity of advection schemes is often of the same order of magnitude as the explicit one (*Kuhlbrodt et al.*, 2007). Such numerical artifacts bear consequences to the simulated tracer distributions (*Oschlies*, 2000; *Doney et al.*, 2004).

Assessing the actual numerical diffusion magnitude in OGCMs is not always straightforward (e.g., *Burchard and Rennau*, 2008). The leaky funnel model on the other hand offers such a possibility. The estimates of both the explicit and numerical diffusivities, together with the advective time scale, allow then to characterize the transport in individual OGCM. From there we may then analyze OGCMs with respect to one another. At this stage it is important to mention that our aim is not to evaluate the OGCMs used in this work but rather to test simple tools and see how relevant is the information they provide.

Extracting any information about the numerical diffusion from the global water age distribution proposed by MA11 proves to be a very complex and intricate task. On the other hand the method from MD08 allows such a derivation. And since MA11 corroborate results from MD08, the latter approach can be used to

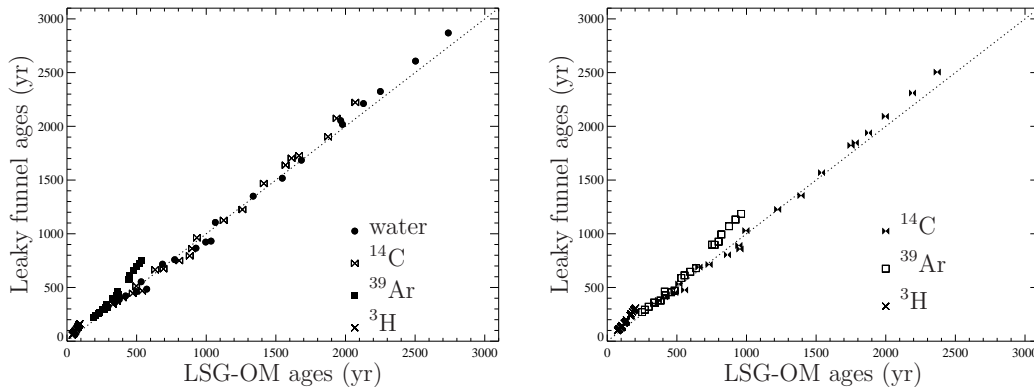


Figure 2.3: Scatter plots of the predicted global ages versus those computed with LSG-OM. The left panel presents results for water and radioactive tracer ages and the right panel for radioages.

derive the leaky funnel parameters and assess the role of numerical diffusion in OGCMs.

The domain-averaged water age in the leaky funnel (Eq. (21) of MD08) reads:

$$a_w = A_0 \frac{Pe}{1 + Pe}, \quad (2.13)$$

with $Pe = UL/K$ and $A_0 = L/U$. L is the e-folding length scale of the funnel envelope while U and K are the 1-D constant velocity and diffusivity driving the transport.

The effective Peclet number to be associated to the transport in the OGCMs takes into account both the explicit and numerical diffusivities. It is given by

$$\frac{1}{Pe} = \frac{K^E + K^N}{UL} = \frac{1}{Pe^E} + \frac{1}{Pe^N} \quad (2.14)$$

where $Pe^E = UL/K^E$ and $Pe^N = UL/K^N$ represent the Peclet numbers associated with the explicit K^E and numerical diffusion K^N , respectively.

The leaky funnel parameters corresponding to UL-OM were already determined by MD08. In the same way we performed M experiments with the LSG-OM, in which the velocity and explicit diffusivity were homogeneously multiplied by constant factors⁴.

Since numerical diffusion is proportional to the velocity magnitude (Roache, 1972), numerical diffusivity in these experiments is affected by the same factor

⁴A description of the OGCMs providing the dynamic fields used in this section may be found in Appendix A.

Table 2.1: Parameters of the leaky funnel model as obtained from a least squares fit to the domain-averaged water ages resulting from several experiments with two 3-D models (UL-OM, column 2, and LSG-OM, column 3). The last line gives the effective Peclet number computed from equation (2.14).

	UL-OM	LSG-OM
A_0 (yr)	1010	690
Pe^E	6.4	14.0
Pe^N	7.0	2.8
Pe	3.3	2.4

as the velocity field. Hence, the velocity and diffusivity corresponding to experiments i ($i = 1, \dots, M$) may be expressed relatively to those of the unperturbed state as

$$U_i = \gamma_i U \quad \text{and} \quad K_i = \beta_i K^E + \gamma_i K^N, \quad (2.15)$$

where β_i and γ_i are constant and positive numbers.

If the leaky funnel adequately represents the circulation in the ocean interior then the predicted global water age for experiment i , $\langle \hat{a}_w \rangle_i$, would be given by (2.13) rewritten with the help of (2.14) and (2.15):

$$\langle \hat{a}_w \rangle_i = \frac{L}{U_i} \frac{Pe_i}{1 + Pe_i} = \frac{A_0}{\gamma_i} \frac{1}{1 + \frac{\beta_i}{\gamma_i} \frac{1}{Pe^E} + \frac{1}{Pe^N}} \quad (2.16)$$

With the LSG-OM we performed $M = 21$ numerical experiments for which $\beta_i \in [1., 8.]$ and $\gamma_i \in [0.125, 1.]$. A least-squares fit of Eq. (2.16) to the 21 OGCM domain-averaged ages $\langle a_w \rangle_i$ provides estimates of the leaky funnel parameters $\{A_0, Pe^E, Pe^N\}$ corresponding to LSG-OM. These values as well as those for UL-OM from MD08 are given in Table 2.1. As seen in Figure 2.3 the agreement between ages predicted by the leaky funnel and those from the LSG-OM is very good. It should be stressed that radioages or radioactive tracer ages do not intervene in the estimation of the parameters of the leaky funnel. We take advantage of their availability in order to evaluate the ability of the simplified model to reproduce the characteristics of the large scale circulation in the 3-D model.

The two models differ drastically with respect to their A_0 scales. As discussed in MA11 the A_0 scale represents the adjustment time to a perturbation. This larger timescale translates, for example, in a longer timescale for anthropogenic CO_2 uptake by UL-OM relative to LSG-OM (Figure 2.4).

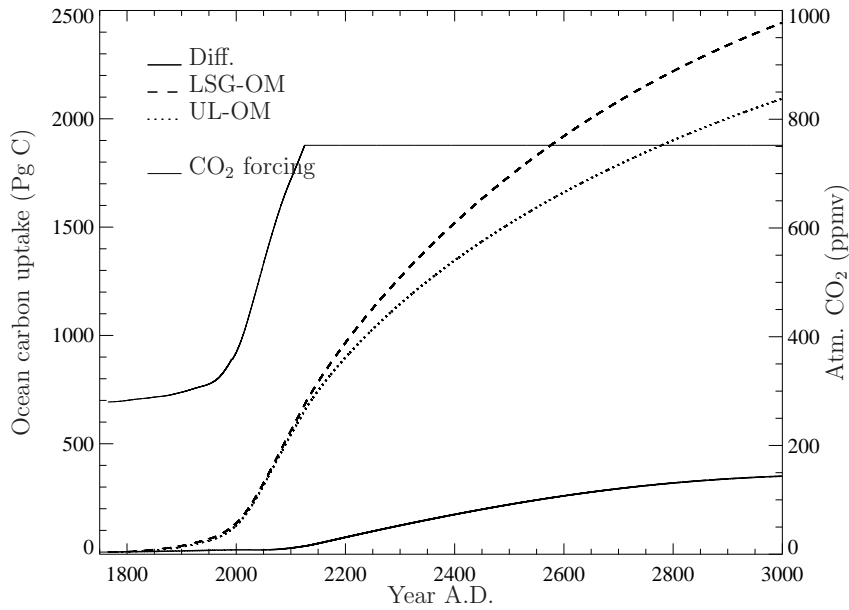


Figure 2.4: Difference in cumulative CO_2 uptake (thick solid line) by two ocean global carbon models. The individual uptakes (represented as anomalies with respect to 1765 A.D.) are obtained from abiotic constrained CO_2 experiments with LSG-OM (dashed line) and UL-OM (dotted line). The thin solid line corresponds to the atmospheric CO_2 forcing used in these experiments. Units for the atmospheric CO_2 are given on the right axis.

The role played by numerical diffusion in the transport is made clear from the values in Table 2.1. These values are in agreement with the the OGCMs mathematical formulation and numerical scheme. Indeed advection in LSG-OM is resolved with an upstream scheme both along the horizontal and the vertical. The use of explicit diffusion in that model, is restricted to convective processes in addition to a small horizontal term preventing mode divergence due to the use of an E-grid (Appendix A). Hence numerical diffusion contributes most to the effective diffusion in that model. In contrast, UL-OM makes use of a less diffusive numerical scheme for advection. This explains the larger Pe^N with respect to LSG-OM, while the generalized use of explicit diffusion translates into a lower Pe^E . Though the global, or effective, Peclet numbers associated to each model are very close (last line of Table 2.1) the underlying mechanisms are very different. This leads to contrasted tracer vertical distributions (Figure 2.6), with UL-OM predicting more structured fields along the vertical.

The results in Table 2.1 contrast with the figures obtained from the global

water age distribution study of MA11. In that work, one model (LSG-OM) seems to be significantly less diffusive than the other (UL-OM). It is important to note that this result is flawed. It is a direct consequence of the fact that it has not been possible to extract any information about the numerical diffusion from the global water age distribution. As explained below, neglecting the contribution from numerical diffusion in the least squares fitting procedure does not bear any consequences on the goodness of the fit for water ages. Omitting it, however, results in biased estimates of A_0 , Pe , as well as of global radioactive tracer ages.

Table 2.2: Best fit parameters of the leaky funnel when numerical diffusion is considered (rows 4 & 5) or not (rows 7 & 8). For each OGCM (column 1) this table gives the advective timescale (column 2), the Peclet numbers associated to the explicit and numerical diffusivities (columns 3 & 4), and the effective Pe (column 5). Column 6 contains the estimated domain averaged water age $\langle \hat{a}_w \rangle$ computed from equation (2.13) with the help of A_0 and Pe in the present table. The global mean age predicted by the standard version of the OGCMs (that is, for $\beta_i = \gamma_i = 1$) is given in column 7.

OGCM	A_0 yr	Pe^E	Pe^N	Pe	$\langle \hat{a}_w \rangle$ yr	$\langle a_w \rangle$ yr
Numerical diffusion considered						
UL-OM	1010	6.4	7.0	3.3	778	764
LSG-OM	690	14.0	2.8	2.4	485	573
Numerical diffusion neglected						
UL-OM	884	7.3	-	7.3	778	764
LSG-OM	511	18.9	-	18.9	485	573

Consider two working hypotheses: either numerical diffusion is significant or it may be neglected.

Under the first hypothesis (i.e., the standard case) the theoretical model to be fitted to the M 3-D domain averaged ages $\langle a_w \rangle_i$ is $\langle \hat{a}_w \rangle_i(\gamma_i, \beta_i, A_0, Pe^E, Pe^N)$ where $\{A_0, Pe^E, Pe^N\}$ are the three unknown parameters. The best-fit parameters will be those minimizing the χ^2 function

$$\chi^2(A_0, Pe^E, Pe^N) = \sum_{i=1}^M \left(\frac{\langle a_w \rangle_i - \langle \hat{a}_w \rangle_i(\gamma_i, \beta_i, A_0, Pe^E, Pe^N)}{\sigma_i} \right)^2, \quad (2.17)$$

in which σ_i is the standard deviation of the uncertainty associated to $\langle a_w \rangle_i$.

The $\langle \hat{a}_w \rangle_i$ intervening in (2.17) are given by

$$\gamma_i \langle \hat{a}_w \rangle_i = \frac{A_0}{\left(\frac{Pe^N + 1}{Pe^N} \right)} \left(\frac{\gamma_i / \beta_i}{\left(\frac{Pe^N}{Pe^N + 1} \right) \frac{1}{Pe^E} + \gamma_i / \beta_i} \right), \quad (2.18)$$

which is obtained after some manipulation of (2.16).

If numerical diffusion is considered to be negligible then the theoretical model to be fitted is $\langle \hat{a}'_w \rangle_i(\gamma_i, \beta_i, A'_0, Pe'^E)$ with only two unknown parameters $\{A'_0, Pe'^E\}$. We use primed quantities in order to differentiate them from those corresponding to the first case. The best-fit parameters will be those minimizing the χ^2 function

$$\chi^2(A'_0, Pe'^E) = \sum_{i=1}^M \left(\frac{\langle a_w \rangle_i - \langle \hat{a}'_w \rangle_i(\gamma_i, \beta_i, A'_0, Pe'^E)}{\sigma_i} \right)^2, \quad (2.19)$$

in which $\langle \hat{a}'_w \rangle_i$ obeys

$$\gamma_i \langle \hat{a}'_w \rangle_i = A'_0 \left(\frac{(\gamma_i / \beta_i)}{\frac{1}{Pe'^E} + (\gamma_i / \beta_i)} \right). \quad (2.20)$$

Expressions (2.18) and (2.20) correspond to two different theoretical models. Since the γ_i s and β_i s are identical in both cases as are the 3-D domain-averaged water ages $\langle a_w \rangle_i$, it can readily be seen that replacing A'_0 and Pe'^E in (2.20) with the following expressions

$$A'_0 = \left(\frac{Pe^N}{Pe^N + 1} \right) A_0, \quad (2.21)$$

$$Pe'^E = \left(\frac{Pe^N + 1}{Pe^N} \right) Pe^E, \quad (2.22)$$

results in (2.18).

This does not mean that any Pe^N value in (2.18) would give equally good fit to the domain-averaged water ages $\langle a_w \rangle_i$. It is indeed important to note that taking into account numerical diffusion results in an additional constraint on the evolution of $\langle a_w \rangle_i$ with γ_i .

The respective sets of unknown parameters ($\{A_0, Pe^E, Pe^N\}$ in the first case, $\{A'_0, Pe'^E\}$ in the second case) are obtained from the minimization of the χ^2 for two different problems. Hence they represent the best-fit set of parameters that may be obtained in each case. When neglecting numerical diffusion the apparent A_0 decreases while the apparent Pe increases as predicted by (2.21) and (2.22) such that

$$\langle \hat{a}_w \rangle_i = \langle \hat{a}'_w \rangle_i. \quad (2.23)$$

We obtained the parameter sets corresponding to the two problems (2.17) and (2.19) for each OGCM. The results are given in Table 2.2. It is readily seen from that table that the values $\{A_0, Pe^E, Pe^N\}$ and $\{A'_0, Pe'^E\}$ obtained with both OGCMs satisfy the ratios (2.21) and (2.22).

Since (2.23) holds true, there is no impact on the fit of water age. Predicted water ages are exactly the same under both hypotheses (Table 2.2). This agreement occurs because any decrease in A_0 is balanced by the increase of Pe . The correlation coefficient as well as the mean residual in the case of water age are strictly identical whether or not numerical diffusion is considered. The constraint (2.23) is also valid for the global water age distribution since it is implicit from the mathematical development in MA11 that $\varphi(\tau)$ must verify $\int_0^\infty \tau \varphi(\tau) d\tau = \langle a_w \rangle$.

The situation is different for the ages of radioactive tracers whose analytical expression involves cross products of α_i and β_i . The linear correlation coefficient increases and the mean residual decreases when the estimate of the leaky funnel parameter is performed while including numerical diffusion. Those impacts are illustrated in Figure 2.5, where it is seen that (2.18) leads to better result than (2.20).

2.2.4 Conclusion

The model presented in this section provides analytical solutions that are simple to deal with, making it possible to obtain characteristic scales of the deep-ocean circulation as reproduced by OGCMs. It also provides a simple means to evaluate the relative roles of advection and diffusion in complex OGCMs. Furthermore, it offers the possibility to evaluate the extent to which numerical diffusion affects this circulation. However we are aware that up to now it has only been tested with coarse grid OGCMs. Testing it against 3-D models with increased resolution and more detailed vertical mixing would be necessary before generalizing the conclusions of this analysis.

In the real ocean, deep-water formation occurs in two distinct locations (North Atlantic and Antarctica). The unique entry of the leaky funnel constitutes a further limitation for assessing ocean ventilation with the help of real tracers (e.g. ^{14}C).

Eventually, the information provided is exclusively global, representing a spatially integrated measure of heterogeneously distributed processes.

The two OGCMs examined in this work have very close Peclet number but differ greatly in their advection timescales A_0 . Such a difference may partly explain the disparities between the radiocarbon distributions predicted by each model (Figure 2.6). In the Pacific Ocean the larger advection timescale characterizing UL-OM is consistent with larger trajectories resulting in older, more radiocarbon-depleted water masses in comparison with the LSG-OM. On the

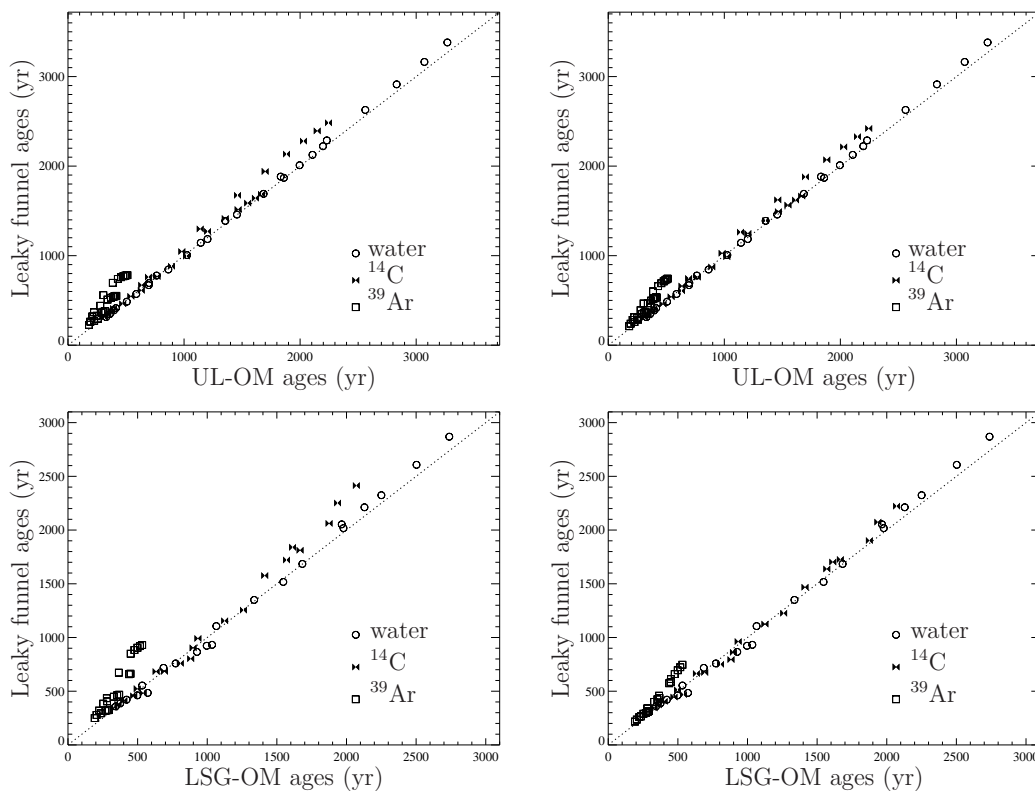


Figure 2.5: Scatter plot of the predicted global ages for water and two radioactive tracer (^{39}Ar and ^{14}C) versus those computed from the 3-D models (UL-OM upper row, LSG-OM lower row). The two columns correspond to predicted ages obtained by neglecting numerical diffusion (left) or explicitly including it (right) in the least-squares fit.

contrary, radiocarbon distributions in the Atlantic Ocean are somewhat closer. Hence we would expect both models to have comparable flow characteristics in that area. This observation and the fact that the volume of the Pacific Ocean is nearly half that of the World Ocean suggest that the global numbers provided by the leaky funnel representation mainly depict the deep Pacific Ocean flow properties.

Another tool with which age biases can be analyzed, provides more insight into regional aspects of the interior ocean circulation, as described in the next section.

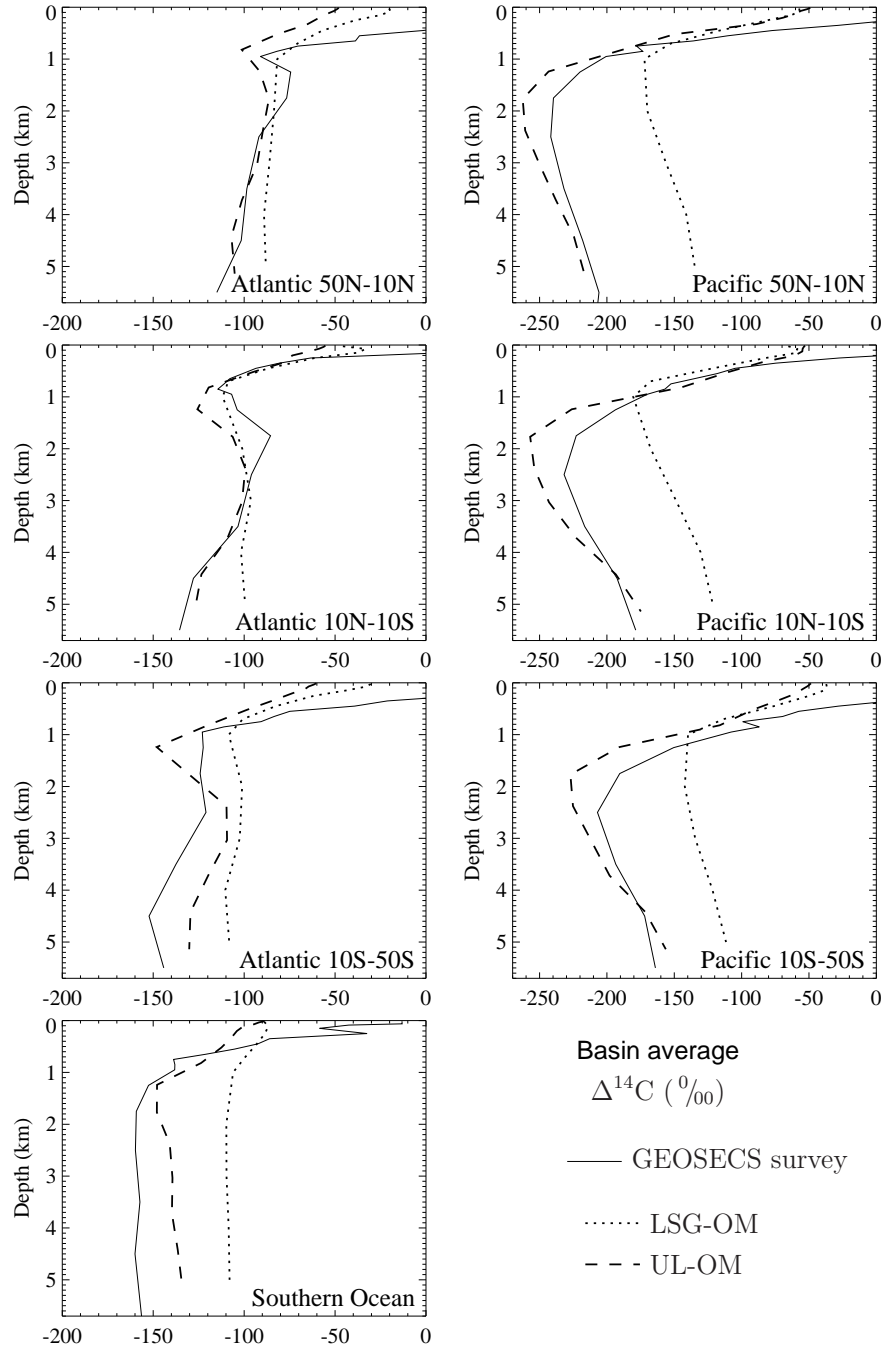


Figure 2.6: Mean $\Delta^{14}\text{C}$ vertical profiles in several ocean basins from GEOSECS (solid lines; *Stuiver et al.*, 1981) and from two pre-industrial experiments with the OGCM standard versions UL-OM (dashed lines) and LSG-OM (dotted lines). The values in the North, Equatorial, and Southern Atlantic and Pacific Oceans are reproduced, respectively, in the upper left and right three panels, with the bottom panel representing the Southern Ocean (south of 50°S). The pre-industrial OGCM $\Delta^{14}\text{C}$ is computed with the simplified method of *Toggweiler et al.* (1989a). The discrepancy between models and data in the upper ocean partly results from the penetration of bomb ^{14}C that is not considered in these numerical experiments.

2.3 Age bias and mixing in OGCMs

A lot of effort is devoted to the evaluation of OGCMs ability to reproduce transport in the ocean or anthropogenic carbon uptake (e.g., *Doney et al.*, 2004; *Dutay et al.*, 2004; *Matsumoto et al.*, 2004; *Cao et al.*, 2009). While these works point to model deficiencies in reproducing the ocean dynamics, the exact causes leading to a particular model behavior are not always fully apprehended. For a better comprehension of the OGCMs internal dynamics, advantage may be taken of simple tools which, by eliminating the complexity of 3-D fields, pave the way for the interpretation of essential processes. Hereafter we propose a method, based on age biases, which proves relevant for the assessment of the relative roles of advection and diffusion in driving the transport in ocean provinces.

Whenever diffusion is present in a flow the ages obtained from tracers, radioactive or not⁵, underestimate the true ventilation age (*Jenkins*, 1987; *Deleersnijder et al.*, 2001; *Khatiwala et al.*, 2001; *Delhez et al.*, 2003). This bias, which is a function of both the e-folding timescale characterizing the tracer and the level of mixing, constitutes a limitation when assessing ventilation rates from field measurements. However one may take advantage of this behavior in order to extract information about the flow dynamics. For example *Maier-Reimer* (1993) illustrated the respective roles of advection and diffusion in the Hamburg OGCM with the help of the relative distributions of ³⁹Ar and ¹⁴C, whose mean lives are of 400 and 8268 yr, respectively. Though field measurements of ³⁹Ar are still sparse, this tracer seems promising when associated to radiocarbon for uncovering ocean deep circulation properties (*Broecker and Peng*, 2000; *Waugh et al.*, 2003).

Hereafter we examine the difference between the ventilation time and radioactive tracer ages with the help of an idealised model, in which the water and tracers circulate along a loop (*Wyrтки*, 1962). Analytical solutions to this problem allow us to determine whether advection or diffusion controls the flow. Sensitivity studies with two 3-D ocean models are then performed to examine the relevance of the conclusions of the 1-D study.

2.3.1 A 1-D upwelling diffusion model

Wyrтки (1962) set the basis of a 1-D model to explain oxygen distribution in the ocean. This model has since been widely used. Among the various applications we may mention the study of tracer profiles in the deep Pacific (*Munk*, 1966), the assessment of O₂ utilization rate (*Craig*, 1971), the estimate of the global vertical diffusion in the ocean (*Munk and Wunsch*, 1998), or the analysis of deep ocean ³⁹Ar and ¹⁴C distributions (*Broecker and Peng*, 2000).

⁵this is also true for tracers not undergoing radioactive decay but characterized by a non-linear atmospheric growth rate, such as CFCs (*Delhez et al.*, 2003)

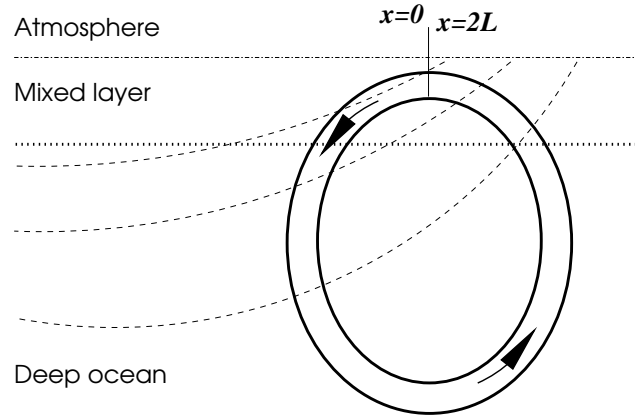


Figure 2.7: Schematic representation of the vertical advection-diffusion balance model (Wyrтки, 1962; Munk, 1966). It consists in a 1-D loop with boundaries situated in the mixed layer. The position x is given by the arc length measured along the loop in the anticlockwise direction. The transport is driven by advection and diffusion.

In this model the ocean transport is depicted as occurring along a 1-D vertical loop of constant section and finite length $2L$ (Figure 2.7). Water masses formed at the surface (where the age is set to zero) sink down and are advected while undergoing mixing before reaching the surface again. The velocity U and diffusivity K prevailing in this vertical advection-diffusion balance model are constant. At steady-state the transport equations (2.8) and (2.9) for the concentration and the age concentration of a tracer with radioactive decay rate λ hence become

$$U \frac{\partial C_\lambda}{\partial x} = K \frac{\partial^2 C_\lambda}{\partial x^2} - \lambda C_\lambda, \quad (2.24)$$

$$U \frac{\partial \alpha_\lambda}{\partial x} = K \frac{\partial^2 \alpha_\lambda}{\partial x^2} - \lambda \alpha_\lambda + C_\lambda. \quad (2.25)$$

with x the along flow distance, $x \in [0, 2L]$.

Solutions to these equations are sought by specifying Dirichlet boundary conditions

$$C_\lambda(0) = 1 = C_\lambda(2L), \quad (2.26)$$

$$\alpha_\lambda(0) = 0 = \alpha_\lambda(2L). \quad (2.27)$$

Solutions to this problem yield the radioactive tracer age $a_\lambda(x) = \alpha_\lambda(x)/C_\lambda(x)$ and the water (or passive tracer) age $a_w(x)$, the latter is obtained by setting $\lambda = 0$ in the above expressions.

Since all tracers are subject to the same flow fields and boundary conditions, any difference in their age may only stem from the action of diffusion. In the

presence of diffusion the radioactive tracer age always lags behind the true ventilation age a_w . It may be shown that for small decay rates λ , the age bias, $a_w - a_\lambda$, is a linear function⁶ of λ (*Delhez et al.*, 2003)

$$a_w(x) - a_\lambda(x) \sim 2\Delta^2(x)\lambda, \quad \text{for } \lambda \rightarrow 0, \quad (2.28)$$

with Δ , the standard deviation of the water age distribution $c(x, \tau)$. In simple flow configurations Δ provides a direct measure of the actual diffusivity (*Delhez and Deleersnijder*, 2002). In real flows, such as encountered in the ocean, the relationship between the level of mixing and Δ is more complex. Nevertheless, the standard deviation of the age distribution may still be of help in quantifying diffusion since it appears to yield an integrated measure of the mixing encountered by elements during their journey from the surface to their present position (*Delhez and Deleersnijder*, 2002).

The age, at a specific location, is also set by that of the source water. In order to be able to estimate the role of diffusion in determining the actual tracer and age distributions, influences from the source water and the specific location should be reduced as much as possible (if not eliminated) from the diagnostic variable.

For this purpose we introduce the relative age bias r_λ defined as

$$r_\lambda(x) = \frac{a_w(x) - a_\lambda(x)}{a_w(x) + a_\lambda(x)} \quad (2.29)$$

The radioactive tracer age tends to the water age a_w for $\lambda \rightarrow 0$ and decreases asymptotically toward zero with increasing values of λ (*Delhez et al.*, 2003). It is then readily seen that $r_\lambda \rightarrow 0$ as $\lambda \rightarrow 0$ or $K \rightarrow 0$, while $r_\lambda \rightarrow 1$ when $\lambda \rightarrow \infty$ and $K \neq 0$.

The analytical solutions (concentrations, ages, age bias...) for the 1-D upwelling diffusion problem are obtained with the help of the *Mathematica* software. Since most of these expressions are rather long and intricate, the full details are not systematically presented here. The interested reader will find some detailed analytical solutions at the end of this text (Section 2.3.B).

In the following we take advantage of the linear behavior of age differences at small λ and restrict our study to small decay rates. A series expansion of r_λ for $\lambda \rightarrow 0$, limited to first order terms, reads

$$r_\lambda(x) \sim r'_\lambda(x) = \lambda (\coth(LU/K) - 1) \times \left(\frac{K - 2UL \left(\left(3e^{\frac{2LU}{K}} + e^{\frac{Ux}{K}} \right) \left(1 - e^{\frac{Ux}{K}} \right) L - 2e^{\frac{Ux}{K}} \left(1 - e^{\frac{2UL}{K}} \right) x \right)}{2U^2 \left(2 \left(e^{\frac{Ux}{K}} - 1 \right) L - \left(e^{\frac{2LU}{K}} - 1 \right) x \right)} \right). \quad (2.30)$$

⁶Note: this approximation does no longer hold when too close to $2L$.

It should be noted that figures 2.8 and 2.9 display the full expression r_λ and not its approximation r'_λ .

We then examine the behavior of r'_λ at low and high diffusivity levels. At low K , the relative age bias behaves as

$$\lim_{K \rightarrow 0} r'_\lambda(x) = \lambda \frac{K}{U^2} = \frac{1}{Je}, \quad (2.31)$$

in which we introduce the Jenkins number $Je = U^2/(K\lambda)$. Je is equivalent to a Peclet number in which the length scale is given by $U\lambda^{-1}$ (Jenkins, 1987). Expression (2.31) shows that when diffusion is weak r_λ is independent of the position. Further, when $K \rightarrow 0$, the relative age bias is a linearly increasing function of K .

The behavior of r_λ dramatically changes when diffusion becomes dominant. Indeed when K is large, r_λ is no longer independent on the position and is inversely proportional to K :

$$\lim_{K \rightarrow \infty} r'_\lambda(x) = \lambda \frac{L^2}{12K} (x^2 + (L-x)^2). \quad (2.32)$$

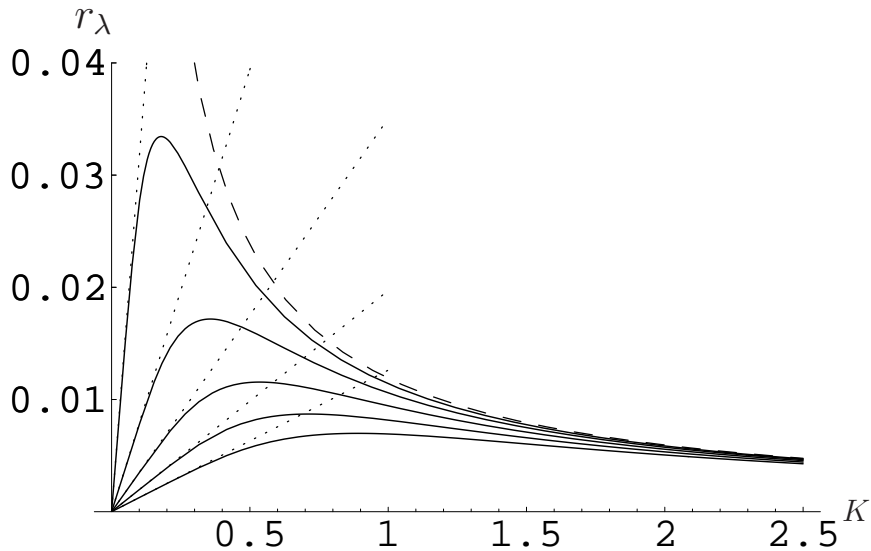


Figure 2.8: Relative age bias as a function of K for different velocities in the 1-D advection-diffusion model (solid lines). Units for K are $10^{-4} \text{m}^2/\text{s}$. Velocity increases from 1 m/yr (upper curve) to 5 m/yr (lower curve) by step of 1 m/yr. The dotted lines correspond to the slope as $K \rightarrow 0$ and the dashed curve reproduces the asymptotic behavior as $K \rightarrow \infty$ (equations 2.31 and 2.32, respectively). For the purpose of this plot we set $x = L/2$, $\lambda = 10^{-4} \text{yr}^{-1}$ and $L = 3000 \text{m}$.

For a given K , r_λ is a decreasing function of U but at any position⁷ in the loop the age bias is a non-monotonic function of K (Figure 2.8). If there were no diffusion in the advection-dominated case, Eq. (2.31), r_λ would be zero. At low K , the magnitude of the departure from that ideal situation is measured by the Jenkins number, a modified version of the Peclet number. At low velocities the relative change in r_λ with K are much larger than those occurring when U is large (Figs 2.8 and 2.9). On the other hand, when diffusion prevails, advection does not play any role in the control of r_λ .

Figures 2.8 and 2.9 depict r_λ as a function of K at different positions in the domain for various values of U . The parameter values used in these figures are set to those corresponding best to the 3-D model cases (see next section). Various sensitivity tests on the parameters U , K , and λ were performed. The conclusions presented here remain valid as long as the observation point is situated far enough from boundaries.

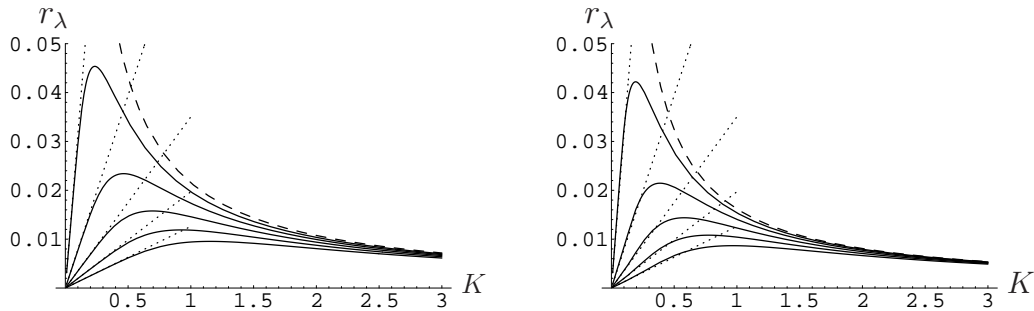


Figure 2.9: Same as Figure 2.8 but for $x = 0.1L$ (left) and $x = 1.6L$ (right).

2.3.2 Experiments with 3-D ocean models

The circulation fields from two OGCMs are used to drive off-line the age model with which we compute the concentrations and age concentrations of water and several radioactive tracers. We impose a no flux boundary condition across the ocean floor. At the ocean surface S identical Dirichlet boundary conditions apply to all tracers:

$$C_\lambda(\mathbf{x}, t) = 1 \text{ and } \alpha_\lambda(\mathbf{x}, t) = 0, \text{ for } \mathbf{x} \in S. \quad (2.33)$$

It is worth noting that this boundary condition is equivalent to assuming an infinite piston velocity. Indeed, the air-sea exchange of a gas is usually represented

⁷except in a reduced area next to the boundaries where restoring conditions to the surface values prevail.

Table 2.3: Details of the different experiments performed in the framework of the age bias study. The names of the experiment and of the OGCM providing the circulation fields are specified in columns 1 and 2, respectively. Column 4 gives the global water age (a_w).

Exp. name	OGCM	Conditions	$\langle a_w \rangle$ yr
A0	LSG-OM	Standard run.	572.71
AV	LSG-OM	Halved velocities relative to A0.	996.12
AK	LSG-OM	Double explicit diffusivity, relative to A0.	498.08
L0	UL-OM	“Reduced” upwind scheme along the vertical.	677.48
LC	UL-OM	Centered scheme along the vertical.	794.00

with a law that specifies the tracer flux \mathcal{F} through S as

$$\mathcal{F} = \kappa_g (HC_A - C_S),$$

with the gas concentration in the lower atmosphere (C_A) or at the ocean surface (C_S), and H the gas solubility. The piston velocity κ_g determines the rate of transfer across S .

The condition $\kappa_g \rightarrow \infty$ leads to $HC_A - C_S = (\mathcal{F}/\kappa_g) \rightarrow 0$, which is equivalent to the Dirichlet boundary condition $C(\mathbf{x}) = HC_A$ for $\mathbf{x} \in S$.

The rate of air-sea exchange in the real ocean is tracer-dependent and occurs at a finite pace. Henceforth distributions of radio-isotopes obtained in this work may significantly differ from field measurements. However, formulation (2.33) is convenient for the purpose of model analysis since it ensures that no external process would influence modelled tracer distributions. Each experiment was allowed to run until changes in the domain averaged mean age of the longest living isotope could be considered as negligible.

Several experiments were performed for which the details are listed in Table 2.3. The effect of direct changes in the velocity or in the diffusivity fields are tested with the LSG-OM fields. In experiment AK, the explicit diffusivity is doubled with respect to the standard run A0. Velocities in experiment AV are smaller by a factor 2 relative to A0.

The impact of the vertical advection scheme is examined with the UL-OM fields. Vertical transport is computed with the help of a upwind scheme with reduced diffusion (referred to as “reduced” upwind) in L0 and with a 2^d order centered scheme in LC. An identical advection scheme is used in both experiments for resolving the horizontal transport. The same vertical velocity and explicit diffusivity fields are used for driving both L0 and LC. However, the explicit vertical diffusion in L0 is adapted at each grid point so as to compensate for the local numerical diffusion of the upwind scheme. This correction results in a reduction of the explicit diffusion in L0 relative to LC. However, the actual

diffusion at work in L0 exceeds that in LC since the correction applied in L0 may not result in negative diffusivity coefficients. Figure 2.10 presents the scatter plot of the radioage of the tracer with mean lifetime $1/\lambda = 500$ yr versus that of the tracer with mean lifetime $1/\lambda = 10^4$ yr in the deep ocean as obtained from the experiments in Table 2.3. Would mixing be extremely low, then the ages would distribute along lines with a 1:1 slope from points characterizing the preformed ages. A lower slope is actually obtained as a consequence of the action of mixing.

Maier-Reimer (1993) showed that for a purely diffusive transport in a semi-infinite pipe, the radioages of two different tracers would distribute along a straight line with slope $\sqrt{\lambda_1/\lambda_2}$, where λ_1 and λ_2 are the decay rates corresponding to the tracers with radioage given on the X-axis and Y-axis, respectively. Yet in the general case, $U \neq 0$ and $K \neq 0$, it can be shown that the relationship between the two radioages is linear with slope in the interval $[\sqrt{\lambda_1/\lambda_2}, 1]$ (Section 2.3.A). The results from the 3-D experiments seem to verify this property; it is indeed noticeable from Fig. 2.10 that the correlation between the two radioages is comprised in that interval.

However this model fails to reproduce the observed slope modification obtained with changing flow conditions. The semi-infinite pipe representation predicts that, at constant U , the slope should decrease when K increases. Accordingly, the scatter plot for experiment L0 (AK) should exhibit a shallower slope than that obtained with experiments LC (A0, resp.), since diffusivity is larger in the former than in the latter. Actually, as evidenced by the results in Figure 2.10, the opposite behaviour occurs. The finite length of seawater particles trajectories combined with the constraint that particles meet surface conditions at the end of their path rules out any interpretation based on the semi-infinite pipe model.

The middle right panel of figure 2.10 presents the radioage scatter plot predicted by the 1-D upwelling-diffusion model of section 2.3.1 for the same tracers. Global tendencies of the 3-D results are very similar to those from the 1-D model. Increasing the diffusion (i.e., experiments AK relative to A0 and exp. LC relative to L0) results in a smaller loop with anticlockwise tendency. On the other hand, a reduction of both the velocity and the diffusivity (exp. A0 to AV) leads to a larger spread of the distribution similarly in the 3-D and the 1-D models.

The 1-D upwelling-diffusion model seems then pertinent for the aim of gaining more insight of transport processes in 3-D ocean models.

2.3.3 Age biases analysis of the 3-D OGCM results

Basin averaged mean water age and relative age bias obtained with the five experiments in Table 2.3 are presented in Figures 2.11 and 2.12, respectively. Homogeneous changes in the velocity or diffusivity fields impact mean water ages in a very similar way in all basins (Figure 2.11). Ages increase (exp. AV) or decrease (exp. AK) by the same order of magnitude everywhere with decreasing

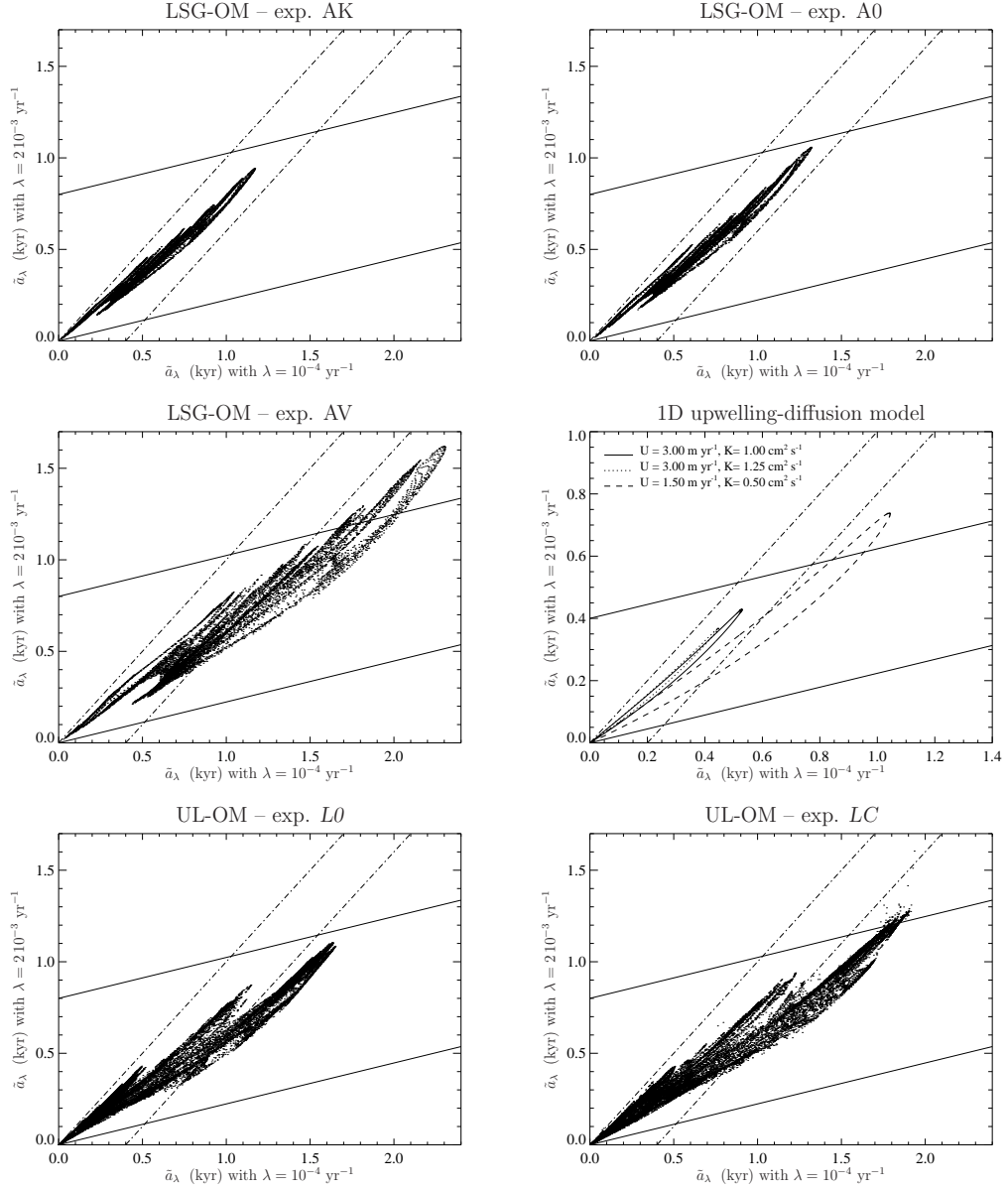


Figure 2.10: Scatter plots of the radioage for $\lambda = 2 \times 10^{-3} \text{ yr}^{-1}$ versus that for $\lambda = 1 \times 10^{-4} \text{ yr}^{-1}$ obtained for the five numerical experiments of Table 2.3: LSG-OM model for the standard run (A0, top right), halved velocities (AV, middle left) and increased explicit diffusion (AK, top left), and UL-OM model with diffusive (L0, bottom left) or second order scheme along the vertical (LC, bottom right). The 3-D experiments results only display values corresponding to depths larger than 500m. Distributions predicted with the 1-D advection-diffusion model of section 2.3.1 are reproduced in the middle right panel for three sets of velocity U and diffusivity K . The dash dot lines in each panel illustrate the 1:1 relationship. The relationship between radioages for a diffusive flow in a semi-infinite pipe (Eq. (2.41), Section 2.3.A) is also reproduced in each panel (solid lines).

velocity or increasing diffusivity, respectively. On the contrary, the circulation changes between experiments LC and L0 are not homogeneously distributed. Hence the magnitude of the response to the change differs among ocean basins. More structured vertical profiles in the Atlantic Ocean and much older North Pacific intermediate water correspond to the less diffusive case (exp. LC). Some of the changes with the LSG-OM model are also confined to specific areas; e.g., more vertical structures seem to be present in the Atlantic Ocean with exp. AV. Hence the response of water ages to the global perturbation appears to be driven by both global and local changes. At a given position in the deep ocean, any modification of the water age obtained with these sensitivity experiments may be attributed to one or several causes. First, the *pre-formed* or source water age(s) may have changed (e.g., water from the Southern Ocean filling the deep Pacific). Second, either the transit time or the ventilation pathways or both differ from the reference state. The relative age bias as defined by (2.29) will only reflect adjustment pertaining to the second group. It helps to discriminate between different functioning modes of the OGCMs deep circulation.

With the exception of the deep Pacific Ocean in the UL-OM case, Figure 2.12) reveals that for all experiments the relative age bias decreases everywhere with increasing diffusivity. Figure 2.8 together with expressions (2.31) and (2.32) indicate that such a behavior correspond to a diffusion-dominated transport. This conclusion may be drawn from the results of experiments AK (relative to A0) and L0 (relative to LC).

The additional experiment AV fits also well in the framework suggested by the 1-D upwelling-diffusion model. A decrease in velocity is accompanied by an increase of r_λ . However, the observed increase of r_λ from A0 to AV may not be explained by the sole change in velocity. Indeed, (2.31) predicts a 4-fold increase of r_λ with halved velocities, while (2.32) states that no modification of r_λ should occur. The actual change in r_λ from A0 to AV is due to an explicit decrease in the velocity but also to an implicit decrease in diffusivity of numerical origin. Indeed, advection in LSG-OM is solved with the help of a first-order upstream scheme. The numerical diffusivity of such a scheme is proportional to the velocity field (Roache, 1972). Hence both U and K decrease in experiments AV with respect to A0. Experiment AV may help in evaluating the relative role of numerical and explicit diffusivities in the model transport. From Figure 2.12 it is noticeable that changes in r_λ from A0 to AK are relatively modest. Numerical diffusivity is exactly at the same level in A0 and AK. Let's now suppose that numerical diffusion is the main contributor to the total diffusion in the 3-D model, and that the explicit term may be neglected at first approximation. Then according to (2.32) the relative change in r_λ from A0 to AV should be predicted by the ratio of numerical diffusivities. Since the numerical diffusivity K^N in A0 is twice that

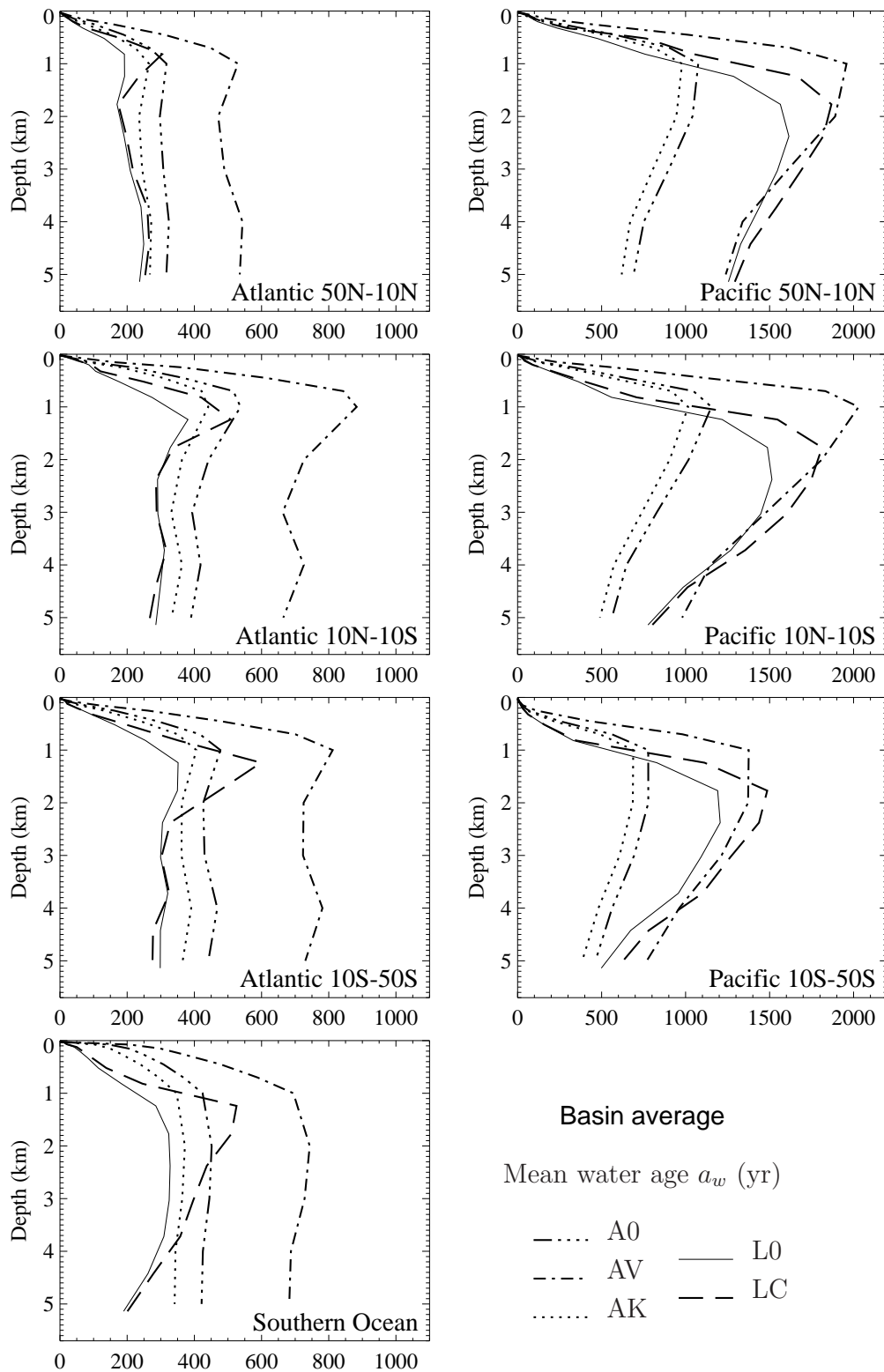


Figure 2.11: Distribution with depth of basin averaged mean water age corresponding to the five experiments in Table 2.3.

active in AV, one has

$$r_\lambda(\text{AV}) \sim \frac{K^N(\text{A0})}{K^N(\text{AV})} = 2 r_\lambda(\text{A0}). \quad (2.34)$$

The same result may also be obtained with the help of (2.31); hence it is not dependent on any hypothesis about the flow nature. It is seen in Figure (2.12) that $r_\lambda(\text{AV})$ is about twice the value of $r_\lambda(\text{A0})$. This concordance means that numerical diffusivity dominates the diffusion term in the LSG-OM transport; a conclusion in agreement with the study of section 2.2.3. Experiments with the UL-OM model also indicate a diffusivity-driven transport in most part of the ocean. In LC, the vertical diffusion is prescribed, it is directly taken from the fields provided by the circulation model. Let's denote this diffusion field $K^E(\text{LC})$. The very same field defines the original explicit diffusion in L0. However this explicit diffusion is adapted in L0 so as to take into account the numerical diffusion stemming from the upwind scheme used to solve vertical advection. Therefore the actual explicit vertical diffusion in L0 is

$$K^E(\text{L0}) = \max [(K^E(\text{LC}) - K^N), 0]. \quad (2.35)$$

Since $K^E(\text{L0}) \geq 0$, the total vertical diffusivity active in the L0 version is at least that in the LC version. Indeed, the total vertical diffusivity in L0 is

$$K(\text{L0}) = \max [(K^E(\text{LC}) - K^N), 0] + K^N \geq K^E(\text{LC}), \quad (2.36)$$

since no vertical numerical diffusion is associated with the second order scheme used in LC. Whenever K^N exceeds $K^E(\text{LC})$, the diffusion in L0 is larger than in LC. This explains why r_λ decreases from experiment LC to L0.

However this decrease is not observed in every basins. In the Pacific ocean r_λ hardly changes and even increases slightly below 1 km depth in the Equatorial and North Pacific. In accordance with Equation 2.31, such an increase occurs when advection is dominant. Individual profiles (Figure 2.13) from the Pacific Ocean illustrate the evolution from diffusion-driven flows in the south to a more advection-dominated transport in the north. Such a trend is also clearly seen in the lower two panels of figure 2.10: the largest values of the radioage associated to mid-depth Pacific waters increase from L0 to LC by following a line with slope close to 1. In that area the transport in the UL-OM model must then be controlled mostly by advection.

2.3.4 Conclusion

The 1-D upwelling-diffusion model does not provide easily handled analytical solutions for the general case. However analytical solutions for the relative age

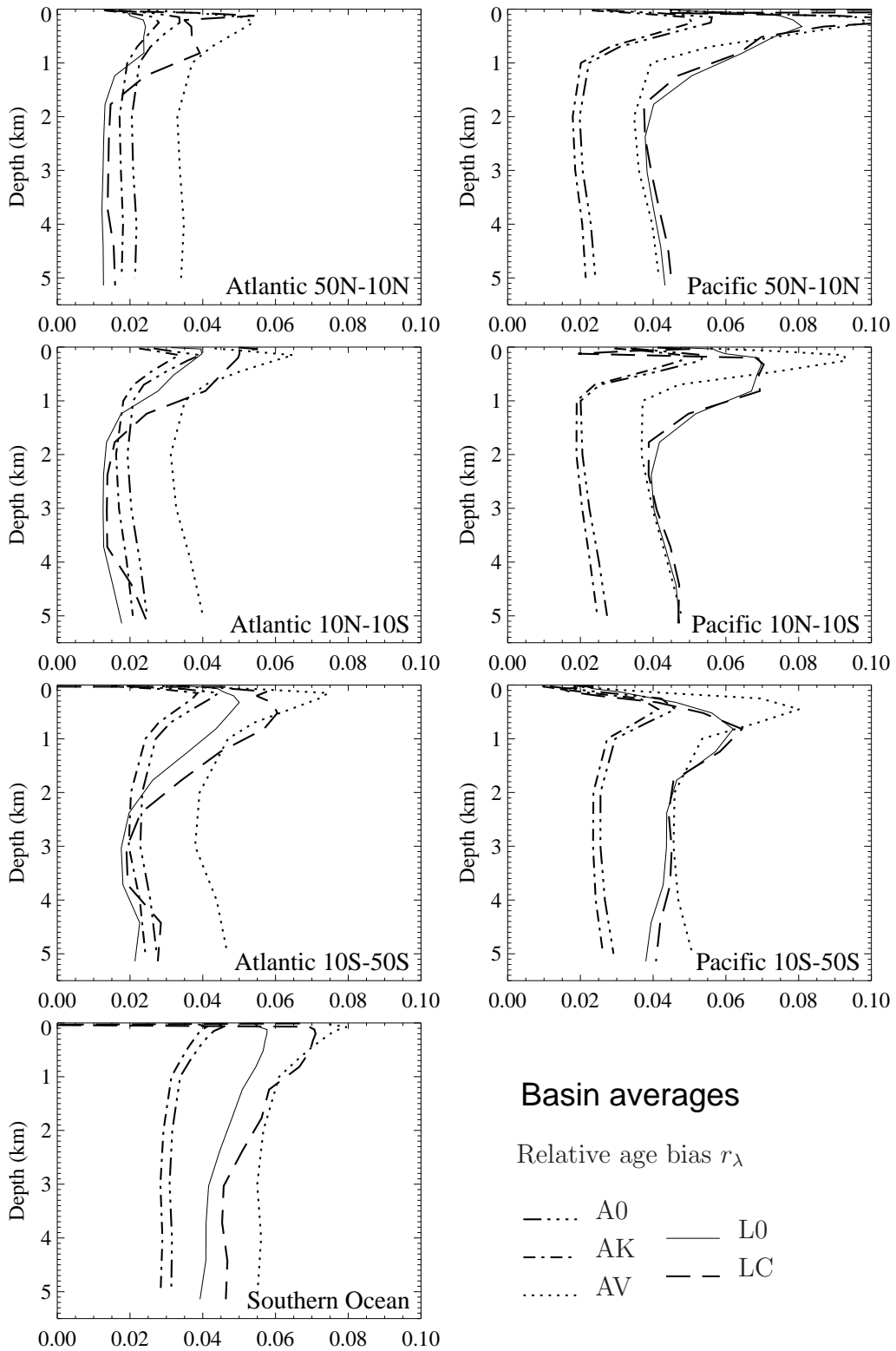


Figure 2.12: Distribution with depth of basin averaged r_λ for the five experiments from Table 2.3. These results correspond to $\lambda = 10^{-4} \text{ yr}^{-1}$.

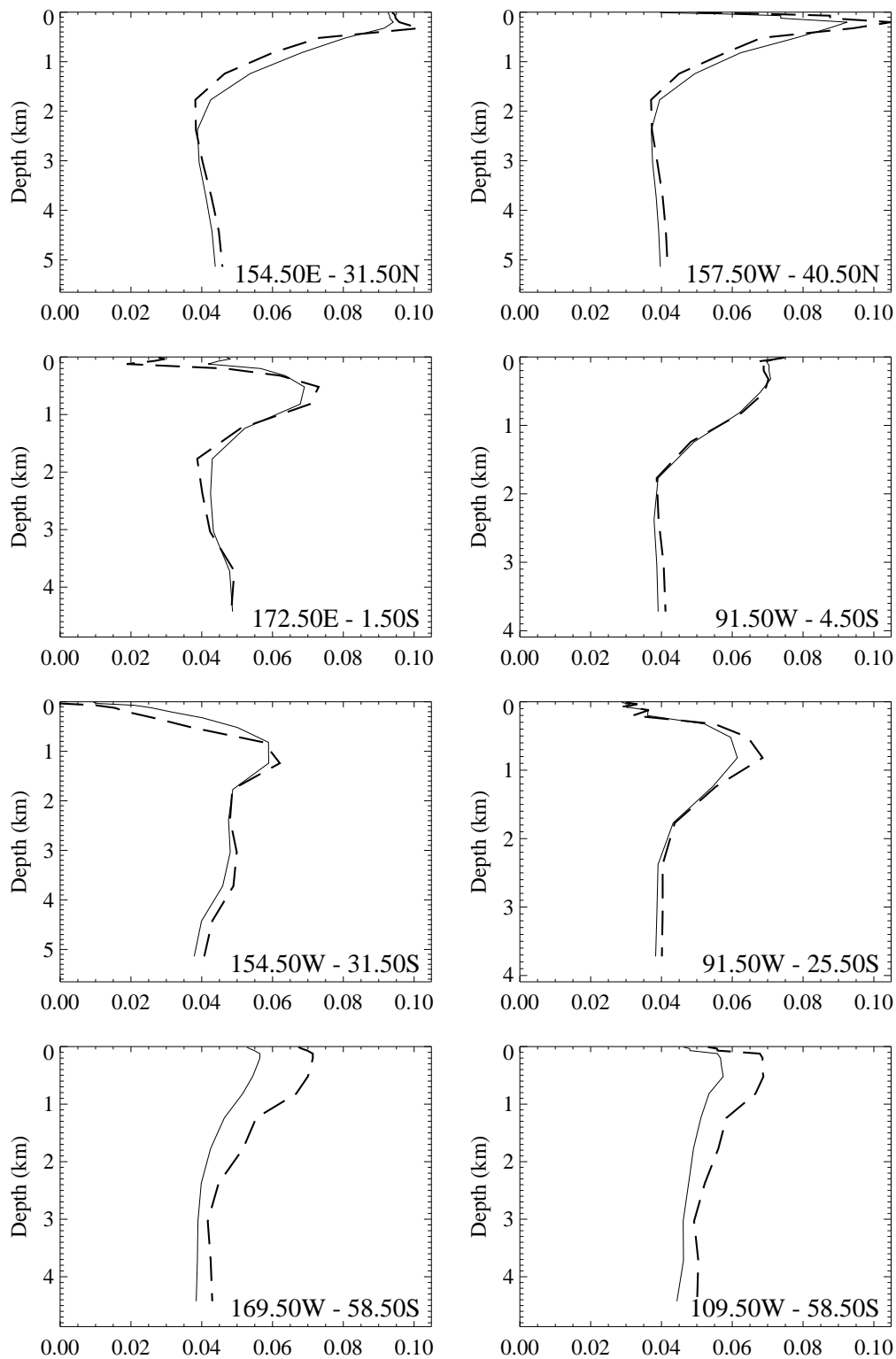


Figure 2.13: Vertical profiles of r_λ at several locations in the Pacific Ocean for experiments L0 (solid) and LC (dashed) with the UL-OM model. The relative age bias is computed for $\lambda = 10^{-4} \text{ yr}^{-1}$.

bias in the case of slowly decaying radioactive tracers are available. They provide additional means for assessing the deep ocean circulation as reproduced by OGCMs. The predicted changes of r_λ with K obtained in section 2.3.1 seem to be of relevance for assessing the relative importance of advection and diffusion in 3-D OGCMs transport. Such approach also provides a means to evaluate the role played by numerical diffusion in the total mixing. Hence r_λ could be a valuable tool to understand difference in behaviour among models and could be useful in case of models with high sophistication in the representation of mixing processes (isopycnal; TVD schemes, ...). Further, the information may be obtained at any spatial scale, from the local to the global.

The experiments carried out for this work indicate that transport in the LSG-OM model is dominated by diffusion (consistent increase of r_λ with diminishing K). A similar behavior is encountered in most part of the ocean with the UL-OM model. In the latter model the flow in some areas of the North Pacific seems to be dominated by advection .

The present study agrees and reinforces the conclusions obtained with the leaky funnel model. It is seen that diffusion, especially numerical diffusion, plays a non-negligible role in setting the ventilation timescales in OGCMs. Previous works performed with similar type of OGCMs lead to identical conclusions (*Oschlies, 2000; Deleersnijder et al., 2002; Holzer and Primeau, 2006*). According to MD08, a global diffusivity of 10^{-4} m²/s may be associated to the motion at its largest scale in the OGCMs. This is in agreement with several field estimates. However one may seriously question the circulation in OGCMs on the basis that it seems dominated by diffusion everywhere. This is at odds with field studies which evidence very low background diffusivities and very localized areas of intense mixing (*Ledwell et al., 1993; Polzin et al., 1997; Toole and McDougall, 2001; Webb and Sugimotohara, 2001; Kunze et al., 2006; St. Laurent and Simmons, 2006*).

Addressing this point is important because the model versions used in long term climate studies do not differ much from those examined here.

The present study as well as other works (*Maier-Reimer, 1993; Broecker and Peng, 2000; Dutay et al., 2004*) evidence how the use of easy to model tracers characterized by different timescales would be helpful for assessing ocean circulation models. Up to now this task is however limited by the paucity of available measurements.

2.3.A Semi-infinite domain

Let us consider a one-dimensional transport problem in a semi-infinite pipe ($x \in [0, \infty[$). At steady-state, with Dirichlet boundary conditions at the origin

$$C_\lambda(0, t) = 1 \quad \text{and} \quad \alpha_\lambda(0, t) = 0,$$

one obtains (*Deleersnijder et al.*, 2001; *Delhez et al.*, 2003)

$$a_\lambda(x, t) = \frac{x}{U} \frac{1}{\sqrt{1 + 4K\lambda/U^2}}, \quad (2.37)$$

$$\tilde{a}_\lambda(x, t) = \frac{2x}{U} \frac{1}{\sqrt{1 + 4K\lambda/U^2 + 1}}. \quad (2.38)$$

It is readily seen from these solutions that the age of the inert tracer or the water age a_w reduces to the advective timescale

$$a_w = \frac{x}{U}. \quad (2.39)$$

Hence, in this model the water age is not affected by diffusion.

Maier-Reimer (1993) took advantage of this model to assess the relative role of advection and diffusion in determining the distribution of tracers in OGCMs. His results, expressed for the ratios of tracer concentrations, are easily generalized to radioages.

If the same boundary conditions apply to all tracers at $x = 0$, it is readily seen that all conservative tracers share the same solution for their concentration. Taking the conservative tracer intervening in Eq. (2.11) as water, the radioage corresponding to a tracer with decay rate λ is given by

$$\tilde{a}_\lambda(x) = \frac{1}{\lambda} \ln \frac{1}{C_\lambda(x)}, \quad (2.40)$$

since $C_w(x) = 1$.

In the case of a purely diffusive flow the equation for the radioactive tracer concentration,

$$K \frac{\partial^2 C_\lambda}{\partial x^2} = \lambda C_\lambda,$$

has solution of the form (*Maier-Reimer*, 1993)

$$C_\lambda(x) \sim e^{-\sqrt{\lambda/K} x}.$$

Let us consider now two radioactive tracers with decay rates λ_1 and λ_2 , respectively. The ratio of their radioages obeys

$$\frac{\tilde{a}_{\lambda_1}}{\tilde{a}_{\lambda_2}} = \sqrt{\frac{\lambda_2}{\lambda_1}}. \quad (2.41)$$

It is worth mentioning that this ratio is independent of K .

If the flow in the pipe is purely advective, one obviously has

$$\frac{\tilde{a}_{\lambda_1}}{\tilde{a}_{\lambda_2}} = 1. \quad (2.42)$$

We followed the line of reasoning as in *Maier-Reimer* (1993) but identical conclusions may be drawn from the asymptotic analysis of (2.38).

2.3.B Analytical solutions

The following equations present the complete analytical solutions to the 1-D upwelling-diffusion problem of section 2.3.1 for the mean water age and the mean radioactive tracer age

$$a_w(x) = \frac{x}{U} - \frac{L}{U} \left(\exp \frac{Ux}{K} - 1 \right) \left(\coth \frac{UL}{K} - 1 \right), \quad (2.43)$$

$$\begin{aligned} a_\lambda(x) = & \frac{\left(-1 + \coth \left[\frac{L\sqrt{4\lambda K + U^2}}{K} \right] \right)}{2\sqrt{4\lambda K + U^2}} \\ & \left\{ \left(1 + \exp \left(\frac{\sqrt{4\lambda K + U^2} 2L}{K} \right) - 2 \exp \left(\frac{(U + \sqrt{4\lambda K + U^2}) L}{K} \right) \right) \right. \\ & \quad \left(-1 + \exp \left(\frac{\sqrt{4\lambda K + U^2} x}{K} \right) \right) 2L \\ & + \left(-1 + \exp \left(\frac{\sqrt{4\lambda K + U^2} 2L}{K} \right) \right) \\ & \quad \left(-1 + \exp \left(\frac{(U + \sqrt{4\lambda K + U^2}) L}{K} \right) - \exp \left(\frac{\sqrt{4\lambda K + U^2} x}{K} \right) \right. \\ & \quad \left. \left. + \exp \left(\frac{LU + \sqrt{4\lambda K + U^2}(x - L)}{K} \right) \right) x \right\} \\ & / \left\{ -1 + \exp \left(\frac{(U + \sqrt{4\lambda K + U^2}) L}{K} \right) + \exp \left(\frac{\sqrt{4\lambda K + U^2} x}{K} \right) \right. \\ & \quad \left. - \exp \left(\frac{LU + \sqrt{4\lambda K + U^2}(x - L)}{K} \right) \right\}. \quad (2.44) \end{aligned}$$

Chapter 3

Modelling the Ocean Carbon Cycle

LOCH: Dispositif qui sert à mesurer la vitesse du navire à partir de la distance parcourue pendant un temps donné.

(*CILF*, 1989)

This chapter is divided into three parts. Section 3.1 presents an overview of the ocean carbon cycle. Section 3.2 contains a description of LOCH (Liege Ocean Carbon Heteronomous model), the ocean carbon cycle model I developed. Sections 3.3 and 3.4.1 address the performances of LOCH when embedded in LOVECLIM and its sensitivity to the formulations of particulate organic matter flux and biogenic opal.

The ocean carbon cycle we describe (and model) is limited to processes occurring in the water column and does not consider sediments. According to *Archer et al.* (1998) they can be neglected on time frames we mostly focus on (less than 10^3 yr).

3.1 Overview of the ocean carbon cycle

Carbon dioxide CO_2 dissolves in the ocean where it reacts with seawater to form a weak acid in equilibrium with bicarbonate and carbonate ions (*Stumm and Morgan*, 1996). The dissolved inorganic carbon (DIC) concentration, C_T , in seawater is given by

$$C_T = \text{CO}_{2w} + [\text{HCO}_3^-] + [\text{CO}_3^{=}], \quad (3.1)$$

where CO_{2w} , $[\text{HCO}_3^-]$ and $[\text{CO}_3^{2-}]$ represent the concentrations of dissolved carbon dioxide, bicarbonate and carbonate ions, respectively¹. In seawater DIC is mainly found as HCO_3^- . The latter amounts to about 90% of C_T , the remnant consisting mostly in CO_3^{2-} , with CO_{2w} contributing for less than 1% (*Stumm and Morgan, 1996*).

Carbon is also found in the ocean under organic forms, either dissolved or particulate. The approximate ratio between DIC and dissolved (particulate) organic carbon DOC (POC, resp.) is DIC:DOC:POC = 2000:38:1 (*Denman et al., 2007*).

The exchange of CO_2 between the atmosphere and the ocean is controlled by physico-chemical and biological processes. They are usually described as the *solubility pump*, the *organic pump*, and the *CaCO₃ counter pump*, respectively (*Broecker and Peng, 1982; Volk and Hoffert, 1985; Heinze et al., 1991*). These three components are illustrated in Figure 3.1.

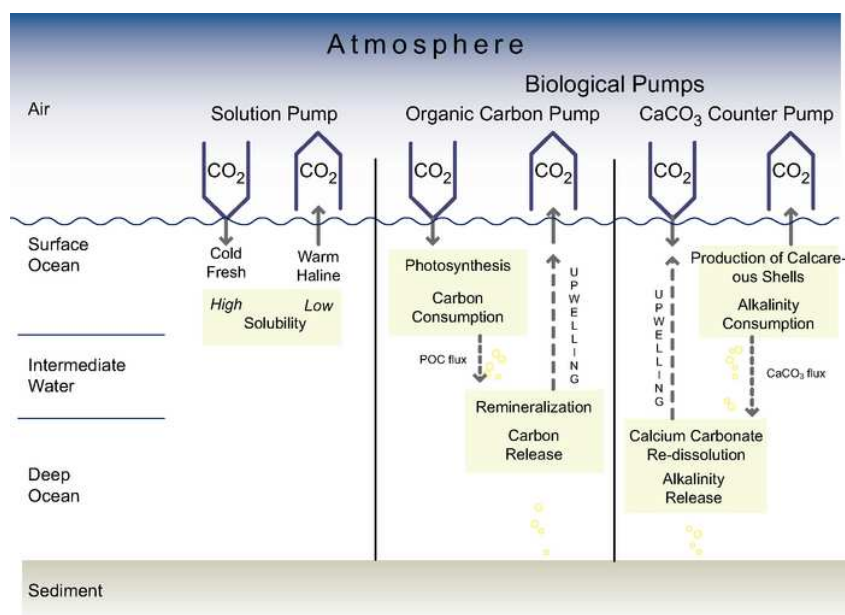


Figure 3.1: Schematic representation of the solubility pump, the organic carbon pump and the CaCO₃ counter pump. Figure 7.10 from *Denman et al. (2007)* redrawn after the original work of *Heinze et al. (1991)*.

The net air-sea flux depends on the actual difference between CO_{2w} at the air-sea interface and the concentration at equilibrium with the atmosphere, $K_H p\text{CO}_2$,

¹In expression (3.1) we neglect the H_2CO_3 species, which is present in negligible amounts in natural seawater.

where K_H is the Henry's law constant, or solubility. Temperature (and to a lesser extent salinity) controls the CO_2 solubility in seawater. The quantity which is exchanged with the atmosphere is CO_2 , not DIC. Since the former is much less abundant than the latter, the actual inorganic carbon content of seawater is two orders of magnitude larger than what it would be without the carbonate speciation.

The two other pumps are biologically mediated. The organic carbon pump (Fig. 3.1) is sustained by the photosynthetic activity of organisms in the upper well-lit layers of the ocean which assimilate carbon during their growth. A fraction of the detritus related to that activity (fecal pellets, dead organisms...) is exported to depth. This transport occurs at a much faster rate than does replenishment by the circulation and maintains a low surface CO_{2w} in productive areas. The degradation of the sinking material constitutes a source of DIC for deep waters. When these waters come back to the surface the excess CO_2 is outgassed to the atmosphere.

Some of the planktonic species build calcium carbonate (CaCO_3) shells. This process increases the CO_{2w} concentration (CaCO_3 counter pump, Fig. 3.1). However this source is much lower than the sink related to the organic carbon pump. Upon the death of the organisms these shells sink to depth and undergo dissolution, a process which lowers CO_{2w} concentrations in surrounding waters. A fraction of these shells is preserved into deep sea sediments.

Biological activity creates larger vertical gradients of carbon (and alkalinity) than would exist with only the solubility pump. According to *Bacastow and Maier-Reimer* (1990) the latter explains on average only 17% to 25% of the observed surface-to-deep C_T gradient.

All together these processes result in a contrasted distribution of the differences between ocean CO_{2w} concentrations at the surface and atmospheric CO_2 (Figure 3.2). Cold water areas (e.g., the North Atlantic) constitute a sink for atmospheric CO_2 . In the warm water sphere carbon is released to the atmosphere. In warm areas characterized by deep water upwelling this process is enhanced (e.g., the eastern equatorial Pacific). In the Southern Ocean, the upwelling of carbon-rich water in the Antarctic divergence area counterbalances to some degree the effect of lower temperatures. It should be noted that Figure 3.2 includes the anthropogenic perturbation and does not represent the pre-industrial air-sea CO_2 disequilibrium.

3.1.1 Control on atmospheric CO_2 levels

The respective roles of the ocean circulation and biogeochemical states in setting atmospheric CO_2 levels can be illustrated with simple numerical experiments (Table 3.1). Experiment *B* in that table corresponds to the reference state: active biota and standard circulation. Removing biological activity in the model

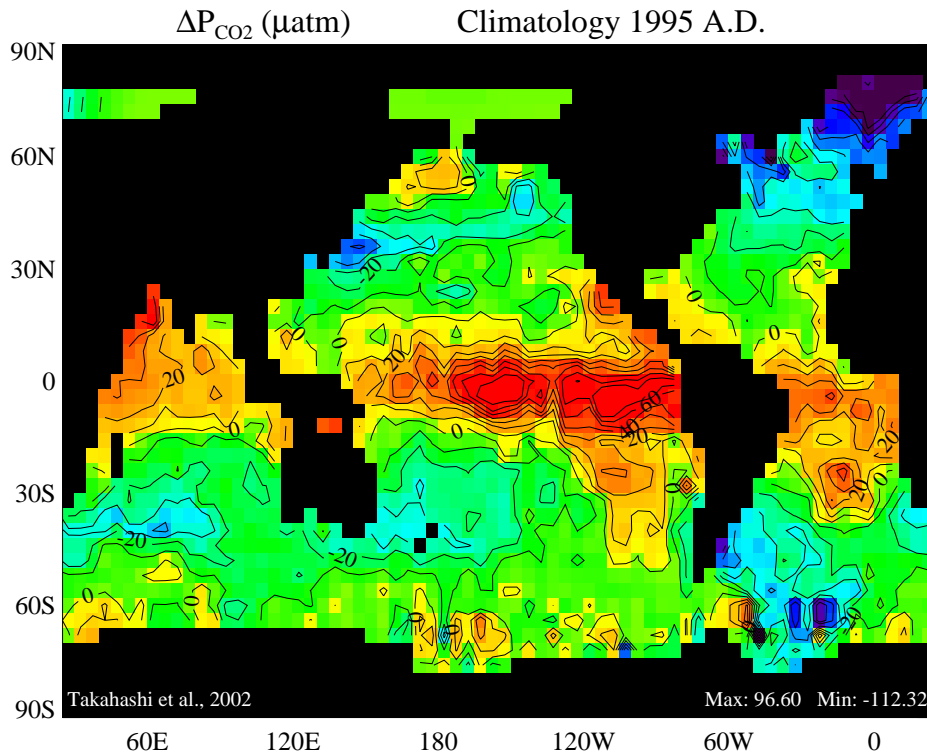


Figure 3.2: Climatology of the difference between sea and air CO_2 partial pressures for the reference year 1995. Positive values (yellow to red) indicate excess CO_2 in the sea, negative (purple to green) correspond to areas where atmospheric CO_2 enters the ocean. Data from *Takahashi et al.* (2002).

approximately doubles the atmospheric pCO_2 (exp. *A*). If the ocean were motionless and homogeneous in biogeochemical variables, atmospheric pCO_2 would rise further (exp. *H*). The second part of Table 3.1 addresses the consequences of modifying essential components of the ocean circulation. In this context we only considered the case of an abiotic ocean. Reducing velocities by 50% (exp. *S*) lowers pCO_2 by 36 ppmv. The more sluggish the circulation becomes, the more opportunity surface waters have to equilibrate with the atmosphere in areas such as the Southern Ocean characterized by low residence times at the surface. The role of surface-deep ocean mixing in the cold water sphere is emphasized with experiments in which we reduce the convection frequency, which, among other processes, controls the rate of deep water formation in the model. A 50% reduction results in an increase of 20 ppmv in atmospheric CO_2 , with respect to the same advection state (exp. *M* to be compared to exp. *S*).

Such tests should not be interpreted as analogues for past climate transitions. They correspond to equilibrium situations obtained by globally changing the ocean state. In the real world, global or regional and transient changes, such as

Table 3.1: Equilibrium atmospheric CO₂ partial pressure (column 4, ppmv) for different states of the ocean biogeochemistry (column 2) and of the large scale circulation (column 3). The corresponding experiment name is displayed in column 1. V represents the 3-D velocity field and τ_C the convection rate.

Exp.	BGC state	Circulation	pCO ₂
<i>B</i>	Biotic	V, τ_C	272
<i>A</i>	Abiotic	V, τ_C	543
<i>H</i>	Homogeneous	motionless	888
<i>L</i>	Abiotic	$V/2, \tau_C$	507
<i>M</i>	Abiotic	$V/2, \tau_C/2$	527
<i>A</i>	Abiotic	V, τ_C	543
<i>F</i>	Abiotic	$2 \times V, 2 \times \tau_C$	560

Experiments performed with the LSG-OM fields driving LOCH. For each of the experiments the same inventory of carbon in the ocean-atmosphere system. The inventory of total alkalinity is the same in abiotic and biotic experiments. The pCO₂ value in exp. *H* is obtained with the help of the mean SST and SSS predicted by the OGCM (16.7°, and 34.7, resp.) and the global mean DIC and alkalinity (2.27 mmol/kg, and 2.37 meq/kg, resp.). Moderate changes in the reference state may lead to pCO₂ values which differ by ~ 100 ppmv from the 888 ppmv value corresponding to exp. *H*

a slowdown of the Atlantic meridional overturning circulation (AMOC), would lead to very different results. Furthermore, experiments in which the velocity field and convective rates are modified, as is done here, contradict the internal OGCM physics (there are no concomitant changes in temperature, salinity, energy fields). Additionally, these simple tests do not consider potential feedbacks between circulation changes and biological activity. *Bacastow and Maier-Reimer* (1990) performed similar tests with their OCCM. With halved velocities, they obtain a pCO₂ reduction of 39 ppmv with biota and of 21 ppmv without biota, with respect to a reference state characterized with an atmospheric pCO₂ of 290 ppmv.

Despite their limited pertinence these tests illustrate the potential of the ocean to control atmospheric CO₂. Now let us turn to the transient response.

3.1.2 Atmospheric adjustment time

Gases do not cross the air-sea interface with infinite speed. Viscous micro-layers on both sides provide resistance to their transfer. The piston, or transfer, velocity for CO₂ is approximately equal to 1500 m/yr; it is of the same order of magnitude for CFCs, or O₂. Hence a non-reacting gas would need about 12 days to equilibrate with a 50 m deep mixed layer.

However CO₂ reacts with carbonates in seawater. At constant temperature,

salinity, and chemical conditions, the magnitude of the C_T change with respect to CO_{2w} change is given by the homogeneous buffer factor or Revelle factor (*Broecker et al.*, 1979). This factor, illustrated in Figure 3.3, reads

$$\beta_{Hom} = \frac{C_T}{CO_{2w}} \left(\frac{dCO_{2w}}{dC_T} \right), \quad (3.2)$$

where CO_{2w} is at equilibrium with the atmosphere. Expression (3.2) may be

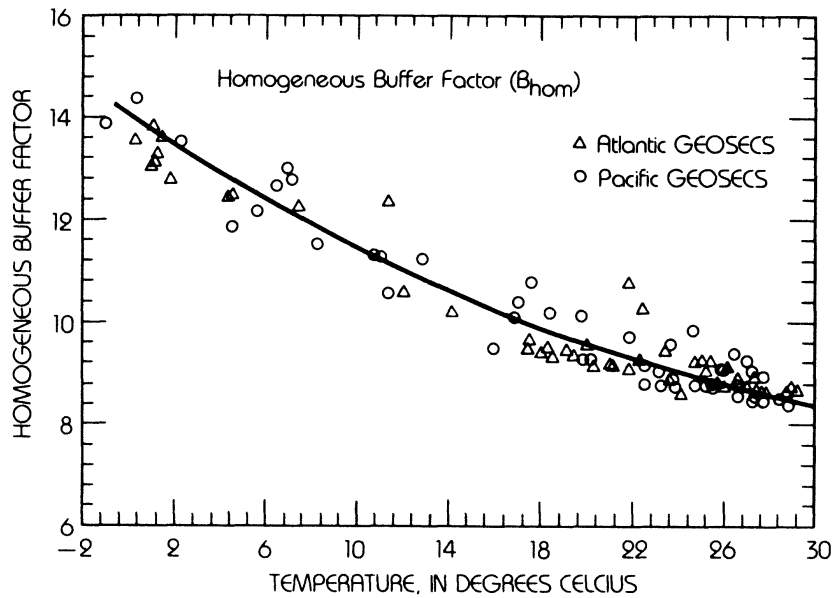


Figure 3.3: Plot of the homogeneous buffer factor β_{Hom} against the temperature (solid line). The symbols correspond to observed values at the ocean surface. Figure 1b from (*Sundquist et al.*, 1979)

transformed into

$$\frac{dC_T}{C_T} = \frac{1}{\beta_{Hom}} \left(\frac{dCO_{2w}}{CO_{2w}} \right). \quad (3.3)$$

For temperate waters β_{Hom} is of the order of 10 (Figure 3.3). Expression (3.3) implies that for an increase of 1% in C_T inventory, the CO_2 content of the atmosphere must rise by 10%. Consequences are that it takes about ten times longer for CO_2 to equilibrate with the mixed layer than for a non-reactive gas with similar solubility (*Broecker and Peng*, 1992).

This chemical control constitutes the limiting step for air-sea exchange of CO_2 .

Under global warming and larger atmospheric CO_2 concentrations concern is being raised about the ocean capacity to absorb excess atmospheric CO_2 . Indeed

not only will solubility decrease but the buffer factor will also increase with CO_2 levels (*Maier-Reimer et al.*, 1995; *Plattner et al.*, 2008), providing so more resistance to CO_2 invasion. The model studies presented in Chapter 1 illustrate this process.

An additional limit to the ocean capacity to absorb excess atmospheric CO_2 takes its origin in the replacement rate of equilibrated waters by undersaturated ones. This rate is controlled by the overturning circulation. Hence ocean ventilation constitutes the rate limiting step for the adjustment of atmospheric CO_2 following a perturbation (Figure 1.3).

3.2 Modelling the ocean carbon cycle

LOCH (Liege Ocean Carbon Heteronomous) is a three-dimensional ocean carbon cycle model. This model has been continuously evolving since we designed it (*Mouchet and François*, 1996, Section 3.4.3) but several concepts remain identical. The ‘H’ in LOCH acknowledges the fact that it needs an OGCM to provide 3-D salinity, temperature, and circulation fields.

LOCH considers the following prognostic variables:

- dissolved inorganic carbon C_T (molC/m^3),
- total alkalinity Alk (eq/m^3),
- dissolved inorganic phosphorus P (molP/m^3),
- dissolved organic matter DOM (molP/m^3),
- silica Si (molSi/m^3),
- oxygen O_2 (molO_2/m^3),
- phytoplankton biomass B (molP/m^3),
- particulate organic matter POM (molP/m^3).

An atmospheric module embedded in LOCH allows the prognostic computation of atmospheric gas concentrations, O_2 and CO_2 .

The various exchanges among variables are detailed below. Isotopes are addressed later on, in Chapter 4. Most of the parameters used in LOCH are listed in Table 4 in *Goosse et al.* (2010) (see Appendix A).

3.2.1 Speciation

Redfield ratio

The carbon cycle is intimately coupled to the cycles of the elements composing the organic matter. The knowledge of the relative composition of the latter in the primary elements (C, N, P, Si, O_2) is hence necessary in order to determine

the biologically-mediated fluxes between the different reservoirs. Although the ratios between these elements may exhibit large excursions among species or during the growing season (e.g., *Banse*, 1994), on average the composition of phytoplankton is fairly constant (*Redfield et al.*, 1963). Analyses of the correlated changes in nutrients in the deep ocean confirm the constancy and uniformity of the ratio between elements released during the remineralization of organic matter (*Takahashi et al.*, 1985; *Broecker et al.*, 1991; *Anderson and Sarmiento*, 1994; *Anderson*, 1995). The latter analyses lead to updated values of the Redfield ratios in the ocean.

Similarly to other simplified models of the ocean carbon cycle (e.g. *Maier-Reimer*, 1993; *Najjar et al.*, 2007) we assume the stoichiometric constancy of organic material. We use the ratio suggested by *Anderson and Sarmiento* (1994)

$$C : N : P : -O_2 = 117 : 16 : 1 : 170. \quad (3.4)$$

The silica cycle is also dominated by biological uptake (*Broecker and Peng*, 1982; *Nelson et al.*, 1995) but the ratio Si:P is highly heterogeneous in the ocean. Indeed, Si:P ratios in living organisms are comprised between 14 and 50 (*Jacques and Tréguer*, 1986; *Broecker and Peng*, 1982; *Nelson et al.*, 1995). LOCH uses a constant value, Si:P=35:1.

Other organisms build calcareous shells as addressed later.

In subsequent model equations and the text, the “Redfield” ratio of two elements X and Y is represented as $S_{X:Y}$.

Alkalinity

We deliberately limit our description to some aspects of the aquatic chemistry. Comprehensive discussions of the ocean carbon chemistry with accurate definitions may be found in *Stumm and Morgan* (1996), *Munhoven* (1997) and *Wolf-Gladrow et al.* (2007).

Alkalinity and dissolved inorganic carbon (3.1) are both needed to determine the concentration of dissolved CO_2 in surface waters or the $CaCO_3$ saturation level in deep waters. Alkalinity may be interpreted as a measure of the acid neutralizing capacity of seawater (*Stumm and Morgan*, 1996). The exact expression for total alkalinity (*Dickson*, 1981; *Dickson and Goyet*, 1994) is obtained from the constraint of electroneutrality and reads

$$\begin{aligned} \text{Alk} = & [\text{HCO}_3^-] + 2 [\text{CO}_3^{2-}] + [\text{B}(\text{OH})_4^-] + [\text{H}_3\text{SiO}_4^-] + 2 [\text{H}_2\text{SiO}_4^{2-}] \\ & + [\text{NH}_3] + [\text{HS}^-] + 2 [\text{S}^{2-}] + [\text{OH}^-] \\ & + [\text{HPO}_4^{2-}] + 2 [\text{PO}_4^{3-}] - [\text{H}_3\text{PO}_4] - [\text{H}^+]. \end{aligned} \quad (3.5)$$

This expression contains the concentration of species which result from the dissociation in seawater of boric acid $\text{B}(\text{OH})_3$ ($\text{B}(\text{OH})_4^-$), silicic acid H_4SiO_4

(H_3SiO_4^- and $\text{H}_2\text{SiO}_4^{2-}$), phosphoric acid H_3PO_4 (HPO_4^{2-} and PO_4^{3-}), hydrogen sulfide H_2S (HS^- and S^{2-}), and water (OH^- and H^+). Ammonia NH_3 also participates to Alk.

Expression (3.5) includes all species contributing to seawater alkalinity and allows an immediate estimate of the changes linked to oceanic biogeochemical processes (*Stumm and Morgan, 1996; Wolf-Gladrow et al., 2007*).

Removal of a strong acid increases Alk through the decrease of H^+ ions. This process occurs during photosynthesis as a consequence of phytoplankton assimilation of HNO_3 . The assimilation of phosphates by phytoplankton also increases Alk through the removal of H_3PO_4 . Hence the build-up of plankton cells in Redfield ratio is accompanied by a relative change in Alk equal to $S_{\text{Alk:P}} = 17$.

Calcifying organisms lower alkalinity through the removal of CO_3^- ions. The precipitation of 1 mol of CaCO_3 decreases Alk by 2 eq.

Addition or removal of CO_2 (air-sea exchange, respiration, ...) and H_4SiO_4 (opal shell building) have no effect on Alk.

However any modification of Alk leads to the opposite change of $\text{CO}_{2\text{w}}$; i.e., an increase (or decrease) in Alk results in a lower (or larger, resp.) $\text{CO}_{2\text{w}}$.

Concentrations of NH_3 and H_2S are typically very low in open ocean water and their contributions to Alk would only be significant in areas with dominant anoxic processes (*Dickson and Goyet, 1994*). In the upper layers phosphorous and silicon are nearly depleted. We will then further simplify Eq. (3.5) by dropping these contributions. We estimated the error on $\text{CO}_{2\text{w}}$ resulting from that further simplification. It is negligible in most part of the ocean and of the order of 2% in the Southern Ocean where surface silica concentrations are larger than elsewhere. Such an error is far smaller than other uncertainties inherent to climate modelling.

In terms of concentration boron intervenes only for 2% in Alk. However, its role is extremely important. Neglecting it would result in a pCO_2 bias of at least 100 ppmv. Actually, the borate system increases the ocean CO_2 storage capacity by more than 20% (*Maier-Reimer and Hasselmann, 1987*).

In the model, alkalinity is then represented, with sufficient accuracy, with a reduced form of (3.5) which retains the essential contributions (bicarbonate, carbonate and borate),

$$\text{Alk} = [\text{HCO}_3^-] + 2 [\text{CO}_3^{=}] + [\text{B}(\text{OH})_4^-] + [\text{OH}^-] - [\text{H}^+]. \quad (3.6)$$

C_T and Alk are conservative properties in the sense that if expressed in mol $(\text{kg seawater})^{-1}$ they are rigorously independent of pressure and temperature (*Dickson, 1981; Stumm and Morgan, 1996*).

The system is then fully determined by using dissociation constants (e.g., for water *Millero (1995)*, for borate *Dickson (1990)*, for carbonates *Dickson and Millero (1987)*). The boron concentration is computed from salinity (*Millero, 1995*).

In Eq. (3.5) H^+ is measured on the seawater pH scale, that is it includes hydrogen ions complexed with fluor and sulfur (HF and HSO_4^-) and OH^- includes $MgOH$ (Dickson, 1981; Millero, 1995; Stumm and Morgan, 1996). The constants required to determine the various chemical equilibria in seawater are then expressed on the seawater pH scale. When needed transformation from the free pH scale to the seawater pH scale are performed with the help of formulations from Millero (1995) and Dickson and Riley (1979).

3.2.2 Organic carbon pump

It should be noted that although B and POM are prognostic variables they are not subject to the 3-D transport. The rationale underlying this choice is that the characteristic lifetimes of these variables are much shorter than the time scales of interest in the context of climate studies.

Soft tissues

In a somewhat similar approach to that used in HAMOCC 3 (Maier-Reimer, 1993; Heinze et al., 2003) LOCH is aimed at reproducing the export production, i.e., the flux of organic carbon to the deep ocean. Therefore, we do not consider the total primary production but only the fraction which escapes recycling in the upper layers. The LOCH biological module should therefore not be understood as a model of ocean ecosystems but rather as a model of biogenically mediated fluxes of constituents in the ocean.

The basis for the export-production model is a pool of phytoplankton whose growth is driven by the availability of P and light. The phytoplankton biomass B is only defined for depths smaller than 100m. B has the same units as P. Its evolution follows

$$\frac{dB}{dt} = \mu B - r_B B. \quad (3.7)$$

The actual growth rate μ is a function of temperature T, light \mathcal{L} , and DIP,

$$\mu = \mu_{Max} \frac{\mathcal{L}}{K_L + \mathcal{L}} \frac{T}{K_T + T} \frac{P}{K_P + P}, \quad (3.8)$$

with μ_{Max} the maximum growth rate, K_L , K_T , and K_P half-saturation constants. The rate of removal of phytoplankton r_B is defined as

$$r_B = G_M \frac{B}{K_B + B} + m_B, \quad (3.9)$$

in which m_B and G_M represent the mortality and the maximum grazing rate, respectively. The use of a Michaelis-Menten like formulation for grazing in (3.9) allows for a non-linear closure of the system which is necessary in order to properly reproduce the productivity (Fasham, 1993).

POM

Upon death, organisms feed the fast sinking particulate organic matter POM pool.

An instantaneous POM flux is distributed with depth below the productive layers according to a power law (*Martin et al.*, 1987)

$$\mathcal{J}(Z) = J_0 Z^{-\alpha_{\text{POM}}}, \quad (3.10)$$

where Z measures the downward distance from the euphotic layer.

J_0 represents the flux of particles from the euphotic layer (the *export production*), it is given by

$$J_0 = \int_0^{Z_E} r_B B dz, \quad (3.11)$$

with Z_E the depth of the euphotic layer.

Below the productive layers POM remineralizes into P or transforms into dissolved organic matter (DOM). The remineralization rate of organic matter (POM or DOM) depends primarily on the oxygen availability. Anoxic remineralization is allowed but occurs at a slower pace than oxic processes. The remineralization rate reads

$$r_i = r_i^o \frac{\text{O}_2}{K_{\text{O}_2} + \text{O}_2} + r_i^a \frac{K_{\text{O}_2}}{K_{\text{O}_2} + \text{O}_2}, \quad (3.12)$$

where i stands either for POM or for DOM. In (3.12) r_i^o and r_i^a represent the maximum oxic and anoxic remineralization rates, respectively. These maximum rates are taken as constant since it seems that the hypothesis of a lower bacterial efficiency in colder areas is not supported (*Jahnke*, 1996).

Then the equation governing the temporal evolution of POM reads

$$\frac{d\text{POM}}{dt} = -\frac{d}{dZ}\mathcal{J}(Z) - d_{\text{POM}}\text{POM} - r_{\text{POM}}\text{POM} - f_{\text{sed}}(\text{POM}), \quad (3.13)$$

with d_{POM} the dissolution rate, r_{POM} the remineralization rate and f_{sed} a sink representing permanent sequestration into the sediments. The latter takes into account that in the open ocean, approximately 1% of the primary production reaches the sediments and out of that only a few percent undergoes permanent sequestration, of the order of $1.3 \text{ TmolC yr}^{-1}$ (*Hedges and Keil*, 1995; *Jahnke*, 1996).

3.2.3 Shells

Together with soft tissues, many living organisms develop shells made either of silicate (diatoms, radiolarians) or calcium carbonate (coral, foraminifera, pteropods, coccoliths).

There is no pool associated to the hard tissues (opal and CaCO_3). Therefore the flux of shells at depth and the population growth at the surface are out of phase. This would be a serious shortcoming if we were addressing ecosystem studies. However, over longer time scales this bias is of no consequence. In forthcoming versions this bias will be corrected for.

Diatoms

Diatoms contribute to approximately half the net oceanic primary production. Further, their relative abundance in the phytoplankton increases as primary productivity increases (*Nelson et al.*, 1995). In the Eastern Equatorial Pacific upwelling area, diatoms are believed to carry out all the export or “new” production (*Dugdale and Wilkerson*, 1998). They seem to dominate the foodweb as soon as Si concentrations are larger than $2\mu\text{M}$ (*Egge and Aksnes*, 1992; *Rixen et al.*, 2005).

Their importance lead us to consider them as foodweb regulator. They are not differentiated from the other species within B but regulate the rain ratio and the POM flux to depth when accounting for them in the \mathcal{J} flux (Section 3.4.2). A constant $S_{Si:P}$ ratio is used to determine the export of opal accompanying the export production. The vertical distribution of biogenic silica below the productive layers follows an exponential law $e^{-\beta Z}$ where β takes into account the influence of temperature T on the dissolution rate (*Wollast*, 1974; *Bidle et al.*, 2002; *Fujii and Chai*, 2005):

$$\beta = \beta_d \exp(\kappa_d T(Z)).$$

The dissolution flux at depth Z is then

$$\mathcal{D}_{Si} = -\beta S_{Si:P} J_O e^{-\beta Z}$$

CaCO_3 “counter” pump

The ratio of inorganic carbon to organic carbon in sinking material, or the *rain ratio*, is highly variable (*Tsunogai and Noriki*, 1991). In oligotrophic areas large rain ratio values are found, from 0.5 to 1.0. In the polar oceans this ratio drops down to less than 0.1, while typical values for coastal and upwelling regions ranges from 0.1 to 0.5.

Since diatoms dominate the foodweb in very productive areas LOCH computes the rain ratio $S_{\text{CaCO}_3:P}$ according to the availability of silica. The influence of temperature and the ubiquity of calcareous organisms are also included in the parameterization of this process. $S_{\text{CaCO}_3:P}$ is defined as

$$S_{\text{CaCO}_3:P} = r_{\text{CaCO}_3} + \frac{T}{K_{\text{CaCO}_3} + T} (\Psi_{\text{zoo}} + \Psi_{\text{phy}}(1 - f_{\text{Dia}})), \quad (3.14)$$

and must be less or equal to $S_{\text{CaCO}_3:P}^M$, a maximum rain ratio. Expression (3.14) calls for the following parameters or variables: r_{CaCO_3} the minimum rain ratio, K_{CaCO_3} half-saturation constant for CaCO_3 precipitation ($^{\circ}\text{C}$), Ψ_{zoo} the rain ratio associated to zooplankton, Ψ_{phy} the rain ratio associated to non-siliceous phytoplankton, and f_{Dia} the fraction of siliceous phytoplankton, $f_{\text{Dia}} \in [0, 1]$. f_{Dia} represents the fraction in J_0 which is supported by diatoms, it is computed from J_0 with Si concentrations and a half-saturation constant for silica uptake. A constant fraction f_{Arag} of calcium carbonate shells is also assumed to be made of aragonite which is more soluble than calcite.

Deep waters are undersaturated with respect to CaCO_3 but the depth of the transition between super-saturated (above) and under-saturated (below) waters is shallower in the North Atlantic than in the the North Pacific (Figure 3.4). Homogeneous dissolution rates appear then inadequate. The total flux of dissolving CaCO_3 shells reads

$$\mathcal{D}_{\text{CaCO}_3} = S_{\text{CaCO}_3:P} (r_{\text{Arag}} f_{\text{Arag}} + r_{\text{Calc}} (1 - f_{\text{Arag}})) J_0 \quad (3.15)$$

The dissolution of shells occurs in the bottom layer under the production area at a rate proportional to the CaCO_3 under-saturation degree. The remainder of the particle flux is preserved in marine sediments. Hence LOCH implicitly includes some carbonate compensation mechanisms. The expressions for the solubility of calcite and aragonite are from *Mucci* (1983) and *Millero* (1995) while the coefficients for the pressure dependence of the chemical equilibrium constants are from *Millero* (1995).

3.2.4 3-D equations

The equation governing the transport of a variable X is

$$\frac{\partial}{\partial t} X + \mathcal{H}(X) = q_v(X). \quad (3.16)$$

The term $q_v(X)$ represents the source-minus-sink term for X . It takes into account biotic or abiotic processes, at the exclusion of radioactive decay. The operator \mathcal{H} represents physical transport (advection, diffusion as well as convection). It takes the following form

$$\mathcal{H}(X) = \nabla \cdot (\mathbf{u} X - \mathbf{K} \nabla X), \quad (3.17)$$

with \mathbf{u} and \mathbf{K} the three-dimensional velocity and diffusivity fields. Gathering all the processes described above, one obtains the transport equations for P, DOM,

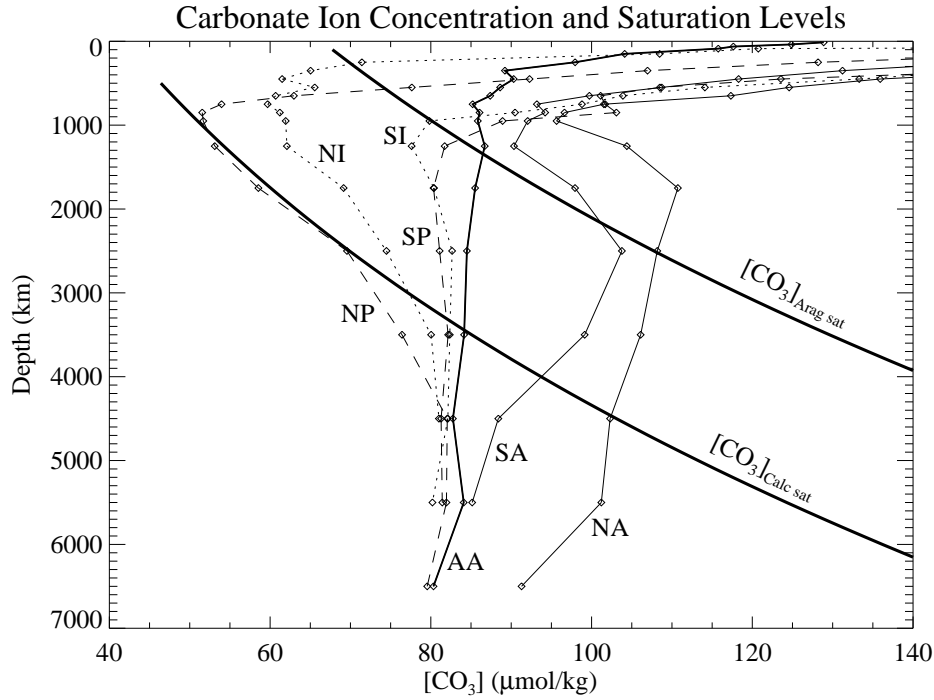


Figure 3.4: Vertical profiles of $[\text{CO}_3^{2-}]$ in different ocean basins (North and South Atlantic, Indian and Pacific). Superimposed are the saturation levels for aragonite $[\text{CO}_3^{2-}]_{\text{Arag sat}}$ and calcite $[\text{CO}_3^{2-}]_{\text{Calc sat}}$. Below the saturation level waters are undersaturated with respect to the corresponding CaCO_3 form. Figure 1.11 from *Munhoven* (1997).

O_2 , and Si

$$q_v(\text{P}) = -\mu B + r_{\text{POM}} \text{POM} + r_{\text{DOM}} \text{DOM} \quad (3.18)$$

$$q_v(\text{DOM}) = d_{\text{POM}} \text{POM} - r_{\text{DOM}} \text{DOM} + f_{\text{riv}}(\text{DOM}), \quad (3.19)$$

$$q_v(\text{O}_2) = S_{\text{O}_2:P} (\mu B + r_{\text{POM}} \text{POM} + r_{\text{DOM}} \text{DOM}), \quad (3.20)$$

$$q_v(\text{Si}) = -S_{\text{Si:P}} \mu B + \mathcal{D}_{\text{Si}} + f_{\text{riv}}(\text{Si}). \quad (3.21)$$

Since C_T and Alk are conservative properties they may be described adequately in the model by means of the usual transport equations. The source and sink terms for C_T and Alk are therefore simply derived from the biological fluxes with the help of the ‘‘Redfield’’ ratios.

$$q_v(C_T) = S_{C:P} (-\mu B + r_{\text{POM}} \text{POM} + r_{\text{DOM}} \text{DOM}) - S_{\text{CaCO}_3:P} \mu B + f_{\text{riv}}(C_T) + \mathcal{D}_{\text{CaCO}_3} \quad (3.22)$$

$$q_v(\text{Alk}) = S_{\text{Alk:P}} (\mu B - r_{\text{POM}} \text{POM} - r_{\text{DOM}} \text{DOM}) - 2 S_{\text{CaCO}_3:P} \mu B + f_{\text{riv}}(\text{Alk}) + 2 \mathcal{D}_{\text{CaCO}_3}. \quad (3.23)$$

Some organic matter and shells escape remineralization or dissolution, and are permanently preserved in sediments. On the other hand, river input ($f_{riv}(X)$) of Alk, Si, DOM and C_T represent net sources for the ocean. The main rivers of the world and their relative inflow are taken into account in this process.

3.2.5 Boundary conditions

We impose that the advective and diffusive fluxes across the ocean floor are zero.

At the ocean-atmosphere interface we specify the gas fluxes. The boundary condition for a gas with atmospheric concentration C is

$$\mathcal{F} = \kappa_C K_H p_C - \kappa_C C_d \quad (3.24)$$

In these equations κ_C is the gas transfer velocity, K_C its solubility in seawater, p_C the atmospheric partial pressure of C at sealevel, and C_d the concentration of the dissolved gas in seawater.

The piston velocity is based on the formulation of *Wanninkhof* (1992). We consider a reduced air-sea exchange rate in the presence of sea ice. Therefore the piston velocity in the model is computed in the following way

$$\kappa_C = (1 - f_{ice}) K_W \overline{w^2} \sqrt{660/Sc} \quad (3.25)$$

with $\overline{w^2}$ the square wind magnitude, f_{ice} the fraction of the sea surface covered with sea ice, Sc the Schmidt number and 660 a normalisation factor.

Expression (3.25) is purely empirical and does not represent any physical mechanism. The parameter K_W was determined from a fit to gas transfer data obtained using bomb ^{14}C .

If the gas considered is CO_2 then an additional term accounts for the chemical enhancement of its exchange at low wind speeds and high temperatures (*Wanninkhof and Knox*, 1996) and (3.25) for CO_2 reads

$$\kappa_{\text{CO}_2} = (1 - f_{ice}) (b(T) + K_W \overline{w^2}) \sqrt{660/Sc} \quad (3.26)$$

Here b is a second-order polynomial in temperature T (*Wanninkhof and Knox*, 1996).

Solubilities are taken from *Wanninkhof* (1992) for O_2 and from *Weiss* (1974) for CO_2 . Schmidt numbers are gas-dependent and calculated according to *Wanninkhof* (1992).

The coefficient K_W in (3.26) is adjusted in the model so to obtain an average value of the CO_2 invasion rate (i.e., $\kappa_{\text{CO}_2} \times K_H$) for pre-industrial times of the order of $0.061 \text{ mol } \mu\text{atm}^{-1} \text{ m}^{-2} \text{ yr}^{-1}$ (*Siegenthaler*, 1986; *Watson and Liss*, 1998).

3.2.6 Atmosphere

LOCH includes an atmospheric module with the purpose of providing the prognostic evolution of concentrations of the various gases intervening in biogeochemical cycles. This module is also active in LOVECLIM. The evolution of gases in the atmosphere module is based on a 1D diffusion equation in the meridional direction, i.e., one implicitly assumes instantaneous mixing in the zonal and vertical directions. Hence the transport in the atmosphere of a gas with concentration C obeys

$$\frac{\partial C}{\partial t} = \frac{\partial}{\partial y} \sin(\theta) K_y \frac{\partial C}{\partial y} - \mathcal{P}_C \quad (3.27)$$

where t is time, θ the colatitude, and y the meridional position. The diffusion coefficient K_y [m^2/s] is homogeneous within each hemisphere and allows mixing within a few weeks. A lower value of K_y is used at the equator so that inter-hemispheric mixing occurs with a characteristic time scale of 2 years (*Bacastow and Maier-Reimer*, 1990). In (3.27) \mathcal{P}_C includes local sink terms where relevant, e.g., radioactive decay for ^{14}C .

At the lower boundary one imposes a flux, \mathcal{F}_C . It includes the exchange of gases between the atmosphere on the one hand, and the ocean and the continental biosphere on the other hand. \mathcal{F}_C may also include other sources (e.g., anthropogenic emissions).

The considered gases are carbon dioxide CO_2 , oxygen O_2 (as well as the two isotopic forms ^{13}C and ^{14}C , which are discussed in Chapter 4).

3.3 LOCH performances

The various parameters of the biological module were first determined by forcing LOCH with climatological phosphate reconstructions and comparing the predicted fields (export-production, silica...) with available estimates. LOCH was mainly calibrated and validated in off-line mode, initially with the LSG-OM and UL-OM circulation fields (Appendix A), and later on with the circulation fields provided by CLIO (*Campin*, 1997). Afterwards LOCH was fully embedded in LOVECLIM (*Goosse et al.*, 2010, See Appendix A). In LOVECLIM, LOCH also computes the evolution of gases in the atmosphere. More details on the coupling aspects together with the present-day values of many parameters of LOCH may be found in *Goosse et al.* (2010). Since LOCH performances have been presented and discussed in a series of documents (*Gérard et al.*, 1996; *Fichefet et al.*, 2007; *Menviel*, 2008) and papers (*Mouchet and François*, 1996; *Menviel et al.*, 2008b, 2011b) we will not discuss them in details here. The modelled anthropogenic CO_2 uptake and inventory may be found in Figures 2.4 and 4.3. Export pro-

duction and air-sea pCO₂ differences are presented below. The silica cycle and particulate organic matter flux are discussed in Sections 3.4.1 and 3.4.2.

Several parameters (mainly those regulating downward fluxes) are tuned to the model circulation, in order to reproduce at best the deep-sea tracer distributions. Such parameters are thus empirical and mostly reflect vertical characteristic of the circulation fields, as discussed in Section 3.4.3 (*Mouchet and François, 1996*).

3.3.1 Export production

Table 3.2 presents a compilation of available estimates of the global export production. The values predicted by LOCH with different circulation fields are also displayed. A source of discrepancy among estimates may stem from the reference level at which the downward POM flux is computed. Usually it is assumed to be 100 m. The model study of *Najjar et al. (2007)* considers it to be at 75 m. With UL-OM and LOVECLIM this flux is evaluated at 91 m, with LSG-OM at 110 m.

Table 3.2: Global export production (XPP) estimates (column 1) from the literature as from observational methods (lines 2 to 5) or by means of models (lines 6 & 7). The lower part of the table gives the export values as predicted by LOCH with different circulation fields. Column 2 gives the original source. Only the POM flux is retained from the model study of *Najjar et al. (2007)*.

XPP (GtC/yr)	References
16	<i>Falkowski et al. (1998)</i>
11.1	<i>Laws et al. (2000)</i>
5.3±0.8	<i>Louanchi and Najjar (2000)</i>
10.2–12.3	<i>Gnanadesikan et al. (2001)</i>
8.7	Hamburg LSG ; <i>Heinze et al. (2003)</i>
7–17	OCMIP models; <i>Najjar et al. (2007)</i>
7.9	LSG-OM
8.2	UL-OM (version L0)
6.2	LOVECLIM

LOVECLIM global export production (XPP) is in the low range of model values. The calibration of the model was performed under two criteria: best agreement between model and DIP fields, and a not too excessive export production in the eastern equatorial Pacific Ocean. The large upwelling predicted by the circulation model in that area might be the cause for the globally low export production. This feature of the circulation generates a ‘nutrient trapping’

(*Najjar et al.*, 1992) a problem which is common to many coarse grid models. It has been shown to be caused by model deficiencies in reproducing the complex pattern of currents in that area (*Aumont et al.*, 1999), or by advection numerics, even when the model is based on a central-difference advection scheme (*Oschlies*, 2000).

Nevertheless the geographical distribution of export production seems reasonably reproduced (Figure 3.5). The distribution of XPP north of the ACC is in qualitative agreement with the study of *Schlitzer* (2002).

3.3.2 Air-sea pCO₂ difference

Figure 3.6 compares the air-sea Δp_{CO_2} (i.e., $p_{\text{CO}_2}^{\text{w}} - p_{\text{CO}_2}^{\text{a}}$) for 2000 A.D. computed with LOVECLIM to the field reconstruction of *Takahashi et al.* (2009). The agreement is generally good except in the Southern Ocean. North of the ACC, Δp_{CO_2} in the model is not as negative as in the data field. This might be explained by slightly too high surface temperatures predicted by LOVECLIM in that area (see Fig. 9 of *Goosse et al.* (2010), Appendix A). Close to Antarctica model and data disagree. It could either be related to a circulation bias (the Si distribution at depth close to Antarctica is not well reproduced either, Section 3.4.1) or because the model presents values averaged over all seasons, while data are biased toward the summer months.

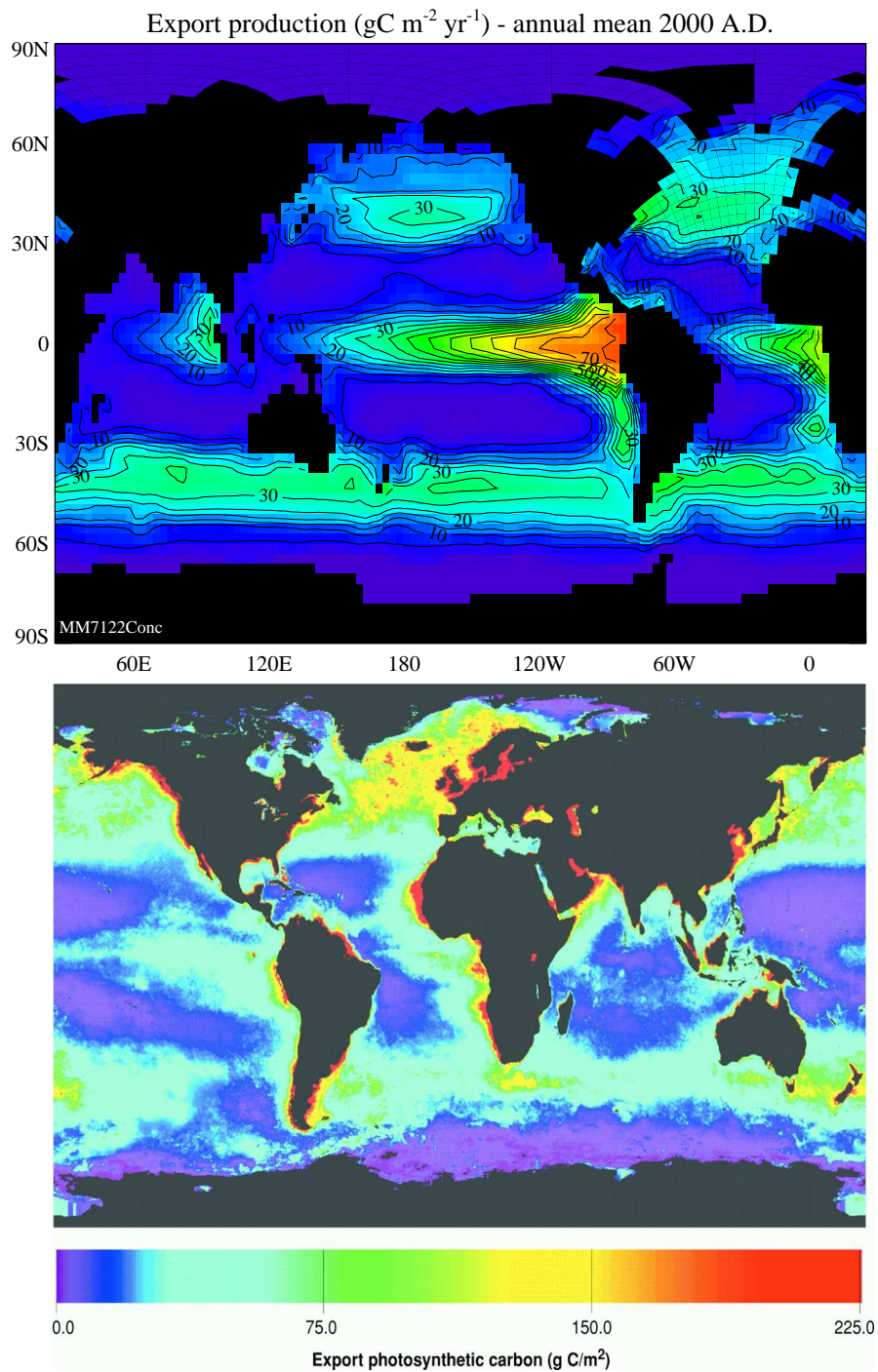


Figure 3.5: (top) Annual mean export production in LOVECLIM1.2. (bottom) Annual mean export production for the world oceans. Figure 2 from *Falkowski et al. (1998)*.

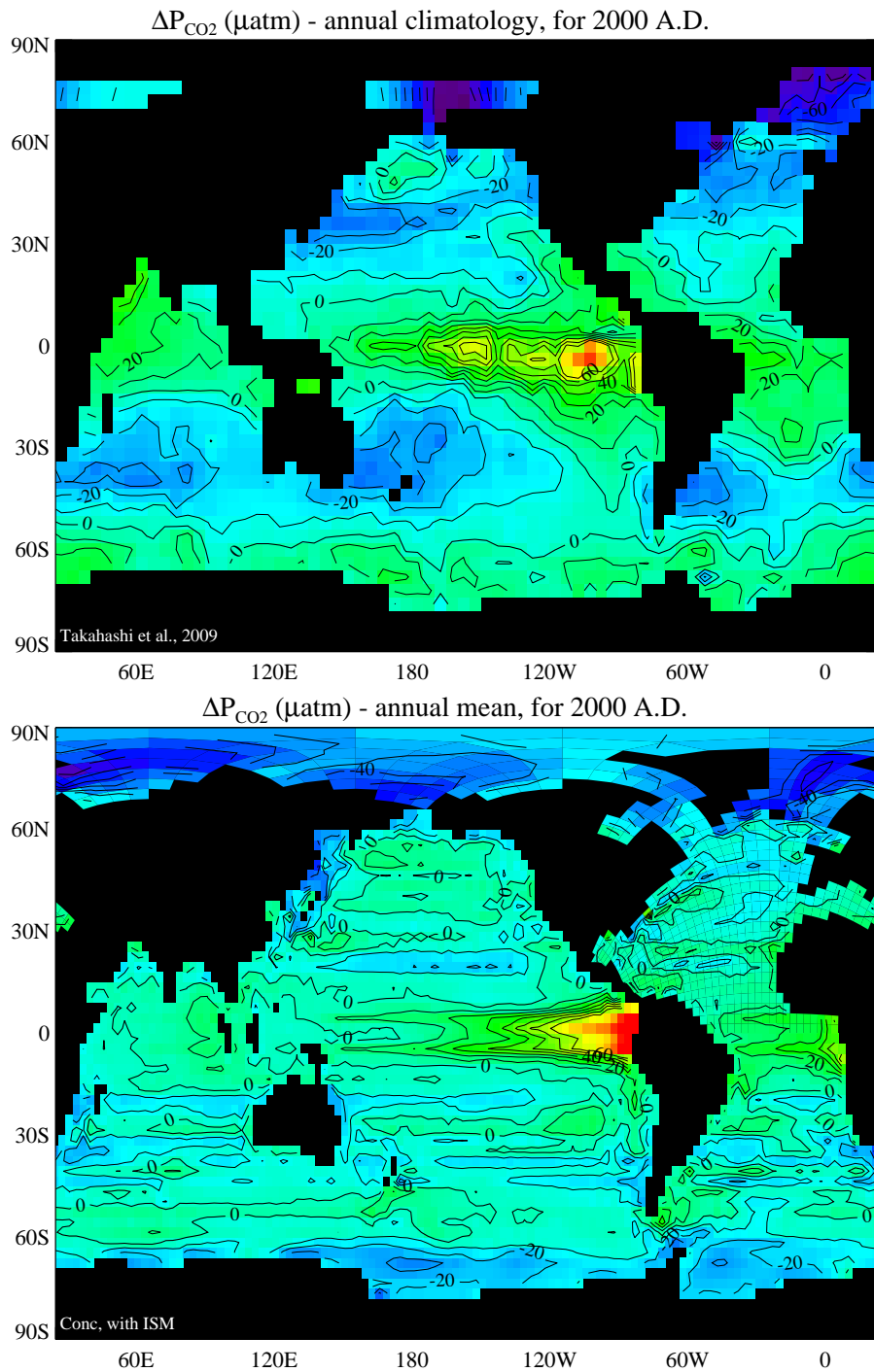


Figure 3.6: (top) Air-sea CO_2 partial pressure difference for 2000 A.D. in climatology (Takahashi et al., 2009) and (bottom) in LOVECLIM1.2. Positive values indicate excess CO_2 in the ocean.

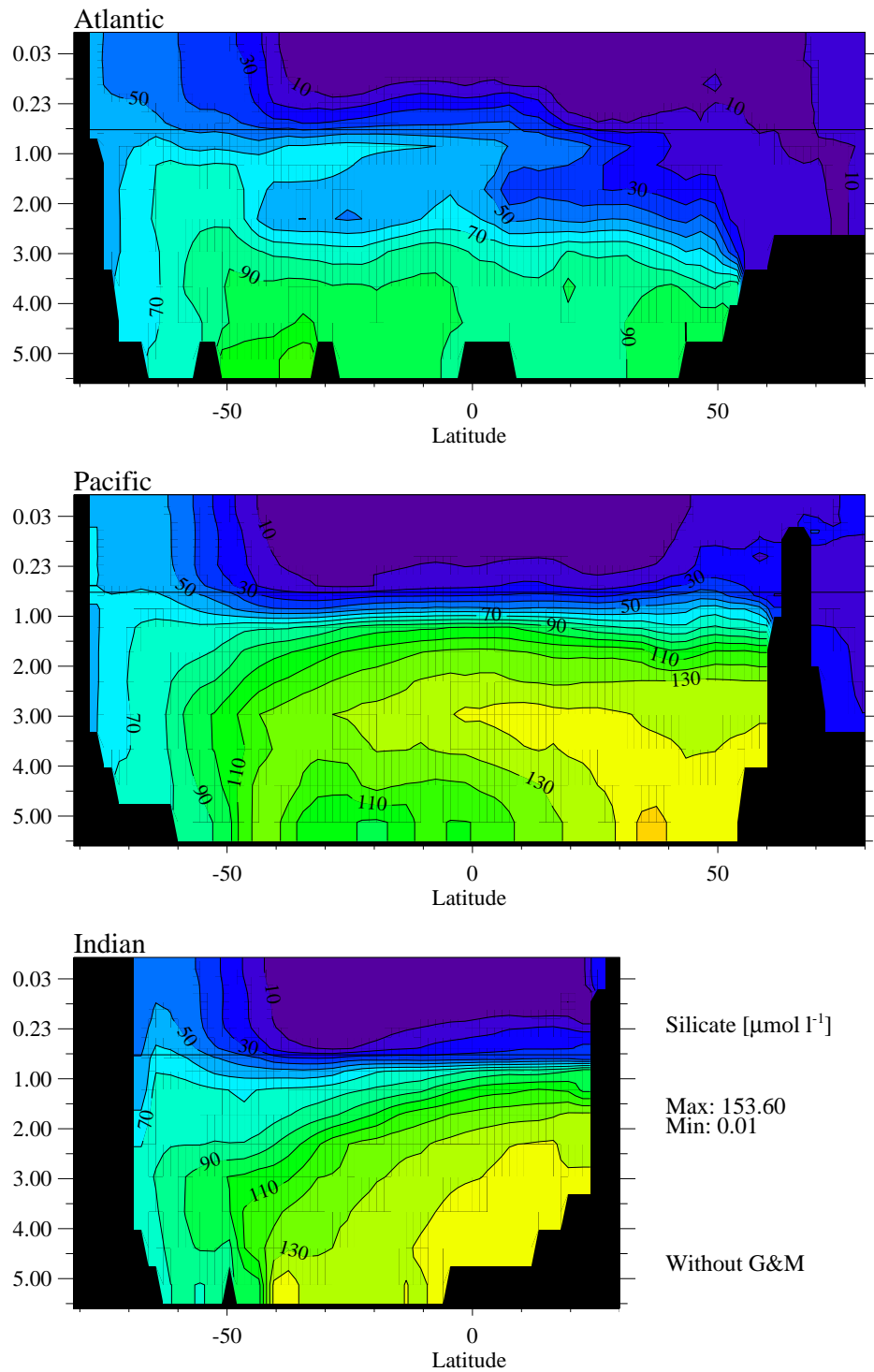


Figure 3.7: Model-predicted contemporary distribution of Si in the Atlantic (top), Pacific (middle), and Indian (bottom). The vertical axis represents depth in km. Please note the scale switching from non-linear (above 500m) to linear (deeper than 500 m). Results have been zonally averaged within each ocean basin.

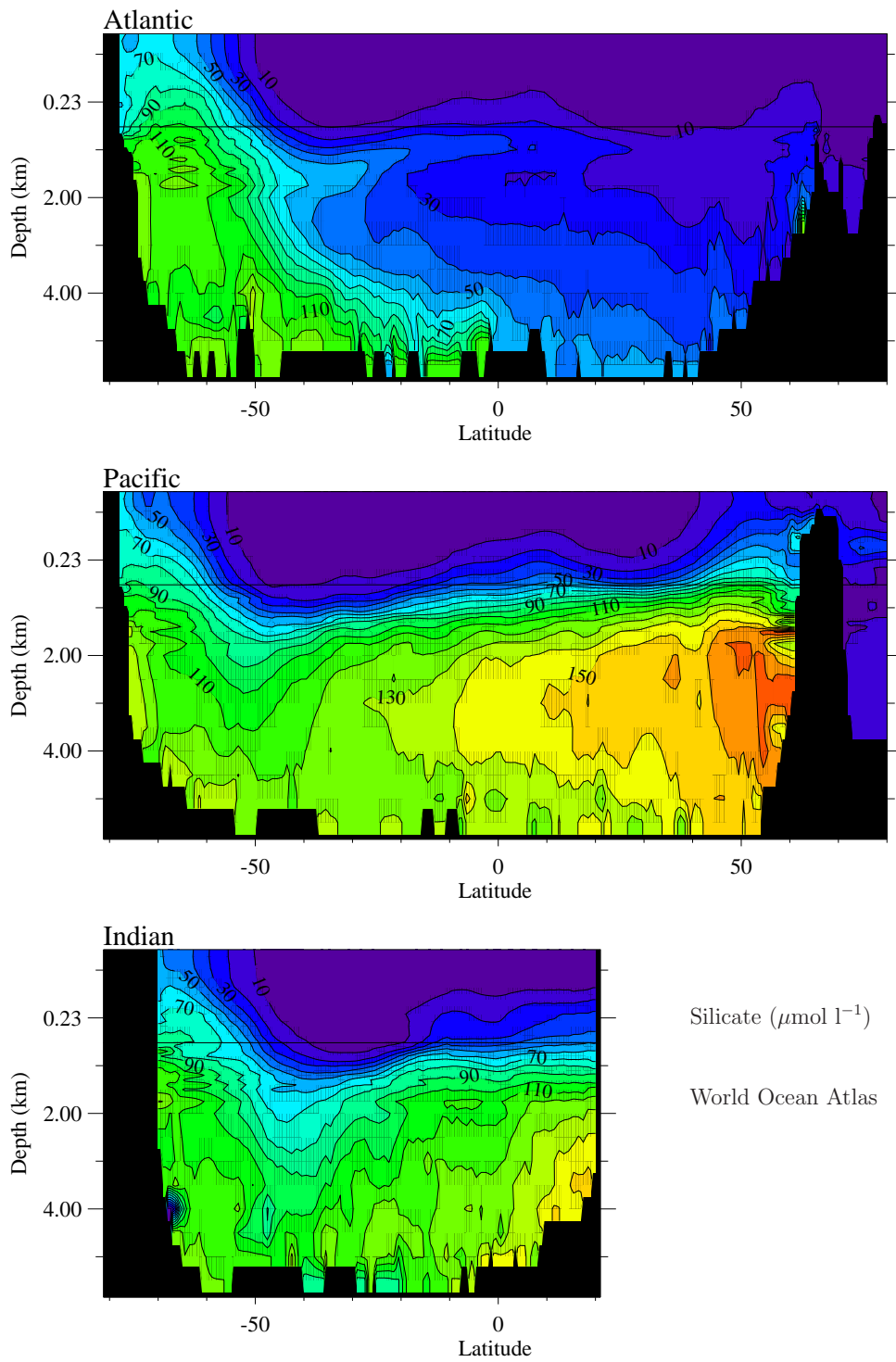


Figure 3.8: Same as Fig. 3.7 but as reconstructed from field measurements (Conkright et al., 1994).

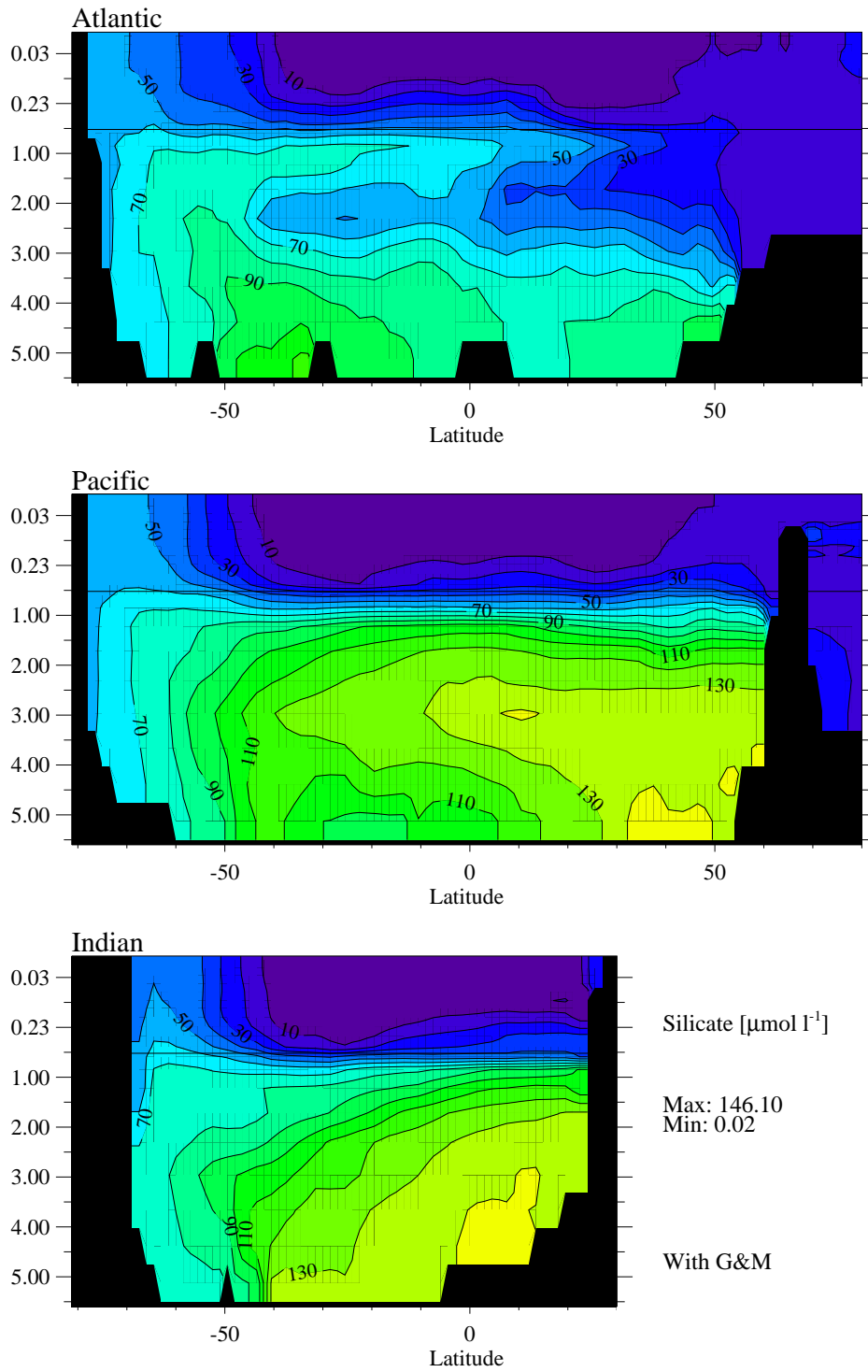


Figure 3.9: Same as Fig. 3.7 with the Gent-McWilliams mixing scheme considered in the transport of tracers.

3.4 Sensitivity studies

3.4.1 Si dissolution profiles

Figure 3.7 shows the contemporary distribution of silica in the ocean as obtained from experiments performed with LOCH when included in LOVECLIM. The corresponding distribution based on field measurements (*Conkright et al., 1994*) is reproduced in Figure 3.8. While a quite reasonable distribution is obtained with the model in most basins, large discrepancies do exist in the Southern Ocean and in the deep North Atlantic.

The use of a Gent-McWilliams mixing parametrization (*Gent and McWilliams, 1990*) in the OGCM does not result in much improvement of the silica distribution in the Southern Ocean (Figure 3.9). This is in contrast with the study of *Gnanadesikan (1999)*.

The discrepancy between model and data was then addressed in a series of sensitivity experiments corresponding to different formulations of the opal-tests dissolution scheme. In these, the fate of biogenic opal below the productive layers is represented in four different ways (Table 3.3). Experiment Si1 is equivalent to bottom dissolution only, in Exp. Si2 there is no temperature effect, while Exp. Si3 and Exp. Si4 have different temperature factors.

Table 3.3: Biogenic opal dissolution rules for the sensitivity experiments (column 1). Columns 2 and 3 display the parameters intervening in the flux formulation. A prescribed fraction Υ (column 4) of the flux reaching the ocean floor is permanently preserved in sediments. The remainder dissolves in the bottom mesh. Column 5 gives the global opal export (XSI) and column 6 the fraction of export production supported by diatoms in the model.

Exp.	β_{Si}	κ_{Si} ($^{\circ}\text{C}^{-1}$)	Υ	XSI (Tmol/yr)	XPP _{SI} (%)
Si1	0	-	0.06	75	38%
Si2	$25 \cdot 10^{-5}$	0	0.15	93	46%
Si3	$12 \cdot 10^{-5}$	0.10	0.11	90	44%
Si4	$12 \cdot 10^{-5}$	0.12	0.11	91	46%

The global export in the model remains below the 100–140 Tmol/yr field estimate from *Nelson et al. (1995)*. It is probably a consequence of the low export production since with other circulation fields and the same parameters we obtain values in the range of the field estimates.

The results of these four experiments are summarized in a *Taylor (2001)* diagram (Figure 3.10). Although overall model-data agreement varies slightly be-

tween versions, none of the Si dissolution schemes led to an improved Si distribution in the Southern Ocean. The differences in the global statistics in Figure 3.10 are nearly all attributable to a redistribution between the Atlantic and the Pacific Oceans as well as between the intermediate and deep layers within each ocean basin.

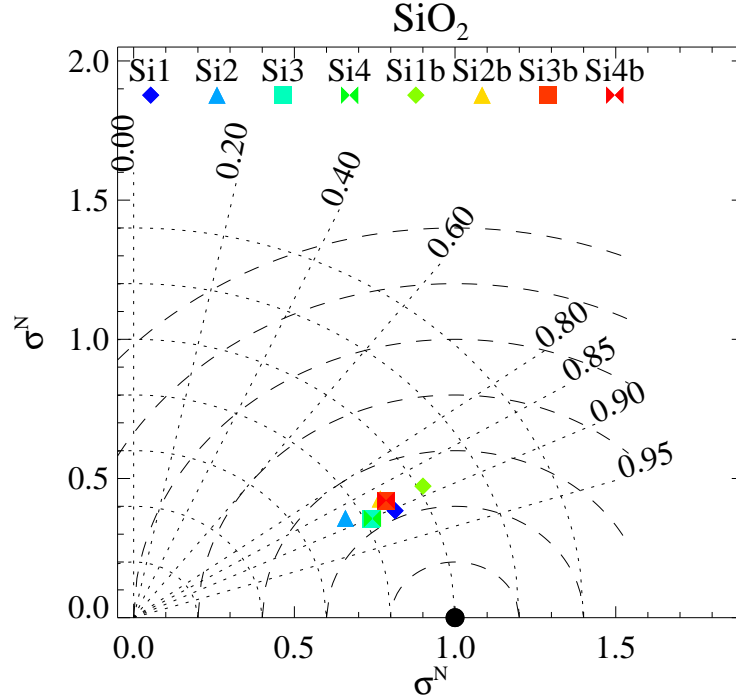


Figure 3.10: Statistical summary of the correspondence between model and data distributions of Si in the global ocean. Data are represented by the big filled circle on the x-axis, model results with colour symbols. The distance between the data point and any symbol gives an estimate of the root mean square error over the global domain. The ratio of model variance over data variance is given along the x-axis. The oblique lines with labels shows the level of spatial correlation between data and model. Exp. Si1 to Si4 obtained with LOVECLIM and Exp. Si1b to Si4b with LOCH driven by UL-OM (version L0). Data from *Boyer et al.* (2006).

The same sensitivity tests were also performed with UL-OM (version L0). For that set of experiments LOCH was driven in an off-line mode and no seasonal effect is considered since UL-OM predicts the annual mean circulation fields. These experiments are identified with the letter ‘b’ at the end of the labels in Figure 3.10.

All experiments result in a correlation factor close to 0.9. None of the proposed dissolution schemes affects seriously this correlation factor. It must then be hypothesized that the circulation is the process controlling this correlation.

Variance is better captured with method Si1 than with Si2. Circulation fields also impact this variance which is better reproduced with the UL-OM circulation fields.

The striking fact put forward with these tests is that method Si1 (bottom dissolution) leads, with each of the circulation fields, to the best global agreement between model results and observations. This is rather at odds with experimental work and field-related studies (*Wollast, 1974; Bidle et al., 2002; Fujii and Chai, 2005*). We do not have a better explanation to provide for this behavior than suspecting a too large vertical exchange mechanism in the OGCMs.

3.4.2 Particulate organic matter flux

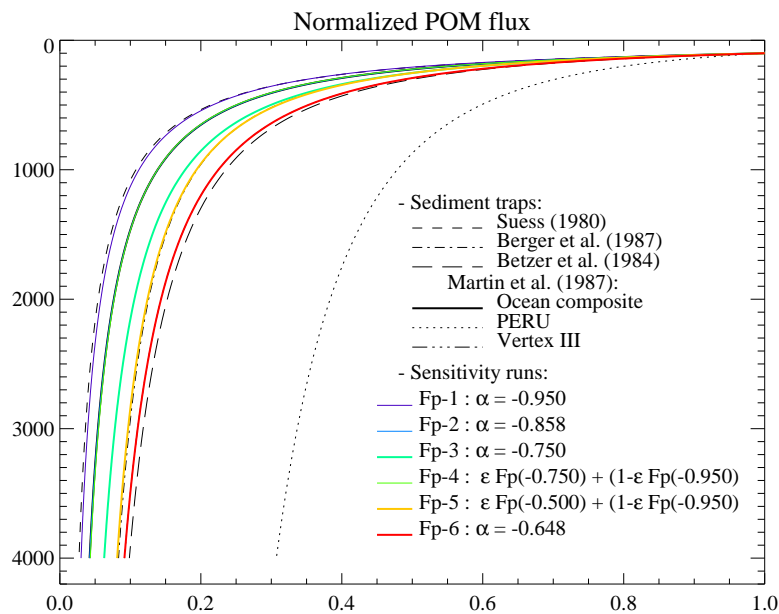


Figure 3.11: Illustration of POM flux with depth as from the literature. These fluxes have been normalized to their value at 100m. The sensitivity experiments performed with LOVECLIM correspond to the colour curves. ϵ represents the fraction of export production supported by diatoms. Please note that α in this figure should read α_{POM} .

The vertical flux of POM is one factor controlling the sequestration of CO_2 in the deep ocean. It is represented in the model by a power law as in Eq. (3.10). Several formulations of these flux were proposed (Figure 3.11). The various formulations and observed fluxes correspond to different ocean provinces and different estimation methods. The spread in the vertical POM flux profile could also be explained by differences in ecosystems (e.g., *Klinck and Smith, 2002*).

A shallow profile leads to a large export production by making nutrients more readily available in the upper ocean. But this may be accompanied by a less effective carbon sequestration in the deep ocean.

We varied the α_{POM} factor in Eq. (3.10) from -0.950 to -0.648 and obtained the export production range summarized in Table 3.4. A variant of this formulation is found by associating different factors to different foodwebs. In this case, the flux of POM is modelled by associating a deep POM profile (less negative α_{POM}) to the production supported by diatoms. The remainder of the production is due to organisms characterized by smaller settling velocities, hence experiencing a shallower remineralization. With such a parameterization the effect of a potential ecosystem change on the global carbon cycle may be accounted for.

Table 3.4: Export productions (GtC/yr) obtained with different POM distribution profiles. Columns 5 and 6 correspond to the mixed formulation in which we differentiate between the flux law for diatoms ($\alpha = -0.750$ and -0.500 , respectively) and for other species ($\alpha = -0.950$).

Exp.	Fp-1	Fp-2	Fp-3	Fp-4	Fp-5	Fp-6
α_{POM}	-0.950	-0.858	-0.750	-0.750/-0.950	-0.500/-0.950	-0.648
XP (GtC/yr)	6.5	6.2	5.7	6.2	5.5	5.3

Figure 3.12 displays the same statistics as in Fig. 3.10 this time for P. The best agreement with data is obtained for Fp-5, and the worst for Fp-1. The model predicts a rather low global export production with Fp-5 (5.5 GtC/yr). The largest export is obtained with Fp-1. The fact that the best agreement for P fields is obtained with a deep POM profile, resulting in a too low predicted export production is indicative of excessive vertical exchange (*Gnanadesikan et al.*, 2001).

3.4.3 Sensitivity of a global ocean carbon cycle model to the circulation and to the fate of organic matter: preliminary results

This work, published as *Mouchet and François* (1996), is included in pages 113 to 117.

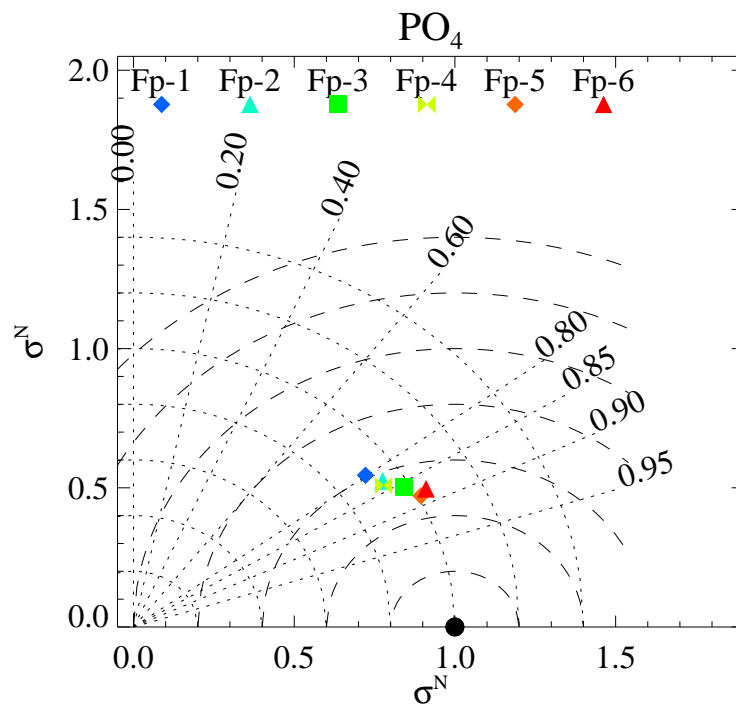


Figure 3.12: Same as Fig. 3.10 for P. Labels correspond to experiments performed with LOVECLIM and listed in Table 3.4 and in Figure 3.11. Data from *Boyer et al.* (2006).



Sensitivity of a Global Oceanic Carbon Cycle Model to the Circulation and to the Fate of Organic Matter: Preliminary Results

A. Mouchet and L. M. François

Laboratoire de Physique Atmosphérique et Planétaire, Institut d'Astrophysique, Université de Liège, Avenue de Coïnte 5, B-4000 Liège, Belgium

Received 17 June 1996; accepted 7 March 1996

Abstract. We examine the effect of the circulation on the resulting distribution of tracers in the ocean and the sensitivity of surface CO_2 to the remineralization cycle of organic matter. For this purpose we built a 3-dimensional global model of the oceanic carbon cycle. The processes considered are air-sea CO_2 exchanges, export production of organic matter and its remineralization, CaCO_3 precipitation and dissolution or sedimentation. The annual mean fields needed to drive the model are provided by two different OGCM's. The sensitivity of the tracer distribution to the circulation is evaluated by examining the results obtained with each set of hydrodynamic fields driving the geochemical model with identical parameterizations of the biochemical processes in both cases. The model is then applied to investigate the consequences on the surface Δp_{CO_2} of various behavior of the dead organic material. The consideration of fast sinking particles leads to a distribution which is in better agreement with measurements than the one obtained under the assumption that the organic matter is mainly under dissolved form.

©1997 Elsevier Science Ltd

1 Introduction

Uptake of atmospheric CO_2 by the ocean on decadal timescales is driven by the slow exchanges between surface waters and the deeper layers of the ocean. The solubility and biological pumps both determine the carbon distribution between the surface and the deep ocean. Due to the complexity of the system, 3-dimensional models are needed to assess the role of the ocean in the present carbon cycle. Different circulation fields and representations of the biological cycle characterize the models already in use (Bacastow and Maier-Reimer, 1990; Sarmiento and Orr, 1991; Maier-Reimer, 1993; Anderson and Sarmiento, 1995). The study presented here is an attempt to examine the sensitivity of a carbon cycle model (described in section 2) to the circulation and to the way organic matter is dealt with. The first objec-

tive is met by driving our model with the fields predicted by two different OGCM's (section 3). Since the organic matter is treated as a state variable, its remineralization cycle can be varied from a purely particulate to a fully dissolved state by acting on the sedimentation and decay rates. Section 4 addresses more specifically the relation between surface CO_2 and organic matter remineralization pattern.

2 Model description

The state variables considered in the model are the dissolved inorganic carbon (DIC), total alkalinity, phosphates (P), organic products (OP), oxygen as well as inorganic and organic ^{13}C . The atmosphere is represented by a single zonally homogeneous layer dominated by diffusion in the meridional direction and exchanging CO_2 and O_2 with the ocean. The new primary production is computed in the euphotic zone (0 to 120 m) with the help of a biomass variable. This represents a "standing stock" of phytoplankton and is not advected. The aim of this work is not to model phytoplankton population but to represent fluxes from the inorganic to the organic carbon pool. The biomass grows at a rate depending on the availability of light and phosphate (Michaelis-Menten relationship) and on the temperature. Phosphate is taken as the limiting nutrient. The biomass declines due to mortality and grazing which are respectively taken into account through constant and stock-dependent decay rates. The OP pool increases as the biomass decays; OP settle down through the water column at a constant pace while being oxidized. Remineralization is allowed only in layers located below the euphotic zone. The decay rate depends on the oxygen availability but anoxic remineralization is also allowed in O_2 -depleted areas. During the remineralization the O_2 :P ratio is fixed to 170 (Takahashi et al., 1985) while for photosynthetic processes its value stems from the requirement that all the O_2 consumed at depth be balanced by its production in the euphotic zone. The O_2 :P ratio may then be slightly different when considering surface or deep water processes.

Correspondence to: A. Mouchet

Hard tissues are made of calcium carbonate. We do not consider silica in our model yet. CaCO_3 precipitation is proportional to the soft tissue formation with a smaller efficiency at low temperatures as calcareous organisms are less common in cold waters (Broecker and Peng, 1982). Shells contain calcite and aragonite with a relative occurrence fixed to 0.2, a figure which lies in the observed range of 0.1 to 0.5 (Berner, 1977; Fabry, 1989). Hard tissues, unlike the organic material, are assumed to sink rapidly to the bottom. The model assumes that dissolution takes place within the same time step (1 year) in the deepest layer of the water column in which shells are produced if this bottom water is undersaturated. The fraction of CaCO_3 which does not dissolve and is deposited on the seafloor results in alkalinity and DIC losses which are compensated for by inflows to the ocean from the world main rivers. Each river contribution is proportional to its participation in the global load, computed after river data from (Berner and Berner, 1987; Probst, 1992). Air-sea exchanges of CO_2 and O_2 are proportional to the difference of partial pressures between the two media. The exchange coefficient for CO_2 varies with latitude and its mean is chosen such as to obtain a flux of 84 GtC yr^{-1} corresponding to the pre-industrial value (Bacastow and Maier-Reimer, 1990; Siegenthaler, 1993). The boundary condition for oxygen is the solubility value from Benson and Krause (1984). Production-destruction terms for inorganic and organic ^{13}C are those specified for ^{12}C corrected for isotopic ratio and fractionation factor.

3 Circulation and biological cycle

The 3-dimensional annual mean hydrodynamic fields needed to drive the model are provided by either the OGCM developed at the Max-Planck Institut für Meteorologie, Hamburg (Maier-Reimer et al., 1993) or by the one designed at the Université Catholique de Louvain, Louvain-la-Neuve, Belgium (Deleersnijder and Campin, 1995). For simplicity these models are hereafter referred to as HB and LL respectively. Both of them have a free-surface, use the same datasets for surface forcing (temperature, salinity and winds) and run in a prognostic mode. The differences lie in the numerical scheme, the grid and in the formulation of boundary conditions. We designed our model so that it can be run with any of these circulation fields. The aim is twofold: first the comparison of results obtained with each hydrodynamics helps in evidencing problems specific to the biogeochemical model; second, it provides a useful tool to test the sensitivity of the carbon cycle to the circulation. In the following experiments the biological parameters are exactly the same when running the biogeochemical model with the two circulation fields. The global export production obtained with the HB fields is 8.5 GtC yr^{-1} (local production range from 2 to $72 \text{ gC m}^{-2} \text{ yr}^{-1}$) while it amounts to 8.3 GtC yr^{-1} with the LL circulation (values from 0.5 to $59 \text{ gC m}^{-2} \text{ yr}^{-1}$). Most commonly cited values range from 3.5 to 12 GtC yr^{-1} (Longhurst, 1982; Shaffer, 1993). The vertical profile of phosphate mean values

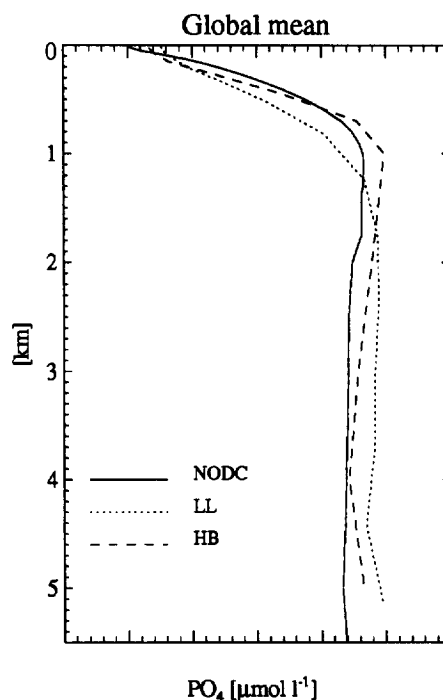


Fig. 1. Global mean phosphate concentration versus depth. The dashed and dotted lines correspond to the results obtained with the HB and LL fields respectively. The solid one shows the observed mean profile (NODC, 1994).

is displayed in Fig. 1. Slightly too high values are predicted near the surface, a feature also present in the horizontal distributions shown in Fig. 2. The concentrations in central gyres should be somewhat lower. This is possibly due to the use of a too high phosphate half-saturation constant preventing high nutrient depletion in those areas. This parameter is set to $0.1 \mu\text{M}$ which is at the upper limit of cited values (0.02 to $0.1 \mu\text{M}$, Carrada et al., 1983; Fasham, 1993; Maier-Reimer, 1993). The North Pacific sharp gradient visible in the data is not reproduced in our simulations. In the Antarctic, a shortcoming in the representation of convective events might partially be responsible for predicted P values lower than the measured ones.

The reason for the deeper location of the P maximum for the LL model (Fig. 1) is to be found in the lower value of the global vertical transport at 1500 m in that model (33 Sv against 48 Sv for HB). The P distributions in the Atlantic Ocean (Fig. 2) are rather similar for both models. The circulation of the LL and HB models differs predominantly in the Indian and Pacific Oceans. At 35 S in the Pacific Ocean (between 150E and 70W) the meridional transport above 1500 m is northward in the LL case with the return flow occurring in the upper layers between Asia and Australia. The HB transport in the Pacific is southward above 1500 m and northward below that level and exhibits higher upwelling rates in the different parts of that ocean. These differences in the flow

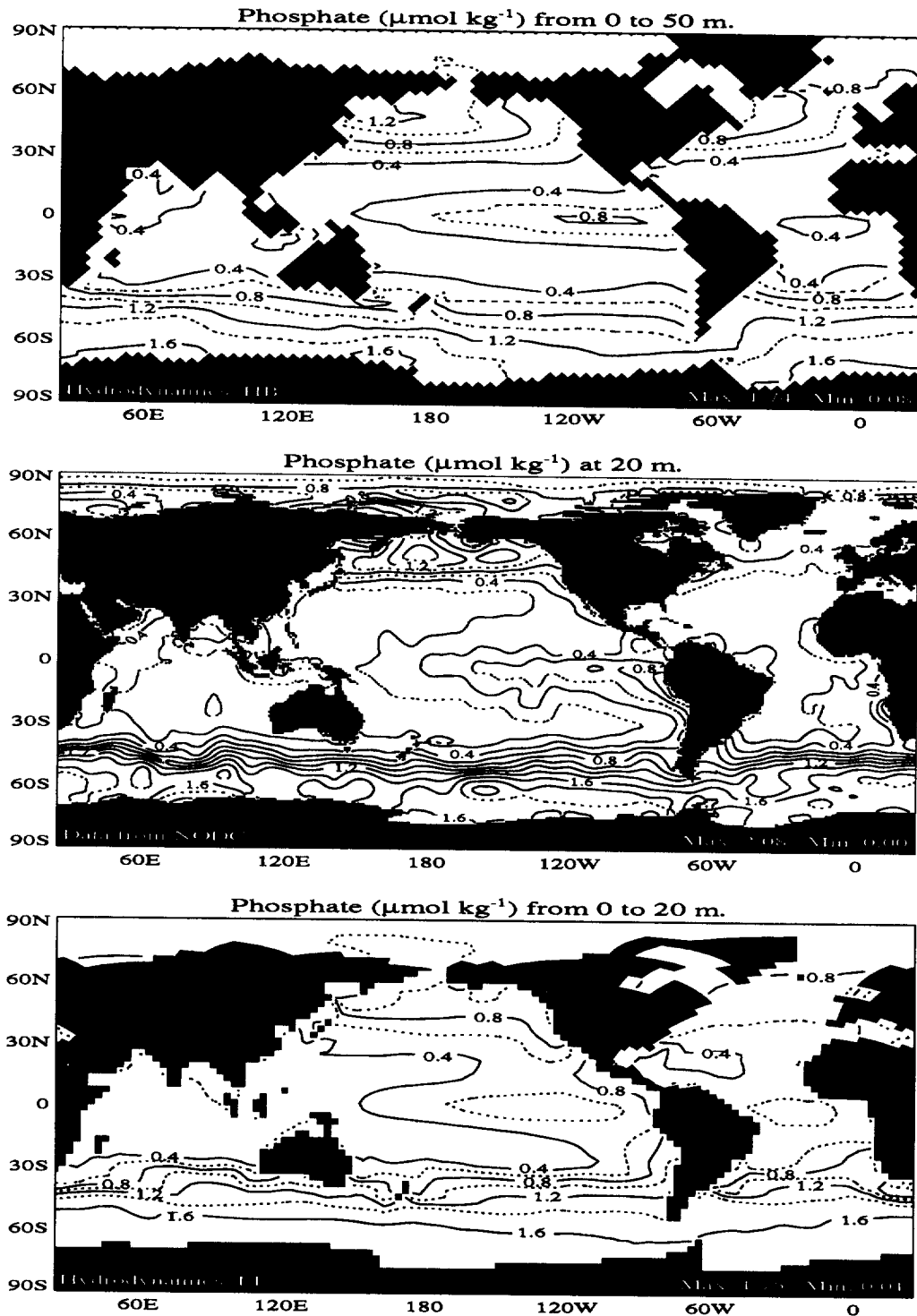


Fig. 2. Distribution of surface fields of phosphate concentrations. Middle panel: NODC data; upper and lower panels: results respectively obtained with the HB and LL fields.

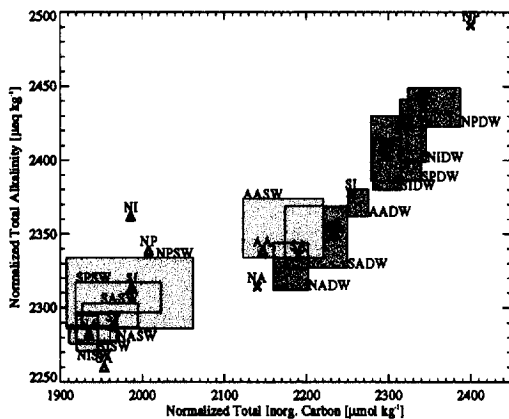


Fig. 3. Basin averages of normalized alkalinity versus those of DIC. Model results are shown with triangles for the upper layer and with Xs for the deep layers. Rectangles correspond to data (mean value \pm standard deviation) from Takahashi et al. (1981). The basin denomination is the following: NA and SA, North and South Atlantic; NI and SI, North and South Indian; NP and SP, North and South Pacific; AA, Antarctica. DW stands for deep water (1200 to 5900 m) and SW for the upper layer (0 to 50m).

pattern explain the higher P values encountered in the equatorial band for the HB simulation. In the Southern Indian Ocean (south of 35S and between 30E and 150E) the vertical transport at 1500m is upward in the LL circulation and downward in the HB one. This generates higher P values along Antarctica in the LL simulation.

4 Carbon cycle

The complete carbon cycle model was run with the HB hydrodynamic fields and with the biological model described in the previous section. At the end of the run the atmospheric CO_2 pressure was 287 ppm and its $\delta^{13}\text{C}$ value was -6.8‰ . The global rain ratio, defined as the ratio of the amount of DIC fixed during new production to that of DIC needed for hard tissue formation, is 5.8. Typical values for that ratio range from 3.5 to 7.5 (Broecker and Peng, 1982; Shaffer, 1993). In Fig. 3, model results are compared to DIC and alkalinity data from GEOSECS (Takahashi et al., 1981). The origin of the high alkalinity value in deep northern Pacific can probably be ascribed to either a too low rain ratio or a too high CaCO_3 dissolution rate. Sluggish circulation in the North Indian Ocean results in a low mixing of quantities brought to the ocean by the rivers. In the remainder of the ocean a fairly good agreement between data and results is obtained.

One specificity of our model is that it considers dead organic matter as a state variable. It is usually admitted that most of the organic matter produced in the upper layers is exported to deeper layers by means of large, fast sinking particles which are not advected by oceanic currents and are recycled below the region of their production. However, mod-

els in which organic matter is treated in such a way usually overestimate the phosphate concentration in the main thermocline, especially in the equatorial Pacific (Bacastow and Maier-Reimer, 1990; Matear and Holloway, 1995). By providing a means of horizontally transporting organic matter out of the production region, models including dissolved or suspended organic matter eliminate the nutrient trapping in those high upwelling areas (Anderson and Sarmiento, 1995; Matear and Holloway, 1995). In the run described up to now OP had been considered as occurring mainly under dissolved or suspended form (the sedimentation speed of 400 m yr^{-1} allows efficient lateral transport by ocean currents). The difference between the oceanic and atmospheric CO_2 partial pressures (Fig. 4, upper panel) obtained under this assumption does not agree well with observations (Tans et al., 1990). Sensitivity tests show that this pressure difference is better reproduced in the equatorial Pacific if the organic matter is viewed as being mainly composed of fast sinking particles. The lower panel of Fig. 4 shows the result of one of these experiments, in which a 15-fold increase of the settling and remineralization rates leads to the increase of the carbon content of upwelled waters hence resulting in a higher CO_2 partial pressure difference and to a better reproduction of the observations. The global results obtained in this exercise are similar to those described earlier except for a higher phosphate maximum value at depth in the equatorial Pacific Ocean.

5 Conclusion

These preliminary experiments illustrate that uncertainties in the circulation fields have non-negligible consequences on the distribution of biological tracers. Biological activity is responsible for establishing and maintaining strong gradients but the hydrodynamics influences the geochemical cycle by imposing the rates of upwelling and deep water ventilation. From the results of section 3 it can be concluded that slightly distinct parameterizations of the remineralization process are needed for both circulation fields in order to satisfactorily reproduce the observations. The results of section 4 evidence the necessity of simultaneously validating the model against several tracer distribution. They also illustrate the key role played by the organic matter remineralization pattern in the distribution of CO_2 values in the upper layer of the ocean. Future developments will concentrate on this aspect. Global oxygen data (concentration and AOU) now available might be a useful tool for the validation of the organic matter transformation patterns. However their use is not straightforward as they are also strongly dependent on the circulation pattern.

Acknowledgements. We wish to thank Dr. E. Maier-Reimer and J.-M. Campin for kindly providing the hydrodynamic fields and for fruitful discussions. Financial support for this research is provided by the Federal Global Change Impulse Program of the Belgian Federal Office for Scientific, Technical and Cultural Affairs under contract number GC/12/017. L. François is supported by the Belgian Fund for Scientific Research (FNRS).

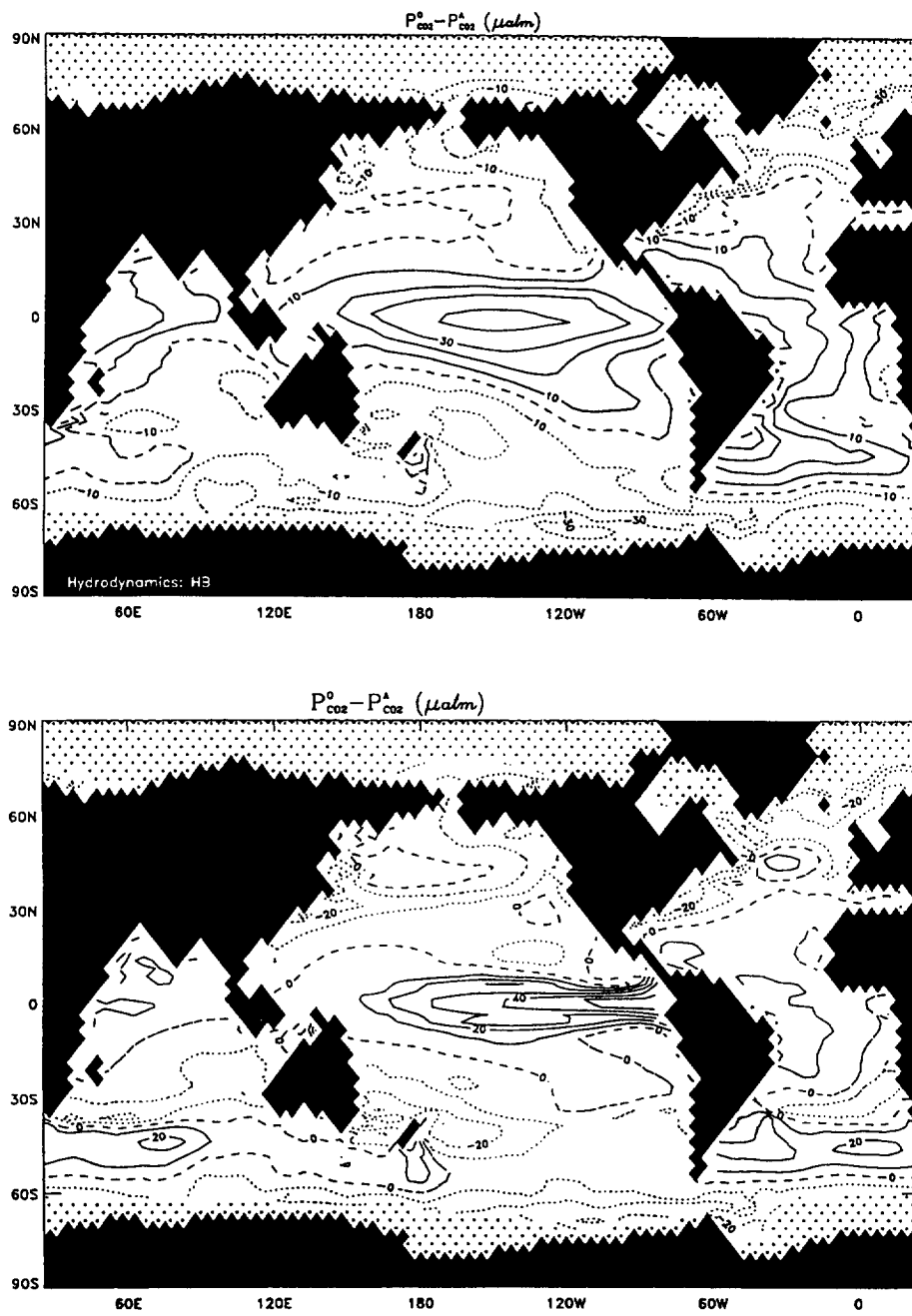


Fig. 4. Difference between the oceanic and atmospheric partial pressures of CO₂. Solid lines correspond to positive values and dotted ones to negative values. Organic matter is assumed to be mainly under dissolved (upper panel) or particulate form (lower panel).

References

- Anderson, L. and Sarmiento, J., Global ocean phosphate and oxygen simulations, *Global Biogeochemical Cycles*, 9, 621–636, 1995.
- Bacastow, R. and Maier-Reimer, E., Ocean-circulation model of the carbon cycle, *Climate Dynamics*, 4, 95–125, 1990.
- Benson, B. and Krause, D., The concentration and isotopic fractionation of oxygen dissolved in freshwater and seawater in equilibrium with the atmosphere, *Limnology and Oceanography*, 29, 620–632, 1984.
- Berner, E. and Berner, R., *The global water cycle*, Geochemistry and environment, Prentice Hall, 397p., 1987.
- Berner, R., Sedimentation and dissolution of pteropods in the ocean, in *The fate of fossil fuel CO₂ in the ocean*, edited by N. Andersen and A. Malahoff, pp. 243–260, Plenum Press, N.Y., 1977.
- Broecker, W. and Peng, T., *Tracers in the sea*, Columbia University Press, N.Y., 690p., 1982.
- Carrada, G., Hopkins, T., Jeftić, L., and Morcos, S., eds., *Quantitative analysis and simulation of Mediterranean coastal ecosystems: The Gulf of Naples, a case study*, vol. 20 of *Unesco reports in marine sciences*, Unesco, Paris, 158p., 1983.
- Deleersnijder, E. and Campin, J.-M., On the computation of the barotropic mode of a free-surface World Ocean model, *Annales Geophysicae*, 13, 675–688, 1995.
- Fabry, V., Aragonite production by pteropod mollusks in the subarctic Pacific, *Deep-Sea Research*, 36, 1735–1751, 1989.
- Fasham, M., Modeling of the marine biota, in *The global carbon cycle*, edited by M. Heimann, vol. 115 of *NATO ASI*, pp. 457–504, Springer Verlag, Berlin, 1993.
- Longhurst, A., Role of the marine biosphere in the global carbon cycle, *Limnology and Oceanography*, 36, 1507–1526, 1982.
- Maier-Reimer, E., Geochemical cycles in an ocean general circulation model. Pre-industrial tracer distribution, *Global Biogeochemical Cycles*, 7, 645–677, 1993.
- Maier-Reimer, E., Mikolajewicz, U., and Hasselman, K., Mean circulation of the hamburg LSG-OGCM and its sensitivity to the thermohaline surface forcing, *Journal of Physical Oceanography*, 23, 731–757, 1993.
- Matear, R. and Holloway, G., Modeling the inorganic phosphorus cycle of the North Pacific using an adjoint data assimilation model to assess the role of dissolved organic phosphorus, *Global Biogeochemical Cycles*, 9, 101–119, 1995.
- NODC, *World ocean atlas 1994. Volume 1: nutrients*, National Oceanographic Data Center, NOAA, Washington DC, 150p., 1994.
- Probst, J.-L., *Géochimie et hydrologie de l'érosion continentale. Mécanismes, bilan global actuel et fluctuations au cours des 550 derniers millions d'années*, vol. 94 of *Mémoires Sciences Géologiques*, ULP-CNRS, Strasbourg, France, 164p., 1992.
- Sarmiento, J. and Orr, J., Three-dimensional simulations of the impact of southern ocean nutrient depletion on atmospheric CO₂ and ocean chemistry, *Limnology and Oceanography*, 36, 1928–1950, 1991.
- Shaffer, G., Effects of the marine biota on global carbon cycling, in *The global carbon cycle*, edited by M. Heimann, vol. 115 of *NATO ASI*, pp. 431–455, Springer Verlag, Berlin, 1993.
- Siegenthaler, U., Modeling the present-day oceanic carbon cycle, in *The global carbon cycle*, edited by M. Heimann, vol. 115 of *NATO ASI*, pp. 367–395, Springer Verlag, Berlin, 1993.
- Takahashi, T., Broecker, W., and Bainbridge, A., The alkalinity and total carbon dioxide concentration in the world ocean, in *Carbon cycle modeling*, edited by B. Bolin, pp. 271–286, John Wiley and Sons, New-York, 1981.
- Takahashi, T., Broecker, W., and Langer, S., Redfield ratio based on chemical data from isopycnal surfaces, *Journal of Geophysical Research*, 90, 6907–6924, 1985.
- Tans, P., Fung, I., and Takahashi, T., Observational constraints on the global atmospheric CO₂ budget, *Science*, 247, 1431–1438, 1990.

Chapter 4

Modern times and carbon isotopes

“On ne se voit pas dans la mer”

J. Prévart

Carbon isotopes are extensively used in ocean sciences. They are of help in reconstructing past changes (e.g., *Duplessy*, 1986; *Robinson et al.*, 2005) as well as in gaining a better understanding of a variety of processes, productivity (e.g., *Sackett*, 1991), contemporary or paleo air-sea fluxes (e.g., *Quay et al.*, 1992; *Tans et al.*, 1993; *Maslin et al.*, 1996), and ventilation (e.g., *Stuiver et al.*, 1983; *Winguth et al.*, 1999).

There are three naturally occurring carbon isotopes: ^{12}C is the dominant form, ^{13}C with occurrence of about 1.1%, and ^{14}C with very low abundance (approx. 1 atom in every 10^{12} carbon atoms). Both ^{12}C and ^{13}C are stable to the contrary of radiocarbon ^{14}C whose mean half-life is 5730 yr (*Godwin*, 1962).

In section 4.1 we examine the methods in use for modelling ^{14}C and their impacts on model-derived estimates of bomb radiocarbon ocean uptake - an indirect way of assessing ocean ventilation. Section 4.2 details the biologically-mediated flux terms intervening in the modelling of carbon isotopes in LOCH.

4.1 Bomb radiocarbon

Radiocarbon, ^{14}C , occurs naturally from the interaction between cosmic rays and nitrogen 14 in the upper atmosphere and decays with a mean lifetime of 8267 yr. The ratio of radiocarbon to total carbon¹ $^{14}\text{R} = ^{14}\text{C}/\text{C}$ in atmospheric

¹In this context total carbon refers to the sum of all isotopic carbon forms. We refer to this *total carbon* when mentioning carbon quantities not identified with an atomic number.

CO₂ (or its $\Delta^{14}\text{C}$ – see below) remained nearly constant and nearly uniformly distributed over the globe for the 2 kyr preceding the industrial era (*Broecker et al.*, 1985; *Stuiver and Braziunas*, 1998; *Stuiver et al.*, 1998), a length of time much larger than the ventilation age of the oldest oceanic water. Since the 18th century atmospheric ^{14}C has been decreasing as a consequence of the injection of ^{14}C free carbon from fossil fuel consumption (Suess effect). This effect yielded a decrease between -15‰ and -25‰ in $\Delta^{14}\text{C}$ from 1765 to 1950 (*Tans et al.*, 1979; *Stuiver and Quay*, 1981; *Joos and Bruno*, 1998).

A further perturbation of the natural cycle originated in nuclear bomb testing which resulted in a 60–90% increase of the atmospheric $^{14}\text{C}/\text{C}$ ratio between 1952 and 1964 (Figure 4.1). That ratio slowly declined afterwards with the gradual storage of excess atmospheric ^{14}C in the natural reservoirs.

The ^{14}C released by atmospheric nuclear weapons testing provides a means to constrain global air-sea CO₂ exchange (*Wanninkhof*, 1992; *Krakauer et al.*, 2006; *Sweeney et al.*, 2007; *Naegler*, 2009). Nevertheless, radiocarbon is not a perfect analogue for anthropogenic CO₂ ocean uptake since $^{14}\text{CO}_2$ equilibrates with the atmosphere ten times slower than does CO₂ (*Broecker and Peng*, 1974). Further, since anthropogenic CO₂ and bomb ^{14}C have very different time histories in the atmosphere, their respective ocean distributions do not correlate well (*Heimann and Maier-Reimer*, 1996). The bomb ^{14}C penetration in the ocean also offers the opportunity to assess near-surface circulation, vertical transport and mixing schemes in OGCMs (*Toggweiler et al.*, 1989b; *Jain et al.*, 1995; *Joos et al.*, 1997; *England and Rahmstorf*, 1999; *Orr et al.*, 2001; *Müller et al.*, 2006).

An imbalance in the global budget of the order of $82 \pm 78 \cdot 10^{26}$ ^{14}C atoms for 1990 (*Hesshaimer et al.*, 1994) questioned the ocean uptake of bomb ^{14}C as initially estimated by *Broecker et al.* (1985) and confirmed in their following work *Broecker et al.* (1995). A rather large ($\sim 25\%$) downward revision of this uptake was suggested in order to reconcile stratospheric and tropospheric measurements with modelled values (*Hesshaimer et al.*, 1994; *Broecker and Peng*, 1994). Since then, new methods (e.g., *Rubin and Key*, 2002; *Peacock*, 2004) and field-based measurements (*Key et al.*, 2004) have become available. Several works questioned the *Broecker et al.* (1995) bomb radiocarbon inventories (among others, *Peacock*, 2004; *Sweeney et al.*, 2007; *Naegler*, 2009). Despite an increased inventory in the Southern Ocean (*Leboucher et al.*, 1999) most of these works point toward a downward revision of the global bomb ^{14}C uptake proposed by *Broecker et al.* (1995). The most important consequence of this conclusion is the downward revision of the air-sea gas exchange rate initially proposed by *Wanninkhof* (1992).

However the use of bomb radiocarbon as an ocean tracer is not straightforward since the exact amount that entered the sea may only be indirectly obtained. Indeed, except for measurements on corals or seashells, we do not have any direct evidence of pristine ocean values (*Broecker et al.*, 1995; *Rubin and Key*, 2002). Bomb ^{14}C is computed by subtracting the observed (post-bomb) ^{14}C con-

centrations from an estimate of the natural pre-anthropogenic values (*Broecker et al.*, 1995). The natural ^{14}C is reconstructed on the basis of empirical relationships linking $\Delta^{14}\text{C}$ to other tracers (*Broecker et al.*, 1995; *Rubin and Key*, 2002; *Peacock*, 2004; *Sweeney et al.*, 2007). These procedures also require separating bomb-free water masses from those already contaminated. This is usually performed with the help of transient tracers such as CFCs or Tritium or with the help of OGCMs. Other factors significantly contribute to the uncertainty of field-based estimates. First, the incomplete spatial and temporal coverage of ocean basins may bias estimates. The second significant source of uncertainty comes from the fact that bomb inventories are computed on the basis of DIC concentrations observed at the time of $\Delta^{14}\text{C}$ measurements (*Naegler*, 2009). The same DIC is used in the computation of pre- and post-bomb ^{14}C inventories from ^{14}R . Hence data-based inventories are more than probably underestimated since they neglect the fact that DIC levels were lower in earlier decades (*Naegler*, 2009). Eventually data-based estimates often rely on the hypothesis that fluxes into the ocean are directly proportional to the atmospheric perturbation.

Model studies on the other hand do not yet provide a means for solving these difficulties. Bomb ^{14}C ocean inventories as estimated by different models encompass a wide range of values (*Joos*, 1994; *Duffy and Caldeira*, 1995; *Joos and Bruno*, 1998; *Müller et al.*, 2008) and are usually much larger than data-based inventories.

Joos et al. (1997), *Joos and Bruno* (1998) and *Müller et al.* (2008) attribute most of the discrepancy to the gas exchange coefficient. Models indeed usually rely on the piston velocity parametrization of *Wanninkhof* (1992) which was determined on the basis of ^{14}C inventories by *Broecker et al.* (1985). Other sources for differences in model predicted values may also be found in surface boundary conditions in the Southern Ocean (*Toggweiler and Samuels*, 1993) or in the vertical mixing (*Toggweiler et al.*, 1989b; *Müller et al.*, 2008). It must also be stressed that the ventilation rate strongly depends on the numerical scheme (*Bryan*, 1987; *Duffy et al.*, 1997).

Another source of discrepancy among model results is to be found in the way radiocarbon is represented in models (models which sometimes will complement field information to provide data-based estimates). Several model studies adopted the simplified formulation of *Toggweiler et al.* (1989a) to describe the transport of radiocarbon in the ocean (*Duffy and Caldeira*, 1995; *Stocker et al.*, 1994; *Maier-Reimer et al.*, 1993; *Campin et al.*, 1999; *England and Rahmstorf*, 1999; *Rodgers et al.*, 2000; *Mahadevan*, 2001; *Orr et al.*, 2001; *Butzin et al.*, 2005; *Müller et al.*, 2006). This approach does not much affect the simulated equilibrium (or pre-industrial) radiocarbon distribution in the ocean (*Maier-Reimer*, 1993; *Orr et al.*, 2001). However its effect on simulated bomb radiocarbon inventory may be more substantial since it relies on the hypothesis that air-sea CO_2 disequilibrium remains constant over the period of interest.

In this work we examine the stationary and transient distributions of ^{14}C from modelling studies based on different formulations for radiocarbon. This is achieved by using a full 3-D model of the carbon cycle driven by two different circulation fields. The natural and bomb radiocarbon distributions in the ocean are then simulated with both circulation fields using different approaches. In the first, all carbon isotopes are transported; in the second, $\Delta^{14}\text{C}$ is considered as the state variable. A third experiment also includes the full biological cycle. The methods and model setup are presented in Section 4.1.1. The description of numerical experiments results (Section 4.1.2) precedes general discussion and conclusions (Section 4.1.3).

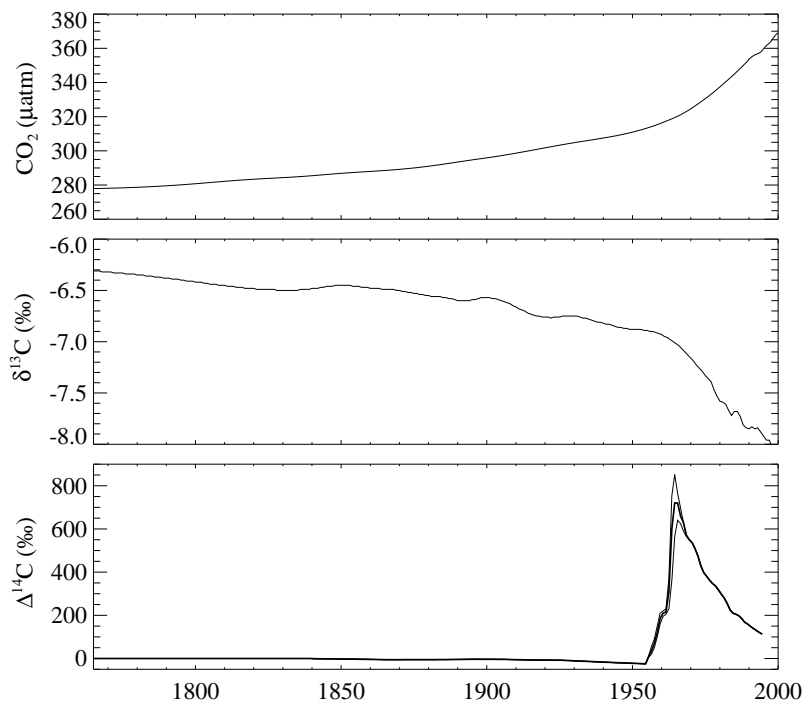


Figure 4.1: Temporal evolution of atmospheric CO₂ (top), $\delta^{13}\text{C}$ (middle) and $\Delta^{14}\text{C}$ (bottom) over the industrial era. The three curves in the bottom panel correspond, from top to bottom, to three latitudinal bands: 20°-90°N, 20°S-20°N and 90°-20°S, respectively. CO₂ and $\Delta^{14}\text{C}$ are from *Enting et al.* (1994) and OCMIP-2 (*Orr et al.*, 2000). Data for $\delta^{13}\text{C}$ are from *Francey et al.* (1999) up to 1978 and from *Keeling et al.* (2010) onward.

4.1.1 Methods

Modelling radiocarbon

Carbon isotopic ratios in a sample are expressed by way of the following quantities

$$\delta^{13}\text{C} = \left(\frac{{}^{13}\mathcal{R}}{{}^{13}\mathcal{R}_{PDB}} - 1 \right) 10^3 = \left(\frac{{}^{13}\text{R}}{(1 - {}^{13}\text{R}) {}^{13}\mathcal{R}_{PDB}} - 1 \right) 10^3, \quad (4.1)$$

$$\Delta^{14}\text{C} = \left(\frac{{}^{14}\text{R}}{{}^{14}\text{R}_{\text{OXA}}} \left(\frac{0.975}{1 + \delta^{13}\text{C}/10^3} \right)^2 - 1 \right) 10^3. \quad (4.2)$$

in which ${}^{13}\mathcal{R}_{PDB} = 1.12372 \times 10^{-2}$ is the Pee Dee Belemnite standard ${}^{13}\text{C}/{}^{12}\text{C}$ ratio, ${}^{14}\text{R}_{\text{OXA}} = 1.176 \times 10^{-12}$ the oxalic acid standard, and 0.975 a constant term corresponding to the average terrestrial wood \mathcal{R} ratio for the pre-industrial period (*Stuiver and Polach, 1977; Keeling, 1981*).

A distinction has to be made between ratios relative to the number of ${}^{12}\text{C}$ atoms in the sample (\mathcal{R}) or to the total number of carbon atoms (R). The former intervenes in the expression for $\delta^{13}\text{C}$ while the latter is to be used in $\Delta^{14}\text{C}$ (*Keeling, 1981*). R is the ratio most readily computed in the numerical model. Transformations from one expression to the other are performed when necessary.

The $\Delta^{14}\text{C}$ value represents the ratio that would have been observed if isotopic fractionation did not occur. As such it may be used as a physical tracer of ocean ventilation (*Broecker et al., 1961; Toggweiler et al., 1989a; Maier-Reimer, 1993*).

The equations governing the transport of total dissolved inorganic carbon concentration C_T and that of its isotopes ${}^i\text{C}_T$ (with $i = 13$ or 14) in the ocean read

$$\frac{\partial}{\partial t} \text{C}_T + \mathcal{H}(\text{C}_T) = q_v(\text{C}_T), \quad (4.3)$$

$$\frac{\partial}{\partial t} {}^{13}\text{C}_T + \mathcal{H}({}^{13}\text{C}_T) = q_v({}^{13}\text{C}), \quad (4.4)$$

$$\frac{\partial}{\partial t} {}^{14}\text{C}_T + \mathcal{H}({}^{14}\text{C}_T) = q_v({}^{14}\text{C}) - \lambda {}^{14}\text{C}_T, \quad (4.5)$$

where λ is the decay rate for ${}^{14}\text{C}$ and $q_v(X)$ represents the source-minus-sink term for X . The latter accounts for biotic and abiotic (e.g., CaCO_3 dissolution) processes, but excludes radioactive decay.

The operator \mathcal{H} represents physical transport (advection, diffusion as well as convection). It takes the following form

$$\mathcal{H}(X) = \nabla \cdot (\mathbf{u} X - \mathbf{K} \nabla X), \quad (4.6)$$

with \mathbf{u} and \mathbf{K} the three-dimensional velocity and diffusivity fields.

At the ocean-atmosphere interface we specify the gas fluxes. The boundary condition for carbon is

$$\mathcal{F} = F^{aw} - F^{wa}$$

with

$$F^{aw} = \kappa_{\text{CO}_2} K_H p_{\text{CO}_2}^a \quad \text{and} \quad F^{wa} = \kappa_{\text{CO}_2} \text{CO}_{2w}. \quad (4.7)$$

In these equations κ_{CO_2} is the carbon dioxide transfer velocity, K_H the CO_2 solubility in seawater, $p_{\text{CO}_2}^a$ the atmospheric CO_2 pressure at sea level, and CO_{2w} the concentration of dissolved carbon dioxide in seawater. The superscripts *aw* and *wa* refer to the air-to-water and water-to-air transfers, respectively.

The air-sea boundary conditions for isotopes are based on Eq. (4.7) with fractionation factors and isotopic ratios weighting the different fluxes (*Heimann and Maier-Reimer, 1996*). They read

$${}^{13}\mathcal{F} = {}^{13}\alpha^{aw} {}^{13}R_a F^{aw} - {}^{13}\alpha^{wa} {}^{13}R_{\text{CT}} F^{wa}, \quad (4.8)$$

$${}^{14}\mathcal{F} = {}^{14}\alpha^{aw} {}^{14}R_a F^{aw} - {}^{14}\alpha^{wa} {}^{14}R_{\text{CT}} F^{wa}. \quad (4.9)$$

Here, iR_a represents the ratio of isotope i ($i = 13, 14$, resp.) to carbon in atmospheric CO_2 and ${}^iR_{\text{CT}}$ its equivalent in ocean DIC. Fractionation effects between atmospheric and dissolved carbon dioxide are represented by ${}^{13}\alpha^{aw}$ while ${}^{13}\alpha^{wa}$ contains the fractionation factors between dissolved CO_2 and carbonate species. The temperature dependent formulations for these equilibrium factors are from *Vogel et al. (1970)* and *Mook et al. (1974)*, and the small kinetic effect on gas exchange velocities is taken in *Siegenthaler and Münnich (1981)*. Fractionation factors for ${}^{14}\text{C}$ are the squares of those for ${}^{13}\text{C}$ (*Siegenthaler and Münnich, 1981*).

The three equations (4.3)–(4.5) together with the boundary conditions (4.7)–(4.9) and appropriate expressions for the source and sink terms constitute the complete set of equations of use in radiocarbon modelling. In the following we refer to this way of doing as the F-method when performing abiotic simulations or the B-method when including biological activity in the model.

A simplified formulation

By combining the transport equations (4.3) and (4.5) one obtains the equation governing the evolution of the ratio ${}^{14}R_{\text{CT}}$

$$\frac{\partial}{\partial t} {}^{14}R_{\text{CT}} + \mathcal{H}({}^{14}R_{\text{CT}}) = \frac{1}{C_{\text{T}}} (q_v({}^{14}\text{C}) - {}^{14}R_{\text{CT}} q_v(\text{C}_{\text{T}})) - \lambda {}^{14}R_{\text{CT}} + \frac{2}{C_{\text{T}}} \nabla C_{\text{T}} \cdot K \cdot \nabla {}^{14}R_{\text{CT}} \quad (4.10)$$

The last term on the right hand side is generated by mixing processes and has no equivalent in the equation governing concentrations. This term may in

most parts of the deep ocean be considered as a sink term. Indeed the oldest ocean water (lowest ^{14}R) would generally correspond to those with the highest C_T content as a result of the remineralization of organic debris and dissolution of shells.

In many model studies the ratio $\Delta^{14}\text{C}$ is transported rather than the individual concentrations. Initially suggested by *Toggweiler et al.* (1989a,b) this simplified form demands that the mixed product in equation (4.10) vanishes. It is equivalent to assuming that the C_T field is homogeneous and constant, i.e.,

$$\text{C}_\text{T}(\mathbf{x}, t) = \overline{\text{C}_\text{T}}, \quad (4.11)$$

with $\overline{\text{C}_\text{T}}$ a typical DIC concentration and \mathbf{x} the position. In this case ^{14}R is considered as a purely physical tracer. Therefore biological activity and fractionation factors are ignored. Under these hypotheses (4.10) becomes

$$\frac{\partial}{\partial t} {}^{14}\text{R}_{\text{C}_\text{T}} + \mathcal{H}({}^{14}\text{R}_{\text{C}_\text{T}}) = -\lambda {}^{14}\text{R}_{\text{C}_\text{T}}. \quad (4.12)$$

The associated boundary condition derives from (4.9) adapted according to the hypotheses above. Then the tracer flux through the air-sea interface reads

$${}^R\mathcal{F} = \frac{1}{\text{C}_\text{T}} {}^{14}\mathcal{F} - \frac{{}^{14}\text{R}_{\text{C}_\text{T}}}{\text{C}_\text{T}} \mathcal{F} = \frac{\kappa_{\text{CO}_2} K_{\text{HP}}^{\text{a}}}{\overline{\text{C}_\text{T}}} ({}^{14}\text{R}_a - {}^{14}\text{R}_{\text{C}_\text{T}}), \quad (4.13)$$

since fluxes out of the ocean cancel out. In this method $\overline{\text{C}_\text{T}}$ is determined from the average surface DIC distribution and remains constant over time.

Assumption (4.11) has implications that go beyond taking the ocean DIC concentration to be constant. It also bears consequences on air-sea carbon exchange as represented in the model. Indeed it presupposes that carbonate chemistry does not intervene in determining air-sea exchange rate. This formulation is equivalent to the assumption of local rather than global air-sea equilibrium for CO_2 in an unperturbed atmosphere–ocean system.

The method represented by the set of equations (4.12) and (4.13) will hereafter be referred to as the R-method.

Model setup

Mean annual values of temperature, salinity, convective index and velocity fields from the LSG-OM and UL-OM are used to drive in off-line mode the LOCH model. Forcing with UL-OM also requires annual mean surface freshwater fluxes as well as vertical diffusivities (for more model details see Appendix A).

The piston velocity in LOCH is based on the empirical formulation of *Wanninkhof* (1992). We consider a reduced air-sea exchange rate in the presence of

sea ice. Therefore the piston velocity in the model is computed in the following way

$$\kappa_{\text{CO}_2} = (1 - f_{\text{ice}}) K_W \overline{w^2} \sqrt{660/Sc} \quad (4.14)$$

with f_{ice} the fraction of the sea surface covered with ice, Sc the Schmidt number and 660 a normalisation factor.

The long-term average of the squared wind magnitude $\overline{w^2}$ is taken from the annual climatology of *Trenberth et al.* (1989). The annual average of sea-ice fraction is computed with the help of the OCMIP-2 sea-ice cover climatology (*Orr et al.*, 2000). Both wind and sea ice fields were carefully interpolated onto both OGCM grids so as to eliminate as many differences as possible among carbon experiments. Sea-ice covers about 5.23% and 5.27% of the ocean surface for the LSG-OM and UL-OM fields, respectively.

The Schmidt number Sc as well as the CO_2 solubility (*Weiss*, 1974) are computed with the OGCM temperature and salinity fields. Gas exchange coefficients depend only weakly on the temperature as the effect of solubility decrease with temperature is nearly compensated for by the Schmidt number increase (*Bard*, 1988; *Wanninkhof*, 1992). The use of the same wind and ice cover fields for both models hence guarantees that gas air-sea exchange will be as similar as possible in both cases. The coefficient K_W in (4.14) is then adjusted to obtain a global average value of the CO_2 invasion rate (i.e., $\kappa_{\text{CO}_2} \times \text{solubility}$) of the order of $0.061 \text{ mol } \mu\text{atm}^{-1} \text{ m}^{-2} \text{ yr}^{-1}$ (*Siegenthaler*, 1986; *Watson and Liss*, 1998). The globally averaged piston velocity is 17.2 cm/h with LSG-OM and 17.7 cm/h with UL-OM. In the end the global mean CO_2 invasion rate differs by less than 1% between the two OGCMs. Similar invasion rates allow the comparison of results obtained with different circulation fields and the interpretation of departure among these results in terms of ventilation rates.

In abiotic experiments, alkalinity behaves as a passive tracer. Its equilibrium distribution should then be linearly correlated to salinity². We could hence simply compute it from the salinity field as was practiced during OCMIP-2. However off-line modelling does not guarantee a complete coherency between an off-line modelled passive tracer and salinity. Since dissolved CO_2 is very sensitive to the relative magnitudes of DIC and Alk, and in order to obtain the maximal coherency between both fields, alkalinity is also transported in all abiotic experiments performed according to the F-method.

The $\Delta^{14}\text{C}$ values in the ocean are initialized to a globally uniform prebomb value of -140‰ . The model is then run over a total of 10 ka constrained by pre-industrial (i.e., corresponding to 1765 A.D.; Fig. 4.1) atmospheric CO_2 , $\delta^{13}\text{C}$ and $\Delta^{14}\text{C}$ from the reconstructions of *Enting et al.* (1994), *Orr et al.* (2000), *Francey*

²all transported variables in the model are subject to air-sea freshwater fluxes either explicitly for UL-OM or implicitly (i.e., contained in the velocity divergence) for LSG-OM

et al. (1999), and *Keeling et al.* (2010). For the value of $\overline{C_T}$ intervening in Eq. (4.13) we use the surface mean C_T concentration predicted in the equilibrium abiotic experiments.

It is important to note that each of the radiocarbon modelling methods presented earlier requires its own equilibrium, hence several pre-industrial states are prepared (respectively denoted R0, F0 and B0 after the letter identifying the method, Section 4.1.1). These equilibrium experiments provide the initial conditions to the corresponding transient experiments.

Transient experiments setup

To simulate ocean ^{14}C during the industrial era, we force atmospheric CO_2 and $\Delta^{14}\text{C}$ to follow the historical estimates as given by *Enting et al.* (1994) and OCMIP-2 (*Orr et al.*, 2000), reproduced in the upper and lower panels of Figure 4.1. The evolution of the atmospheric ^{13}R ratio in experiments F or B is constrained by the data provided by *Francey et al.* (1999) and *Keeling et al.* (2010) as illustrated in Figure 4.1 (middle panel).

Two additional experiments are performed in which the atmospheric CO_2 (and consequently ^{13}C) is maintained at its pre-industrial level. The purpose of these additional experiments is to illustrate the role of the anthropogenic CO_2 increase in the bomb radiocarbon ocean uptake. The consequences of this increase are twofold. First it results in a larger radiocarbon invasion rate into the ocean for all model formulations (R or F). Second, experiments with carbon biogeochemistry (F or B), exhibit an enhanced air-sea CO_2 disequilibrium, hence larger air-sea ^{14}C fluxes.

Transient experiments are identified with two letters: the first indicating the radiocarbon modelling method (R, F or B), and the second relative to the type of CO_2 forcing over the industrial era (C: CO_2 maintained at pre-industrial value, or P: CO_2 from the historical record).

In total five transient experiments were designed. They may be summarized as follows

- FC: F-method; initial state: F0; historical $\Delta^{14}\text{C}$ forcing.
- FP: F-method; initial state: F0; historical CO_2 , $\delta^{13}\text{C}$ and $\Delta^{14}\text{C}$ forcing.
- RC: R-method; initial state: R0; historical $\Delta^{14}\text{C}$ forcing.
- RP: R-method; initial state: R0; historical CO_2 , and $\Delta^{14}\text{C}$ forcing.
- BP: B-method; initial state: B0; historical CO_2 , $\delta^{13}\text{C}$ and $\Delta^{14}\text{C}$ forcing.

Except for FC, each one of these methods has its equivalent in the literature. The biological cycle (BP) is considered in the works of *Bacastow and Maier-Reimer* (1990), and *Heimann and Maier-Reimer* (1996). The analysis of *Joos*

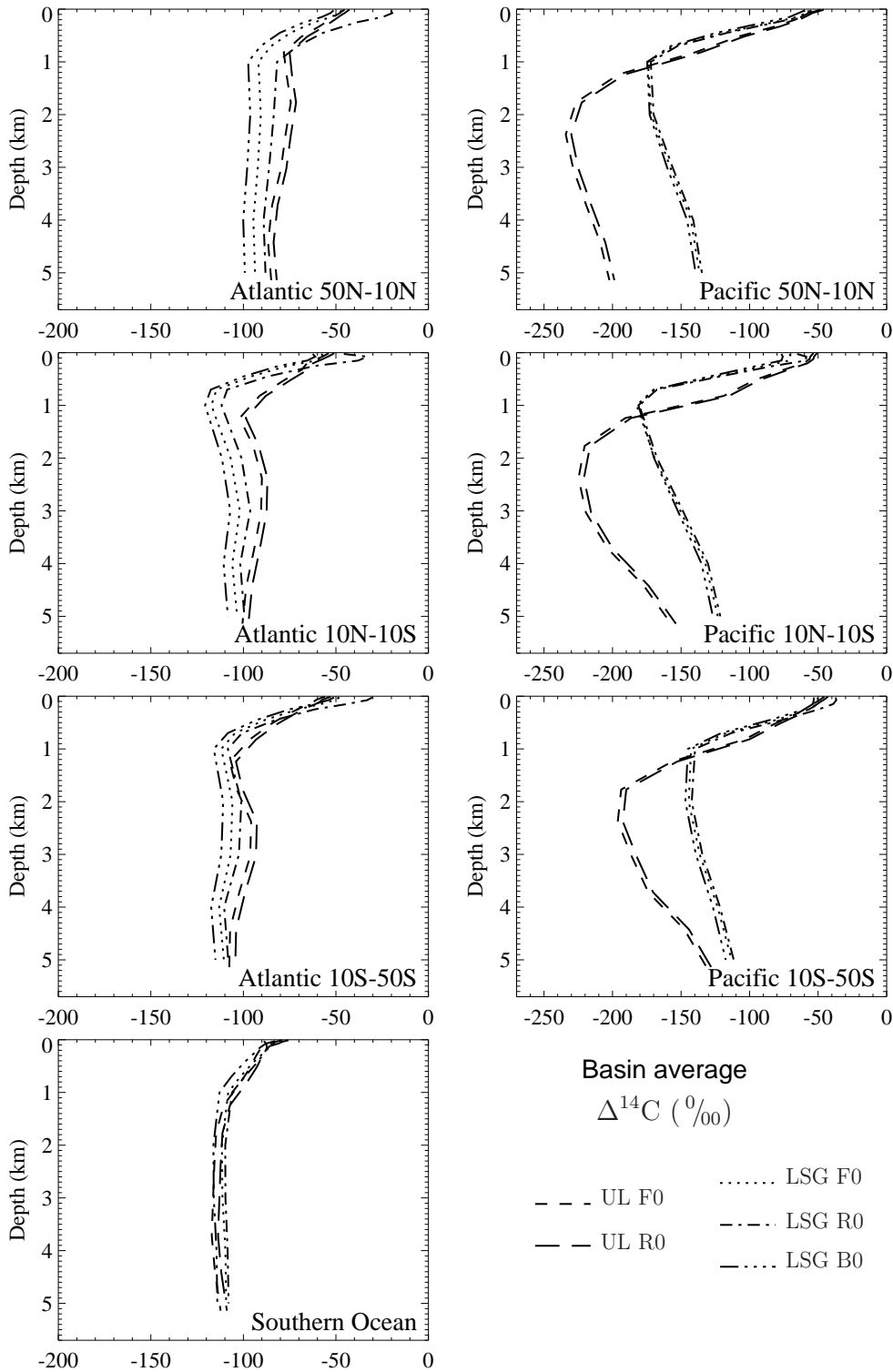


Figure 4.2: Mean $\Delta^{14}\text{C}$ vertical profiles in ocean basins for the five pre-industrial experiments. Circulation fields are provided by LSG-OM (LSG) or UL-OM (UL) OGCMs. $\Delta^{14}\text{C}$ for experiments identified with R0 is computed with the simplified method of Toggweiler *et al.* (1989a). The other experiments include the full CO_2 chemistry with (B0) or without (F0) biology. The Southern Ocean corresponds to the entire ocean south of 50°S .

et al. (1997) and *Müller et al.* (2008) are performed in a similar way as FP. The transient experiments of *Toggweiler et al.* (1989b), *Rodgers et al.* (2000) and *Mahadevan* (2001) are identical to those that we call RC. The radiocarbon experiments during OCMIP-1 (*Orr et al.*, 2001) and in *Müller et al.* (2006) are based on the RP protocol. In addition, *Krakauer et al.* (2006) and *Sweeney et al.* (2007) rely at some stage for their field estimates on model experiments performed the same way as RP.

4.1.2 Results

Pre-industrial state

Pre-industrial or equilibrium $\Delta^{14}\text{C}$ distributions do not differ much among the different configurations (figure 4.2). The close correspondence of R0 and F0 profiles may be explained by the lower C_T gradients observed in the deep ocean when no biological cycle is included. The contribution of this gradient to the mixed product term in (4.10) is very small. The close correspondance between the F0 and B0 results is in agreement with previous studies (*Bacastow and Maier-Reimer*, 1990; *Joos et al.*, 1997; *Maier-Reimer*, 1993). Biological activity contributes to the ^{14}C pool at depth, but its impact is nearly totally eliminated by the use of fractionation-corrected ^{14}R .

Both models fail to reproduce deep $\Delta^{14}\text{C}$ in the Atlantic. One of them (UL-OM) does a better job in the Pacific. At this stage it is worth mentioning that a less diffusive UL-OM version performs much better with respect to the Atlantic $\Delta^{14}\text{C}$ distribution but at the expense of a significant ageing of deep Pacific water masses (see Fig. 2.6). It is rather well known that ocean general circulation models generally do not simulate the deep natural radiocarbon distribution well (e.g., *Orr et al.*, 2001; *Matsumoto et al.*, 2004). One may not invoke any shortcoming in the biological model in order to explain the disagreement between data and model. As already stated above the deep ocean $\Delta^{14}\text{C}$ is insensitive to the formulation of the biota model (*Maier-Reimer*, 1993). Further, while biotic transport significantly contributes to the ^{14}C content of the deep Pacific Ocean (*Craig*, 1969) the error on $\Delta^{14}\text{C}$ is less than 10% (*Stuiver et al.*, 1981). In other less productive areas, the error would be much lower. The main reasons for such discrepancies between model and data are probably to be found in the representation of convective events and vertical mixing processes in coarse grid OGCMs. However this shortcoming does not necessarily affect processes characterized by short timescales, such as the one at stake.

The larger departure of LSG-OM -R0 with respect to LSG-OM -F0 and -B0 in the North Atlantic may be explained by the impact on ^{14}R of surface freshwater fluxes which are included in the velocity field divergence. Evaporation being quite large in the North Atlantic Ocean it leads to increased concentrations in that

area. In experiments LSG-OM -F0 and -B0 these fluxes affect individual tracers and mostly cancel out when ratios are computed. This problem is not present with the UL-OM fields since evaporation and precipitation are represented by means of an explicit flux condition at the ocean surface. When performing R experiments with UL-OM we set these fluxes to zero. We did not attempt to correct for these fluxes in experiments performed with LSG-OM and addressing the R-method. The results presented hereafter suggest that the impact of these fluxes is not critical.

Radiocarbon ratios may be interpreted in terms of a radiocarbon age relative to the atmosphere, \tilde{a}_{14} , with the following expression

$$\tilde{a}_{14} = 8267 \times \ln \left(1 + \frac{\Delta^{14}\text{C}}{10^3} \right). \quad (4.15)$$

For example a $\Delta^{14}\text{C}$ of -110 ‰ corresponds to a radiocarbon age of 963 yr.

The typical residence time of surface waters being much shorter than the time required for carbon isotopic equilibration (~ 10 yr; *Broecker and Peng, 1974*) the surface ocean has a much lower ^{14}R ratio than the atmosphere. The difference between the two may be interpreted in terms of an “apparent” or “reservoir” age (*Lal and Suess, 1968; Kitagawa and van der Plicht, 1998; Matsumoto, 2007*). The age difference between the ocean surface and the atmosphere, or the reservoir age is not homogeneously distributed. Water masses flowing at the surface in western boundary currents have more time to equilibrate with the atmosphere than waters upwelling in the Southern Ocean. Also there is a strong dependency of the isotopic exchange rate upon wind magnitude (*Broecker and Maier-Reimer, 1992*). The pre-industrial $\Delta^{14}\text{C}$ of surface waters is estimated to be in the range -50 to -60 ‰ ($\tilde{a}_{14} \sim 468$ yr) for areas north of 40°S whereas Southern Ocean surface waters were characterized by $\Delta^{14}\text{C}$ of -110 to -150 ‰ or even lower (\tilde{a}_{14} of the order of 900–1200 yr) (*Broecker et al., 1985; Chen, 1993; Toggweiler and Samuels, 1993; Berkman and Forman, 1996; Rubin and Key, 2002*).

The radiocarbon age of deep waters does not reflect the true ventilation age as defined in *England (1995)* or *Deleersnijder et al. (2001)*. Further since air-sea exchange and surface water renewal rates strongly impact the radiocarbon distribution any climatic modification or ocean water mass re-organisation may result in radiocarbon age changes at depth that would not necessarily reflect actual ventilation age changes (*Campin et al., 1999*).

The importance of the water mass pathways in setting radiocarbon at depth is evidenced by comparing Figures 4.2 and 2.11. Deep Southern Ocean true ventilation ages are about 200 yr lower for UL-OM (exp. L0 in Fig. 2.11) than for LSG-OM (exp. A0). On the contrary, radiocarbon ages obtained with the same model configurations (figure 4.2) are very close (a 200 yr delay would result in a decrease in $\Delta^{14}\text{C}$ of ~ 24 ‰). As explained earlier in the text air-sea exchange rates do not differ significantly between the UL-OM and LSG-OM

models. Considering what happens in the Southern Ocean two possibilities arise. One possibility is that similar water masses fill that area in each model, however with different proportions. The second possibility is that water masses filling that area differ among the two models with respect to the conditions they encountered at the surface. This example puts forward some limitations in using $\Delta^{14}\text{C}$ in order to assess OGCMs ventilation timescales since it is obvious that it significantly departs from the wate age.

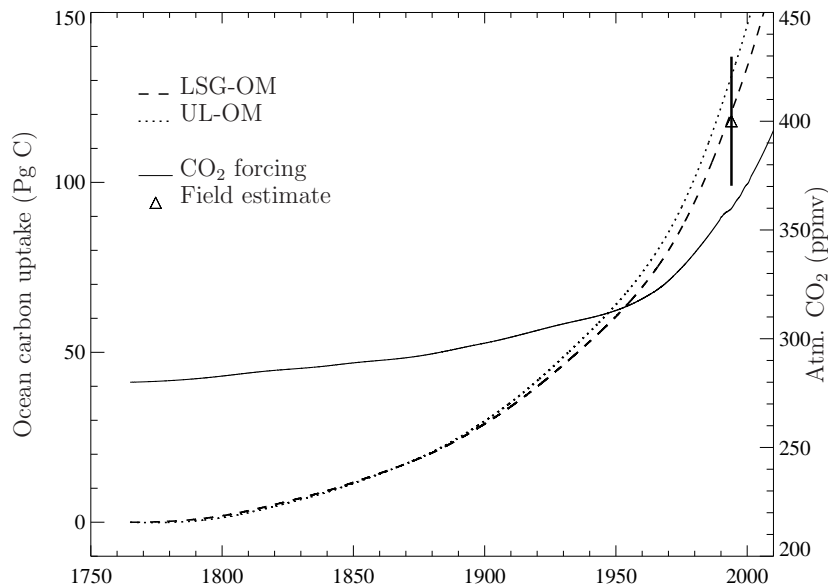


Figure 4.3: Time series of CO₂ uptake by the ocean with the carbon model driven by LSG-OM (dashed line) and UL-OM (L0 version, dotted line). The individual uptakes (represented as anomalies with respect to 1765 A.D.) are obtained from abiotic constrained CO₂ experiments. The thin solid line corresponds to the atmospheric CO₂ forcing, for which units are given on the right axis. The global ocean carbon inventory for 1994 relative to 1800 as obtained from field estimates (*Prentice et al.*, 2001) is represented by the triangle and error bars.

Response to anthropogenic forcing at the global scale

For the year 1990, the global net CO₂ fluxes into the ocean amount to 2.4 GtC/yr and 2.1 GtC/yr for the carbon model driven by UL-OM and LSG-OM fields, respectively. These values are within the range of estimates based on observations and model studies (*Gruber et al.*, 2009). The global inventory of ocean anthropogenic carbon predicted with both circulation fields is also in good agreement with field reconstructions (Figure 4.3).

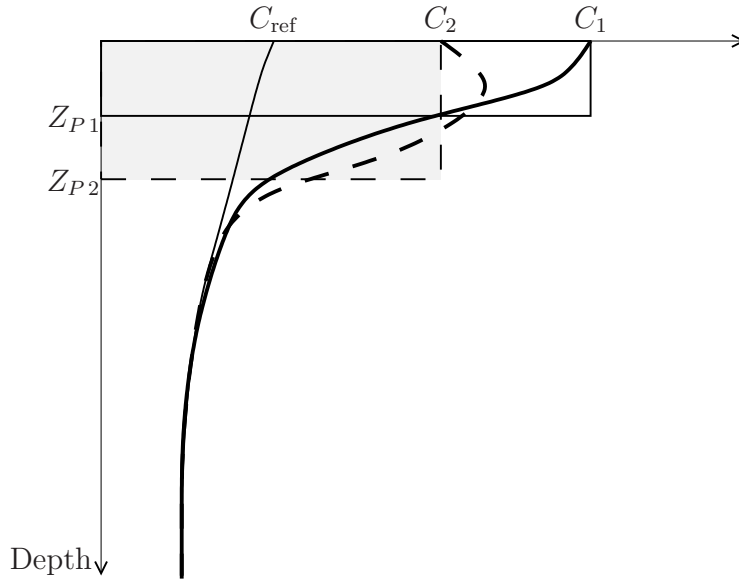


Figure 4.4: Illustration of the concept of the penetration depth. The unperturbed profile is represented by the thin solid line with concentration C_{ref} at the surface. The thick solid line and the dashed line correspond to the perturbed profiles at times t_1 and t_2 , respectively. Z_p is computed as column inventory anomaly divided by surface concentrations difference (Broecker and Peng, 1993). As time goes by, surface concentration decreases (from C_1 to C_2) while Z_p increases. Areas and depths were designed for the sole purpose of illustration; they are only indicative.

With respect to bomb radiocarbon one usually reports information by means of the mean penetration depth and of inventories relative to the pre-bomb era.

Quoting Broecker and Peng (1993): “The mean penetration depth is defined as the depth to which the isotope anomaly for the surface has to be extended to yield a water column inventory equal to the observed inventory”. The penetration depth is considered as not being affected by gas exchange rate (Joos *et al.*, 1997). Under the hypothesis of nil lateral transport, the penetration depth provides a means to gather information on vertical transport processes in the upper ocean.

The global averages of the mean penetration depth $\langle Z_p \rangle$ for the 9 experiments are given in Table 4.1. The range among experiments performed with the same circulation is about the same for both OGCMs (44 m with LSG-OM and 47 m with UL-OM). The highest values correspond to FP experiments, the lowest to FC and RC. The BP experiment produces only a slightly lower $\langle Z_p \rangle$. There is a systematic difference of the order of 30 m between the same experiments obtained with a different circulation. The UL-OM fields predict a deeper $\langle Z_p \rangle$. In LSG-OM there are no explicit vertical mixing terms, while the UL-OM circulation relies

Table 4.1: Global mean bomb ^{14}C penetration depths in 1974 (in m, line 3) and ocean bomb radiocarbon inventories (in 10^{26}at.) relative to 1940 for 1974 (line 4) and 1990 (line 5). The last line presents the difference between these two inventories. The last column contains values of $\langle Z_p \rangle_{1974}$ as estimated from data (B95; Broecker *et al.*, 1995) and from the OCMIP-1 model range (O1; Orr *et al.*, 2001).

	UL-OM				LSG-OM					
	RC	RP	FC	FP	RC	RP	FC	FP	BP	
$\langle Z_p \rangle_{1974}$	285	296	284	331	255	267	255	299	281	391 (B95) 283–375 (O1)
$^{14}\text{I}_{1940-1974}$	246	281	242	299	241	274	237	290	291	
$^{14}\text{I}_{1940-1990}$	334	380	328	417	324	368	319	401	403	
Diff	88	99	86	118	83	94	82	111	112	

on a vertical mixing coefficient depending on the stratification (Appendix A). The larger $\langle Z_p \rangle$ is in agreement with a more active diffusivity near the surface³.

As expected, inventories are also larger with UL-OM than with LSG-OM. But the spread among experiments is much larger than the differences due to the circulation fields. These differences are also reported in Figure 4.5. Not surprisingly experiments FC and RC predict similarly low inventories. Larger inventories are obtained with RP experiments while FP and BP predict the largest uptake. The marine biological cycle impact on bomb radiocarbon inventories is less than 1% in 1990. This number agrees with a quoted impact of less than 2% in Müller *et al.* (2008). Similar bomb radiocarbon inventories as those predicted with the FP configuration were obtained by Joos and Bruno (1998) in their inverse modelling study and by Müller *et al.* (2008) in a model setup similar to FP (Figure 4.7).

The reason for the low RC and FC inventories lies in the atmospheric reservoir. Neglecting the increase in atmospheric CO_2 leads to a lower amount of ^{14}C atoms for an identical $\Delta^{14}\text{C}$. This is probably the cause for the low inventories obtained with some former model studies (Duffy and Caldeira, 1995).

Experiments RP take into account the atmospheric CO_2 increase but still lag behind experiments FP and BP. The reason is to be found in ocean overturning rate and carbonate chemistry. As mentioned when introducing the method consisting in transporting the ^{14}R ratio, this method implicitly assumes that air-sea CO_2 equilibrium prevails. The air-sea ^{14}C fluxes in Eq. (4.13) are fully determined by the difference in the ^{14}R ratios. Solubility and wind magnitude

³Note that this is not in contradiction with the analysis presented in Chapter 2). This process concerns the early uptake rate which is larger with UL-OM than with LSG-OM. In the long term processes connecting the deep ocean and the surface control the uptake.

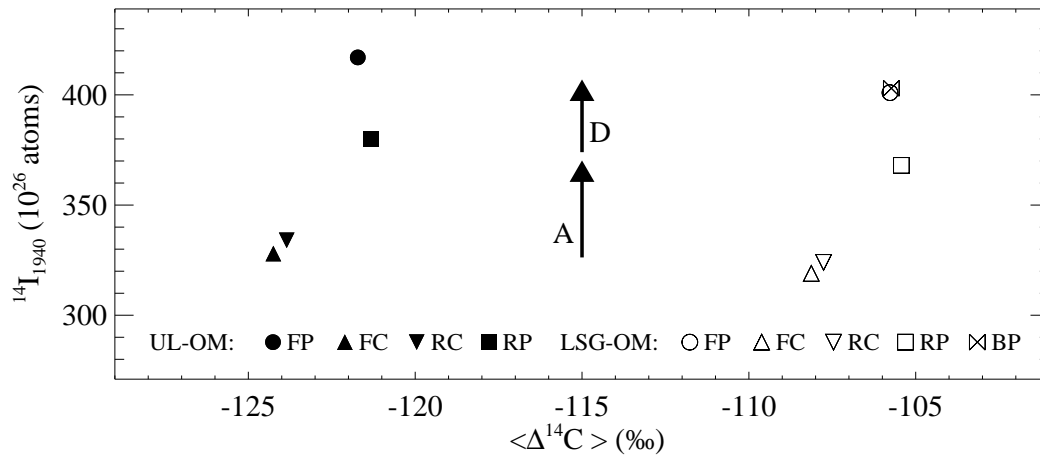


Figure 4.5: Bomb radiocarbon inventories in 1990 relative to 1940. Experiment results are distributed according to their globally averaged $\Delta^{14}\text{C}$ at the same time (x axis). Filled and open symbols refer to transport by UL-OM and LSG-OM fields respectively. Symbols identify the different transient experiments: FP (●), FC (▲), RC (▼), RP (■), and BP (⊗). For the purpose of this illustration the global mean $\Delta^{14}\text{C}$ corresponding to the same OGCM were corrected for small differences among their initial state $\Delta^{14}\text{C}$ ($\sim 4\text{‰}$). The A-labelled arrow represents the effect of the atmospheric CO_2 increase. The role of air-sea CO_2 disequilibrium is illustrated by the D-labelled arrow.

determine their geographical distribution, but they are not affected by changes in ocean carbon.

The atmospheric CO_2 perturbation increases exponentially after 1940. Due to the limited rate of the CO_2 exchange between the atmosphere and the ocean (typically 1 yr for a 50 m deep column) and the constant renewal rate of surface waters, the ocean dissolved CO_2 increases less rapidly than atmospheric CO_2 . When carbonate chemistry is included in the model, the air-sea disequilibrium increases with time since the increase of dissolved CO_2 in the ocean lags behind that in the atmosphere. This is illustrated in Figure 4.6 which reproduces the net air-sea CO_2 fluxes predicted by experiments FC, RP and FP for the same year (1990). The FC fluxes reflect the pre-industrial CO_2 distribution. Negative fluxes (into the ocean) are typical for cold water areas. The net global CO_2 flux corresponding to that experiment is zero. For FP the air-sea disequilibrium increases over the industrial era. The ocean CO_2 uptake is enhanced and results both in a net CO_2 uptake but also in a larger ^{14}C flux to the ocean. The RP (and RC, resp.) CO_2 fluxes are globally but also locally equal to zero.

Therefore any method based on the hypothesis that the fluxes into the oceans have a time history proportional to the perturbation in the overlying atmosphere may underestimate ocean inventories. The bias in the figures in Table 4.1 is of

the order of 10% for the 1990 inventories but it is about 20% for the inventory difference between 1974 and 1990.

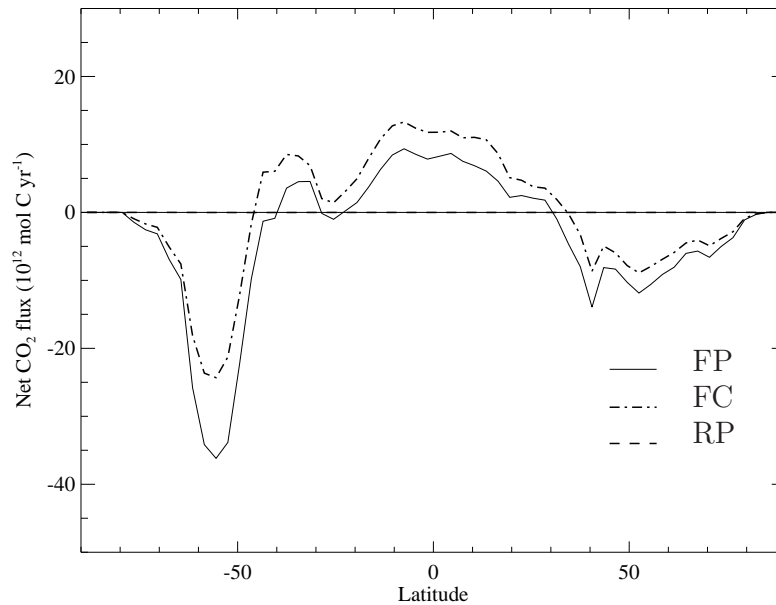


Figure 4.6: Net sea-to-air CO_2 fluxes with respect to latitude for experiments FP, FC and RP. Negative values indicate a net flux into the ocean. The RP flux is locally zero, by definition. Values shown are for 1990 with UL-OM .

Response to anthropogenic forcing at the regional scale: biological impact

The regional distribution of bomb radiocarbon predicted with UL-OM is in reasonable agreement with GEOSECS data (Figures 4.8 and 4.9). A similar agreement is obtained with LSG-OM (not illustrated). Regional inventories and penetration depths follow the same pattern as global figures: lower inventories with experiment RP than with FP but similar penetration depths.

The neglect of biological activity has a negligible impact on global inventories. Its impact is similarly small in most ocean areas (Table 4.2). However, there are differences between the regional distributions of bomb $\Delta^{14}\text{C}$ with and without biology. There is a moderate increase of both the inventory and Z_p in cold water areas where biological activity reinforces the flux to the ocean. Areas characterized by a low organic activity do not exhibit significant changes (South Atlantic and South Pacific central gyres). There is, however, a dramatic change due to biological activity in areas with strong upwelling (Equatorial Pacific). The

Table 4.2: Regional inventories U_t (in 10^{26} at.), and mean penetration depth \bar{Z}_p (in m.) at the time of GEOSECS. Values corresponding to experiments FP and BP with the LSG-OM circulation fields. These inventories are computed relative to 1765.

Experiment Region	FP		BP	
	U_t	\bar{Z}_p	U_t	\bar{Z}_p
Atlantic 10°N–50°N	19	306	21	327
Atlantic 10°S–10°N	7	253	6	222
Atlantic 50°S–10°S	26	247	26	245
Pacific 10°N–50°N	46	265	43	241
Pacific 10°S–10°N	13	210	6	76
Pacific 50°S–10°S	57	279	54	261
Southern Ocean (> 50°S)	37	452	38	472

DIC content in these upwelled waters significantly increases as a consequence of organic carbon remineralization at depth. As a result CO_2 fluxes in the equatorial Pacific, which are toward the ocean in experiment FP are directed outward in experiment BP. This seriously affects the uptake rate of excess radiocarbon and translates by a much reduced penetration depth (Table 4.2) The difference can be clearly seen in Figures 4.10 and 4.11 which show the zonal mean of $\Delta^{14}\text{C}$ in the three ocean main basins. Superimposed on this distribution is the zonal average of Z_p (deepest level of the hatched area). A close examination of these figures reveals that biological activity significantly impacts radiocarbon uptake in two areas: the north Indian Ocean and the equatorial Pacific. While further investigation is needed in order to provide a confident estimate of the exact magnitude of this impact, the potential consequences should be kept in mind when addressing bomb radiocarbon studies in areas characterized by intense biological activity.

4.1.3 Discussion and conclusions

We tested various methods in use for ^{14}C modelling with the circulation fields of two OGCMs. The response time of these OGCM versions to an atmospheric perturbation are different both on short and long time scales. With respect to inventories, the different methods lead to a larger range of results than those obtained with different circulation fields. All the differences between the various experiments may be explained by constraints at the air-sea interface.

The hypothesis of similar time histories for the atmospheric and the upper ocean CO_2 and ^{14}C has limitations. The increase for atmospheric CO_2 since 1945 is simply too fast with respect to the renewal rate of ocean surface water.

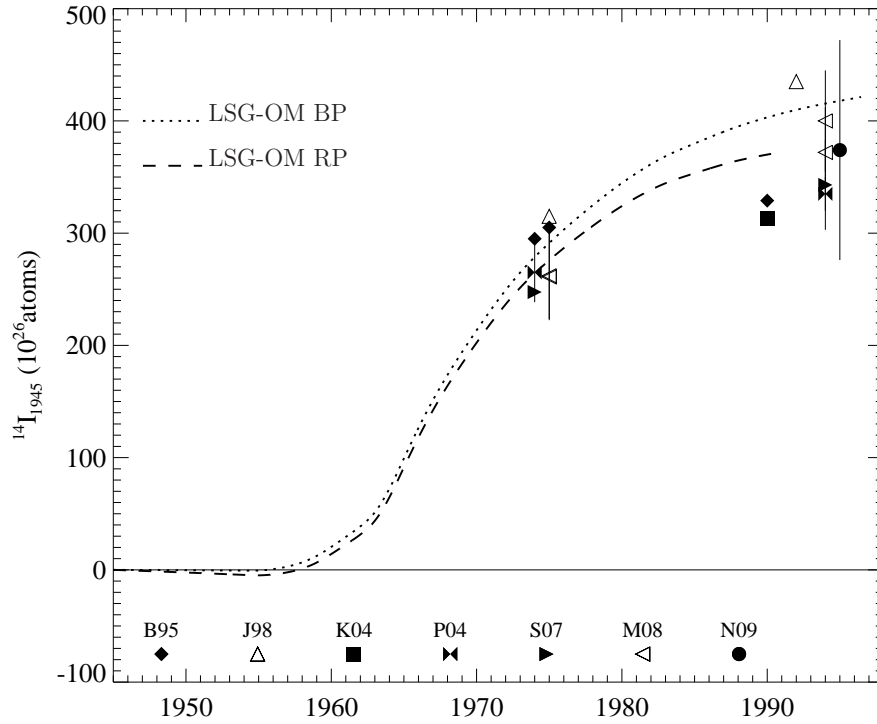


Figure 4.7: Ocean bomb ^{14}C inventory relative to 1945 for experiments LSG-OM BP and LSG-OM RP compared to estimates from the literature. Filled symbols refer to data-based estimates and open symbols to model-based estimates. Data and model sources as originally published by Broecker *et al.* (1995) B95, Key *et al.* (2004) K04, Peacock (2004) P04, Sweeney *et al.* (2007) S07, Joos and Bruno (1998) J98, Müller *et al.* (2008) M08, Naegler (2009) N09. Where available, error bars (P04 and N09) or model result range (M08) are also shown.

Our bomb ^{14}C inventories differ significantly, both in the 1970s and in the 1990s, between simulation experiments where we adopted this simplification and those where we did not.

Relaxing this hypothesis leads to bomb ^{14}C inventories that are usually greater than field-estimates (Figure 4.7). The piston velocity κ_{CO_2} in our experiments is of the same order of magnitude as recently revised values (Müller *et al.*, 2008; Naegler, 2009). Inventories obtained with experiments FP or BP agree (within the range of uncertainty) with other modelling studies (Joos and Bruno, 1998; Müller *et al.*, 2008) and with the revised estimate of Naegler (2009) (Figure 4.7).

One important point to notice is that data-based estimates also rely on the idea that the magnitude of air-sea CO_2 disequilibrium remained constant over

time. *Sweeney et al.* (2007) rely for their reconstruction on numerical experiments performed with the RP configuration. Hence, an upward revision of field estimates is probably also necessary.

The fact that some methods used in OGCMs may significantly bias bomb radiocarbon inventories does not only have consequences for the estimated gas exchange rates but also for surface mixing rates in models which rely on such estimates for their calibration or validation.

However, we should also question model estimates of bomb radiocarbon inventories on the basis of the model ventilation time scale. Indeed OGCMs have deficiencies in reproducing the actual ocean ventilation rate at decadal to centennial time scales (e.g., *Dutay et al.*, 2002; *Doney et al.*, 2004; *Matsumoto et al.*, 2004).

The ^{14}C perturbation due to nuclear weapon testing in the atmosphere occurred over a very short period of time in comparison with ocean ventilation. In the early years after the nuclear weapon tests the gas exchange rate was the main factor setting the bomb ^{14}C invasion rate into the oceans. Later on, ocean transport processes took control of the pace of this uptake (*Joos et al.*, 1997; *Key*, 2004). This statement is supported by the maximum ^{14}C concentrations during GEOSECS being found at the surface while now they are frequently found at depths greater than 100 m (*Key*, 2004). After a while, the ocean response to that perturbation may be interpreted in the light of the pulse response presented in Section 2.2.2. At low ages, but yet over a longer time than the duration addressed with the bomb ^{14}C analysis, diffusion is the main process controlling the response to a surface perturbation in OGCMs (*Mouchet et al.*, 2011). It is common knowledge that the level of vertical diffusion active in 3-D OGCMs is probably too high (see also sections 2.2.3 and 2.3; *Duffy et al.*, 1997; *England and Rahmstorf*, 1999; *Oschlies*, 2000; *Schmittner et al.*, 2009). This additional factor could explain discrepancies among the various available estimates. Further analyses with lower diffusion model versions are currently being carried out.

It must also be mentioned that our study does not include seasonal processes. Since the bomb radiocarbon uptake appears to be strongly affected in areas with significant control from biological activity on air-sea CO_2 exchange, this aspect would merit further attention.

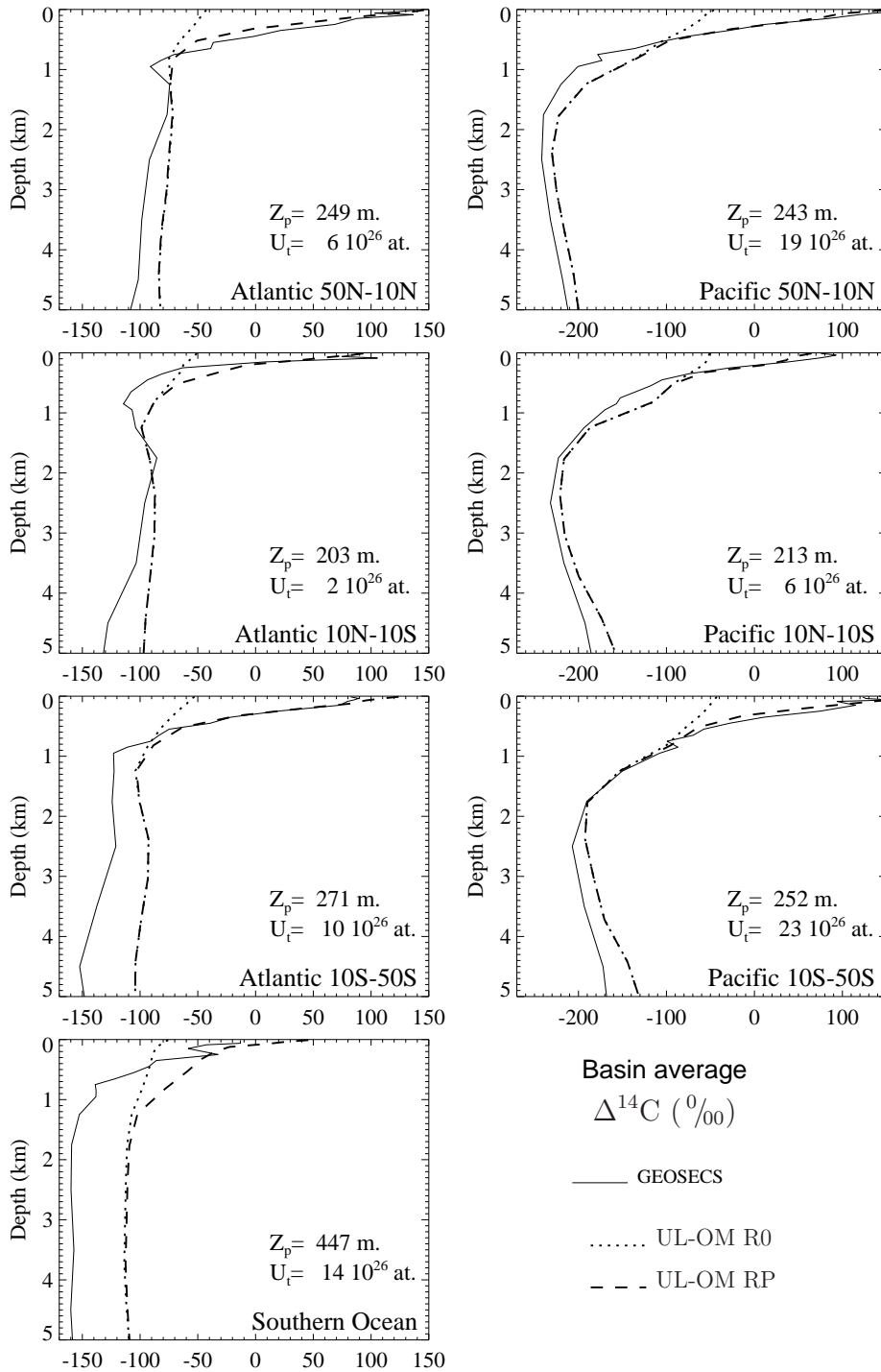


Figure 4.8: Mean $\Delta^{14}\text{C}$ vertical profiles in ocean basins for experiments R0 (dot) and RP (dash) with the UL-OM circulation fields. Corresponding profiles during the GEOSECS survey (*Stuiver et al.*, 1981) are reproduced with solid lines. U_t is the total bomb ^{14}C uptake by the respective basin computed in 1974 relative to pre-industrial times. Z_p is the basin-averaged penetration depth at the same time. The Southern Ocean corresponds to the entire ocean south of 50°S .

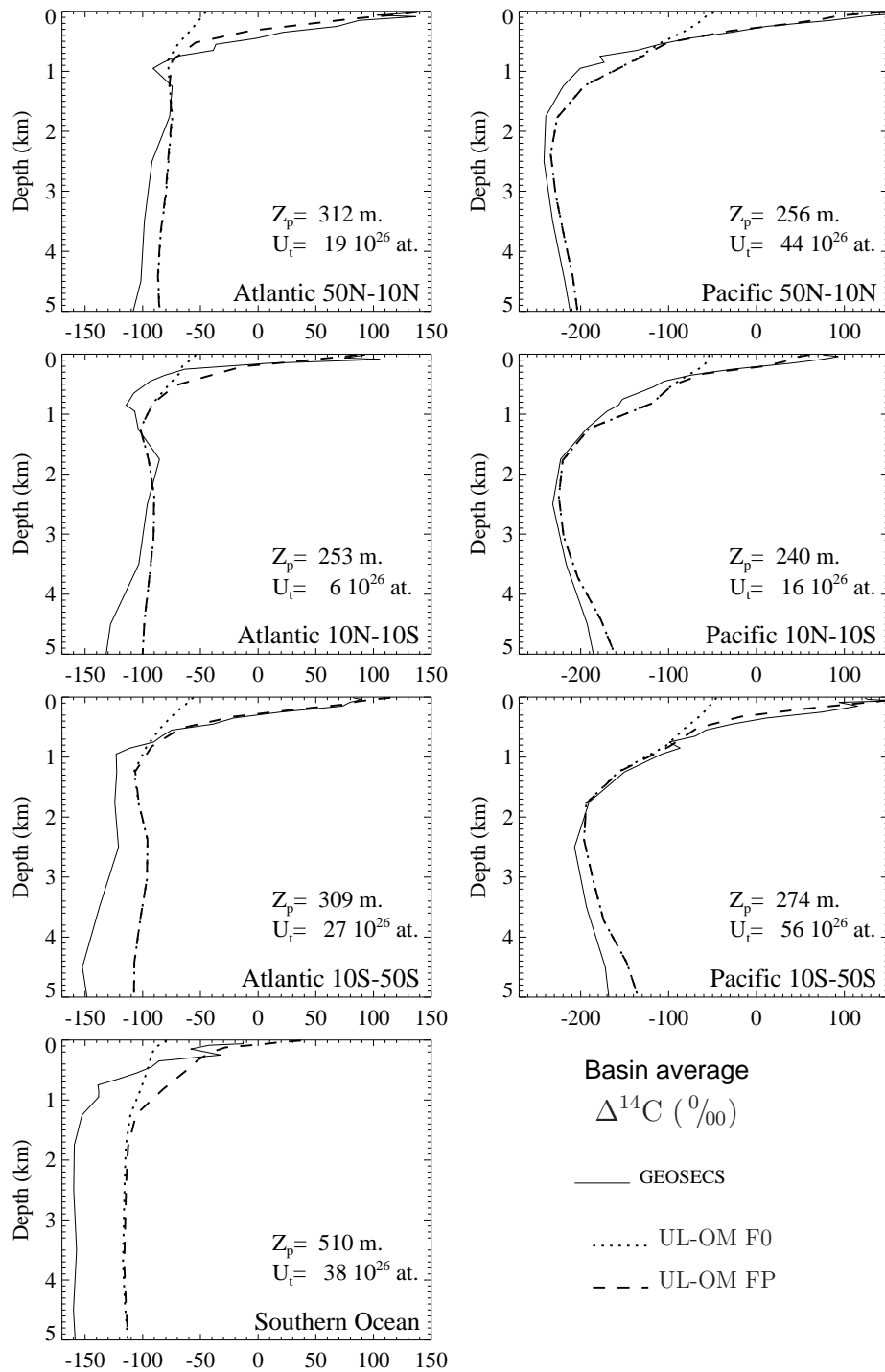


Figure 4.9: Mean $\Delta^{14}\text{C}$ vertical profiles in ocean basins for experiments S0 (dot) and SP (dash) with the UL-OM circulation fields. Corresponding profiles during the GEOSECS survey (Stuiver *et al.*, 1981) are reproduced with solid lines. U_t is the total bomb ^{14}C uptake by the respective basin computed in 1974 relative to pre-industrial times. Z_p is the basin-averaged penetration depth at the same time. The Southern Ocean corresponds to the entire ocean south of 50°S .

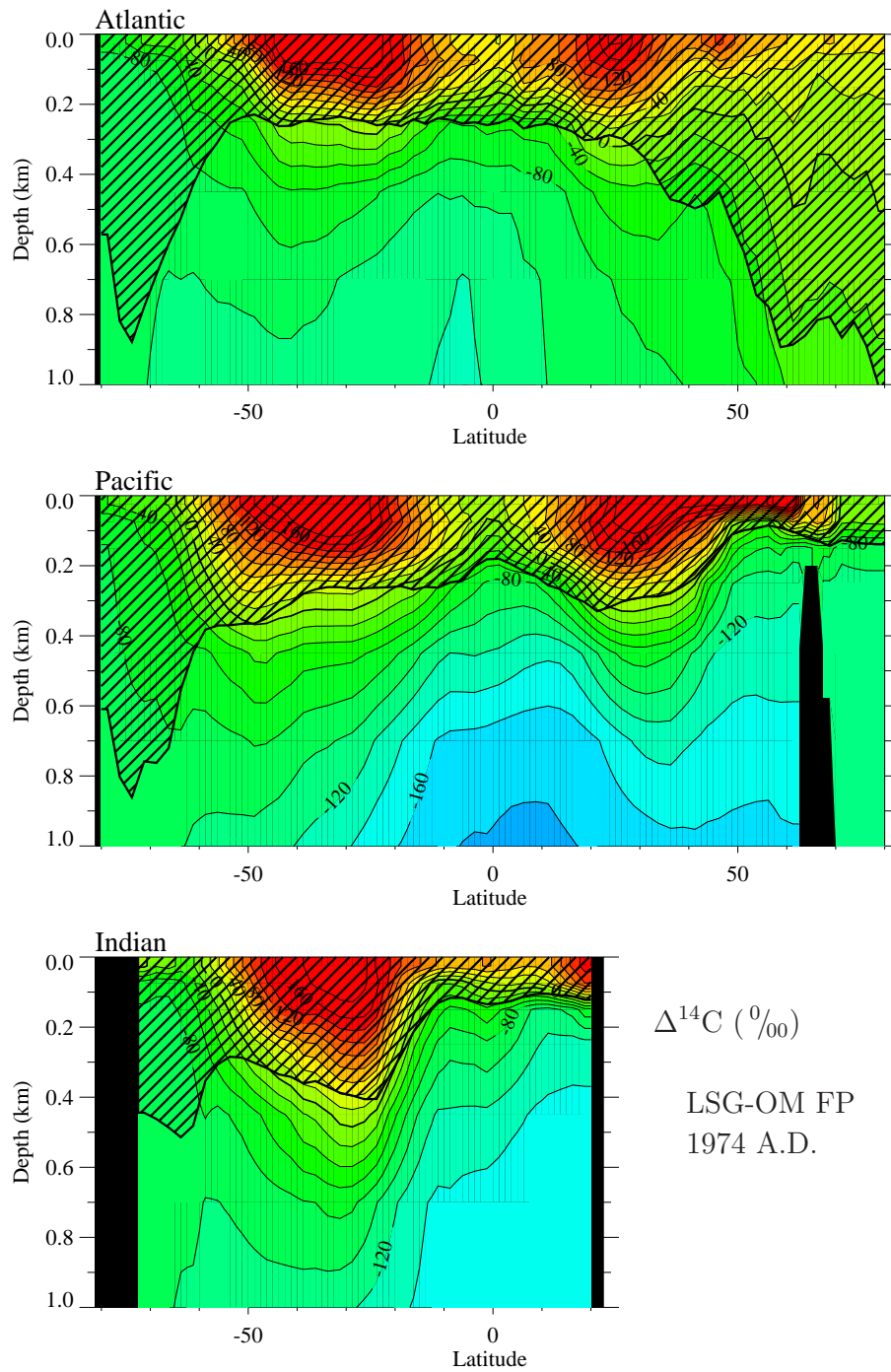


Figure 4.10: Zonal average of $\Delta^{14}\text{C}$ in the three oceans: Atlantic (top), Pacific (middle) and Indian (bottom) for experiment FP with the LSG-OM circulation fields at GEOSECS times. The zonally averaged penetration depths are indicated by the hatched area.

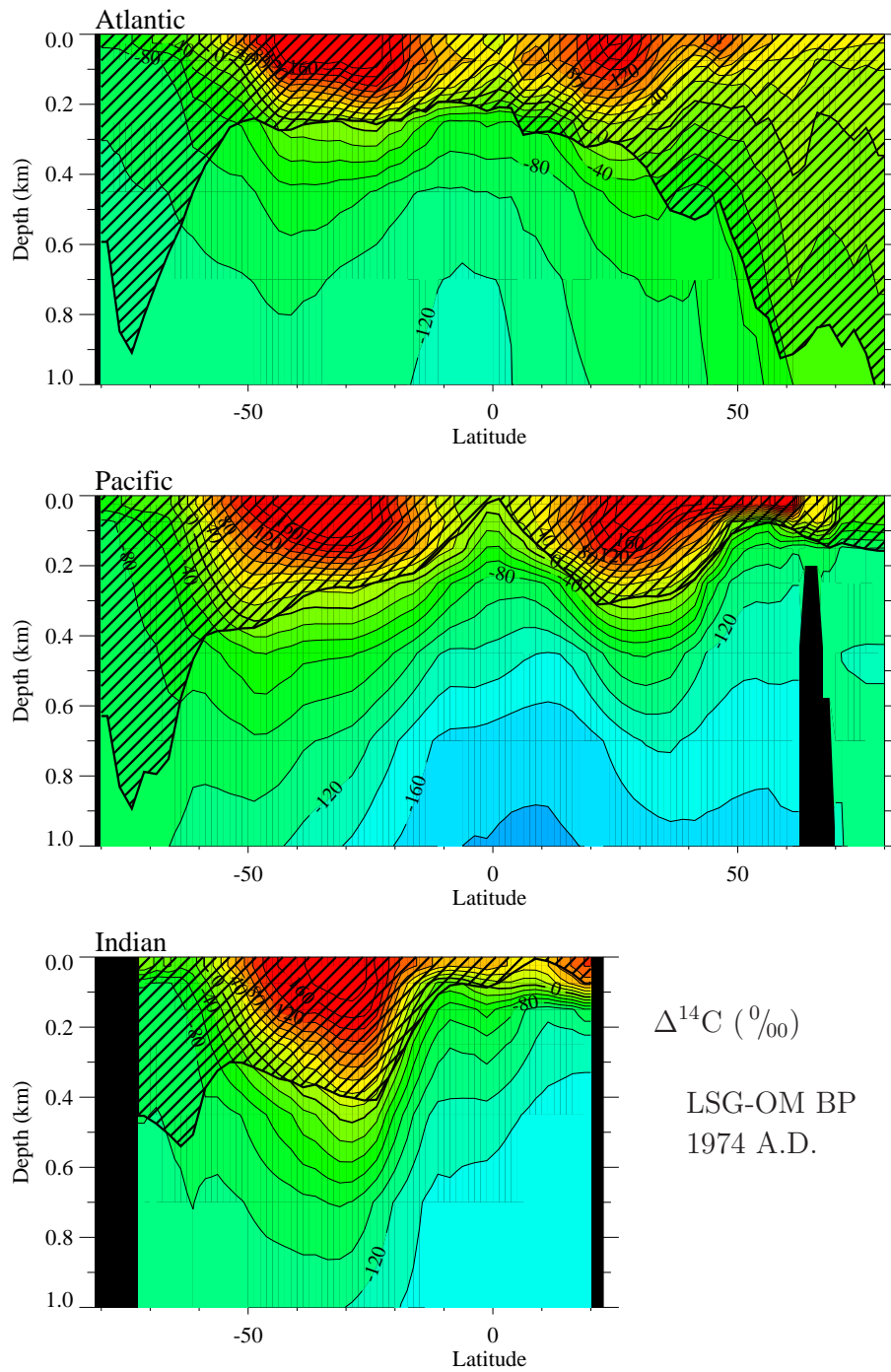


Figure 4.11: Zonal average of $\Delta^{14}\text{C}$ in the three oceans: Atlantic (top), Pacific (middle) and Indian (bottom) for experiment BP with the LSG-OM circulation fields at GEOSECS times. The zonally averaged penetration depths are indicated by the hatched area.

4.2 Modelling carbon isotopes

When establishing the biologically-mediated fluxes in Chapter 3 we did not discriminate among isotopes. All equations were given for the total content of carbon atoms, i.e., the sum of all isotopic forms.

The atmospheric module of LOCH allows for the prognostic computation of carbon isotopes in the atmosphere. The evolution of atmospheric concentrations results from the balance between the various fluxes from the ocean, the continental biosphere, and, when relevant, from anthropogenic activity. It is also possible to perform experiments with a prescribed atmospheric isotopic composition.

Relationships between concentrations and ratios as well as air-sea fluxes are given in Section 4.1 (Equations (4.1)–(4.2), and (4.8)–(4.9), respectively). We focus here on the terms ${}^i q_v$ ($i = 13, 14$, resp.) intervening in the transport equations for carbon isotopes (Eq. (4.4) and (4.5)), taking into account biotic processes.

4.2.1 Sources and sinks terms due to biological activity

The temporal evolution of the different isotopic pools obeys similar equations to those written for C_T . Differences stem from fractionation factors and isotopic ratios, reflecting isotope availability, which weight the various flux terms.

Carbon isotopes are included in all biogenic reservoirs of LOCH. In order to correctly represent their cycles, isotopically-tagged phytoplankton biomass, particulate and dissolved organic matter, as well as dissolved inorganic carbon pools were added to the model. A left superscript with the isotope atomic number helps to identify those reservoirs.

Phytoplankton exhibits a preferential uptake of the lighter carbon isotope. This assimilation does however not depend on the cell isotopic ratio. The uptake of ${}^{13}\text{C}$ during phytoplankton growth is further regulated by the isotope availability in the surrounding waters. The growth rate of the ${}^{13}\text{C}$ pool in soft tissues is then given by

$${}^{13}\mu = {}^{13}\alpha_\phi {}^{13}R_{C_T}\mu, \quad (4.16)$$

with ${}^{13}\alpha_\phi$ the fractionation factor characterizing photosynthesis.

During biomass removal or organic matter decay no fractionation intervenes. The probability of disappearance with respect to these processes is the same for all carbon isotopes. The same rate of removal applies to carbon isotopes and carbon in B , DOM and POM.

The equations established in Chapter 3 are now expressed for the ${}^{13}\text{C}$ content of the different pools. The ${}^{13}\text{C}$ contents in phytoplankton biomass ${}^{13}C_B$ and in

particulate organic matter ^{13}POM obey

$$\frac{d^{13}\text{C}_B}{dt} = {}^{13}\alpha_\phi {}^{13}\text{R}_{\text{C}_T} \text{S}_{\text{C}:P} \mu B - {}^{13}\text{R}_B \text{S}_{\text{C}:P} r_B B, \quad (4.17)$$

$$\frac{d^{13}\text{POM}}{dt} = -\frac{d^{13}\mathcal{J}(Z)}{dZ} - f_{\text{sed}}(^{13}\text{POM}) - (d_{\text{POM}} + r_{\text{POM}}) ^{13}\text{POM}, \quad (4.18)$$

where ${}^{13}\text{R}_B$ is the ^{13}R ratio in B , ${}^{13}\mathcal{J}(Z)$ is the flux of dead organic matter carrying ^{13}C to depth, and $f_{\text{sed}}(^{13}\text{POM})$ represents ^{13}C burial into sediments.

In order to close the system, and guarantee conservation, we need to introduce an additional variable representing the ^{13}C content of dissolved organic matter. This variable, represented as ^{13}DOM , is transported by the 3-D circulation, and obeys

$$\frac{\partial^{13}\text{DOM}}{\partial t} + \mathcal{H}(^{13}\text{DOM}) = f_{\text{riv}}(^{13}\text{DOM}) + d_{\text{POM}} ^{13}\text{POM} - r_{\text{DOM}} ^{13}\text{DOM}, \quad (4.19)$$

where $f_{\text{riv}}(^{13}\text{DOM})$ represents the ^{13}C flux to the ocean in dissolved organic carbon carried by rivers.

The source-minus-sink term intervening in Eq. (4.4) for the total dissolved inorganic ^{13}C is then

$$q_v(^{13}\text{C}_T) = \text{S}_{\text{C}:P} (-{}^{13}\alpha_\phi {}^{13}\text{R}_{\text{C}_T} \mu B + r_{\text{POM}} ^{13}\text{POM} + r_{\text{DOM}} ^{13}\text{DOM}) + f_{\text{riv}}(^{13}\text{C}_T) - {}^{13}\text{R}_{\text{C}_T} \text{S}_{\text{CaCO}_3:P} \mu B + {}^{13}\text{R}_{\text{CaCO}_3} \mathcal{D}_{\text{CaCO}_3}. \quad (4.20)$$

The last three terms in this equation represent river inputs of inorganic ^{13}C , the ^{13}C uptake during carbonate shell building, and the dissolution of shells containing ^{13}C , respectively. The content of ^{13}C in carbonate shells is taken care of through the introduction of an additional reservoir whose evolution results from the balance between the last two terms in Eq. (4.20). Dissolution rates of CaCO_3 are the same for all isotopic forms.

We assume that no fractionation occurs during CaCO_3 precipitation. It seems that some fractionation does actually occur during shell building but its magnitude is highly species-dependent and no clear relationship with the environment has been established yet (*Hoefs, 1997*).

Procedure and equations for radiocarbon are exactly the same except for fractionation factors and radioactive decay. Fractionation factors for ^{14}C are the square of those for ^{13}C (*Siegenthaler and Münnich, 1981*). Similarly to what is done for ^{13}C we introduce additional pools of ^{14}C . Their evolution is then given by a similar set of three equations (Eq. (4.17) to Eq. (4.19)) in which we replace the superscript 13 by 14 and add the radioactive decay sink. Radioactive decay of radiocarbon incorporated in the biomass pool may be neglected since that pool has a much smaller lifetime than the mean lifetime $1/\lambda$ of radiocarbon. With all

terms having the same meaning as before but written this time for ^{14}C , we get

$$\frac{d^{14}\text{C}_B}{dt} = (^{13}\alpha_\phi)^2 {}^{14}\text{R}_{\text{C}_T \text{S}_{\text{C}:P}} \mu B - {}^{14}\text{R}_B \text{S}_{\text{C}:P} r_B B, \quad (4.21)$$

$$\begin{aligned} \frac{d^{14}\text{POM}}{dt} &= -\frac{d^{14}\mathcal{J}(Z)}{dZ} - f_{sed}(^{14}\text{POM}) \\ &\quad - d_{\text{POM}} {}^{14}\text{POM} - r_{\text{POM}} {}^{14}\text{POM} - \lambda {}^{14}\text{POM}, \end{aligned} \quad (4.22)$$

$$\begin{aligned} \frac{\partial^{14}\text{DOM}}{\partial t} + \mathcal{H}(^{14}\text{DOM}) &= f_{riv}(^{14}\text{DOM}) \\ &\quad + d_{\text{POM}} {}^{14}\text{POM} - r_{\text{DOM}} {}^{14}\text{DOM} - \lambda {}^{14}\text{DOM}, \end{aligned} \quad (4.23)$$

and the expression for $^{14}q_v$ to be used in Eq. (4.5) reads

$$\begin{aligned} q_v(^{14}\text{C}_T) &= \text{S}_{\text{C}:P} \left(-(^{13}\alpha_\phi)^2 {}^{14}\text{R}_{\text{C}_T \mu} B + r_{\text{POM}} {}^{14}\text{POM} + r_{\text{DOM}} {}^{14}\text{DOM} \right) \\ &\quad + f_{riv}(^{14}\text{C}_T) - {}^{14}\text{R}_{\text{C}_T \text{S}_{\text{CaCO}_3:P}} \mu B + {}^{14}\text{R}_{\text{CaCO}_3} \mathcal{D}_{\text{CaCO}_3}. \end{aligned} \quad (4.24)$$

Note that this last expression does not involve any radioactive decay term since that process is already considered in Eq. (4.5).

4.2.2 Sensitivity to fractionation during photosynthesis

Several studies point toward a strong dependency upon water chemistry of the fractionation factor during plankton growth (*Hinga et al.*, 1994; *Jasper et al.*, 1994; *Rau et al.*, 1997). We implemented in LOCH the formulation of *Jasper et al.* (1994) who propose that fractionation during soft tissue formation is inversely related to dissolved CO_2 concentrations. With this formulation the fractionation factor during photosynthesis is given by

$$^{13}\alpha_\phi = (1 + \epsilon_p/10^3). \quad (4.25)$$

Here ϵ_p is expressed in permil and related to the dissolved CO_2 concentration through the empirical relationship

$$\epsilon_p = 27 - 130/\text{CO}_2$$

where CO_2 has units μM ($\mu\text{mol}/\text{kg}$).

The impact of this new formulation for the biological fractionation is evaluated with the help of two experiments which only differ by the representation of ^{13}C fractionation during biological assimilation: the fractionation factor is constant in experiment F-CST while in experiment F-CO2 it is set according to Eq. (4.25). These experiments were carried out with LOVECLIM and correspond to long-duration simulations constrained with pre-industrial state forcings (climate parameters and atmospheric concentrations).

The global average of the fractionation factor in F-CO₂ is 0.9758 (this factor is constant in F-CST and set to 0.9780⁴). On average, the upper ocean (0 to 100m) $\delta^{13}\text{C}$ is 2.02 ‰ in F-CO₂ and 2.03 ‰ in F-CST. The model runs differ most when comparing the global mean ocean $\delta^{13}\text{C}$: the ocean is more depleted with respect to ¹³C in F-CO₂ (0.37 ‰) than in F-CST (0.43 ‰). These global values for the surface and deep ocean are within the range of field estimates for pre-industrial times (*Broecker and Maier-Reimer, 1992; Hoefs, 1997*).

The largest changes occur in the Southern Ocean and at intermediate depths in the equatorial Pacific Ocean (Figure 4.12). The lower $\delta^{13}\text{C}$ values at depth in the Southern Ocean in experiment F-CO₂ can be explained by the stronger discrimination of ¹³C during phytoplankton soft tissue building in deep ocean ventilation areas since such regions are characterized by low temperatures, hence relatively large dissolved CO₂ concentrations. The organic matter sinking to depth hence incorporates less ¹³C in model run F-CO₂ than in F-CST. In turn this explains the larger values obtained at the surface close to 50°S in F-CO₂. The same principle may be applied to the equatorial Pacific where the intense upwelling of carbon rich water maintains high CO₂ levels at the surface. However surface water here are less enriched with respect to experiment F-CST since the water brought to the surface is comparatively more depleted.

Such differences of the order of 0.1 ‰ are significant: $\delta^{13}\text{C}$ changes between the last glacial maximum and the Holocene are also of the order of a few tens of permil only (*Duplessy, 1986; Smith et al., 1999*).

⁴The same constant factor was used for the radiocarbon experiments presented in Section 4.1.

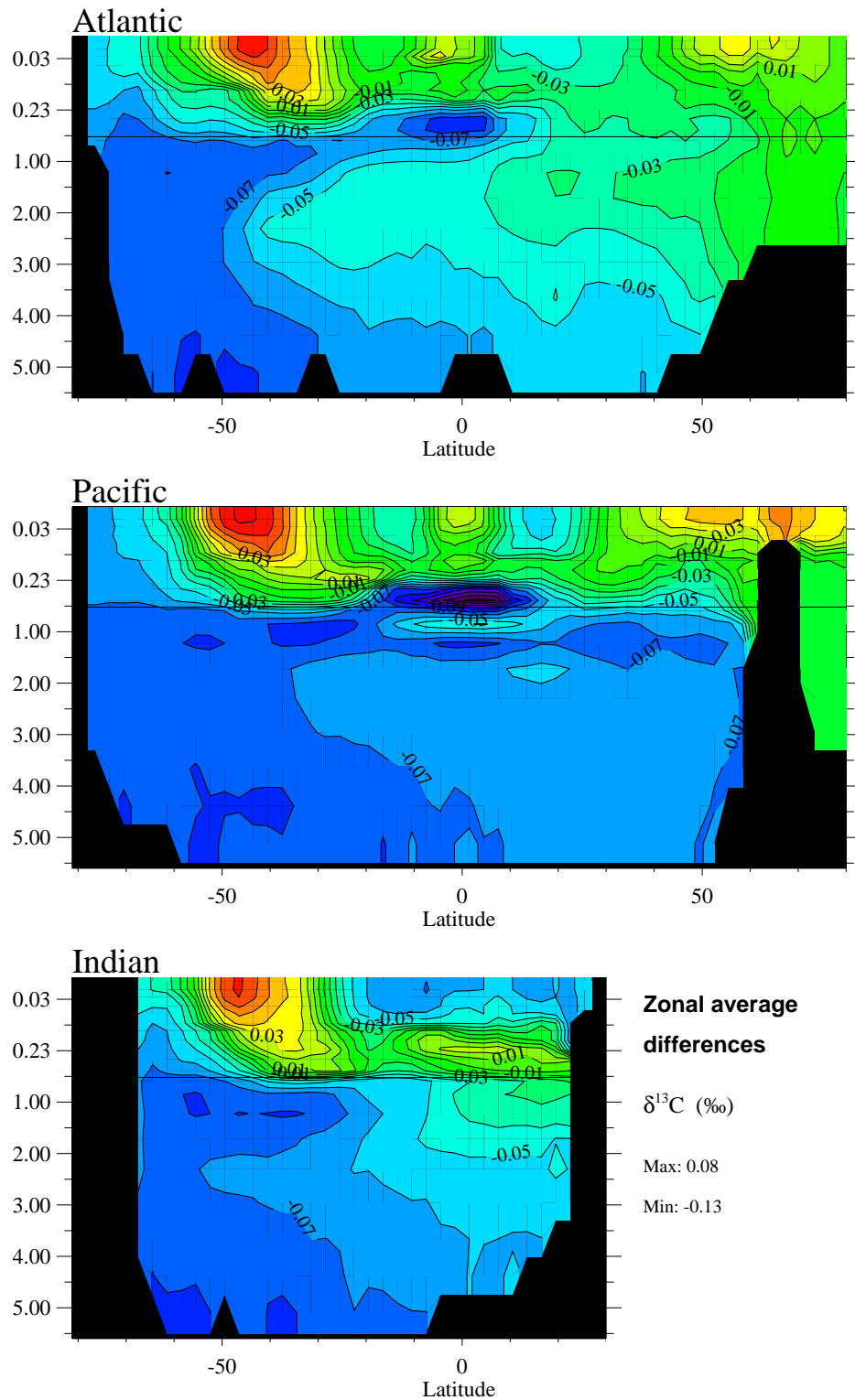


Figure 4.12: Differences in ocean dissolved inorganic carbon $\delta^{13}\text{C}$ between run F-CO₂ and F-CST. Positive (negative) values indicate ^{13}C enrichment (depletion) in run F-CO₂ with respect to run F-CST. The vertical axis represents depth in km. Please note the scale switching from non-linear (above 500m) to linear (deeper than 500 m).

Chapter 5

Conclusions

“-Alors, voyez-vous...
l’océan...
vous êtes là,
à vous promener
à regarder...
à le guetter,
du rivage, bien sûr,
et lui
pendant ce temps
lui, il vous prend
vos pensées de pierre
celles qui étaient route
et certitude...”

A. Baricco

In this work we addressed the ocean uptake of CO₂ in two different ways. First, we examined several aspects of the ocean ventilation as obtained from three-dimensional models. The motivation for such studies was that the rate at which the anthropogenic perturbation in the atmosphere will subside is actually controlled by the large-scale ocean circulation. The assessment of this circulation and its future evolution can only be performed with 3-D OGCMs.

Second, we developed an ocean carbon cycle model (LOCH) which we coupled to the Earth system model of intermediate complexity LOVECLIM. This tool is intensively used to study the interactions between past climate changes and the carbon cycle (*Menviel et al.*, 2008a, 2010; *Okazaki et al.*, 2010).

The ocean bomb radiocarbon inventory is then examined with a series of numerical experiments which differ in their formulation of air-sea ¹⁴C fluxes.

In Chapter 2 we discussed the excellent agreement between the domain-averaged ages and the age volume distribution as obtained with OGCMs and reproduced by an idealized tool, the leaky funnel. It was further shown that the leaky funnel

allows to extract relevant information on spatial and temporal scales characterizing ocean ventilation as reproduced in OGCMs. We succeeded in evaluating the advection and diffusion time scales in two different OGCMs. It has also been possible to estimate the fraction attributable to the numerical diffusion. The associated Peclet numbers are rather low (2.4 and 3.3). A third study based on another simplified tool also suggests that the transport in these OGCMs is dominated by diffusion and that in one of them numerical diffusion is dominant. This analysis reinforces the conclusions of other studies (*Kuhlbrodt et al.*, 2007; *Schmittner et al.*, 2009). This point is of great importance. Indeed, one of the reasons invoked by *Archer et al.* (2000) to explain the failure in reproducing the glacial/interglacial $p\text{CO}_2$ change is that the models used for simulating the carbon cycle are much more diffusive than the real ocean. *Schmittner et al.* (2009) explain the large range of sensitivities among climate models by the range in vertical mixing in the ocean within these models.

Several studies (*Sweeney et al.*, 2007; *Müller et al.*, 2008) call for a downward revision of gas exchange velocities to resolve the large discrepancies between data-based estimates and model reconstructions of the bomb radiocarbon inventory in the ocean (Chapter 4). We showed that a significant part of these discrepancies can be explained by the method that the data-based reconstructions are based upon, mainly the assumption that the air-sea CO_2 disequilibrium remained constant with time. Our conclusion that data-based inventories are probably underestimated is in agreement with the results of *Naegler* (2009) who adopted another method of investigation. Excessive vertical mixing or a too high gas exchange velocity may explain the remainder of the discrepancy. However, this problem might be difficult to solve. Indeed, the processes involved in the ocean uptake of bomb radiocarbon (atmospheric CO_2 , wind exchange, mixing, and global overturning) are characterized by widely different time scales. Available field estimates provide information on the early stages of the uptake only (approx. 30 years). This is possibly too short a duration to allow for a clear discrimination among the processes.

LOCH, the ocean carbon cycle model appears to perform well when coupled to a climate model of intermediate complexity, despite its simplified formulations of the carbon-related biogeochemical cycles (Chapter 3). The advantages of LOCH are twofold. First, its simplicity allows to perform numerous experiments over long time spans. Second, essential processes, such as the carbonate compensation mechanism, or the consideration of different food webs have been retained in its formulation. LOCH is therefore a useful tool to address the climate-carbon cycle feedbacks either in the past or the future. We also analyzed the sensitivity of LOCH to different formulations of biologically-mediated fluxes. These tests emphasize the difficulty in assessing the ocean carbon model due to several shortcomings in the circulation fields.

OGCMs are usually validated against physical properties, such as the distri-

butions of ^{14}C and CFCs. Similarly to radiocarbon, CFCs allow to assess the transient response in the model. Biogeochemical tracers are characterized by many different time and length scales. A large amount of ocean data is now available, allowing state-of-the-art validation of the circulation–biogeochemical cycles model. Hence these tracers offer a unique opportunity for the identification of shortcomings in the circulation model and for their improvement (*Najjar et al.*, 2007).

We would also call for a generalized practice of assessing circulation with water age. This tracer offers an unambiguous and objective diagnostic of the model ventilation characteristics. This diagnostic is not hampered by boundary conditions in contrast to that based upon $\Delta^{14}\text{C}$. Finally the age volume distribution function proves useful in obtaining the OGCM ventilation characteristics.

Many questions about biogeochemical cycles still remain open. For the purpose of addressing the response of atmospheric CO_2 on very long time scales (several thousand to tens of thousand years and longer) we need to consider additional natural processes. This is why LOCH has been coupled to a sediment model describing the early diagenesis of biogenic matter (*Munhoven*, 2007). The biological module of LOCH has furthermore been improved by including the nitrogen cycle and a better representation of the silica cycle, while still retaining its efficiency. This will allow us to address biogeochemical cycles in a larger range of natural environments (e.g., semi-enclosed seas). Both these new developments are currently being tested.

Appendix A

Model descriptions

A.1 Main features of the OGCMs used in this study

The transport model is driven by three-dimensional fields of velocity components, potential temperature, salinity, and convective mixing from two OGCMs in their annually averaged versions. The numerical scheme of the off-line transport model is adapted according to the OGCM fields driving it so that the physics determining the distribution of tracers is as close as possible to that determining the distribution of active variables in the dynamical model. Both these models belong to the coarse-grid OGCM class as none of them is eddy-resolving. They nevertheless capture the essential of deep ocean circulation. A short description of both OGCMs follows.

A.1.1 UL-OM

Louvain-la-Neuve OGCM (*Deleersnijder and Campin, 1995; Campin and Goosse, 1999*).

UL-OM is a primitive-equation, free-surface OGCM resting on the usual set of assumptions, i.e., the hydrostatic equilibrium and the Boussinesq approximation. The horizontal resolution is $3^\circ \times 3^\circ$. The so-called “z-coordinate” underlies a vertical discretization with 15 levels ranging in thickness from 20 m at the surface to 700 m in the deep ocean. A realistic bathymetry is used. The parameterization of vertical mixing is based on the *Pacanowski and Philander (1981)* formulation. Wherever the vertical density profile is unstable, the vertical diffusivity (*Marotzke, 1991*) is increased to $10 \text{ m}^2 \text{ s}^{-1}$. The parameterization of dense water flow down topographic features of *Campin and Goosse (1999)* is applied in the model. The experimental set up for the OGCM circulation corresponds to the control run described in *Campin et al. (1999)*. This OGCM was assessed against

the global distributions of temperatures, salinities as well as the estimated values of water transport in different locations (North Atlantic, Drake passage...). The circulation of this OGCM reasonably reproduces the pre-bomb $\Delta^{14}\text{C}$ distribution in the deep ocean (*Mouchet and Deleersnijder, 2008*). Two versions of the transport within LOCH with UL-OM were designed for the aim of the present study. One is more diffusive (version L0) than the other (LC). The former has the advantage of not creating spurious oscillations in the computed solution; such oscillations are particularly unwelcome when dealing with isotopic ratios with active biology. Differences among these two versions are illustrated in Chapter 2, Section 2.2.3.

A.1.2 LSG-OM

Large-Scale Geostrophic Ocean General Circulation Model (*Maier-Reimer et al., 1993; Mikolajewicz et al., 1993*).

The Hamburg large-scale geostrophic model (LSG) has been used in a number of climate and ocean tracer studies (e.g., *Mikolajewicz et al., 1997; Winguth et al., 1999; Heinze et al., 2003; Dutay et al., 2004*). It is based on the conservation laws for heat, salt, and momentum, the full equations of state, the hydrostatic approximation and the Boussinesq approximation. The circulation is divided into a barotropic and a baroclinic components, allowing for free surface elevation changes. It also includes a simple sea ice model to account for brine release during freezing. The formulation of the model is fully implicit. It has a horizontal resolution of $3.5^\circ \times 3.5^\circ$ on a E-grid (*Arakawa and Lamb, 1977*). The water column is subdivided into 11 layers. This model has a smoothed realistic topography. Advection of tracers is solved with the help of an upstream scheme both horizontally and vertically. A horizontal diffusion term ($200 \text{ m}^2 \text{ s}^{-1}$) suppresses mode divergence resulting from the use of a staggered E-grid. Our off-line transport model formulation is very close to that of *Heinze et al. (2003)*. The only difference lies in the treatment of open-ocean convection process, which in our model version takes the form of an explicit diffusion term. As in *Heinze and Dittert (2005)* the annually averaged fields needed to drive the model represent the pre-industrial ocean state and are obtained from a LSG run resolving the seasonal cycle (*Winguth et al., 1999*).

A.2 LOVECLIM

Pages 155 to 185 include the paper by *Goosse et al. (2010)* describing the Earth system model of intermediate complexity LOVECLIM.

Description of the Earth system model of intermediate complexity LOVECLIM version 1.2

H. Goosse¹, V. Brovkin², T. Fichefet¹, R. Haarsma³, P. Huybrechts⁴, J. Jongma⁵, A. Mouchet⁶, F. Selten³, P.-Y. Barriat¹, J.-M. Campin⁷, E. Deleersnijder^{8,1}, E. Driesschaert⁹, H. Goelzer⁴, I. Janssens⁴, M.-F. Loutre¹, M. A. Morales Maqueda¹⁰, T. Opsteegh³, P.-P. Mathieu¹, G. Munhoven⁶, E. J. Pettersson¹, H. Renssen⁵, D. M. Roche^{5,11}, M. Schaeffer^{3,*}, B. Tartinville¹², A. Timmermann¹³, and S. L. Weber³

¹Université Catholique de Louvain, Earth and Life Institute, Georges Lemaître Centre for Earth and Climate Research, Chemin du Cyclotron, 2, 1348 Louvain-la-Neuve, Belgium

²Max Planck Institute for Meteorology, Hamburg, Germany

³Royal Netherlands Meteorological Institute (KNMI), De Bilt, The Netherlands

⁴Earth System Sciences & Departement Geografie, Vrije Universiteit Brussel, Brussel, Belgium

⁵Section Climate Change and Landscape Dynamics, Dept. of Earth Sciences, Vrije Universiteit Amsterdam, The Netherlands

⁶Laboratoire de Physique Atmosphérique et Planétaire, Université de Liège, Liège, Belgium

⁷Massachusetts Institute of Technology, Cambridge, USA

⁸Université Catholique de Louvain, Institute of Mechanics, Materials and Civil Engineering, Louvain-la-Neuve, Belgium

⁹International Polar Foundation, Brussels, Belgium

¹⁰Proudman Oceanographic Laboratory, Liverpool, UK

¹¹Laboratoire des Sciences du Climat et de l'Environnement, LSCE/IPSL, Laboratoire CEA/INSU-CNRS/UVSQ, CE Saclay, l'Orme des Merisiers, Gif-sur-Yvette Cedex, France

¹²Numeca International, Brussels, Belgium

¹³International Pacific Research Center, SOEST, University of Hawai'i, Honolulu, USA

* currently at: Climate Analytics, Potsdam, Germany

Received: 12 March 2010 – Published in Geosci. Model Dev. Discuss.: 30 March 2010

Revised: 5 October 2010 – Accepted: 8 October 2010 – Published: 2 November 2010

Abstract. The main characteristics of the new version 1.2 of the three-dimensional Earth system model of intermediate complexity LOVECLIM are briefly described. LOVECLIM 1.2 includes representations of the atmosphere, the ocean and sea ice, the land surface (including vegetation), the ice sheets, the icebergs and the carbon cycle. The atmospheric component is ECBilt2, a T21, 3-level quasi-geostrophic model. The ocean component is CLIO3, which consists of an ocean general circulation model coupled to a comprehensive thermodynamic-dynamic sea-ice model. Its horizontal resolution is of 3° by 3°, and there are 20 levels in the ocean. ECBilt-CLIO is coupled to VECODE, a vegetation model that simulates the dynamics of two main terrestrial plant functional types, trees and grasses, as well as desert. VECODE also simulates the evolution of the carbon cycle over land while the ocean carbon cycle is represented by LOCH, a comprehensive model that takes into ac-

count both the solubility and biological pumps. The ice sheet component AGISM is made up of a three-dimensional thermomechanical model of the ice sheet flow, a visco-elastic bedrock model and a model of the mass balance at the ice-atmosphere and ice-ocean interfaces. For both the Greenland and Antarctic ice sheets, calculations are made on a 10 km by 10 km resolution grid with 31 sigma levels. LOVECLIM1.2 reproduces well the major characteristics of the observed climate both for present-day conditions and for key past periods such as the last millennium, the mid-Holocene and the Last Glacial Maximum. However, despite some improvements compared to earlier versions, some biases are still present in the model. The most serious ones are mainly located at low latitudes with an overestimation of the temperature there, a too symmetric distribution of precipitation between the two hemispheres, and an overestimation of precipitation and vegetation cover in the subtropics. In addition, the atmospheric circulation is too weak. The model also tends to underestimate the surface temperature changes (mainly at low latitudes) and to overestimate the ocean heat uptake observed over the last decades.



Correspondence to: H. Goosse
(hugues.goosse@uclouvain.be)

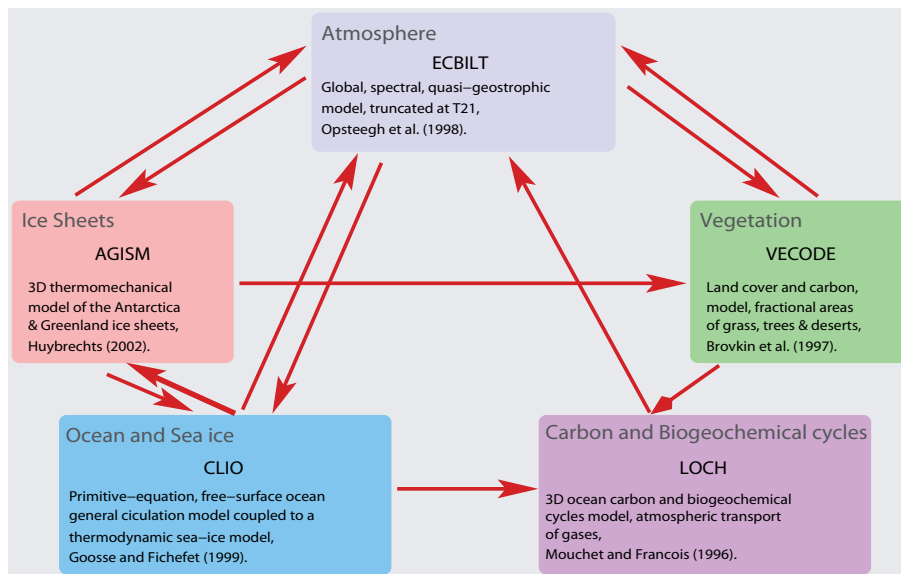


Fig. 1. Sketch of the LOVECLIM model showing the interactions between the five components.

1 Introduction

LOVECLIM (Fig. 1) is a three-dimensional Earth system model of intermediate complexity (EMIC, Claussen et al., 2002), i.e. its spatial resolution is coarser than that of state-of-the-art climate General Circulation Models (GCMs) and its representation of physical processes is simpler. In LOVECLIM, the most important simplifications are applied in the atmospheric component because it is usually the most demanding one in terms of computing time in GCMs. Thanks to those modelling choices, LOVECLIM is much faster than GCMs. On one single Xeon processor (2.5 GHz), it is possible to run 100 years, with all the components activated, in about 4 h of CPU time. This is a key advantage as it is affordable to perform large ensembles of simulations (as required to test the influence of parameter choices or to analyse natural variability of the system) and the long simulations needed to study past climates and long-term future climate changes. Compared to some other EMICs, LOVECLIM includes a 3-D representation of the system, facilitating the description of some physical processes such as the formation and development of weather systems as well as the comparison with data coming from different regions.

The first two components of LOVECLIM, which were coupled at the end of the 1990's, are the atmospheric model ECBilt (Opsteegh et al., 1998) and the sea-ice-ocean model CLIO (Goosse and Fichefet, 1999), forming what has been later referred to as ECBilt-CLIO2 (e.g., Goosse et al., 2001, 2002). Those two components are still presently the core of LOVECLIM, but with significant improvements compared to the original versions. In particular, the radiative scheme and the parameterization of the surface fluxes in ECBilt have been completely revised (e.g., Schaeffer

et al., 1998, 2004, see <http://www.knmi.nl/onderzk/CKO/differences.html>). Initially, in ECBilt-CLIO2, ECBilt and CLIO were interacting through the OASIS software (Terray et al., 1998). This has been modified in later versions where new Fortran routines, specifically developed for the model, take care of the exchanges between all the model components.

ECBilt-CLIO was further coupled to the terrestrial biosphere model VECODE (Brovkin et al., 2002), leading to ECBilt-CLIO-VECODE (e.g., Renssen et al., 2003, 2005). More recently, two additional components were added (Driesschaert et al., 2007): the ocean carbon cycle model LOCH (Mouchet and François, 1996) and the ice sheet model AGISM (Huybrechts, 2002). As the list of acronyms ECBilt-CLIO-VECODE-LOCH-AGISM was becoming too long, it has been decided to form a new acronym, based on the names of all model components: LOVECLIM which stands for LOCh-VeCode-EcBilt-CLio-agIsM. For simplicity, the new name LOVECLIM should be used even if only some components of the model are activated in a particular study.

ECBilt-CLIO and LOVECLIM 1.0 have been publicly released on the KNMI (Koninklijk Nederlands Meteorologisch Instituut) webiste (<http://www.knmi.nl/onderzk/CKO/ecbilt.html>) and UCL (Université catholique de Louvain) website (<http://www.climate.be/modx/index.php?id=81>), respectively. However, the public version of LOVECLIM does not include LOCH and AGISM, as the main developers of those two components wish that potential users contact them first to organize a collaboration before obtaining the permission to activate those parts of the code.

In contrast to LOVECLIM 1.0, version 1.1 of LOVECLIM (Goosse et al., 2007) has not been publicly released. However, the new LOVECLIM1.2, which is publicly

available since December 2009 (<http://www.astr.ucl.ac.be/index.php?page=LOVECLIM%40Description>), is very similar to LOVECLIM 1.1 regarding the physics of the model. Some minor modifications were included and some small bugs, which had limited impacts on model results, have been corrected (<http://www.astr.ucl.ac.be/index.php?page=LOVECLIM@bugs>). In addition, some technical updates have been performed before the official release. In particular, a standard set up for simulating the Last Glacial Maximum (LGM) climate is now available (Roche et al., 2007).

Up to now, more than 100 papers have been published with the various versions of ECBilt-CLIO, ECBilt-CLIO-VECODE and LOVECLIM (<http://www.knmi.nl/onderzk/CKO/ecbilt-papers.html>, <http://www.astr.ucl.ac.be/index.php?page=LOVECLIM%40papers>). They were mainly devoted to idealised process studies (e.g., Timmermann and Goosse, 2004; Timmermann et al., 2005; de Vries and Weber, 2005; van der Schrier et al., 2007; Lorenzo et al., 2008), the LGM climate (e.g., Timmermann et al., 2004; Roche et al., 2007; Flückiger et al., 2008; Menviel, 2008; Menviel et al., 2008), the last deglaciation (e.g. Timm et al., 2009), the Holocene climate (e.g., Renssen et al., 2001, 2003, 2005; Jiang et al., 2005), the previous interglacials (e.g., Duplessy et al., 2007; Yin et al., 2008), the last millennium (e.g., Goosse et al., 2005; van der Schrier and Barkmeijer, 2005), the present-day climate variability (e.g. Goosse et al., 2001, 2002), and future climate changes (e.g., Schaeffer et al., 2004; Driesschaert et al., 2007; Swingedouw et al., 2008).

However, no full description of the model is currently available. For each new version, only the new components and the major differences compared to previous versions were described. As a consequence, in order to determine exactly which processes are represented in a version of LOVECLIM, a new user or a scientist interested in model results has to follow the full history of the code over the last 10 years. He/she will thus likely miss some elements because they are too briefly mentioned or only available in internal reports. In addition, he/she will not know for sure if some physical parameterizations or model parts described in early papers are still valid for the latest versions.

We take here the opportunity of the release of LOVECLIM1.2 to describe in more detail the present state of the model. We will not discuss extensively all the model equations and parameterizations as this would correspond to hundreds of pages. Nevertheless, the main characteristics of the model will be described and a short evaluation of model results performed. We consider that it is sufficient, in the large majority of cases, for new users and to estimate if the model is an adequate tool for performing a particular analysis (as well as to estimate the associated limitations). Scientists interested in a specific point are referred to the cited papers, the present manuscript providing an up-to-date list of useful references and web addresses where the important internal reports can be obtained.

2 Model description

2.1 ECBilt: the atmospheric component

The atmospheric model, developed at KNMI, was first coupled to a simple ocean model (which used a flat bottom) and a thermodynamic sea-ice model (e.g., Haarsma et al., 1996; Opsteegh et al., 1998; Selten et al., 1999, Weber and Oerlemans, 2003). Those ocean and sea-ice components have been removed and replaced by CLIO, keeping only the atmospheric part in ECBilt-CLIO and in LOVECLIM.

ECBilt has a dynamical core derived from the work of Marshall and Molteni (1993). It is governed by the equation for q , the quasi-geostrophic potential vorticity, written in isobaric coordinate (Holton et al., 2004; Opsteegh et al., 1998):

$$\begin{aligned} \frac{\partial q}{\partial t} + \mathbf{V}_\psi \cdot \nabla q + k_d \nabla^8 (q - f) + k_r \frac{\partial}{\partial p} \left(\frac{f_0^2}{\sigma} \frac{\partial \psi}{\partial p} \right) \\ = - \frac{f_0 R}{c_p} \frac{\partial}{\partial p} \left(\frac{Q}{\sigma p} \right) - F_\zeta - \frac{\partial}{\partial p} \left(\frac{f_0 F_T}{\sigma} \right) \end{aligned} \quad (1)$$

q is defined as

$$q = \nabla^2 \psi + f + f_0^2 \frac{\partial}{\partial p} \left(\sigma^{-1} \frac{\partial \psi}{\partial p} \right) \quad (2)$$

\mathbf{V}_ψ is the rotational component of the horizontal velocity, f is the Coriolis parameter, f_0 is f at 45° (north and south), k_d and k_r are diffusion and damping coefficients, R is the ideal gas constant, c_p is the specific heat for constant pressure, σ is the static stability parameter, α is the specific volume, Q is the diabatic heating, F_ζ contains the ageostrophic terms in the vorticity equation and F_T is the advection of the temperature by the ageostrophic wind. Equation (1) is written with ψ , the streamfunction, as an independent variable. ψ is thus the main variable in the dynamical core of ECBilt. ψ is related to ζ , the vertical component of the relative vorticity vector, by

$$\zeta = \nabla^2 \psi \quad (3)$$

Knowing ψ , it is then possible to compute the geopotential height ϕ , using the linear balance equation:

$$\nabla^2 \phi = \nabla (f_\nabla \psi) \quad (4)$$

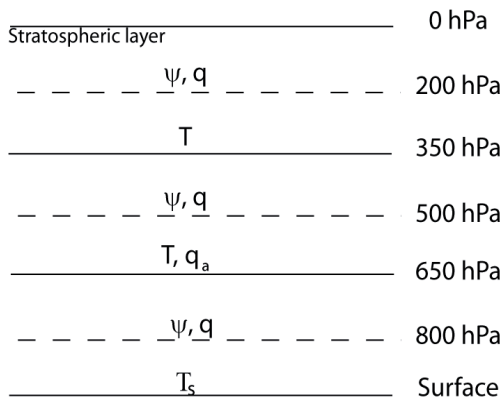
The temperature T is computed from ϕ using the hydrostatic equilibrium and the ideal gas law:

$$T = - \frac{p}{R} \frac{\partial \phi}{\partial p} \quad (5)$$

The ageostrophic terms F_ζ and F_T are included in Eq. (1) in order to improve the representation of the circulation at low latitudes, in particular the Hadley cells. These terms are obtained by computing the vertical velocity and the horizontal divergence diagnostically (Opsteegh et al., 1998).

Table 1. Major parameters of ECBilt.

Parameters	Term	Value	Unit
Scaling coefficient in the longwave radiative scheme	amplw	1	
Exponent in the longwave radiative scheme	explw	0.40	
Relative Rossby radii of deformation, applied in the Rayleigh damping term of the equation of the quasi-geostrophic potential vorticity in the 300–500 hPa layer	λ_2	0.131	
Relative Rossby radii of deformation, applied in the Rayleigh damping term of the equation of the quasi-geostrophic potential vorticity in the 500–800 hPa layer	λ_4	0.071	
Drag coefficient to compute wind stress	cwdrag	2.1×10^{-3}	
Drag coefficient to compute sensible and latent heat fluxes	cdrag	1.4×10^{-3}	
Reduction of the wind speed between 800 hPa and 10 m	uv10rfx	0.8	
Rotation of the wind vector in the boundary layer	dragan	15	°
Albedo of snow	alphd	0.72	
Albedo of bare ice	alphdi	0.62	
Albedo of melting snow	alphs	0.53	
Albedo of melting ice	albice	0.44	
Increase in snow/ice albedo for cloudy conditions	cgren	0.04	
Reduction of precipitation in the Atlantic	corA	0.085	
Reduction of precipitation in the Arctic	corAC	0.25	

**Fig. 2.** Vertical discretization of the atmospheric model ECBilt. Ψ is the streamfunction, q is the quasi-geostrophic potential vorticity, T is the air temperature, T_s is the surface temperature and q_a is the total water content.

Equation (1) is solved using spectral methods with a horizontal T21 truncation and three vertical levels at 800 hPa, 500 hPa and 200 hPa (Fig. 2). This corresponds in the physical space to a grid resolution of about 5.6° in latitude and in longitude. The radiative scheme and the thermodynamic exchanges between the layers and with the surface are computed in this physical space. Temperature is obtained at the surface and at the 650 hPa and the 350 hPa horizons. The model also contains a thermodynamic stratosphere.

The humidity in the atmosphere is represented in ECBilt by a single prognostic variable: the total precipitable water content between the surface and 500 hPa. This variable is transported horizontally using a fraction (60%) of the sum of geostrophic and ageostrophic winds at 800 hPa to take into account the fact that humidity is generally higher close to the surface where wind speeds are lower. Above 500 hPa, the atmosphere is assumed to be completely dry in the model. All the water that is transported by atmospheric flow above this 500 hPa level thus precipitates. Precipitation also occurs if the total precipitable water in the layer is above a relevant threshold (in the LOVECLIM1.2, this threshold is set equal to 0.83 times the vertically integrated saturation specific humidity below 500 hPa, assuming a constant relative humidity in the layer, see Table 1). The convection and associated precipitation are parameterized as in Held and Suarez (1978).

The longwave radiative scheme of ECBilt is based on a Green's function method (Chou and Neelin, 1996; Schaeffer et al., 1998). The following formula is applied for all the model levels:

$$\text{Flw} = \text{Fref} + \text{FG}(T', \text{GHG}') + G1 \cdot \text{amplw} \cdot (q_a')^{\text{explw}} \quad (6)$$

where Flw is the longwave flux, Fref is a reference value of the flux when temperature, humidity and the concentrations of greenhouse gases are equal to the reference values, FG is a function allowing one to compute the contribution associated with the anomalies compared to this reference in the vertical profile of temperature (T') and in the concentrations of the various greenhouse gases in the atmosphere

(GHG'). The last term represents the anomaly in the long-wave flux due to the anomaly in humidity q'_a (see Schaeffer et al., 1998 for an explicit discussion of those terms). The coefficients Fref, G1 and those included in the function FG are spatially dependent. *amplw* and *explw* are adjustable coefficients to take into account the uncertainties in the model, in particular those related to its crude representation of the changes in the vertical profiles of temperature and humidity. In LOVECLIM1.2, *explw* is equal to 0.40; *amplw* is equal to 1, except between 15° S and 15° N, where it is equal to 1.8. All the reference states are derived from a climatology based on the NCEP-NCAR reanalysis (Kalnay et al., 1996). Equation (6) is applied for both clear sky and overcast conditions. The total upward and downward longwave fluxes are then the weighted average of the two contributions as a function of the cloud cover, using prescribed clouds (ISCCP D2 dataset, see Rossow et al., 1996).

The downward and upward shortwave fluxes in ECBilt are computed at the 3 levels in the atmosphere, at the surface and at the top of the atmosphere using also a linearised scheme. The transmissivity of the atmosphere (as the cloud cover, see above) depends on the location and the season but is not computed prognostically. The surface albedo is a function of the fraction of the grid box covered by ocean, sea ice, trees, desert and grass (see Sects. 2.2, 2.3 and 2.7). The insolation at the top of the atmosphere is obtained using the orbital parameters computed following Berger (1978).

The surface fluxes of sensible and latent heat are computed from estimates of temperature, humidity and wind speed at 10 m and from the characteristics of the surface using standard bulk formulae. The wind speed at 10 m is supposed to be equal to 0.8 times the wind speed at 800 hPa. For the temperature and humidity, the extrapolation from the higher levels is based on anomalies compared to spatially dependent reference profiles derived from the NCEP-NCAR reanalysis (Kalnay et al., 1996), as in the longwave radiative scheme.

The land-surface model is part of the ECBilt code and has the same grid as the atmospheric model. The surface temperature and the development of the snow cover are computed by performing the heat budget over a single soil layer, which has a spatially homogenous heat capacity. For the moisture, a simple bucket model is used. The maximum water content of the bucket is a function of the vegetation cover. If, after evaporation, precipitation and snow melting, the water content is higher than this maximum, the water is transported immediately to an ocean grid point corresponding to the mouth of the river whose basin includes the model grid box.

More details about model equations, parameters and numerical schemes are available in two internal reports (Haarsma et al., 1996; Schaeffer et al., 1998, <http://www.astr.ucl.ac.be/index.php?page=CLIO%40Description>).

2.2 CLIO: the sea-ice and ocean component

The CLIO (Coupled Large-scale Ice Ocean) model (Goosse et al., 1997, 1999; Goosse and Fichefet, 1999; Tartinville et al., 2001) results from the coupling of a comprehensive sea-ice model (Fichefet and Morales Maqueda, 1997, 1999) and an ocean general circulation model (Deleersnijder and Campin, 1995; Deleersnijder et al., 1997, Campin and Goosse, 1999) both developed at the Institut d'Astronomie et de Géophysique G. Lemaître, Louvain-la-Neuve (ASTR) of the UCL.

The equations governing the ocean flows are deduced from the Navier-Stokes equations written in a rotating frame of reference with some classical approximations such as the Boussinesq approximation, the thin shell approximation, and the hydrostatic approximation. The effects of small-scale processes, not explicitly represented by the model, are included in the momentum equation using a simple harmonic operator along the horizontal. For the scalar quantities (in particular potential temperature and salinity), the model relies on both the isopycnal mixing formulation (Redi, 1982), using the approximation of small slopes (Cox, 1987), and the eddy-induced advection term, as proposed by Gent and McWilliams (1990) (see also Mathieu and Deleersnijder, 1999 and Table 2). The parameterization of vertical mixing (Goosse et al., 1999) is derived from Mellor and Yamada's level 2.5 model (Mellor and Yamada, 1982). The vertical viscosity and diffusivity are considered to be proportional to the characteristic velocity (q_t) and length (l) of the turbulent motions. The characteristic velocity q_t is computed through a prognostic differential equation for the turbulent kinetic energy, while l is derived from a simple diagnostic equation. While applied over the whole water column, this turbulence closure is mainly active in the surface layer. At depth, the vertical viscosity and diffusivity is generally equal to a background value which follows a profile similar to the one proposed by Bryan and Lewis (1979). In addition, a convective adjustment scheme is applied when the water column is statically unstable on a vertical depth range greater than 100 m. This is achieved by increasing the vertical diffusivity to $10 \text{ m}^2 \text{ s}^{-1}$.

In order to improve the representation of the dense water that flows out of the continental shelves and descends toward the bottom along the continental slope, CLIO includes Campin and Goosse's (1999) parameterization of downsloping currents. If the density of a grid box on the continental shelf (or on a sill) is higher than the density of the neighbouring box over the deep ocean at the same depth, shelf water flows along the slope until it reaches a depth of equal density. In order to verify volume conservation, this transport is compensated by a vertical and then horizontal return flow from the deep ocean to the shelf.

CLIO has a free surface. To avoid imposing for all the model equations the small time step needed to explicitly resolve fast external inertia-gravity waves, the split-explicit

Table 2. Major parameters of CLIO.

Parameters	Term	Value	Unit
Scaling factor in the computation of the Bering Strait throughflow	bering	0.3	
Coriolis term in the equation of motion computed in an implicit (=1) or semi-implicit way (=0.5) for the barotropic mode	txicfb	1.0	
Coriolis term in the equation of motion computed in an implicit (=1) or semi-implicit way (=0.5) for the baroclinic mode	txifcu	1.0	
Minimum vertical diffusivity for scalars	avkb	1.5×10^{-5}	$\text{m}^2 \text{s}^{-1}$
Minimum vertical viscosity	avnuv	1×10^{-4}	$\text{m}^2 \text{s}^{-1}$
Coefficient of isopycnal diffusion	ai	300	$\text{m}^2 \text{s}^{-1}$
Gent-McWilliams thickness diffusion coefficient	aitd	300	$\text{m}^2 \text{s}^{-1}$
Horizontal diffusivity for scalars	ahs	100	$\text{m}^2 \text{s}^{-1}$
Horizontal viscosity	ahu	10^5	$\text{m}^2 \text{s}^{-1}$
Conservation (1) or not (0) of the volume of the ocean, whatever the freshwater forcing applied	vcor	1	
First bulk-rheology parameter in sea-ice rheology	pstar	2.5×10^4	N m^{-2}
Second bulk-rheology parameter	c	20.0	
Creep limit used in sea-ice rheology	creepl	4.0×10^{-8}	s^{-1}
Minimum fraction of leads	acrit	10^{-6}	
Ice thickness for lateral accretion	hgcrit	0.3	m
Emissivity of the ice	emissi	0.96	
Drag coefficient for ocean stress	cw	4×10^{-3}	

method is applied (Gadd, 1978). The numerical integration is carried out in two stages: the depth-integrated part (or barotropic mode) and the depth-dependent one with a zero vertical mean (baroclinic mode). The low numerical-cost 2-D barotropic mode, which includes the surface gravity waves, is integrated with a small time step (5 min), while the more expensive 3-D baroclinic mode is solved using a much longer time step (3 h).

The various variables are staggered on a B-grid following the classification of Arakawa (Mesinger and Arakawa, 1976) (Fig. 3). The horizontal discretization is based on spherical coordinates, using a resolution of 3° in longitude by 3° in latitude and a realistic bathymetry (within the limits of the model resolution). Actually, two spherical subgrids (Deleersnijder et al., 1997) are associated to avoid the singularity at the North Pole (Fig. 4). The first one is based on classical longitude-latitude coordinates. It covers the Southern Ocean, the Pacific Ocean, the Indian Ocean and the South Atlantic. The second spherical subgrid has its poles located at the equator, the “north pole” in the Pacific (111°W) and the “south pole” in the Indian Ocean (69°E). The remaining parts of the ocean are represented on this “rotated” grid, i.e., the North Atlantic and the Arctic. The two subgrids are connected in the equatorial Atlantic where there is a correspondence between the meridians of the South Atlantic on one

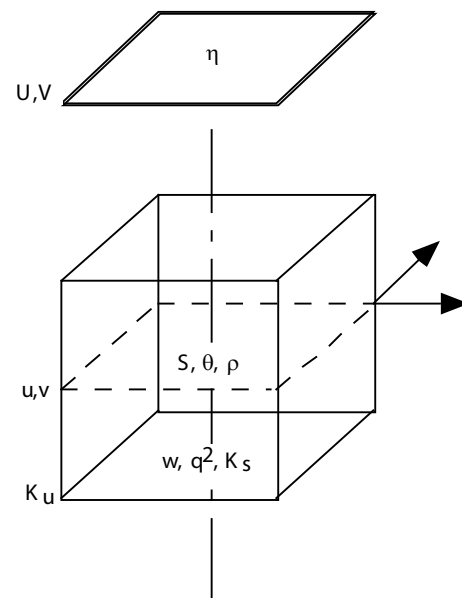


Fig. 3. Location of the various variables on the grid of CLIO. U , V are the two components of the barotropic velocity, η the surface elevation, u , v , and w the three components of the velocity, S the salinity, θ the potential temperature, q^2 (two times) the turbulent kinetic energy, and K_s and K_u the vertical diffusion and vertical viscosity.

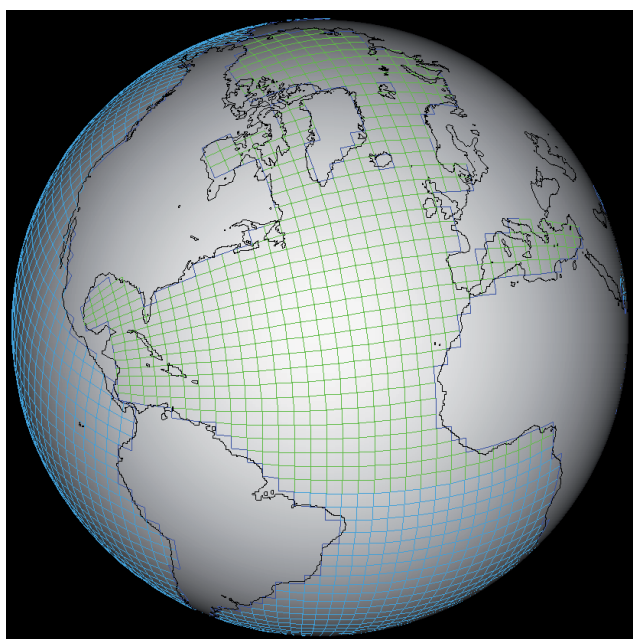


Fig. 4. The horizontal grid of CLIO at a resolution of 3° by 3° . The view is centred on the Atlantic. The two spherical subgrids in two different colors are connected in the Atlantic at the “geographical equator”.

grid and the parallels of the other grid in the North Atlantic. Because of the grid system, the direct connection between the Pacific and the Arctic through the Bering Strait is not explicitly computed, but the transport there is parameterized by a linear function of the cross-strait sea-level difference in accordance with the geostrophic control theory (Goosse et al., 1997). The vertical discretization follows the simple so-called “z-coordinate”, with 20 levels in the vertical in the standard version.

The sea-ice component of CLIO is an updated version of the sea-ice model of Fichfet and Morales Maqueda (1997, 1999). It uses the same horizontal grid as the ocean model. Sensible heat storage and vertical heat conduction within snow and ice are determined by a three-layer model (one layer for snow and two layers for ice). Each grid box is partly covered by sea ice of uniform thickness (i.e., the model includes only one sea-ice thickness category) and open water (leads). Vertical and lateral growth/decay rates of the ice are obtained from prognostic energy budgets at both the bottom and surface boundaries of the snow-ice cover and in leads. When the load of snow is large enough to depress the snow-ice interface under the water level, seawater infiltrates in the model the entirety of the snow layer below the ocean surface and freezes there. This snow and the frozen seawater form then a new layer (snow ice), implying in the model an increase in sea ice thickness (Fichfet and Morales Maqueda, 1997). The parameterization of the surface albedo is taken

from Shine and Henderson-Sellers (1985), with corrections for clear and overcast conditions as recommended by Greenfell and Perovich (1984). This albedo formulation takes into consideration the state of the surface (frozen or melting) and the thickness of the snow and ice covers.

For the momentum balance, sea ice is considered as a two-dimensional continuum in dynamical interaction with the atmosphere and the ocean. The viscous-plastic constitutive law proposed by Hibler (1979) is used for computing the internal ice force. The ice strength is taken as a function of the ice thickness and compactness (Hibler, 1979). The physical fields that are advected are the ice concentration, the snow volume per unit area, the ice volume per unit area, the snow enthalpy per unit area, the ice enthalpy per unit area, and the brine reservoir per unit area.

The model equations are solved numerically as an initial value-boundary value problem by using finite difference techniques. A staggered spatial grid of type B is utilized. The heat diffusion equation for snow and ice is solved by means of a fully implicit numerical scheme, which avoids the development of numerical instabilities when the snow or ice thickness becomes small. The ice momentum balance is treated basically as in Zhang and Hibler (1997). A no-slip condition is imposed on land boundaries. The contribution of advection to the continuity equations is determined by making use of the forward time marching scheme of Prather (1986). This method is based on the conservation of the second-order moments of the spatial distribution of the advected quantities within each grid cell. It preserves the positiveness of the transported variables and has very small numerical diffusion. The advantage of employing this elaborate scheme is that, for a coarse resolution grid such as the one used here, it determines the location of the ice edge with a higher accuracy than the more conventional upstream schemes do.

A standard quadratic law is applied for calculating the stress at the ice-ocean interface. The heat flux from the ocean to the ice is computed by the parameterization of McPhee (1992), while the salt and freshwater surface exchanges are based on mass conservation. As CLIO includes a free surface, the exchanges of freshwater are represented by a vertical velocity at surface equal to precipitation–evaporation+runoff. However, for relatively subtle reasons linked to the way the free surface is represented in the model, applying such a straightforward method is not possible at the ice-ocean interface (Tartinville et al., 2001). As a consequence, all the mass exchanges between the ocean and sea ice are implemented as negative and positive salt fluxes, the freshwater fluxes being then virtual salt fluxes that have the same dilution effect as the corresponding freshwater exchanges.

All the model equations, parameters, and numerical schemes are described in detail in the user’s guide of the CLIO model (<http://www.astr.ucl.ac.be/index.php?page=CLIO%40Description>).

2.3 VECODE: the continental biosphere component

The model for the terrestrial biosphere VECODE (VEgetation COntinuous DEscription model) (Brovkin et al., 2002; Cramer et al., 2001) was specifically designed with the purpose of interactive coupling with a coarse resolution atmospheric model for long-term simulations. It is a reduced-form dynamic global vegetation model (DGVM), which simulates changes in vegetation structure and terrestrial carbon pools on timescales ranging from decades to millennia.

VECODE consists of three sub-models: (1) a model of vegetation structure (bioclimatic classification) calculates plant functional type (PFT) fractions in equilibrium with climate; (2) a biogeochemical model estimates net primary productivity (NPP), allocation of NPP, and carbon pool dynamics; (3) a vegetation dynamics model. PFTs (see, e.g., Prentice et al., 1992; Chapin et al., 1996 for the PFT concept) are used to describe the vegetation cover. For any given climate, there is a unique stable composition of PFTs corresponding to the climate (in this context, climate is understood as a long-term average of atmospheric fields). If climate changes, the vegetation model simulates the transition from the equilibrium for the previous climate to a new equilibrium with the new climate. The time scale of this transition is determined from the carbon cycle model.

A fractional bioclimatic classification (Brovkin et al., 1997) is developed in order to adapt discrete bioclimatic classifications (e.g. Life Zones by Holdridge, 1947, or BIOME by Prentice et al., 1992) for coarse resolution climate models. Two basic PFTs are used: trees and grasses. The sum of the tree fraction, f , and the grass fraction, g , is equal to the vegetation fraction, v ; the rest corresponds to the desert fraction, $d = 1 - v$. These transient fractions are different from equilibrium fractions (vegetation in equilibrium with climate), denoted by \hat{f} , \hat{v} . Semi-empirical parameterizations are used for \hat{f} and \hat{v} :

$$\hat{f} = f_{\max} \frac{(1 - e^{c(G_0 - G_{\min})}) (P_r)^a}{(P_r)^a + a_{\text{for}} (G_0 - G_{\min})^2 e^{b(G_0 - G_{\min})}} \quad (7)$$

$$\hat{g} = \hat{v} - \hat{f}$$

$$\hat{v} = \begin{cases} 0 & P_r \leq P_r^{\min} \\ \min[1, \hat{V}_m] & P_r \geq P_r^{\min} \end{cases} \quad (8)$$

$$\hat{V}_m = 1 - \frac{1}{1 + a_{\text{des}} (P_r - P_r^{\min})^2 e^{b(G_0 - G_{\min})}}$$

$$P_r^{\min} = P_r^0 e^{b_2(G_0 - G_{\min})}$$

where G_0 is the growing degree-days above 0 (GDD0, i.e., the sum of the surface air temperature for all the days with a mean daily temperature higher than 0 °C), P_r is the annual mean precipitation, c , a , a_{for} , b , a_{des} , b_2 and P_r^0 are bio-

climatic parameters (Table 3), G_{\min} is the minimum GDD0 for trees, and P_r^{\min} is the minimum precipitation for vegetation.

Those equations are based on regularities of distribution of forest and desert in climatic space (Lieth, 1975) which have an ecophysiological basis (Woodward, 1987). The vegetation map of Olson et al. (1985) and an updated version (W. Cramer, personal communication, 1996) of the climate dataset of Leemans and Cramer (1991) were used in the validation procedure.

Carbon in the vegetation is aggregated into two compartments: a ‘fast’ pool of green biomass (leaves), C_{ϕ}^1 , and a ‘slow’ pool of structural biomass (stems, roots), C_{ϕ}^2 . Dead organic matter is described by two pools: a ‘fast’ compartment (woody residues), C_{ϕ}^3 , and a ‘slow’ compartment (humus), C_{ϕ}^4 . Variables C_{ϕ}^i are simulated separately for trees and grass (represented here by ϕ). The dynamics of the carbon pools are integrated with an annual time step. Net primary productivity (NPP), Π , is simulated on an annual basis following the semi-empirical parameterization of Lieth (1975), which is often used for first-guess estimates on a global scale (Post et al., 1997). To find out the NPP per model grid cell, the NPP per square meter is multiplied by the vegetation fraction v , which is in most cases equal to one, and the land area. In dry subtropical regions, v is less than 1 (Eq. 8), and this helps to correct the bias in the productivity per grid cell in these regions. Dependence of NPP on the atmospheric CO₂ concentration is taken into account by the biotic growth factor in a logarithmic form (den Elzen et al., 1995).

NPP allocation between green and structural biomass is estimated as a function of NPP, with increased allocation to C_{ϕ}^2 relative to C_{ϕ}^1 as NPP increases. This function was calibrated using an empirical dataset of NPP and carbon storage from about 500 sites in the northern Eurasia collected by Bazilevich (1993). The same data were used for calibrating parameterizations for the turnover time of biomass τ_{ϕ}^i , $i = \{1, 2\}$, which is assumed to be a function of NPP. The turnover time of soil carbon τ_{ϕ}^i , $i = \{3, 4\}$ is a function of the mean annual temperature following the approach by Schimel et al. (1994). The annual maximum of Leaf Area Index (LAI) is assumed to be proportional to the green biomass.

To account for the subgrid-scale processes of vegetation succession, we apply linear ordinary differential equations for simulating the dynamics of the PFT fractions. The model implies that the vegetation cover reacts to any climate change with a relaxation towards a new equilibrium with a timescale determined by the turnover time of the structural biomass. For instance, if the climate becomes more humid and the equilibrium fraction of trees increases, then the trees become more successful in competing with grasses and occupy an additional fraction of land within the large grid cell with the timescale of tree growth. In the vicinity of an equilibrium,

Table 3. Major parameters of VECODE.

Parameters	Term	Value	Unit
Maximum tree fraction	f_{\max}	0.95	
Minimum GDD0 for trees	G_{\min}	800	degree-days
Precipitation threshold for vegetation in warm areas	pre_{\min}	0.0005	m day^{-1}
Bioclimatic parameter related to minimum precipitation required for vegetation	P_r^0	28	mm yr^{-1}
Reference atmospheric CO_2 concentration	C_{atm}^0	280	ppmv
Maximum NPP for C_{atm}^0	Π_{\max}	1.4	$\text{kg C m}^{-2} \text{yr}^{-1}$
Factor of NPP dependence on atmospheric CO_2 concentration	β	0.25	
Albedo of trees	α_T	0.13	
Albedo of grass	α_G	0.20	
Albedo of desert	α_D	0.33	
Albedo of bright sand desert (Sahara)	α_{BD}	0.40	
Bucket depth for grass area	b_{moismg}	0.15	m
Bucket depth for forests	b_{moismf}	0.25	m
Bucket depth for deserts	b_{moismd}	0.10	m

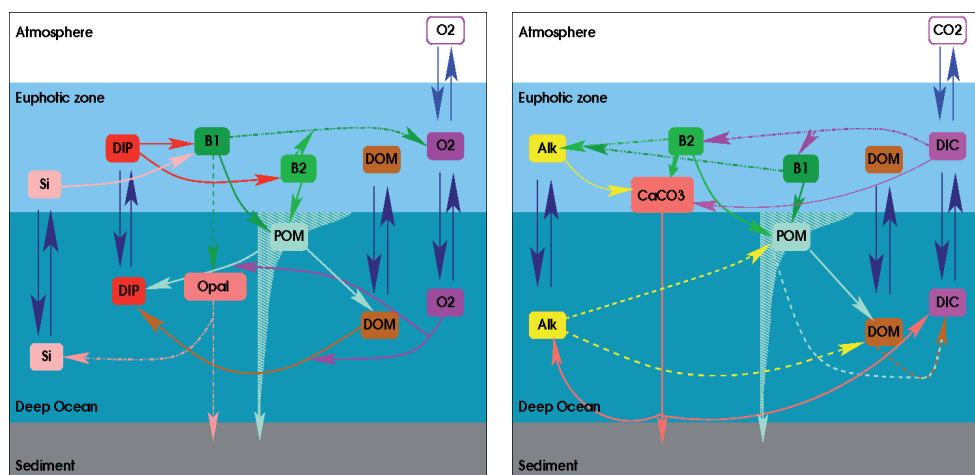


Fig. 5. Schematic representation of the main processes described in the LOCH model (Mouchet, 2010). The left panel focuses on purely biological processes, while the right panel shows the processes affecting the ocean carbon cycle. Up and down blue arrows represent transport processes (advection, diffusion, etc). Transported variables include dissolved inorganic carbon (DIC), alkalinity (Alk), dissolved inorganic phosphorus (DIP), dissolved organic matter (DOM), oxygen (O_2) and silica (Si). At the air-sea interface CO_2 and O_2 are exchanged with the atmosphere. B1 stands for opal building phytoplankton biomass and B2 represents the biomass of phytoplankton not relying on silica for growth (please note the inversion of B1 and B2 boxes between panels). POM decays at depth either as DOM or DIP. The flux of POM is governed following a power law function of the depth. Opal dissolves while sinking to the bottom. Calcareous shells (CaCO_3) reach the deepest layer where chemical conditions drive their dissolution or preservation. Fluxes to sediments, where permanent preservation prevails in this version, are also represented. Rivers (not illustrated) carry Si, DOM, DIC and Alk to the ocean.

the equation for the time development of vegetation is a linearized version of the evolutionary model for vegetation dynamics (Svirezhev, 1999) which accounts for competition between trees and grasses in the idealized form. With respect to the dynamics of the northern treeline under CO_2 -induced climate change, VECODE shows similar performance to other dynamic global vegetation models (Cramer et al., 2001).

2.4 LOCH: the ocean carbon cycle component

LOCH (**L**ière **O**cean **C**arbon **H**eteronomous model; Fig. 5; Mouchet and François, 1996; Mouchet, 2010) is a three-dimensional ocean carbon-cycle model developed at ULg-LPAP (Université de Liège, Laboratoire de Physique Atmosphérique et Planétaire). Its main variables are the dissolved inorganic carbon (DIC), total alkalinity (Alk), dissolved inorganic phosphorus (DIP), dissolved and particulate organic

matter (DOM and POM), silica (Si), oxygen (O₂) as well as organic and inorganic carbon isotopes. The concentration of dissolved CO₂ at the sea surface is controlled by both physical and biological processes (solubility and biological pumps, respectively).

Biology exerts a strong control on the surface CO₂ and is responsible for the fast transfer of carbon to the deep ocean. In a somewhat similar approach to that used in HAMOCC 3 (Maier-Reimer, 1993; Heinze et al., 2003), LOCH intends to reproduce export production (i.e. flux of organic carbon out of the surface ocean). The LOCH biological module should therefore not be viewed as a model of ocean ecosystems but rather as a model of biogenically mediated fluxes of constituents in the ocean. The basis for the export-production model is a pool of phytoplankton whose growth is driven by the availability of nutrients (DIP) and light. The evolution of phytoplankton biomass B follows:

$$\frac{dB}{dt} = \mu_B B - R_B B \quad (9)$$

where μ_B the actual growth rate is a function of temperature T , light L and inorganic phosphorus concentration (DIP):

$$\mu_B = \mu_{\text{Max}} \frac{L}{K_L + L} \frac{T}{K_T + T} \frac{\text{DIP}}{K_P + \text{DIP}} \quad (10)$$

where μ_{Max} is the maximum growth rate and K_L , K_T and K_P are half-saturation constants for temperature, light and inorganic phosphorus concentration, respectively (Table 4).

The sink term $R_B B$ takes into account grazing and mortality and is defined as:

$$R_B = G \frac{B}{K_B + B} + m_B \quad (11)$$

in which m_B and G represent the mortality and the maximum grazing rate, respectively. The use of a Michaelis-Menten-like formulation for grazing in Eq. (11) allows for a non-linear closure of the system, which is necessary in order to properly reproduce the productivity changes (Fasham, 1993).

Upon death, organisms feed the fast sinking particulate organic matter (POM) pool. The distribution of the POM flux with depth below the productive layers is governed by a power law $z^{-\alpha_{\text{POM}}}$ (Martin et al., 1987), with z the depth measured from the bottom of the euphotic zone. In LOCH, the actual vertical profile driving the distribution of the POM flux evolves according to the fraction of the total export production supported by silica shell building organisms; this is achieved by considering different values of α_{POM} for diatoms and other species.

Below the productive layers the POM remineralizes as DIP or transforms into dissolved organic matter (DOM). DOM subsequently decays into DIP. The remineralization rate of organic matter (POM or DOM) depends on the oxygen availability. Anoxic remineralization occurs in O₂-depleted re-

gions but in a less efficient way than oxic processes. The remineralization rate is given by:

$$R_x = r_x^o \frac{\text{O}_2}{K_{\text{O}_2} + \text{O}_2} + r_x^a \frac{K_{\text{O}_2}}{K_{\text{O}_2} + \text{O}_2} \quad (12)$$

where x either stands for POM or DOM. In Eq. (12), r_x^o and r_x^a represent the maximum oxic and anoxic remineralization rates, respectively.

It should be noticed that, although B and POM are prognostic variables, they are not subject to the 3-D transport. The rationale underlying this choice is that the characteristic timescale of these variables is much shorter than the one of interest in the context of climate studies.

The hard tissues (shells) are made up of CaCO₃ or opal, and their precipitation occurs concurrently with the soft-tissue formation. About half of the export production in the ocean is supported by diatoms (Nelson et al., 1995). Hence we discriminate between these organisms, which rely on silicon for their growth, and other species. A constant Si:P ratio is used to determine the export of opal accompanying the export production. The vertical distribution of biogenic silica below the productive layers upon the death of the organism writes $e^{-\beta z}$, where β takes into account the influence of temperature on the dissolution rate with $\beta = \beta_d e^{\kappa_d T}$.

Alkalinity and dissolved inorganic carbon are both needed to determine the concentration of dissolved CO₂ in surface waters as well as the CaCO₃ saturation level in deep waters. The total dissolved inorganic carbon (DIC) represents the sum of dissolved CO₂, bicarbonate and carbonate. Total alkalinity is a measure of the acid neutralizing capacity of seawater, as defined by Dickson (1981). However, in order to reduce the computing time, this definition is simplified by retaining only the essential contributions (bicarbonate, carbonate and borate). The error resulting from the neglect of phosphorus and silica contributions to Alk is far smaller than other uncertainties inherent to climate modelling. The constants required to determine the various chemical equilibria in seawater are expressed on the seawater pH scale. When needed, transformation from the free pH scale to the seawater pH scale is performed with the help of formulations from Millero (1995) and Dickson and Riley (1979). The system is fully determined by using dissociation constants for water from Millero (1995), for borate from Dickson (1990) and for carbonates from Dickson and Millero (1987).

This model, similarly to other simplified models of the ocean carbon cycle (e.g. Maier-Reimer, 1993; Najjar et al., 2007), assumes the stoichiometric constancy of organic material. It means that POM, DOM as well as biomass composition are in Redfield ratio. The sources and sinks terms for DIC and Alk are therefore simply derived from the biological fluxes with the help of the phosphorus to carbon Redfield ratio of Anderson and Sarmiento (1994) and the nitrogen to phosphorus ratio of Redfield et al. (1963).

Table 4. Major parameters of LOCH.

Parameters	Term	Value	Unit
Piston velocity coefficient	k_w	0.438	$(\text{cm h}^{-1})(\text{m s}^{-1})^2$
Redfield ratio	C:N:P:O ₂	117:16:1:-170	
Silica to phosphate ratio	Si:P	35:1	
Maximum phytoplankton growth rate	μ_{Max}	240	yr ⁻¹
Half-saturation constant for nutrient uptake	K_P	0.10×10^{-6}	molP kg ⁻¹
Maximum grazing rate	G	360	yr ⁻¹
Half-saturation constant for grazing	k_B	11.2×10^{-9}	molP l ⁻¹
Phytoplankton mortality rate	m_B	0	yr ⁻¹
Exponent of POM profile, diatoms	α_{diat}	0.858	
Exponent of POM profile, other species	α_{others}	0.858	
Dissolution rate of POM	d_{POM}	2	yr ⁻¹
POM oxic max. remineralization rate	r_{POM}^0	1	yr ⁻¹
DOM oxic max. remineralization rate	r_{DOM}^0	0.05	yr ⁻¹
POM anoxic max. remineralization rate	r_{POM}^a	0.9	yr ⁻¹
DOM anoxic max. remineralization rate	r_{DOM}^a	0.045	yr ⁻¹
Preserved fraction of POM	f_{POM}	0.02	
Half-saturation for O ₂ uptake	K_{O_2}	5×10^{-6}	mol O ₂ kg ⁻¹
Half-saturation for Si uptake	K_{SI}	1×10^{-6}	mol Si kg ⁻¹
Fraction of aragonite in CaCO ₃ shells	F_{Arag}	0.20	
Maximum rain ratio	$R_{\text{CaCO}_3}^{\text{Max}}$	0.25	
Minimum temperature for calcification	T_{CaCO_3}	2	°C
Preserved fraction of opal	f_{SiO_2}	0.11	
Sursaturation degree for CaCO ₃ dissolution	S_{CaCO_3}	150	%

One important factor for the carbon cycle is the rain ratio, which is the amount of organic carbon assimilated during photosynthesis divided by that of inorganic carbon incorporated into shells. The rain ratio R_{CaCO_3} in LOCH depends on the availability of silica, the latter determining which type of shells will be preferentially built. The influence of temperature and the ubiquity of calcareous organisms are also included in the parameterization of this process. R_{CaCO_3} is defined as:

$$R_{\text{CaCO}_3} = r_{\text{CaCO}_3} + \frac{T}{K_{\text{CaCO}_3} + T} (\Psi_{\text{Zoo}} + \Psi_{\text{Phy}}(1 - f_{\text{DIA}})) \quad (13)$$

with $R_{\text{CaCO}_3} \leq R_{\text{CaCO}_3}^{\text{Max}}$, the maximum rain ratio. Expression (13) includes the following parameters or variables: r_{CaCO_3} the minimum rain ratio, K_{CaCO_3} half-saturation constant for CaCO₃ precipitation (°C), Ψ_{Zoo} the rain ratio associated to zooplankton, Ψ_{Phy} the rain ratio associated to non siliceous phytoplankton, and f_{DIA} the fraction of siliceous phytoplankton, $f_{\text{DIA}} \in [0, 1]$. A constant fraction f_{CaCO_3} of calcium carbonate shells is also assumed to be made of aragonite, which is more soluble than calcite.

The dissolution of shells occurs in the deepest ocean layer under the production area at a rate controlled by the CaCO₃ saturation level. Hence LOCH implicitly includes carbonate compensation mechanisms. The expressions for the solubility of calcite and aragonite are from Mucci (1983) and Millero (1995), while the coefficients for the pressure dependence of the chemical equilibrium constants are from Millero (1995).

Some organic matter and shells escape remineralization or dissolution, and are permanently preserved in sediments. On the other hand, river input of alkalinity, silica, organic matter and carbon constitutes a net source for the ocean. In the case of an equilibrium run, this source exactly compensates the permanent preservation in sediments. The main rivers of the world and their respective importance are taken into account in this process.

The magnitude of the air-sea flux of a gas depends on the difference of its partial pressure between the two media, with an exchange rate given by the product of the solubility and the piston velocity. The solubilities are taken from Wanninkhof (1992) for O₂ and from Weiss (1974) for CO₂.

The piston velocity follows the empirical formulation proposed by Wanninkhof (1992), which relates it to the squared wind velocity and the Schmidt number. The latter is gas-dependent and is calculated according to Wanninkhof (1992). An additional term accounts for the chemical enhancement of CO₂ exchange at low wind speeds and high temperatures (Wanninkhof and Knox, 1996).

LOCH also includes an atmospheric module which simulates the evolution of the various gases in the atmosphere. It is based on a 1D diffusion equation in the meridional direction, i.e., one implicitly assumes instantaneous mixing in the zonal and vertical directions. Hence the transport in the atmosphere of a constituent with concentration C (ppmv) obeys to:

$$\frac{\partial C}{\partial t} = \frac{\partial}{\partial y} K_y \frac{\partial C}{\partial y} + F_C - P_C \quad (14)$$

where t is the time and y the position in the meridional direction. The diffusion coefficient K_y (m² s⁻¹) is homogeneous within each hemisphere and allows mixing within a few weeks. A lower value of K_y is used at the equator so that inter-hemispheric mixing occurs with a characteristic timescale of 2 years (Bacastow and Maier-Reimer, 1990).

P_C includes local sink terms where relevant, e.g., radioactive decay for ¹⁴C. F_C represents the exchange of gases between the atmosphere on the one hand and the ocean and the continental biosphere on the other hand. If applicable, F_C may also include other sources (e.g., anthropogenic emissions). The gases taken into account are carbon dioxide CO₂, oxygen O₂ as well as the two isotopic forms ¹³CO₂ and ¹⁴CO₂.

Equation (14) is discretized with a constant spatial step, at the same resolution as CLIO (3°), and with the same time step as LOCH. The atmospheric module offers two options for the study of the carbon cycle: either the concentrations are prescribed in the atmosphere (diagnostic mode) or the concentrations evolve according to the various exchange processes as described above (prognostic mode).

2.5 AGISM: the polar ice sheet component

AGISM (Antarctic and Greenland Ice Sheet Model; Fig. 6) consists of two three-dimensional thermomechanical ice dynamic models for each of the polar ice sheets. Both models are based on the same physics and formulations, however with the major distinction that the Antarctic component incorporates a coupled ice shelf and grounding line dynamics. Ice shelf dynamics is missing from the Greenland component as there is hardly any floating ice under present-day conditions, and this can be expected to disappear quickly under warmer conditions. Having a melt margin on land or a calving margin close to its coast for most of its glacial history, ice shelves probably played a minor role for Greenland also during colder conditions.

Both polar ice sheet models consist of three main components which respectively describe the ice flow, the solid Earth response and the mass balance at the ice-atmosphere and ice-ocean interfaces (Huybrechts and de Wolde, 1999; Huybrechts, 2002; to which papers the interested reader is referred to for a full overview of all equations and model formulations as well as for additional references). Figure 6 shows the structure of the model. At the heart of these models is the simultaneous solution of two evolutionary equations for ice thickness and temperature, together with diagnostic representations of the ice velocity components. Conservation of ice volume and heat is expressed as:

$$\frac{\partial H}{\partial t} = -\nabla \cdot (\bar{\mathbf{v}}H) + M \quad (15)$$

$$\frac{\partial T_i}{\partial t} = \frac{1}{\rho_i} \frac{\partial}{\partial z} \left(\frac{k_i}{c_i} \frac{\partial T_i}{\partial z} \right) - \mathbf{V} \cdot \nabla T_i + \frac{\phi}{\rho_i c_i} \quad (16)$$

$$\frac{\partial T_m}{\partial t} = \frac{k_m}{\rho_m c_m} \frac{\partial^2 T_m}{\partial z^2} \quad (17)$$

where H is the ice thickness, $\bar{\mathbf{v}}$ the depth-averaged horizontal velocity field, M the mass balance and t the time. The thermodynamic equation considers heat transfer to result from vertical diffusion, 3-D advection, and internal frictional heating caused by ice deformation (ϕ). The inclusion of heat conduction in the bedrock gives rise to a variable geothermal heat flux at the ice sheet base depending on the thermal history of the ice and rock. T_i and T_m are ice and rock temperatures, respectively, and k , c , and ρ are thermal conductivity, specific heat capacity and density for respectively ice and rock (subscripts “i” and “m”). The thermal parameters of ice, k_i and c_i , also take into account the temperature dependence, which effect is not negligible as their values may change by up to 30% for ice temperatures ranging between 0 °C and –50 °C (Huybrechts, 1992). Main parameter values are given in Table 5.

In grounded ice, the flow results from both internal deformation and sliding over the bed in places where the temperature reaches the pressure melting point and a lubricating water layer is present. Ice deformation in the ice sheet domain results from vertical shearing, most of which occurring near to the base. Longitudinal deviatoric stresses (i.e., the difference between the total stress and the hydrostatic stress – actually “cryostatic” in this case) are disregarded according to the widely used “Shallow Ice Approximation” (e.g., Hutter, 1983). This does not treat the rapid component of the otherwise badly understood physics specific to fast-flowing outlet glaciers or ice streams. A flow law of “Glen type” is used with exponent $n = 3$ (Glen, 1955; Paterson, 1994). For the sliding velocity, a generalized Weertman relation is adopted (Weertman, 1964), taking into account the effect of the subglacial water pressure. Ice shelves are included by iteratively solving a coupled set of elliptic equations for ice shelf spreading in two dimensions, including the effect of lateral shearing induced by sidewalls and ice rises. At the

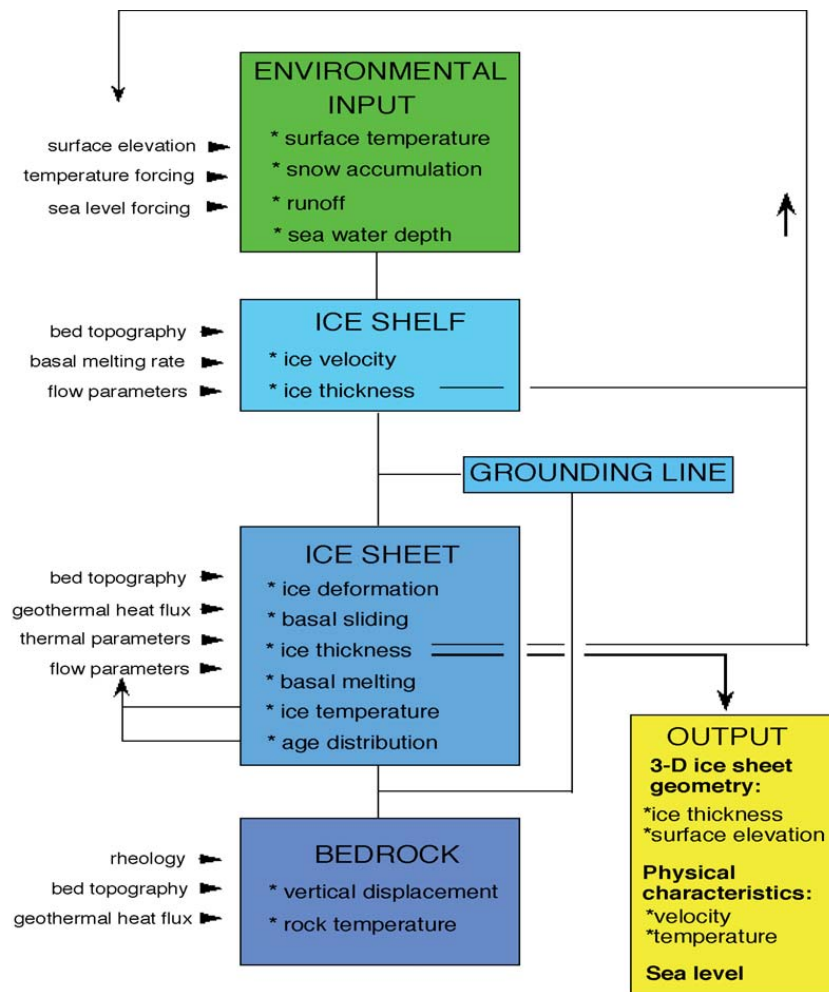


Fig. 6. Structure of the 3-D ice sheet model AGISM. The inputs are given at the left-hand side. Prescribed environmental variables drive the model, which has ice shelves, grounded ice and bed adjustment as major components. For the Antarctic component, the position of the grounding line follows from a flotation criterion and a specific treatment of the force balance. Ice thickness feeds back on surface elevation, an important parameter for the calculation of the mass balance. The main model outputs the time-dependent ice sheet geometry and the coupled temperature and velocity fields.

grounding line, longitudinal stresses are taken into account in the effective stress term of the flow law. These additional stress terms are found by iteratively solving three coupled equations for depth-averaged horizontal stress deviators. The temperature dependence of the rate factor in Glen’s flow law is represented by an exponential Arrhenius equation.

Isostasy is taken into account for its effect on bed elevation near grounding lines and marginal ablation zones, where it matters most for ice sheet dynamics, and because isostasy enables ice sheets to store 25–30% more ice than evident from their surface elevation alone. The bedrock adjustment model consists of a viscous asthenosphere, described by a single isostatic relaxation time, which underlies a rigid elastic plate (lithosphere). In this way, the isostatic compensation accounts for the effects of loading changes within an area several hundred kilometers wide, giving rise to devia-

tions from local isostatic equilibrium. The downward deflection w of the Earth caused by the weight of ice sheets and oceans is determined by the rigidity of the lithosphere and the buoyancy of the mantle, and is a solution of:

$$D\nabla^4 w + \rho_w g w = \begin{cases} \rho_i g H & \text{ice} \\ \rho_w g (\Delta H_{sl} - h) & \text{water} \end{cases} \quad (18)$$

where g is the acceleration due to gravity, h is the bedrock elevation, ρ_w is the density of sea water, and ΔH_{sl} is the eustatic sea-level stand relative to present-day. The standard value for the flexural rigidity D (cf. Table 5) corresponds to a lithospheric thickness of 115 km. The steady state deflection of the surface of the Earth is used to calculate the degree to which the Earth is in isostatic equilibrium,

Table 5. Major parameters of AGISM.

Parameters	Term	Value		Unit
		AISM	GISM	
Ice density	ρ_i	910		kg m^{-3}
Glen's flow law exponent	n	3		
Enhancement factor/multiplier for the rate factor in Glen's flow law	ANEWG	1.8	3.5	
Weertman sliding law exponent	n_p	3		
Basal sliding parameter	ASL	1.8×10^{-10}	1.0×10^{-10}	$\text{m}^8 \text{N}^{-3} \text{year}^{-1}$
Positive degree-day factor for snow melting	DDFS	0.003	0.003297	$\text{m year}^{-1} \text{PDD}^{-1}$ i.e.
Positive degree-day factor for ice melting	DDFI	0.008	0.008791	$\text{m year}^{-1} \text{PDD}^{-1}$ i.e.
Standard deviation of the melt model	σ	4.5		$^{\circ}\text{C}$
Reference basal melting rate below ice shelves	SHMELRO/ M_0	0.25	–	m year^{-1} i.e.
Basal geothermal heat flux	GFLUX	54.6	50.4	mW m^{-2}
Flexural rigidity of lithosphere	D	10^{25}		N m
Mantle density	ρ_m	3300		kg m^{-3}
Relaxation time scale for isostatic adjustment	τ	3000		year

which is asymptotically attained using a relaxation formulation schematically representing the Earth's mantle:

$$\frac{\partial h}{\partial t} = \frac{-(h - h_0 - w)}{\tau} \quad (19)$$

where the unloaded surface elevation h_0 has been determined by assuming that the Earth is in present-day isostatic equilibrium with both the ice and water loading, and τ is the asthenospheric decay timescale. The isostatic treatment produces results close to those from more sophisticated visco-elastic Earth's models, while at the same time being much more efficient in terms of computational cost. The loading takes into account contributions from both ice and ocean water within the respective grids, but ignores any ice loading changes beyond the Greenland and Antarctic continental areas.

For both ice sheets, calculations are made on a $10 \text{ km} \times 10 \text{ km}$ horizontal resolution, with 31 vertical layers in the ice and another 9 layers in the bedrock for the calculation of the heat conduction in the crust (Fig. 7). The vertical grid in the ice has a closer spacing near to the bedrock where the shear concentrates. Rock temperatures are calculated down to a depth of 4 km, which is deemed sufficient to capture most of the effect of temperature changes on glacial-interglacial timescales. This gives rise to between 1.85 and 12.6×10^6 grid nodes for Greenland and Antarctica, respectively. Geometric datasets for surface elevation, ice thickness and bed elevation incorporate most of the recent observations up to 2001, such as ERS-1 derived satellite heights, BEDMAP and EPICA pre-site survey Antarc-

tic ice thicknesses and the University of Kansas collection of airborne radio-echo-sounding flight tracks over Greenland (Huybrechts and Miller, 2005). The grids correspond to those discussed in Huybrechts and Miller (2005). The finite-difference schemes are implicit in time, either alternatively in the x and y directions for the mass conservation equation or only along the vertical for the thermodynamic equations. The 10 km horizontal resolution substantially improves the representation of the fast-flowing outlet glaciers and ice streams which are responsible for the bulk of the ice transport towards the margin. Other physics specific to these features such as higher-order stress components or subglacial sediment characteristics are not included, in common with the current generation of three-dimensional ice-sheet models.

Interaction with the atmosphere and the ocean is effectuated by prescribing the climatic input, consisting of the surface mass balance (accumulation minus ablation), surface temperature and the basal melting rate below the ice shelves surrounding the Antarctic component. The mass balance model distinguishes between snow accumulation, rainfall and meltwater runoff, which components are all parameterized in terms of temperature. The melt- and runoff model is based on the positive degree-day method and is identical to the recalibrated version as described in Janssens and Huybrechts (2000). Following what has become standard practice in large-scale ice sheet modelling, the melting rate is set proportional to the yearly sum of positive degree days at the surface. The expected sum of positive degree days (EPDD) can conveniently be evaluated as:

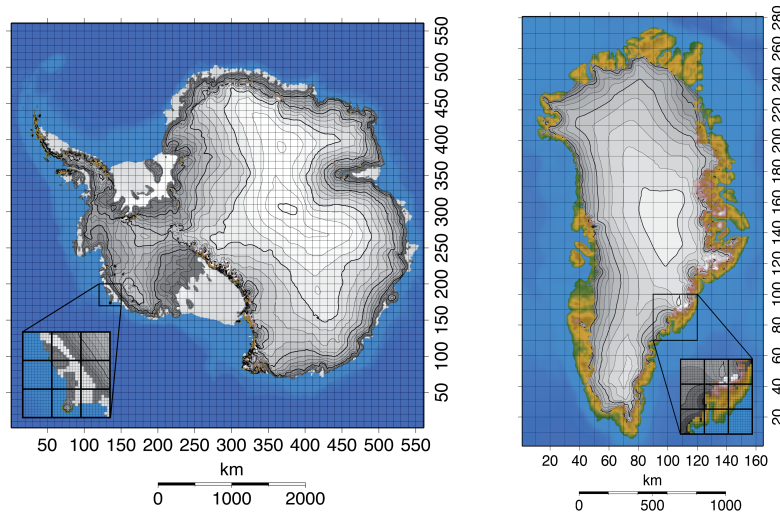


Fig. 7. The numerical grid of AGISM has a horizontal resolution of 10 km for both polar ice sheets (left panel: Antarctic ice sheet; right panel: Greenland ice sheet). Major gridlines are for a distance of 100 km, the insets show the detailed meshes employed in the calculations. The numbers along the axes are gridpoint numbers (561×561 gridpoints for AISM, 165×281 for GISM). For illustrative purposes, we display observed surface elevation of the present-day ice sheets. Ice sheet cover is shaded grey, ice-free range from green to white, and blue colours depict the ocean. Contour lines over the ice sheets are for every 250 m of elevation, major ones for every 1000 m are shown in thick.

$$\text{EPDD} = \sigma \int_0^{12} 30.44 \left[0.3989 \exp \left(-1.58 \left| \frac{T_{\text{mon}}^{\text{sur}}}{\sigma} \right|^{1.1372} \right) + \max \left(0, \frac{T_{\text{mon}}^{\text{sur}}}{\sigma} \right) \right] dt \quad (20)$$

where the standard deviation σ is for temperature with respect to the monthly mean surface temperature $T_{\text{mon}}^{\text{sur}}$ to account for the daily cycle and weather fluctuations. dt represents monthly time steps and the factor 30.44 is the mean amount of days in one month ($365.2422/12$). The expected number of positive degree days (EPDD) is used to melt snow and ice. Meltwater is at first retained in the snowpack by refreezing and capillary forces until the pores are fully saturated with water, at which time runoff can occur. This method to calculate the melt has been shown to be sufficiently accurate for most practical purposes. It moreover ensures that the calculations can take place on the detailed grids of the ice-sheet models so that one can properly incorporate the feedback of local elevation changes on the melt rate, features which cannot be represented well on the generally much coarser grid of a climate model. The melt model is also implemented for Antarctica, but since current summer temperatures remain generally below freezing, melt amounts are currently negligible there. Because of their very low surface slopes, it is further assumed that meltwater produced on the surface of the Antarctic ice shelves, if any, refreezes in situ at the end of the summer season, and therefore does not run off to the ocean. Below the ice shelves, a uniform melting rate is applied which magnitude is linked to the heat input into the cavity, as explained in Sect. 2.7.

2.6 The iceberg model

LOVECLIM has an optional iceberg module which has been activated only in a few studies up to now (Jongma et al., 2009; Wiersma and Jongma, 2009). It will not be used in the experiments discussed in Sect. 3. In such a case, the transport of the icebergs is not taken into account so that the latent and freshwater fluxes caused by iceberg melting takes place at the oceanic grid point where the icebergs leave the ice sheet. However, the iceberg model is briefly described here for completeness as it is part of the code.

This dynamic and thermodynamic iceberg module is based on the iceberg-drift model developed by Smith and Loset (Loset, 1993; Smith, 1993) and Bigg and collaborators (Bigg et al., 1996, 1997; Gladstone et al., 2001). Empirical parameters, including drag and melting coefficients, were adopted from Smith (1993), Bigg et al. (1996, 1997) and Gladstone et al. (2001). A comparison of model results with the observed iceberg limits suggested by Gladstone et al. (2001) was made in Jongma et al. (2009).

The basic equation for horizontal motion of the icebergs is:

$$M \frac{dV_i}{dt} = -Mf\mathbf{k} \times \mathbf{V}_i + \mathbf{F}_a + \mathbf{F}_w + \mathbf{F}_s + \mathbf{F}_p + \mathbf{F}_r \quad (21)$$

for an iceberg with mass M (kg) and velocity \mathbf{V}_i (m s^{-1}), subject to Coriolis force $-Mf\mathbf{k} \times \mathbf{V}_i$, air drag \mathbf{F}_a , water drag \mathbf{F}_w , sea-ice drag \mathbf{F}_s , horizontal pressure gradient force \mathbf{F}_p and wave radiation force \mathbf{F}_r .

Table 6. Major parameters of the iceberg model.

Parameters	Term	Value	Unit
Drag coefficient for air	C_a	1.3	
Drag coefficient for water	C_w	0.9	
Drag coefficient for sea ice	C_s	0.9	

The general drag relationship is given by (Smith, 1993):

$$\mathbf{F}_x = \frac{1}{2} \rho_x C_x A_x |\mathbf{V}_x - \mathbf{V}_i| (\mathbf{V}_x - \mathbf{V}_i) \quad (22)$$

where x refers to air (a), water (w) and sea ice (s) respectively, with medium density ρ_x (kg m^{-3}) and drag coefficient C_x ($C_a = 1.3$, $C_w = 0.9$ (following Smith, 1993, who selected drag coefficients to optimize the fit of the modelled to the observed tracks, but good results were also obtained by Smith with a priori values of 1.0) and $C_s = C_w$ (Bigg, et al., 1997; Gladstone, et al., 2001; see Table 6). A_x is the cross-sectional area of the iceberg perpendicular to the stressing medium x , which has velocity \mathbf{V}_x (m s^{-1}). In accordance with Ekman theory (Bigg et al., 1997), the icebergs are assumed to be travelling with their long axis parallel to the surrounding water and sea-ice flow and at an angle of 45° to the wind flow ($A_w = A_s = 1$ and $A_a = |1.5 \sin(45^\circ)| + |\cos(45^\circ)| \approx 1.77$). The wave radiation force is given by (Smith, 1993):

$$\mathbf{F}_r = \frac{1}{4} \rho_w g a^2 L \frac{\mathbf{V}_a}{|\mathbf{V}_a|} \quad (23)$$

where L the length of the iceberg perpendicular to incident waves, which have amplitude a and are assumed to have the same direction as wind velocity \mathbf{V}_a .

The horizontal pressure gradient force exerted on the water volume that the iceberg displaces \mathbf{F}_p (Bigg et al., 1997) is taken from the free surface ocean model's variable at the iceberg location (Deleersnijder and Campin, 1995). To obtain the strength of the forcing fields at the iceberg's location, linear interpolation from the four surrounding grid corners of the climate model is used.

The icebergs are weakly repelled from the coast using a velocity of 0.003 m s^{-1} in an orthogonal direction when their keel exceeds water depth. They are assumed to remain tabular, maintaining a constant length to width ratio of 1:1.5 (see Bigg et al., 1997). Keel shape or other turbulence related effects are not accounted for. Added mass due to entrained melt water is neglected. Due to real icebergs inertial rotation and individual shapes, this approach can only be considered as a rough approximation. It describes the general behaviour of icebergs but cannot be expected to work well for individual bergs. The drag coefficients for water stress acting along the lower surface of the iceberg and atmospheric

wind stress acting along the top surface are deemed negligibly small (G. R. Bigg, personal communication, 2004). There is no direct interaction between icebergs.

The iceberg thermodynamics must be accounted for in any long-term simulation of its trajectory, since the iceberg mass and shape change due to melting. The iceberg melt is simplified to basal melt, lateral melt and wave erosion (Bigg, et al., 1997). The basal turbulent melting rate (Weeks and Campbell, 1973)

$$M_{\text{basal}} = 0.58 |\mathbf{V}_w - \mathbf{V}_i|^{0.8} \frac{T_w - T_i}{L^{0.2}} \quad (24)$$

is a function of the difference between iceberg ($T_i = -4^\circ\text{C}$) and water temperature (T_w).

The lateral melt due to buoyant convection along the sides of the iceberg is given by an empirical relationship (Eltahan et al., 1983)

$$M_{\text{lateral}} = 7.62 \times 10^{-3} T_w + 1.29 \times 10^{-3} T_w^2 \quad (25)$$

as a function of water temperature T_w ($^\circ\text{C}$) of the corresponding ocean layer in the local grid cell. Wave erosion (Bigg et al., 1997)

$$M_{\text{waves}} = 0.5 S_s \quad (26)$$

is a function of the sea state S_s (based on the definition of the Beaufort scale):

$$S_s = -5 + \sqrt{32 + 2|\mathbf{V}_a|} \quad (27)$$

where \mathbf{V}_a is the wind speed (km h^{-1}).

Iceberg deterioration by atmospheric and radiation effects is considered negligible (Loset, 1993). Break-up of icebergs is not modelled. When the ratio between iceberg length L and height H exceeds a criterion of stability, the icebergs are allowed to roll over (Bigg, et al., 1997):

$$\frac{L}{H} = \sqrt{0.92 + \frac{58.32}{H}} \quad (28)$$

To achieve climatic coupling, the freshwater and latent heat fluxes associated with the iceberg melt are added to the corresponding ocean layer of the local grid cell. Direct feedbacks from the icebergs to the atmosphere are relatively small (e.g., Loset, 1993) and are not accounted for.

2.7 Coupling the different components

The equations of the atmospheric and ocean models are solved on different grids. An interpolation is thus required during the transfers between the two models. CLIO provides ECBilt with the sea surface temperature, the sea-ice temperature, the fraction of sea ice in each ocean grid cell and the sea-ice and snow thicknesses (in order to compute the snow and sea-ice albedo in ECBilt). ECBilt gives to CLIO the wind stresses over the ocean and sea ice, the shortwave and net heat flux over the sea-ice and ocean fractions of the grid

box, and the solid and liquid precipitation (including runoff, evaporation and sublimation). In order to have a conservative interpolation, the surface covered by land, ocean and sea ice is exactly the same in ECBilt and CLIO. This is achieved by decomposing the surface of each atmospheric grid box in three parts. Those fractions are interpolations on ECBilt grid from the one in CLIO. CLIO determines thus the location of the coastlines, and more generally of the land sea mask for the all the components (Fig. 8). The land and ocean fractions and the ocean bathymetry are fixed trough time in LOVECLIM (but can of course be different for simulations devoted to different periods). As a consequence, any change in coastal geometry, for instance implied by a sea level rise, cannot be taken into account explicitly in the model.

No flux correction on stress and heat fluxes is applied between ECBilt and CLIO. However, as precipitation rates in the Atlantic and the Arctic are significantly overestimated in ECBilt, they are reduced by 8.5% and 25%, respectively, before being transmitted to CLIO in order to avoid too large an ocean drift. In order to conserve mass, the excess water is dumped into the North Pacific where ECBilt underestimates precipitation, ensuring an additional constant flux per unit area in the region located between the Bering Strait and the equator.

LOCH and CLIO run on the same grid (Fig. 4). The time step for solute transport in LOCH is the same as the time step for tracer transport in CLIO, thus eliminating the need for any interpolation procedure. However, LOCH uses a numerical scheme for advection which differs from the one of CLIO. The reason for this difference is to be found in the non monotonic behaviour of the CLIO advection scheme.

Transport in LOCH is based on two-dimensional and three-dimensional fields provided by CLIO: downsloping flows and heights, salt and freshwater fluxes at the sea surface, current velocities and vertical and horizontal diffusivities. The chemical constants, the gas exchange coefficients and other parameters of LOCH are computed from the temperature and salinity fields provided by CLIO. The piston velocity is determined from the wind field simulated by ECBilt. The growth rate of the phytoplankton biomass is set according to the same amount of available light at the sea surface (under the ice in ice-covered areas) as in CLIO; we however use a different extinction coefficient with depth. The sea-ice areal coverage modelled by CLIO is also taken into consideration in the calculation of the air sea gas fluxes.

The atmospheric component of LOCH computes the atmospheric CO₂ evolution in zonal bands which are equally spaced in latitude. A spatial interpolation procedure is thus required to transfer to LOCH the annual mean values of the CO₂ fluxes between atmosphere and continents computed by VECODE as well as those from LOCH since over the North Atlantic the grid of CLIO is not regular with latitude. By combining the carbon fluxes from the continents and from the ocean, LOCH computes a globally averaged,

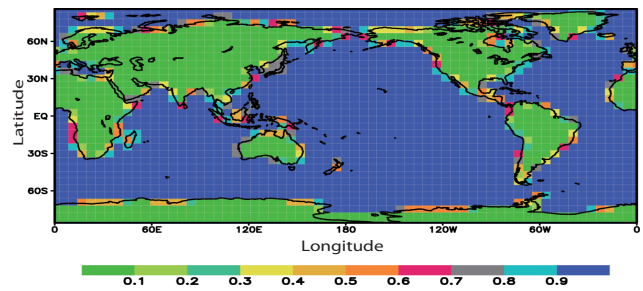


Fig. 8. Fraction of ocean surface in each of the grid cell of ECBilt.

annual mean atmospheric CO₂ concentration which is then transmitted to ECBilt and VECODE, where it impacts on the radiative transfer and fertilization, respectively.

The key atmospheric variables needed as input for AGISM are monthly surface temperature and annual precipitation. Because the details of the Greenland and Antarctica surface climate are not well captured on the ECBilt coarse grid, these boundary conditions consist of present-day observations as represented on the much finer AGISM grid onto which climate change anomalies from ECBilt are superimposed. Monthly temperature differences and annual precipitation ratios, computed against a reference climate corresponding to the period 1970–2000 AD (PD), are interpolated from the ECBilt grid onto the AGISM grid and added to and multiplied by the parameterized surface temperatures and observed precipitation rates, respectively. The perturbation (“delta”) method for temperature is represented by:

$$T_{\text{mon}}^{\text{sur}}(\phi, \lambda, t) = [T_{\text{ECBilt}}^{\text{sur}}(\phi, \lambda, t) - T_{\text{ECBilt}}^{\text{sur}}(\phi, \lambda, \text{PD})] + T_{\text{par}}^{\text{sur}}(\phi, \lambda, \text{PD}) - \gamma [H_{\text{ECBilt}}^{\text{sur}}(\phi, \lambda, t) - H_{\text{ECBilt}}^{\text{sur}}(\phi, \lambda, \text{PD})] \quad (29)$$

where the monthly mean surface temperature is specified as a function of time t and location (ϕ, λ) , the first term on the right-hand side is the mean monthly temperature anomaly from ECBilt, the subscript par denotes the parameterized surface temperature in the ice sheet model, and an additional correction is required to correct for the elevation temperature change in ECBilt (last term) to avoid double counting. γ is a prescribed atmospheric lapse rate.

The treatment of precipitation is similar to that of temperature, except that the ratio is used and not the difference. This is because using the same form of Eq. (29) for precipitation might introduce “negative precipitation” into the climate forcing, which has no physical basis. The appropriate relation reads:

$$P(\phi, \lambda, t) = \left[\frac{P_{\text{ECBilt}}(\phi, \lambda, t)}{P_{\text{ECBilt}}(\phi, \lambda, \text{PD})} \right] \cdot P_{\text{cli}}(\phi, \lambda, \text{PD}) \quad (30)$$

where the yearly precipitation rate distribution is also given as a function of time and location, and $P_{\text{ECBilt}}(\phi, \lambda, t)/P_{\text{ECBilt}}(\phi, \lambda, \text{PD})$ is the ratio of modelled annual precipitation between time t and the reference

period 1970–2000. The subscript cli refers to the observed precipitation climatology over the ice sheets and is representative for the same reference period.

This approach avoids systematic errors in the absolute ECBilt fields and ensures that some processes, such as the melting taking place at the ice sheet margin over a spatial extent narrower than the atmospheric model resolution, can be adequately represented.

The ocean heat flux at the base of Antarctic ice shelves is also calculated in perturbation mode based on a parameterization proposed by Beckmann and Goosse (2003):

$$M(t) = \frac{Q^{\text{net}}(t)}{Q_0^{\text{net}}} \frac{A_0}{A(t)} M_0 \quad (31)$$

where M is the basal melt rate, Q^{net} an estimate of the total heat flux entering the ice shelves integrated all along the perimeter of Antarctica, and A the total area of Antarctic ice shelves. Here the subscripts t and 0 refer to the actual model time and the reference time taken as 1500 AD, respectively. In this approach the melt rate below the ice shelves depends on the net heat input from the oceans into the cavity below the ice shelves. The total melt volume is proportional to changes in the net integrated ocean heat input but inversely proportional to the area of the ice shelves. The underlying assumption is that much of the water in the cavity is recycled locally forming a semi-closed circulation cell. Q^{net} is estimated directly from the mean ocean temperature around Antarctica.

After performing mass balance and ice dynamic computations, AGISM transmits the calculated changes in orography and land fraction covered by ice to ECBilt and VECODE. This involves accounting for the albedo of the ice but also for the monthly snow cover over ice-free areas of Greenland. Land cover changes over Antarctica are not expected for most periods being studied. In addition, AGISM provides CLIO with the geographical distribution of the annual mean surface freshwater flux resulting from ice sheet runoff, iceberg calving, runoff from ice-free land and basal ice melting. The transfer of data from AGISM to ECBilt is rather straightforward since the grid cells of ECBilt are much larger than the AGISM ones. Each AGISM grid cell is associated with an ECBilt grid cell, and an area average is made to determine the value of a specific variable on the ECBilt grid. For the interpolation of data from the ECBilt grid to the AGISM grid, we opted to first transform the AGISM points on the ECBilt grid and subsequently apply a Lagrangian interpolation. The selected interpolation is a third-order Lagrange polynomial. Four ECBilt grid points are taken into account in latitude and four in longitude to determine the polynomial providing the variable value at each particular AGISM grid point.

Regarding the coupling between AGISM and CLIO, a simple procedure was set up to allocate the total freshwater flux from AGISM to the respective surface ocean grid boxes of CLIO that border Greenland and Antarctica. It must also be mentioned that the latent heat associated with iceberg melt-

ing is pumped from these grid boxes. The coupling technique described above leads to heat and water losses/gains in the coupled model. Due to the perturbation method employed and the use of a Lagrangian interpolation, the amount of water received by AGISM in the form of precipitation is not equal to the amount of water leaving ECBilt. Biases are of the order of 10% to 25% of the total runoff from Antarctica and Greenland, respectively. Similarly, the heat available in ECBilt for the ice sheet melting differs from the one in AGISM. Flux adjustments are therefore necessary to ensure strict conservation of heat and water. These are applied uniformly in a given ocean area around each ice sheet. The water correction is treated as an additional freshwater flux and the heat correction as an additional latent heat flux associated with iceberg melting. This ensures the closure of the heat and water balances in the coupled system.

3 Evaluation of model performance

As LOVECLIM is a model of intermediate complexity, it cannot be expected to reproduce all the observations with the same skill and the same level of detail as a GCM. Indeed, previous studies have underlined some clear and strong model biases in LOVECLIM results. Some of those biases are directly linked to the model formulation and reducing significantly their amplitudes can only be achieved by modifying fundamental model assumptions. This would then be at the expense of some of the main advantages of LOVECLIM. As it is not our goal here to modify the philosophy behind the model development, such biases are still present in version 1.2.

Nevertheless, it is instructive to document the regions (and variables) where the discrepancies are the largest and the ones where the agreement between model results and observations is satisfactory because it is an important element when interpreting results of experiments performed with the model. In the following sections, we will thus describe briefly the mean state of the model for present-day conditions and then discuss the model behaviour for 4 key periods: the last decades, the last millennium, the mid-Holocene (6 ky BP) and the Last Glacial Maximum (LGM, 21 ky BP). The last two periods are standard ones in the Paleoclimate Modelling Intercomparison Project (PMIP, see for instance Braconnot et al., 2007).

Idealized experiments have also been performed with the model. They are not described here but it is useful to mention that when the CO_2 concentration is doubled compared to pre-industrial conditions, the surface temperature increases by 1.9°C after 1000 years of integration in LOVECLIM (with fixed ice sheets), giving an estimate of the model climate sensitivity. This is at the lower end of the range of values obtained from GCM results (e.g., Randall et al., 2007). In another experiment, under pre-industrial conditions, a freshwater flux of 0.1 Sv ($1 \text{ Sv} = 10^6 \text{ m}^3 \text{ s}^{-1}$) has been imposed in

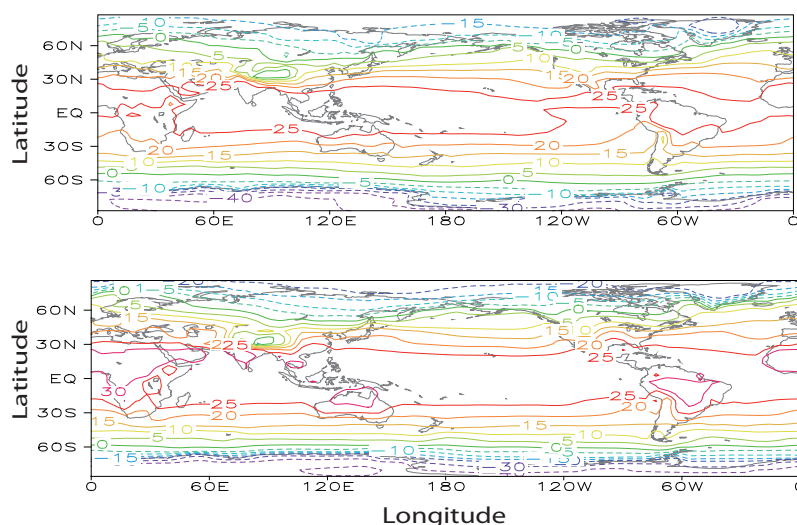


Fig. 9. Surface temperature ($^{\circ}\text{C}$) averaged over the period 1980–2000 in (a) HADCRUT3 dataset (Brohan et al., 2006) and in (b) LOVECLIM1.2.

the North Atlantic during 1000 years, inducing a 30% decrease of the maximum of the overturning streamfunction in the North Atlantic (see below for a description of this variable). This indicates that LOVECLIM1.2 is slightly more sensitive to freshwater perturbations than an early version of ECBILT-CLIO (Rahmstorf et al., 2005).

3.1 Present-day mean climate

In order to compare the model results with recent observations, a transient simulation has first been performed with LOVECLIM over the last 1500 years using all the components of LOVECLIM except the iceberg model. The average over the last decades of this simulation is used first to evaluate the model behaviour for present-day conditions. This simulation will also be analyzed in Sect. 3.2 and 3.3 to study simulated changes during the past decades and the past millennium, respectively.

The initial conditions for LOCH, VECODE, ECBilt and CLIO come from a quasi equilibrium run, of several thousand years duration, corresponding to the forcing applied in 500 AD. For AGISM, as the ice sheets cannot be considered in quasi-equilibrium with the climate at that time, the initial conditions are obtained from a run of AGISM in uncoupled mode covering the last glacial-interglacial cycles and the Holocene up to 500 AD.

During the transient experiments, long-term changes in orbital parameters follow Berger (1978) and the long-term evolutions of non- CO_2 greenhouse gas concentrations are imposed. The variations in the emission of CO_2 from fossil fuel burning are derived from Marland et al. (2003). The influence of anthropogenic (1850–2000) sulfate aerosols is represented through a modification of surface albedo (Charlson et al., 1991). The forcing due to anthropogenic land-use

changes (including both surface albedo and surface evaporation and water storage) is applied as in Goosse et al. (2005a) following Ramankutty and Foley (1999). Finally, natural external forcing due to changes in solar irradiance and explosive volcanism are prescribed following the reconstructions of Muscheler et al. (2007) and Crowley et al. (2003), respectively. The total solar irradiance changes have been scaled to provide an increase of 1 W m^{-2} between the Maunder minimum (late 17th century) and the late 20th century. This roughly corresponds to a threefold reduction in amplitude compared to some previous simulations conducted with the model (e.g., Goosse et al., 2005) but is in better agreement with recent reassessments (Lean et al., 2002; Foukal et al., 2006).

When comparing the mean climate over the last decades of this simulation to observations, we see that LOVECLIM1.2 reproduces reasonably well the main characteristics of the observed surface temperature distribution (Fig. 9). For instance, the zero degree isotherm is quite close to the observed one in both hemispheres, with a more or less constant latitude in the Southern Hemisphere and a wavy structure in the Northern Hemisphere that displays a more northern position on continents than over the oceans. The strong differences at mid- and high-latitudes between the cold western part of the Atlantic compared to the warmer eastern part is also clearly seen in both model results and observations. In the tropics, the model is too warm, with a 25° isotherm located too far away from the equator and an overestimation of the temperature over the continents. Furthermore, the temperature is much too high in the Eastern Pacific. As a consequence, the temperature gradient between the Eastern and Western Pacific is underestimated, reaching in the model about 2.5°C in annual mean at the equator compared to more than 3.5°C in observations interpolated on the model grid.

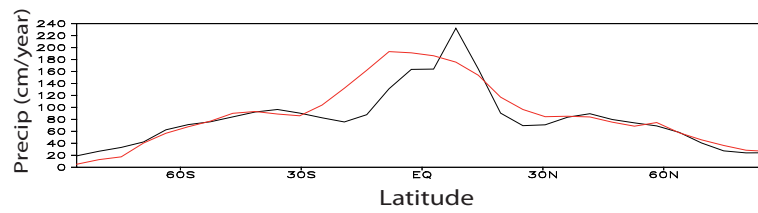


Fig. 10. Zonal mean precipitation (cm year^{-1}) averaged over the period 1980–2000 in Xie and Arkin (1996 and updates) dataset (black) and in LOVECLIM1.2 (red).

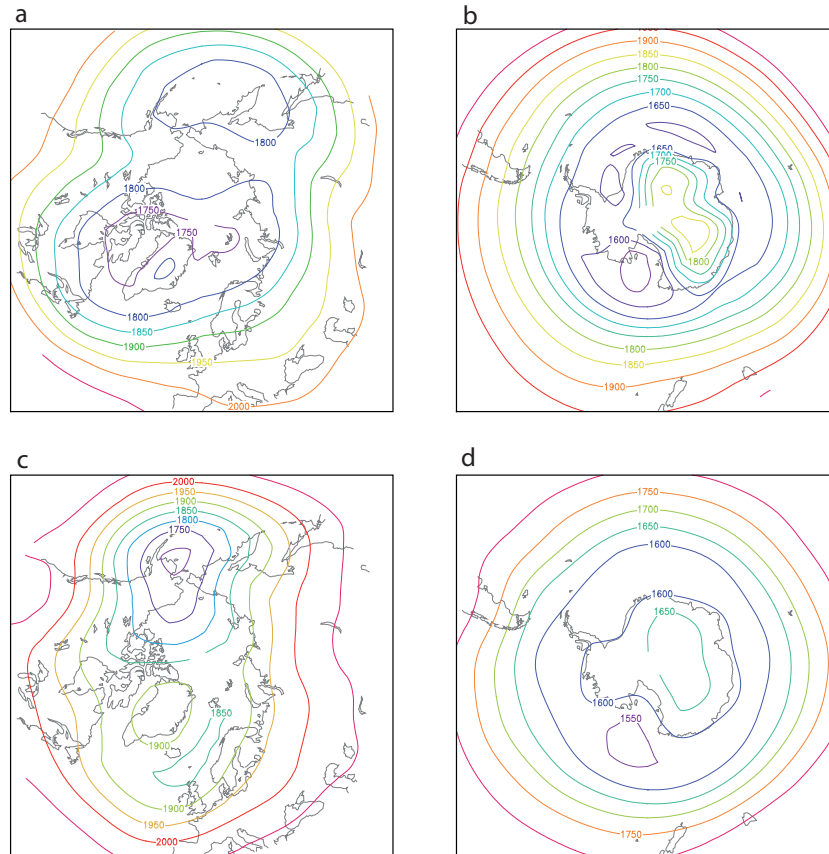


Fig. 11. Geopotential height (in m) at 800 hPa in winter averaged over the period 1980–2000 (DJF in the Northern Hemisphere, JJA in the Southern Hemisphere) in NCEP-NCAR reanalyses (Kalnay et al., 1996, top row, i.e. **a** and **b**) and in LOVECLIM1.2 (bottom row, i.e. **c** and **d**).

The simulated zonal mean precipitation has roughly the right magnitude in nearly all the latitude bands (Fig. 10). However, the simulated pattern is much too symmetric between the hemispheres. In particular, the model is not able to reproduce the clear and strong absolute maximum in the Northern Hemisphere associated with the Intertropical Convergence Zone, displaying its maximum near the equator. A similar problem is also seen in many other EMICs (e.g. Petoukov et al., 2005). Furthermore, the precipitation at the observed local minima around 20° S and 30° N is clearly overestimated by the model. At some latitudes, the model error can reach 50% of the precipitation in zonal mean.

In both hemispheres, the large-scale structure of the near-surface circulation (Fig. 11) is well reproduced by the model with, as expected, a general decrease of the geopotential height with latitudes and local minima in the North Atlantic, the North Pacific and in a belt around 70° S. Except for the Aleutian low, the model underestimates the gradients in both hemispheres, leading to simulated winds weaker than the observed ones. Furthermore, the simulated minimum of the geopotential height in the North Atlantic is located too far eastwards, close to Baffin Bay, while the observations have their minimum near Iceland, inducing a wrong wind direction east of Greenland.

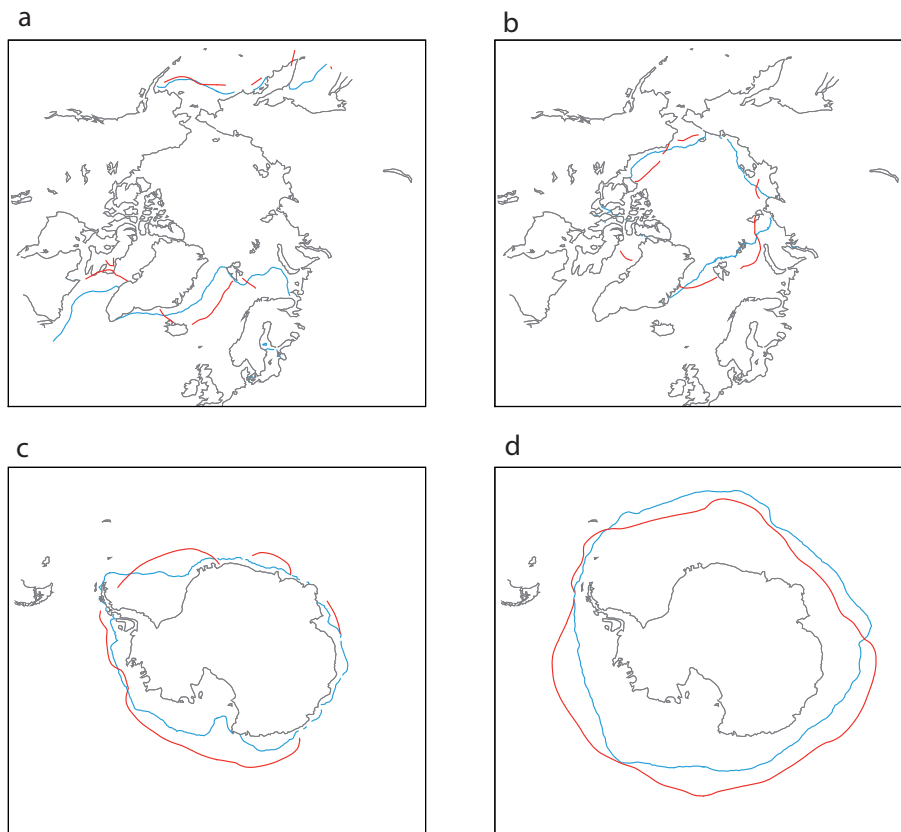


Fig. 12. Location of the sea-ice edge averaged over the period 1980–2000, defined by a monthly ice concentration equal to 15% in (a) March in the Northern Hemisphere, (b) September in the Northern Hemisphere, (c) September in the Southern Hemisphere, (d) March in the Southern Hemisphere. The observations are in blue (Rayner et al., 2003) and LOVECLIM1.2 results are in red.

LOVECLIM is able to simulate reasonably well the sea-ice extent in both hemispheres (Fig. 12). In the Northern Hemisphere, the sea-ice edge is very close to the observed one in the Pacific sector, both during summer and winter. In the Atlantic sector, the simulated sea-ice edge is too far northwards in the Baffin Bay and Labrador region in winter, while, in summer, the sea-ice extent is too large. The amplitude of the seasonal cycle of the sea-ice concentration is thus clearly too weak in this region in the model. In the western part of the North Atlantic, the model tends to slightly overestimate the sea-ice concentration, both in summer and in winter. The sea-ice extent is also slightly overestimated in the Southern Ocean in both seasons. Two exceptions are the regions west of the Antarctic Peninsula in summer and off East Antarctica around 45° E in winter, where the model underestimates the sea-ice extent.

The maximum of the overturning streamfunction in the North Atlantic reaches 22 Sv, with an export towards the Southern Ocean of 13 Sv (Fig. 13). Deep convection in the model occurs both in the Greenland-Norwegian Sea and the Labrador Sea, as observed over the last decades. The maximum of the deep cell close to Antarctica has a value of 12 Sv, while 17 Sv are transported northward close to the bottom in

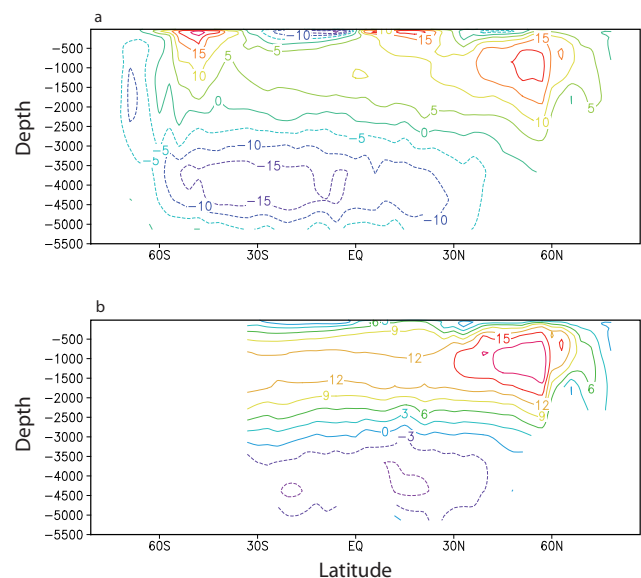


Fig. 13. Simulated meridional overturning streamfunction averaged over the period 1980–2000 (in Sv) for (a) the whole World Ocean and (b) the Atlantic.

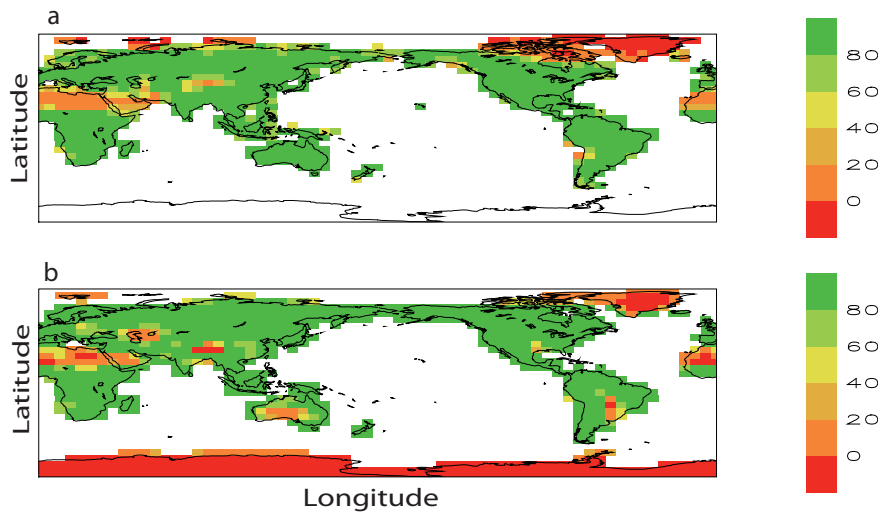


Fig. 14. Total vegetation cover in (a) GSWP2 dataset (International GEWEX Project Office, 2002) and in (b) LOVECLIM1.2 averaged over the period 1980–2000.

the global ocean. The shallow wind-driven cells in the tropics are associated with a total upwelling close to the equator of about 50 Sv. All those values are in relatively good agreement with the data-based estimates and in the range of the values given by other models (Ganachaud and Wunsch, 2000; Karsten and Marshall, 2002; Gregory et al., 2005; Rahmstorf et al., 2005).

As the model tends to overestimate precipitation in the tropics, the vegetation cover is also overestimated in those regions (Fig. 14). The vegetation fraction is also too large at high latitudes, mainly because of an overestimation of the temperature over the continent. By contrast, LOVECLIM has too low a vegetation cover in some regions of Australia and Southern America around 30° S.

3.2 The last decades

In response to the forcing applied, the model simulates a clear increase in the global mean surface temperature (Fig. 15) and in the atmospheric CO₂ concentration (Fig. 16) over the 20th century and the beginning of the 21st century. The model is also able to reproduce the observed intensification of the warming trend over the last decades (Table 7). However, the model significantly underestimates the magnitude of this warming. This can be partly explained by the too large increase in ocean heat content in the model, the ocean playing apparently a larger buffering role in the model than in observations. This is a standard model bias that is discussed in detail in Loutre et al. (2010).

For the atmospheric CO₂ concentration, the model is quite close to observations (Fig. 16), with only a slight underestimation of the trend of the last 50 years (Table 7). The observed decrease in the summer sea-ice extent in the Arctic is

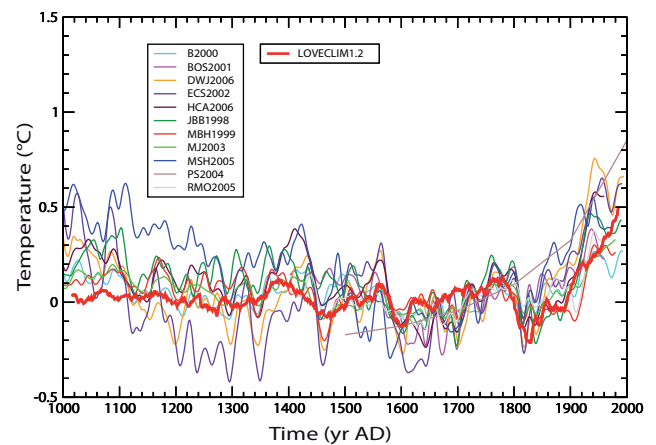


Fig. 15. Annual mean temperature averaged over the Northern Hemisphere in LOVECLIM1.2 (red line) driven by both natural and anthropogenic forcings as well as in several reconstructions based on proxy data. The time series are smoothed with a 31-yr running-mean. The reference period is 1500–1899. The correspondence of acronyms is: B2000 to Briffa (2000) calibrated by Briffa et al. (2004), BOS2001 to Briffa et al. (2001), DWJ2006 to D'Arrigo et al. (2006), ECS2002 to Esper et al. (2002), recalibrated by Cook et al. (2004a), HCA2006 to Hergel et al. (2006), JBB1998 to Jones et al. (1998) calibrated by Jones et al. (2001), MBH1999 to Mann et al. (1999), MJ2003 to Mann and Jones (2003), MSH2005 to Moberg et al. (2005), PS2004 Pollack and Smerdon (2004), reference level adjusted following Moberg et al. (2005), RMO2005, Rutherford et al. (2005).

also reasonably well simulated by the model (Table 7). This underlines that the underestimation of the warming seen at the global scale is mainly related to too weak a response of the model at low latitudes (Driesschaert, 2005).

Table 7. Simulated trends over the last decades of some important variables.

Variable	Observations	LOVECLIM	Unit
Global surface temperature trend over the period 1901–2005	0.0071 ¹	0.0045 ± 0.0004 ⁵	°C yr ⁻¹
Global surface temperature trend over the period 1979–2005	0.017 ¹	0.012 ± 0.002	°C yr ⁻¹
Atmospheric CO ₂ concentration trend over the period 1958–2008	1.44 ²	1.47 ± 0.01	ppmv yr ⁻¹
Trend in summer sea-ice extent in the Arctic over the period 1979–2007	-0.056 ³	-0.046 ± 0.013	10 ⁶ km ² yr ⁻¹
Trend in ocean heat content in the top 700 m of the ocean over the period 1955–2007	0.26 ⁴	0.31 ± 0.02	10 ²² J yr ⁻¹

¹ Brohan et al. (2006) and updates.

² Data from the Mauna Loa record (NOAA ESRL; www.esrl.noaa.gov/gmd/ccgg/trends/).

³ Comiso and Nishio (2008) (http://nsidc.org/data/smmr_ssmi_ancillary/area_extent.html) (NASAtteam algorithm).

⁴ Levitus et al. (2009).

⁵ Uncertainties on the LOVECLIM results are estimated from the standard deviation of an ensemble of 5 experiments performed with the model using the same forcing but slightly different initial conditions.

3.3 The past millennium

The temperatures simulated over the past millennium display decadal to multi-centennial variations as well as a weak cooling trend over the period 1000–1850 before the large warming of the industrial era (Fig. 15). This is broadly consistent with the various reconstructions available as well as with previous model simulations. However, the long-term cooling between the period around 1000–1200 and the one around 1600–1850 is weaker here than in previous simulations performed with the model (e.g., Goosse et al., 2005). This is mainly due to the weaker amplitude of the variations of solar irradiance applied here.

The simulated CO₂ concentration is quite stable in the model over the pre-industrial period (Fig. 16). As a consequence, the model is not able to reproduce the small decrease in CO₂ concentration between the periods 1200–1400 and 1700–1800 suggested by the observations (for a recent discussion of this feature, see for instance Frank et al., 2010).

The changes in the volume of ice sheets as simulated by the standard model over this period are relatively weak. Over Antarctica, the ice volume increases by 0.1% in 1000 years, while it decreases by about 1% over Greenland over the same period (Fig. 17). A small acceleration of the retreat is also seen in Greenland over the last decades. It is hard to tell at this stage if the trend in both curves is due to a long-term response of the ice sheets to past climate changes or results from a small drift introduced by the coupling procedure. Anyway, the simulated changes are small and can be neglected when analyzing future changes as they are at least an order of magnitude smaller than the ones simulated by the model for the 21st century and beyond (Driesschaert et al., 2005; Swingedouw et al., 2008). For analyzing past changes over several thousand years, the problem needs to be considered more carefully, but such simulations have not yet been carried out with LOVECLIM including all its components.

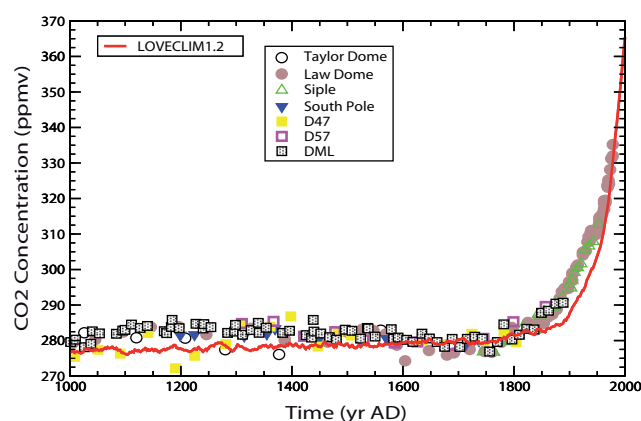


Fig. 16. Atmospheric CO₂ concentration in LOVECLIM1.2 (red line) compared to measures made in various ice cores: Taylor Dome (Indermühle et al., 1999), Law Dome (Etheridge et al., 1998), Siple (Neftel et al., 1994), South Pole (Siegenthaler et al., 2005), D47 (Barnola et al., 1995), D57 (Barnola et al., 1995), Draening Maud Land (DML, Siegenthaler et al., 2005).

3.4 Mid-Holocene conditions

For the mid-Holocene simulation, the orbital parameters have been set at the value corresponding to 6 ka BP and the methane concentration has been reduced to 650 ppbv. The concentrations values for all other greenhouse gases (including CO₂) are the same as for pre-industrial conditions. All the other conditions have been chosen identical to pre-industrial ones and a quasi-equilibrium multi-millennia run has been carried out. For this simulation experiment, LOCH and AGISM were not activated.

In response to the larger summer insolation, LOVECLIM1.2 simulates an increase in JJAS (June–July–August–September) surface air temperature at 6 ka BP over the continents in the Northern Hemisphere and over the Arctic

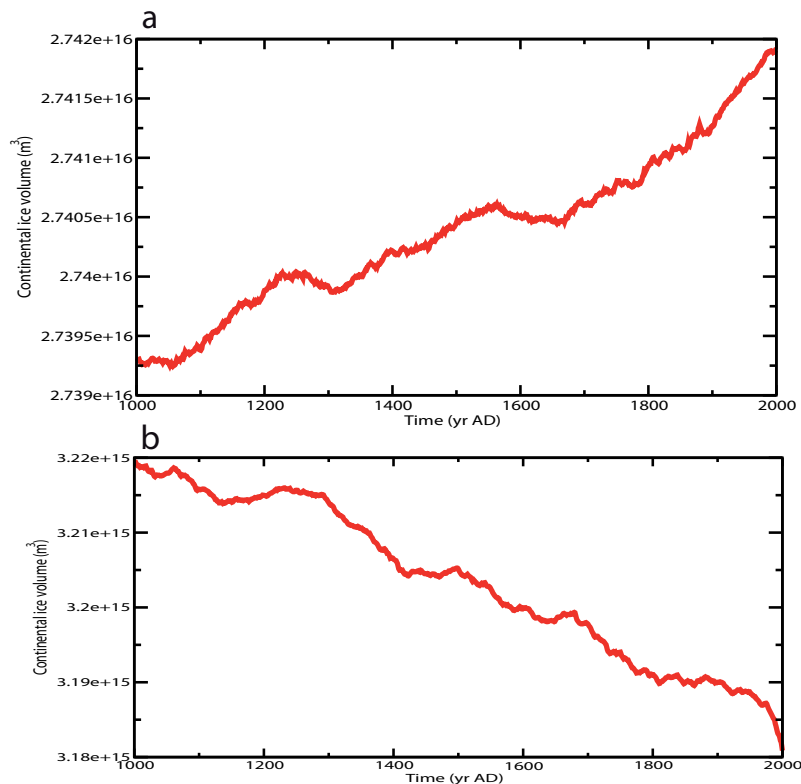


Fig. 17. Continental ice volume changes during the last millennium simulated by AGISM for (a) Antarctic and (b) Greenland ice sheets. In this particular example, the Greenland ice volume budget is equivalent to a positive sea level contribution of about 10 cm over the entire period. The Antarctic ice volume budget is slightly positive but cannot be directly related to sea level change because of ice grounded below sea level. Variability in both indices on centennial timescales arises from the climate forcing and dynamical ice-climate interactions. The modelled trend is not a robust feature of AGISM, but contains a significant component from the model coupling procedure at 500 AD and the specific model parameters selected for ECBilt and CLIO.

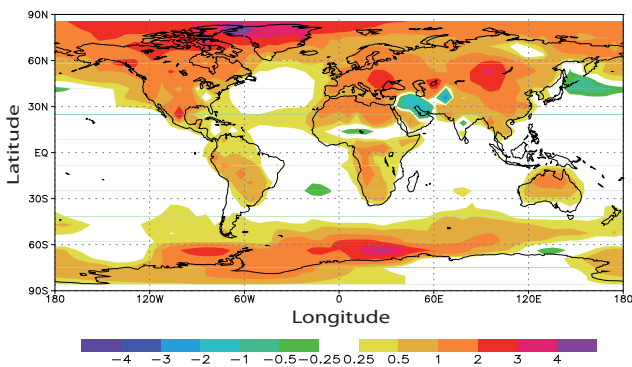


Fig. 18. Simulated difference of summer (JJAS) temperature (in °C) between the mid-Holocene and present-day conditions.

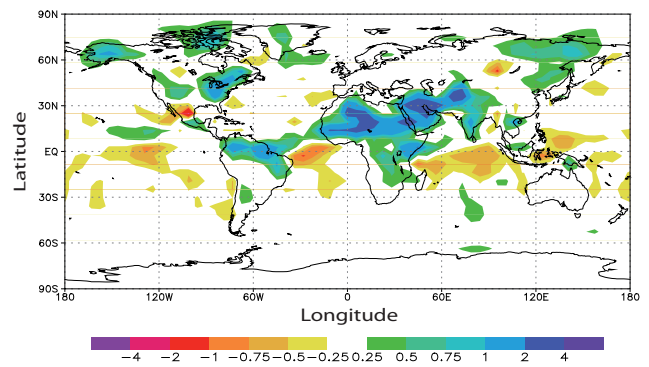


Fig. 19. Simulated difference of summer (JJAS) precipitation (in mm per day) between the mid-Holocene and present-day conditions.

compared to present-day conditions (Fig. 18). The Southern Ocean is also warmer with a local temperature maximum increase of ~ 4 °C between 30° E– 40° E. By contrast, some regions show a small cooling such as seen in Africa just north of the equator, in the Middle East and west of the Japan coast.

The JJAS mean precipitation (Fig. 19) produced by the LOVECLIM1.2 model, captures well the Mid-Holocene characteristic increase over Northern Africa and in the Middle East, associated with an increase of vegetation there (Fig. 20). In the northeast of South America there is also

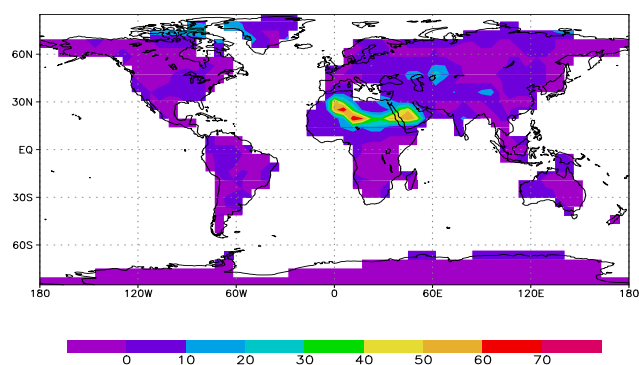


Fig. 20. Simulated difference in total vegetation cover (%) between the mid-Holocene and present-day conditions.

an increase of $\sim 1 \text{ mm day}^{-1}$. Just southward of the equator, there is less precipitation over the ocean in the mid-Holocene than today. All those results agree reasonably well with those from other models participating in the PMIP2 intercomparison (Braconnot et al., 2007), albeit tropical ocean feedbacks are relatively weak due to the quasi-geostrophic approximation in the atmospheric component ECBilt (Zhao et al., 2005).

3.5 The last glacial maximum

In order to simulate the last glacial maximum climate, the orbital parameters have been modified to the values corresponding to 21 ka BP and CO_2 , methane and NO_2 concentrations were set to 185 ppmv, 350 ppbv and 200 ppbv, respectively, following the PMIP2 protocol. In addition, the topography of the ice sheets and the geometry of the coastlines have been imposed according to the ICE-5G reconstruction (Peltier, 2004). As for the run devoted to the mid-Holocene, LOCH and AGISM were not activated. The simulation was started from pre-industrial conditions. After 4000 years, the climate reached a quasi-equilibrium state characterized by a huge cooling of more than 25°C over the Laurentide and Fennoscandian ice sheets (Fig. 21). The model also simulates a large cooling in the Southern Ocean associated with a large increase in the sea-ice extent there. The cooling is larger over the Atlantic than over the Pacific, in particular northward of 45°N . In the tropics, the signal is weaker. In some regions, such as North Australia, the changes are very close to zero. Those results are similar to the ones of other simulations performed in the framework of the PMIP2 project (Braconnot et al., 2007), except in the Southern Ocean where the signal obtained in LOVECLIM is larger than the one given by most other models.

In the North Atlantic, the simulated cooling is associated with a southward shift of the sea-ice edge, with sea ice covering the majority of the Greenland, Iceland and Norwegian Seas both in summer and winter. Only a small area off the southern coast of Norway remains ice free all year long.

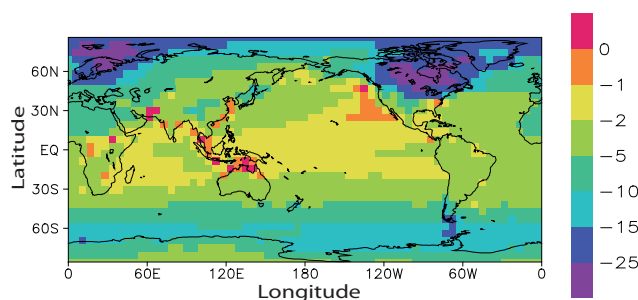


Fig. 21. Simulated difference of annual mean surface temperatures (in $^\circ\text{C}$) between the last glacial maximum and present-day conditions.

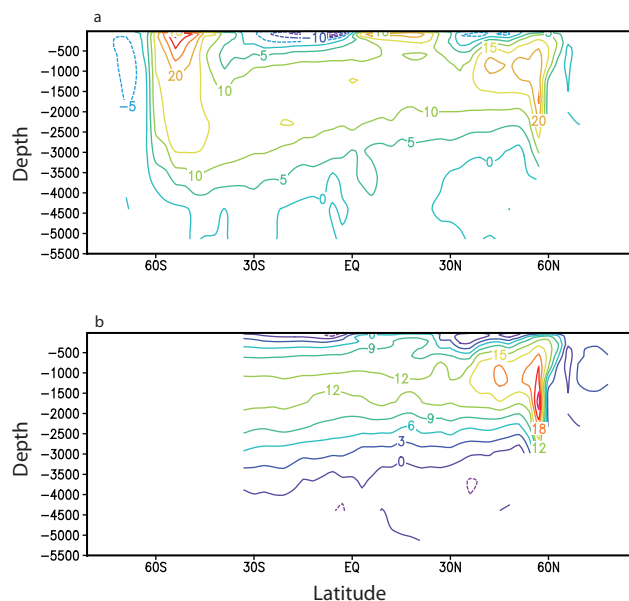


Fig. 22. Simulated meridional overturning streamfunction (in Sv) for (a) the whole World Ocean and (b) the Atlantic simulated for the Last Glacial Maximum.

In winter, deep convection occurs close to this location as well as south-east of Iceland. The North Atlantic meridional overturning streamfunction is quite similar to the one simulated for present-day conditions (Fig. 22), with a small decrease of the magnitude compared to present-day nearly everywhere except between 40° and 60°N in the top 2000 m of the water column. Furthermore, at high latitudes, the maximum is shifted southward, consistently with the change in the location of the convection patterns. Actually, the maximum of the overturning at LGM is lower here than in the previous versions of LOVECLIM that were characterized by a deeper and stronger meridional overturning at the LGM (e.g. Roche et al., 2007), a feature that previous versions of LOVECLIM shared with many of the other models participating in the PMIP2 intercomparison, although it is generally accepted that the circulation associated with North Atlantic

Deep Water was shallower at LGM than at present (Weber et al., 2007; Lynch-Stieglitz et al., 2007). In Fig. 21, we also notice a reduction in the inflow of Antarctic Bottom Water in the Atlantic. At the global scale, the simulated deep circulation appears to be particularly weak in the Pacific and Indian ocean at the LGM and the magnitude of the deep cell close to Antarctica is reduced compared to present-day.

4 Summary and conclusions

In the previous sections, we have summarized the main equations and parameterizations of all the components of LOVECLIM. Furthermore, we have documented the model behaviour for present-day conditions and classical model tests. This provides a general overview and a reference for model users as well as for the scientists who want to learn more about the model, for instance after reading a paper using LOVECLIM results. A brief discussion of model performance is provided for several standard cases. As mentioned in the introduction, a deeper analysis was performed using previous versions of the model for all the experiments presented here. Further analysis is planned for the near future, for instance in the framework of PMIP3 (<http://pmip3.lsce.ipsl.fr/>).

The discussion of model results underlines that the model appears well adapted to study long-term climate changes, in particular at mid- and high- latitudes. However, we recall that it is of course essential to always try to take into account the model limitations and to estimate how they influence the conclusions of a study. Where the biases are strong, in particular in many regions at low latitudes, this requires a particularly careful analysis. In addition to simulations over long periods, the model is suitable and thus more and more used to perform studies that require large ensembles of simulations. This has not been discussed here but recent examples show, for instance, the influence of the choice of parameters in all the components of the model (Loutre et al., 2010; Goetzler et al., 2010) and the way data assimilation in coupled mode could help in reconstructing past climate changes (Crespin et al., 2009; Goosse et al., 2010).

Acknowledgements. E. Deleersnijder, G. Munhoven and H. Goosse are Research Associates with the Fonds National de la Recherche Scientifique (F.R.S. – FNRS-Belgium). This work is supported by the F.R.S. – FNRS and by the Belgian Federal Science Policy Office, Research Program on Science for a Sustainable Development. D. M. Roche is supported by INSU-CNRS and by NWO under the RAPID project ORMEN.

Edited by: M. Kawamiya

References

- Anderson, L. A. and Sarmiento, J. L.: Redfield ratios of remineralization determined by nutrient data analysis, *Global Biogeochem. Cy.*, 8, 65–80, 1994.
- Bacastow, R. and Maier-Reimer, E.: Ocean-circulation model of the carbon cycle, *Clim. Dynam.*, 4, 95–125, 1990.
- Barnola, J.-M., Anklin, M., Porcheron, J., Raynaud, D., Schwander, J., and Stauffer, B.: CO₂ evolution during the last millennium as recorded from Antarctica and Greenland ice, *Tellus B*, 47, 264–272, 1995.
- Bazilevich, N. I.: Biological Productivity of Ecosystems of Northern Eurasia, Nauka, Moscow, 293 pp., 1993 (in Russian).
- Beckmann, A. and Goosse, H.: A parameterization of ice shelf–ocean interactions for climate models, *Ocean Model.*, 5, 157–170, 2003.
- Berger, A. L.: Long-term variations of daily insolation and Quaternary climatic changes, *J. Atmos. Sci.*, 35, 2363–2367, 1978.
- Bigg, G. R., Wadley, M. R., Stevens, D. P., and Johnson, J. A.: Prediction of iceberg trajectories for the North Atlantic and Arctic Oceans, *Geophys. Res. Lett.*, 23, 3587–3590, 1996.
- Bigg, G. R., Wadley, M. R., Stevens, D. P., and Johnson, J. A.: Modelling the dynamics and thermodynamics of icebergs, *Cold Reg. Sci. Technol.*, 26, 113–135, 1997.
- Braconnot, P., Otto-Bliesner, B., Harrison, S., Joussaume, S., Peterchmitt, J.-Y., Abe-Ouchi, A., Crucifix, M., Driesschaert, E., Fichefet, Th., Hewitt, C. D., Kageyama, M., Kitoh, A., Loutre, M.-F., Marti, O., Merkel, U., Ramstein, G., Valdes, P., Weber, L., Yu, Y., and Zhao, Y.: Results of PMIP2 coupled simulations of the Mid-Holocene and Last Glacial Maximum - Part 2: feedbacks with emphasis on the location of the ITCZ and mid- and high latitudes heat budget, *Clim. Past*, 3, 279–296, doi:10.5194/cp-3-279-2007, 2007.
- Briffa, K. R.: Annual climate variability in the Holocene: interpreting the message of ancient trees, *Quaternary Sci. Rev.*, 19(1–5), 87–105, 2000.
- Briffa, K. R., Osborn, T., Schweingruber, F., Harris, I., Jones, P., Shiyatov, S., and Vaganov, E.: Low-frequency temperature variations from a northern tree ring density network, *J. Geophys. Res.*, 106(D3), 2929–2941, 2001.
- Briffa, K. R., Osborn, T. J., and Schweingruber, F. H.: Large-scale temperature inferences from tree rings: a review, *Global Planet. Change*, 40(1–2), 11–26, 2004.
- Brohan, P., Kennedy, J. J., Harris, I., Tett, S. F. B., Jones, P. D.: Uncertainty estimates in regional and global observed temperature changes: A new data set from 1850, *J. Geophys. Res.*, 111, D12106, doi:10.1029/2005JD006548, 2006.
- Brovkin, V., Ganopolski, A., and Svirezhev, Y.: A continuous climate-vegetation classification for use in climate-biosphere studies, *Ecol. Model.*, 101, 251–261, 1997.
- Brovkin, V., Bendtsen, J., Claussen, M., Ganopolski, A., Kutzbach, C., Petoukhov, V., and Andreev, A.: Carbon cycle, vegetation and Clim. Dynam. in the Holocene: experiments with the CLIMBER-2 model, *Global Biogeochem. Cy.*, 16(4), 1139, doi:10.1029/2001GB001662, 2002.
- Bryan, K. and Lewis, L. J.: A water mass model of the world ocean, *J. Geophys. Res.*, 84, 2503–2517, 1979.
- Campin, J. M. and Goosse, H.: A parameterization of density driven downsloping flow for coarse resolution model in z-coordinate, *Tellus A*, 51, 412–430, 1999.

- Charlson, R. J., Langner, J., Rodhe, H., Leovy, C. B., and Warren, S. G.: Perturbation of the Northern Hemisphere radiative balance by backscattering from anthropogenic sulfate aerosols, *Tellus AB*, 43, 152–163, 1991.
- Chapin, F. S., Bret-Harte, M. S., Hobbie, S. E., and Zhong, H. L.: Plant functional types as predictors of transient responses of arctic vegetation to global change, *J. Veg. Sci.*, 7, 347–358, 1996.
- Chou, C. and Neelin, J. D.: Linearization of a long-wave radiation scheme for intermediate tropical atmospheric model, *J. Geophys. Res.*, 101, 15129–15145, 1996.
- Claussen, M., Mysak, L. A., Weaver, A. J., Crucifix, M., Fichet, T., Loutre, M. F., Weber, S. L., Alcamo, J., Alexeev, V. A., Berger, A., Calov, R., Ganopolski, A., Goosse, H., Lohman, G., Lunkeit, F., Mohkov, I. I., Petoukhov, V., Stone, P., and Wang, Z.: Earth System Models of Intermediate Complexity: closing the gap in the spectrum of climate system models, *Clim. Dynam.*, 18, 579–586, 2002.
- Comiso, J. C. and Nishio, F.: Trends in the sea ice cover using enhanced and compatible AMSR-E, SSM/I, and SMMR data, *J. Geophys. Res.*, 113, C02S07, doi:10.1029/2007JC004257, 2008.
- Cook, E. R., Esper, J., and D'Arrigo, R. D.: Extra-tropical Northern Hemisphere land temperature variability over the past 1000 years, *Quaternary Sci. Rev.*, 23(20–22), 2063–2074, 2004.
- Cox, M.: Isopycnal diffusion in a z -coordinate ocean model, *Ocean Model.*, 74, 1–5, 1987.
- Cramer, W., Bondeau, A., Woodward, F. I., Prentice, I. C., Betts, R. A., Brovkin, V., Cox, P. M., Fisher, V., Foley, J. A., Friend, A. D., Kucharik, C., Lomas, M. R., Ramankutty, N., Sitch, S., Smith, B., White, A., and Young-Molling, C.: Global response of terrestrial ecosystem structure and function to CO₂ and climate change: results from six dynamic global vegetation models, *Glob. Change Biol.*, 7, 357–373, 2001.
- Crespin, E., Goosse, H., Fichet, T., and Mann, M. E.: The 15th century Arctic warming in coupled model simulations with data assimilation, *Clim. Past*, 5, 389–401, doi:10.5194/cp-5-389-2009, 2009.
- Crowley, T. J., Baum, S. K., Kim, K. Y., Hegerl, G. C., and Hyde, W. T.: Modeling ocean heat content changes during the last millennium, *Geophys. Res. Lett.*, 30(18), 1932, doi:10.1029/2003GL017801, 2003.
- D'Arrigo, R., Wilson, R., and Jacoby, G.: On the long-term context for late twentieth century warming, *J. Geophys. Res.*, 111, D03103, doi:10.1029/2005JD006352, 2006.
- Deleersnijder, E., Beckers, J.-M., Campin, J.-M., El Mohajir, M., Fichet, T., and Luyten, P.: Some mathematical problems associated with the development and use of marine models, in: *The mathematics of model for climatology and environment*, edited by: Diaz, J. I., NATO ASI Series, Springer-Verlag, I(48), 39–86, 1997.
- Deleersnijder, E. and Campin, J.-M.: On the computation of the barotropic mode of a free-surface world ocean model, *Ann. Geophys.*, 13, 675–688, doi:10.1007/s00585-995-0675-x, 1995.
- den Elzen, M., Beusen, A., and Rothmans, J.: Modelling Global Biogeochemical Cycles: an integrated assessment approach, Bilthoven, RIVM report no. 461502007, 104 pp., 1995.
- de Vries, P. and Weber, S. L.: The Atlantic freshwater budget as a diagnostic for the existence of a stable shut-down of the meridional overturning circulation, *Geophys. Res. Lett.*, 32, L09606, doi:10.1029/2004GL021450, 2005.
- Dickson, A. G. and Riley, J. P.: The estimation of acid dissociation constants in seawater media from potentiometric titrations with strong base. I. The ionic product of water – K_W , *Mar. Chem.*, 7, 89–99, 1979.
- Dickson, A. G.: An exact definition of total alkalinity and a procedure for the estimation of alkalinity and total inorganic carbon from titration data, *Deep-Sea Res.*, 28A, 609–623, 1981.
- Dickson, A. G. and Millero, F.: A comparison of the equilibrium constants for the dissociation of carbonic acid in seawater media, *Deep-Sea Res.*, 34, 1733–1743, 1987.
- Dickson, A. G.: Thermodynamics of the dissociation of boric acid in synthetic seawater from 273.15 to 318.15 K, *Deep-Sea Res.*, 37, 755–766, 1990.
- Driesschaert, E.: Climate change over the next millennia using LOVECLIM, a new Earth system model including the polar ice sheets, Ph.D. thesis, Université catholique de Louvain, available at: <http://hdl.handle.net/2078.1/5375> (last access: 2009), 2005.
- Driesschaert, E., Fichet, T., Goosse, H., Huybrechts, P., Janssens, I., Mouchet, A., Munhoven, G., Brovkin, V., and Weber, S. L.: Modeling the influence of Greenland ice sheet melting on the Atlantic meridional overturning circulation during the next millennia, *Geophys. Res. Lett.*, 34, L10707, doi:10.1029/2007GL029516, 2007.
- Duplessy, J. C., Roche, D. M., and Kageyama, M.: The deep ocean during the last interglacial period, *Science*, 316(5821), 89–91, 2007.
- Eltahan, M., Eltahan, H., and Venkatesh, S.: Forecast of Iceberg Ensemble Drift, *Offshore*, 43, 94–94, 1983.
- Esper, J., Cook, E. R., and Schweingruber, F. H.: Low-frequency signals in long tree-ring chronologies for reconvariability, *Science*, 295(5563), 2250–2253, 2002.
- Etheridge, D. M., Steele, L. P., Langenfelds, R. L., Francey, R. J., Barnola, J.-M., and Morgan, V. I.: Historical CO₂ records from the Law Dome DE08, DE08-2, and DSS ice cores, in: *Trends: A Compendium of Data on Global Change, Carbon Dioxide Information Analysis Center, Oak Ridge National Laboratory, US Department of Energy, Oak Ridge, Tenn., USA*, 1998.
- Fasham, M. J.: Modelling the marine biota, in: *The Global Carbon Cycle*, edited by: Heimann, M., Springer Verlag, Berlin Heidelberg, volume I15 of NATO ASI Series, 457–504, 1993.
- Fichet, T. and Morales Maqueda, M. A.: Sensitivity of a global sea ice model to the treatment of ice thermodynamics and dynamics, *J. Geophys. Res.* 102(C6), 12609–12646, 1997.
- Fichet, T. and Morales Maqueda, M. A.: Modelling the influence of snow accumulation and snow-ice formation on the seasonal cycle of the Antarctic sea-ice cover, *Clim. Dynam.*, 15(4), 251–268, 1999.
- Flückiger, J., Knutti, R., White, J. W. C., and Renssen, H.: Modeled seasonality of glacial abrupt climate change, *Clim. Dynam.*, 31, 633–645, doi:10.1007/s00382-008-0373-y, 2008.
- Foukal, P., Frölich, C., Spruit, H., and Wigley, T. M. L.: Variations in solar luminosity and their effect on the Earth's climate, *Nature*, 443, 161–166, 2006.
- Frank, D. C., Esper, J., Raible, C. C., Buntgen, U., Trouet, V., Stocker, B., and Joos, F.: Ensemble reconstruction constraints on the global carbon cycle sensitivity to climate, *Nature*, 463, 527–U143, 2010.
- Ganachaud, A. and Wunsch, C.: Improved estimates of global ocean circulation, heat transport and mixing from hydrographic data,

- Nature, 408, 453–457, 2000.
- Gadd, A. J.: A split-explicit integration scheme for numerical weather prediction, *Q. J. Roy. Meteor. Soc.*, 104, 569–582, 1978.
- Gent, P. R. and McWilliams, J. C.: Isopycnal mixing in ocean general circulation models, *J. Phys. Oceanogr.*, 20, 150–155, 1990.
- Gladstone, R. M., Bigg, G. R., and Nicholls, K. W.: Iceberg trajectory modeling and meltwater injection in the Southern Ocean, *J. Geophys. Res.-Oceans*, 106, 19903–19915, 2001.
- Glen, J. W.: The creep of polycrystalline ice, *P. R. Soc. Lond.-B*, 228, 519–538, 1955.
- Goelzer, H., Huybrechts, P., Loutre, M. F., Goosse, H., Fichet, T., and Mouchet, A.: Impact of Greenland and Antarctic ice sheet interactions on climate sensitivity, *Clim. Dynam.*, in press, doi:10.1007/s00382-010-0885-0, 2010.
- Goosse, H., Campin, J.-M., Fichet, T., and Deleersnijder, E.: Sensitivity of a global ice-ocean model to the Bering Strait through-flow, *Clim. Dynam.*, 13, 349–358, 1997.
- Goosse, H. and Fichet, T.: Importance of ice-ocean interactions for the global ocean circulation: a model study, *J. Geophys. Res.*, 104, 23337–23355, 1999.
- Goosse, H., Selten, F. M., Haarsma, R. J., and Opsteegh, J. D.: Decadal variability in high northern latitudes as simulated by an intermediate complexity climate model, *Ann. Glaciol.*, 33, 525–532, 2001.
- Goosse, H., Selten, F. M., Haarsma, R. J., and Opsteegh, J. D.: A mechanism of decadal variability of the sea-ice volume in the Northern Hemisphere, *Clim. Dynam.*, 19, 61–83, doi:10.1007/s00382-001-0209-5, 2002.
- Goosse, H., Renssen, H., Timmermann, A., and Bradley, R. S.: Internal and forced climate variability during the last millennium: a model-data comparison using ensemble simulations, *Quaternary Sci. Rev.*, 24, 1345–1360, 2005.
- Goosse, H., Driesschaert, E., Fichet, T., and Loutre, M.-F.: Information on the early Holocene climate constrains the summer sea ice projections for the 21st century, *Clim. Past*, 3, 683–692, doi:10.5194/cp-3-683-2007, 2007.
- Goosse, H., Cressin, E., de Montety, A., Mann, M. E., Renssen, H., and Timmermann, A.: Reconstructing surface temperature changes over the past 600 years using climate model simulations with data assimilation, *J. Geophys. Res.-Atmos.*, 115, D09108, doi:10.1029/2009JD012737, 2010.
- Gregory, J. M., Dixon, K. W., Stouffer, R. J., Weaver, A. J., Driesschaert, E., Eby, M., Fichet, T., Hasumi, H., Hu, A., Jungclaus, J. H., Kamenskovich, I. V., Levermann, A., Montoya, M., Murakami, S., Nawrath, S., Oka, A., Sokolov, A. P., and Thorpe, R. B.: A model intercomparison of changes in the Atlantic thermohaline circulation in response to increasing atmospheric CO₂ concentration, *Geophys. Res. Lett.*, 32, L12703, doi:10.1029/2005GL023209, 2005.
- Greenfell, T. C. and Perovich, D. K.: Spectral albedos of sea ice and incident solar irradiance in the southern Beaufort Sea, *J. Geophys. Res.*, 89, 3573–3580, 1984.
- Hegerl, G. C., Crowley, T. J., Hyde, W. T., and Frame, D. J.: Climate sensitivity constrained by temperature reconstructions over the past seven centuries, *Nature*, 440, 1029–1032, 2006.
- Haarsma, R. J., Selten, F. M., Opsteegh, J. D., Lenderink, G., and Liu, Q.: ECBilt, a coupled atmosphere ocean sea-ice model for climate predictability studies, KNMI, De Bilt, The Netherlands, 31 pp., 1996.
- Heinze, C., Hupe, A., Maier-Reimer, E., Dittert, N., and Rague-neau, O.: Sensitivity of the marine biospheric Si cycle for biogeochemical parameter variations, *Global Biogeochem. Cy.*, 17(3), 1086, doi:10.1029/2002GB001943, 2003.
- Held, I. M. and Suarez, M. J.: A two level primitive equation atmosphere model designed for climate sensitivities experiments, *J. Atmos. Sci.*, 35, 206–229, 1978.
- Hibler, W. D.: A dynamic thermodynamic sea ice model, *J. Phys. Oceanogr.*, 9, 815–846, 1979.
- Holdridge, L. R.: Determination of world plant formation from simple climate data, *Science*, 105, 367–368, 1947.
- Holton, J. R.: An introduction to dynamical meteorology, 4th edn., Elsevier, International Geophysics Series, 88, 535 pp., 2004.
- Hutter, K.: Theoretical Glaciology, D. Reidel, Dordrecht, 510 pp., 1983.
- Huybrechts, P.: The Antarctic ice sheet and environmental change: a three-dimensional modelling study, *Berichte zur Polarforschung*, 99, 241 pp., 1992.
- Huybrechts, P.: Sea-level changes at LGM from ice-dynamic reconstructions of the Greenland and Antarctic ice sheets during glacial cycles, *Quaternary Sci. Rev.*, 21, 203–231, 2002.
- Huybrechts, P. and de Wolde, J.: The dynamic response of the Greenland and Antarctic ice sheets to multiple-century climatic warming, *J. Climate*, 12(8), 2169–2188, 1999.
- Huybrechts, P., and Miller, H.: Flow and balance of the polar ice sheets, in: *Observed global climate, Landolt-Boernstein/ New Series (Numerical data and functional relationships in Science and Technology)*, V/6, edited by: Hantel, M., Springer Verlag, Berlin, Heidelberg, New York, 13/1–13, 2005.
- Indermühle, A., Stocker, T. F., Joos, F., Fischer, H., Smith, H. J., Wahlen, M., Deck, B., Mastroianni, D., Tschumi, J., Blunier, T., Meyer, R., and Stauffer, B.: Holocene carbon-cycle dynamics based on CO₂ trapped in ice at Taylor Dome, Antarctica, *Nature*, 398, 121–126, 1999.
- International GEWEX Project Office: GSWP-2: The Second Global Soil Wetness Project Science and Implementation Plan. IGPO Publication Series No. 37, 65 pp., 2002.
- Janssens, I. and Huybrechts, P.: The treatment of meltwater retention in mass-balance parameterizations of the Greenland ice sheet, *Ann. Glaciol.*, 31, 133–140, 2000.
- Jiang, H., Eiriksson, J., Schulz, M., Knudsen, K.-L., and Seidenkrantz, M. S.: Evidence for solar forcing of sea-surface temperature on the North Icelandic shelf during the late Holocene, *Geology*, 33, 73–76, 2005.
- Jones, P. D., Briffa, K. R., Barnett, T. P., and Tett, S. F. B.: High-resolution palaeoclimatic records for the last millennium: interpretation, integration and comparison with General Circulation Model control-run temperatures, *The Holocene*, 8(4), 455–471, 1998.
- Jones, P. D., Osborn, T. J., and Briffa, K. R.: The evolution of climate over the last millennium, *Science*, 292(5517), 662–667, 2001.
- Jongma, J. I., Driesschaert, E., Fichet, T., Goosse, H., and Renssen, H.: The effect of dynamic-thermodynamic icebergs on the Southern Ocean climate in a three-dimensional model, *Ocean Model.*, 26, 104–113, 2009.
- Kalnay, E., Kanamitsu, M., Kistler, R., Collins, W., Deaven, D., Gandin, L., Iredell, M., Saha, S., White, G., Woollen, J., Zhu, Y., Chelliah, M., Ebisuzaki, W., Higgins, W., Janowiak, J., Mo, K.

- C., Ropelewski, C., Wang, J., Leetmaa, A., Reynolds, R., Jenne, R., and Joseph, D.: The NCEP/NCAR 40-year reanalysis project, *B. Am. Meteorol. Soc.*, 77, 437–471, 1996.
- Karsten, R. and Marshall, J.: Constructing the residual circulation of the Antarctic Circumpolar Current from observations, *J. Phys. Oceanogr.*, 32(12), 3315–3327, 2002.
- Lean, J. L., Wang, Y.-M., and Sheeley, N. R.: The effect of increasing solar activity on the Sun's total and open magnetic flux during multiple cycles: implications for solar forcing of climate, *Geophys. Res. Lett.*, 29(24), 2224, doi:10.1029/2002GL015880, 2002.
- Levitus, S., Antonov, J. I., Boyer, T. P., Locarnini, R. A., Garcia, H. E., and Mishonov, A. V.: Global ocean heat content 1955–2008 in light of recently revealed instrumentation problems, *Geophys. Res. Lett.*, 36, L07608, doi:10.1029/2008GL037155, 2009.
- Leemans, R. and Cramer, W. P.: The IIASA database for mean monthly values of temperature, precipitation and cloudiness on a global terrestrial grid, *Int. Inst. for Appl. Syst. Anal.*, Laxenburg, Austria, Research rep. RR-91-18, 1991.
- Lieth, H.: Modeling the primary productivity of the world, in *Primary Productivity of the Biosphere*, edited by: Lieth, H. and Whittaker, R. H., Springer-Verlag, New York, 237–263, 1975.
- Lorenzo, M. N., Taboada, J. J., Iglesias, I., and Álvarez, I.: The role of stochastic forcing on the behaviour of the thermohaline circulation, *Annals of the New York Academy of Sciences*, in: *Trends and Directions in Climate Research*, 1146(1), 60–86, ISBN:1-57331-732-2, 2008.
- Loset, S.: Thermal-Energy Conservation in Icebergs and Tracking by Temperature, *J. Geophys. Res.-Oceans*, 98, 10001–10012, 1993.
- Loutre, M. F., Mouchet, A., Fichet, T., Goosse, H., Goelzer, H., and Huybrechts, P.: Evaluating climate model performance with various parameter sets using observations over the last centuries, *Clim. Past Discuss.*, 6, 711–765, doi:10.5194/cpd-6-711-2010, 2010.
- Lynch-Stieglitz, J., Adkins, J. F., Curry, W. B., Dokken, T., Hall, I. R., Herguera, J. C., Hirschi, J. J. M., Ivanova, E. V., Kissel, C., Marchal, O., Marchitto, T. M., McCave, I. N., McManus, J. F., Mulitza, S., Ninnemann, U., Peeters, F., Yu, E. F., and Zahn, R.: Atlantic Meridional Overturning Circulation During the Last Glacial Maximum, *Science*, 316, 66–69, 2007.
- Maier-Reimer, E.: Geochemical cycles in an ocean general circulation model. Preindustrial tracer distributions, *Global Biogeochem. Cy.*, 7, 645–677, 1993.
- Mann, M. E., Bradley, R. S., and Hughes, M. K.: Northern hemisphere temperatures during the past millennium: Inferences, uncertainties, and limitations, *Geophys. Res. Lett.*, 26(6), 759–762, 1999.
- Mann, M. E. and Jones, P. D.: Global surface temperatures over the past two millennia, *Geophys. Res. Lett.*, 30(15), 1820, doi:10.1029/2003GL017814, 2003.
- Marland, G., Boden, T., and Andres, R.: Global, Regional, and National Annual CO₂ Emissions from Fossil-Fuel Burning, Cement Production, and Gas Flaring: 1751–2000, in: *Trends: A compendium of data on global change*, published by Carbon Dioxide Information Analysis Center, Oak Ridge, Tennessee, 2003.
- Marshall, J. and Molteni, F.: Towards a dynamic understanding of planetary-scale flow regimes, *J. Atmos. Sci.*, 50, 1792–1818, 1993.
- Martin, J. H., Knauer, G. A., Karl, D. M., and Broenkow, W. W.: VERTEX: carbon cycling in the northeast Pacific, *Deep-Sea Res.*, 34, 267–285, 1987.
- Mathieu, P. P. and Deleersnijder, E.: Accuracy and stability of the discretised isopycnal-mixing equation, *Appl. Math. Lett.*, 12(4), 81–88, 1999.
- Mellor, G. L. and Yamada, T.: Development of a turbulence closure model for geophysical fluid problems, *Rev. Geophys. Space Phys.*, 20(4), 851–875, 1982.
- Menviel, L., Timmermann, A., Mouchet, A., and Timm, O.: Meridional reorganizations of marine and terrestrial productivity during Heinrich events, *Paleoceanography*, 23, PA1203, doi:10.1029/2007PA001445, 2008.
- Menviel, L.: Climate-carbon cycle interactions on millennial to glacial timescales as simulated by a model of intermediate complexity, Ph.D. thesis, University of Hawaii, 179 pp., available at: <http://www.soest.hawaii.edu/oceanography/students/lmenviel/Menvielthesis2008.pdf> (last access: 2009), 2008.
- Mesinger, F. and Arakawa, A.: Numerical methods used in atmospheric models, WMO-ISCU Joint Organizing Committee, GARP Publications Series 17, 37 pp., 1976.
- Millero, F. J.: Thermodynamics of the carbon dioxide system in the oceans, *Geochim. Cosmochim. Ac.*, 59, 661–677, 1995.
- Moberg, A., Sonechkin, D. M., Holmgren, K., Datsenko, N. M., and Karlén, W.: Highly variable Northern Hemisphere temperatures reconstructed from low- and high-resolution proxy data, *Nature*, 433(7026), 613–617, 2005.
- Mouchet, A. and François, L. M.: Sensitivity of a global oceanic carbon cycle model to the circulation and the fate of organic matter: preliminary results, *Phys. Chem. Earth*, 21, 511–516, 1996.
- Mouchet, A.: A 3D model of ocean biogeochemical cycles and climate sensitivity studies, Ph.D. thesis, Université de Liège, Liège, Belgium, in preparation, 2010.
- Mucci, A.: The solubility of calcite and aragonite in seawater at various salinities, temperatures, and one atmosphere total pressure, *Am. J. Sci.*, 283, 780–799, 1983.
- Muscheler, R., Joos, F., Beer, J., Muller, S. A., Vonmoos, M., and Snowball, I.: Solar activity during the last 1000 yr inferred from radionuclide records, *Quaternary Sci. Rev.*, 26(1–2), 82–97, 2007.
- Najjar, R. J., Jin, X., Louanchi, F., Aumont, O., Caldeira, K., Doney, S. C., Dutay, J.-C., Follows, M., Gruber, N., Joos, F., Lindsay, K., Maier-Reimer, E., Matear, R. J., Matsumoto, K., Mouchet, A., Orr, J. C., Plattner, G.-K., Sarmiento, J. L., Schlitzer, R., Weirig, M. F., Yamanaka, Y., and Yool, A.: Impact of circulation on export production, dissolved organic matter, and dissolved oxygen in the ocean: Results from Phase II of the Ocean Carbon-cycle Model Intercomparison Project (OCMIP-2), *Global Biogeochem. Cy.*, 21, GB3007, doi:10.1029/2006GB002857, 2007.
- Neftel, A., Friedli, H., Moor, E., Lotscher, H., Oeschger, H., Siegenthaler, U., and Stauffer, B.: Historic CO₂ record from the Siple Station ice core, in: *Trends '93: A Compendium of Data on Global Change*, edited by: Boden, T. A., Kaiser, D. P., Sepanski, R. J., and Stoss, F. W., Carbon Dioxide Information Analysis Center, Oak Ridge National Laboratory, Oak Ridge, Tenn., USA, ORNL/CDIAC-65, 11–14, 1994.
- Nelson, D. M., Tréguer, P., Brzezinski, M. A., Leynaert, A., and Quéguiner, B.: Production and dissolution of biogenic silica in the ocean: revised global estimates, comparison with regional

- data and relationship to biogenic sedimentation, *Global Biogeochem. Cy.*, 9, 359–372, 1995.
- Olson, J., Watts, J. A., and Allison, L. J.: Major world ecosystem complexes ranked by carbon in live vegetation: A database, CDIAC Numerical Data Collection, Oak Ridge Natl. Lab., Oak Ridge, Tenn., NDP-017, 164 pp., 1985.
- Opsteegh, J. D., Haarsma, R. J., Selten, F. M., and Kattenberg, A.: ECBilt: A dynamic alternative to mixed boundary conditions in ocean models, *Tellus A*, 50, 348–367, 1998.
- Paterson, W. S. B.: *The physics of glaciers*, 3rd edn., Pergamon Press, Oxford, 480 pp., 1994.
- Peltier, W. R.: Global isostasy and the surface of the ice-age Earth: the ice-5g (Vm2) Model and Grace, *Annu. Rev. Earth Pl. Sc.*, 32, 111–149, 2004.
- Petoukhov, V., Claussen, M., Berger, A., Crucifix, M., Eby, M., Eliseev, A., Fichefet, T., Ganopolski, A., Goosse, H., Kamenkovich, I., Mokhov, I., Montoya, M., Mysak, L. A., Sokolov, A., Stone, P., Wang, Z., and Weaver, A. J.: EMIC Inter-comparison Project (EMIP-CO2): Comparative analysis of EMIC simulations of climate, and of equilibrium and transient responses to atmospheric CO₂ doubling, *Clim. Dynam.*, 25 363–385, 2005.
- Pollack, H. N. and Smerdon, J. E.: Borehole climate reconstructions: Spatial structure and hemispheric averages, *J. Geophys. Res.*, 109(D11), D11106, doi:10.1029/2003JD004163, 2004.
- Post, W. M., King, A. W., and Wullschleger, S. D.: Historical variations in terrestrial biospheric carbon cycle, *Global Biogeochem. Cy.*, 11, 99–109, 1997.
- Prather, M. C.: Numerical advection by conservation of second-order moments, *J. Geophys. Res.*, 91(D6), 6671–6681, 1986.
- Prentice, I. C., Cramer, W., Harrison, S. P., Leemans, R., Monserud, R. A., and Solomon, A. M.: A global biome model based on plant physiology and dominance, soil properties and climate, *J. Biogeogr.*, 19, 117–134, 1992.
- Qiuzhen Yin, Berger, A., Driesschaert, E., Goosse, H., Loutre, M. F., and Crucifix, M.: The Eurasian ice sheet reinforces the East Asian summer monsoon during the interglacial 500 000 years ago, *Clim. Past*, 4, 79–90, doi:10.5194/cp-4-79-2008, 2008.
- Rahmstorf, S., Crucifix, M., Ganopolski, A., Goosse, H., Kamenkovich, I., Knutti, R., Lohmann, G., Marsh, B., Mysak, L., Wang, Z., and Weaver, A.: Thermohaline circulation hysteresis: a model intercomparison, *Geophys. Res. Lett.*, 32, L23605, doi:10.1029/2005GL23655, 2005.
- Randall, D. A., Wood, R. A., Bony, S., Colman, R., Fichefet, T., Fyfe, J., Kattsov, V., Pitman, A., Shukla, J., Noda, A., Srinivasan, J., Stouffer, R. J., Sumi, A., and Taylor, K. E.: Climate models and their evaluation. In: *Climate Change 2007: The Physical Science Basis*, in: Contribution of Working Group I to the Fourth Assessment Report of the Intergovernmental Panel on Climate Change, edited by: Solomon, S., Qin, D., Manning, M., Chen, Z., Marquis, M., Averyt, K. B., Tignor, M., and Miller, H. L., Cambridge University Press, Cambridge, United Kingdom and New York, NY, USA, 2007.
- Ramankutty, N. and Foley, J. A.: Estimating historical changes in global land cover: croplands from 1700 to 1992, *Global Biogeochem. Cy.*, 13(4), 997–1027, 1999.
- Rayner, N. A., Parker, D. E., Horton, E. B., Folland, C. K., Alexander, L. V., Rowell, D. P., Kent, E. C., and Kaplan, A.: Global analyses of sea surface temperature, sea ice, and high marine air temperature since the late nineteenth century, *J. Geophys. Res.*, 108(D14), 4407, doi:10.1029/2002JD002670, 2003.
- Redfield, A., Ketchum, B., and Richards, F.: The influence of organisms on the composition of seawater, in: *The Sea*, edited by: Hill, M. N., Wiley Interscience, New York, 2, 26–77, 1963.
- Redi, M. H.: Oceanic isopycnal mixing coordinate rotation, *J. Phys. Oceanogr.*, 12, 1154–1158, 1982.
- Renssen, H., Goosse, H., Fichefet, T., and Campin, J.-M.: The 8.2 kyr BP event simulated by a global atmosphere-sea-ice-ocean model, *Geophys. Res. Lett.*, 28, 1567–1570, 2001.
- Renssen, H., Brovkin, V., Fichefet, T., and Goosse, H.: Holocene climatic instability during the termination of the African Humid Period, *Geophys. Res. Lett.*, 30(4), 1184, doi:10.1029/2002GL016636, 2003.
- Renssen, H., Goosse, H., Fichefet, T., Brovkin, V., Driesschaert, E., and Wolk, F.: Simulating the Holocene climate evolution at northern high latitudes using a coupled atmosphere-sea ice-ocean-vegetation mode, *Clim. Dynam.*, 24, 23–43, 2005.
- Roche, D. M., Dokken, T. M., Goosse, H., Renssen, H., and Weber, S. L.: Climate of the Last Glacial Maximum: sensitivity studies and model-data comparison with the LOVECLIM coupled model, *Clim. Past*, 3, 205–224, doi:10.5194/cp-3-205-2007, 2007.
- Rossow, W. B., Walker, A. W., Beusichel, D. E., and Roiter, M. D.: International satellite cloud climatology project (ISCCP) documentation of new cloud datasets, WMO/TD-No 737, World Meteorological Organisation, 1996.
- Rutherford, S., Mann, M. E., Osborn, T. J., Bradley, R. S., Briffa, K. R., Hughes, M. K., and Jones, P. D.: Proxy-based Northern Hemisphere surface temperature reconstructions: Sensitivity to method, predictor network, target season, and target domain, *J. Climate*, 18(13), 2308–2329, 2005.
- Schaeffer, M., Selten, F., and van Dorland, R.: Linking Image and ECBilt. National Institute for public health and the environment (RIVM), Bilthoven, The Netherlands, Report no 4815008008, 1998.
- Schaeffer, M., Selten, F., Goosse, H., and Opsteegh, T.: On the influence of location of high-latitude ocean deep convection and Arctic sea-ice on climate change projections, *J. Climate*, 17(22), 4316–4329, 2004.
- Schimel, D. S., Braswell, B. H., Holland, E. A., McKeown, R., Ojima, D. S., Painter, T. H., Parton, W. J., and Townsend, A. R.: Climatic, edaphic, and biotic control over storage and turnover of carbon in soil, *Global Biogeochem. Cy.*, 8, 279–293, 1994.
- Selten, F. M., Haarsma, R. J., and Opsteegh, J. D.: On the mechanism of North Atlantic decadal variability, *J. Climate*, 12, 1956–1973, 1999.
- Shine, K. P. and Henderson-Sellers, A.: The sensitivity of a thermodynamic sea ice model to changes in surface albedo parameterization, *J. Geophys. Res. Lett.*, 90, 2243–2250, 1985.
- Siegenthaler, U., Monnin, E., Kawamura, K., Spahni, R., Schwander, J., Stauffer, B., Stocker, T. F., Barnola, J.-M., and Fischer, H.: Supporting evidence from the EPICA Dronning Maud Land ice core for atmospheric CO₂ changes during the past millennium, *Tellus B*, 57, 51–57(7), 2005.
- Smith, S. D.: Hindcasting Iceberg Drift Using Current Profiles and Winds, *Cold Reg. Sci. Technol.*, 22, 33–45, 1993.
- Svirezhev, Y.: Simplest dynamic models of the global vegetation pattern, *Ecol. Model.*, 124, 131–144, 1999.

- Swingedouw, D., Fichefet, T., Huybrechts, P., Goosse, H., Driesschaert, E., and Loutre, M.-F.: Antarctic ice-sheet melting provides negative feedbacks on future climate warming, *Geophys. Res. Lett.*, 35, L17705, doi:10.1029/2008GL034410, 2008.
- Tartinville, B., Campin, J. M., Fichefet, T., and Goosse, H.: Realistic representation of the surface freshwater flux in an ice-ocean general circulation model, *Ocean Model.*, 3(1–2), 95–108, 2001.
- Terray, L., Valcke, S., and Piacentini, A.: OASIS 2.2, Ocean Atmosphere Sea Ice Soil user's guide and reference manuel, CERFACS Tech. Rep. TR/CGMC/98-05, 69 pp., 1998.
- Timm, O., Timmermann, A., Abe-Ouchi, A., Saito, F., and Segawa, T.: On the definition of seasons in paleoclimate simulations with orbital forcing, *Paleoceanography*, 23, PA2221, doi:10.1029/2007PA001461, 2008.
- Timmermann, A. and Goosse, H.: Is the wind stress forcing essential for the meridional overturning circulation?, *Geophys. Res. Lett.*, 31, L04303, doi:10.1029/2003GL018777, 2004.
- Timmermann, A., Justino Barbosa, F., Jin, F. F., and Goosse, H.: Surface temperature control in the North Pacific during the last glacial maximum, *Clim. Dynam.*, 23, 353–370, doi:10.1007/s00382-004-0434-9, 2004.
- Timmermann, A., An, S.-I., Krebs, U., and Goosse, H.: ENSO suppression due to weakening of the North Atlantic thermohaline circulation, *J. Climate*, 18(16), 3122–3139, 2005.
- van der Schrier, G. and Barkmeijer, J.: Bjerknes' hypothesis on the coldness during AD 1790–1820 revisited, *Clim. Dynam.*, 24, 335–371, 2005.
- van der Schrier, G., Drijfhout, S. S., Hazeleger, W., and Noulin, L.: Increasing the Atlantic subtropical jet cools the circum-North Atlantic region, *Meteorol. Z.*, 16(6) 675–684, 2007.
- Wanninkhof, R.: Relationship between wind speed and gas exchange over the ocean, *J. Geophys. Res.*, 97, 7373–7382, 1992.
- Wanninkhof, R. and Knox, M.: Chemical enhancement of CO₂ exchange in natural waters, *Limnol. Oceanogr.*, 41, 689–697, 1996.
- Weber, S. L. and Oerlemans, J.: Holocene glacier variability: three case studies using an intermediate-complexity climate model, *The Holocene*, 13, 353–363, 2003.
- Weber, S. L., Drijfhout, S. S., Abe-Ouchi, A., Crucifix, M., Eby, M., Ganopolski, A., Murakami, S., Otto-Bliesner, B., and Peltier, W. R.: The modern and glacial overturning circulation in the Atlantic ocean in PMIP coupled model simulations, *Clim. Past*, 3, 51–64, doi:10.5194/cp-3-51-2007, 2007.
- Weeks, W. F. and Campbell, W. J.: Towing Icebergs to Irrigate Arid Lands – Manna or Madness, *Science and Public Affairs-Bulletin of the Atomic Scientists*, 29, 35–39, 1973.
- Weertman, J.: The theory of glacier sliding, *J. Glaciol.*, 5(39), 287–303, 1964.
- Weiss, R. F.: Carbon dioxide in water and seawater: the solubility of a non-ideal gas, *Mar. Chem.*, 2, 203–215, 1974.
- Wiersma, A. P. and Jongma, J. I.: A role for icebergs in the 8.2 ka climate event, *Clim. Dynam.*, 35(2–3), 535–549, doi:10.1007/s00382-009-0645-1, 2009.
- Woodward, F. I.: *Climate and Plant Distribution*, Cambridge Univ. Press, New York, 174 pp., 1987.
- Xie, P. and Arkin, P. A.: Analyses of global monthly precipitation using gauge observations, satellite estimates and numerical model predictions, *J. Climate*, 9, 840–858, 1996.
- Zhang, J. L. and Hibler, W. D.: On an efficient numerical method for modeling sea ice dynamics, *J. Geophys. Res.*, 102(C4), 8691–8702, 1997.
- Zhao, Y., Braconnot, P., Marti, O., Harrison, S. P., Hewitt, C. D., Kitoh, A., Liu, Z., Mikolajewicz, U., Otto-Bliesner, B., and Weber, S. L.: A multi-model analysis of ocean feedbacks on the African and Indian monsoon during the mid-Holocene, *Clim. Dynam.*, 25, 777–800, 2005.

Bibliography

- Adkins, J. F., and E. A. Boyle, Changing atmospheric $\Delta^{14}\text{C}$ and the record of deep water paleoventilation ages, *Palaeoceanography*, *12*, 337–344, 1997.
- Alley, R. B., Ice-core evidence of abrupt climate changes, *Proceedings of the National Academy of Sciences*, *97*, 1331–1334, 2000.
- Anderson, L. A., On the hydrogen and oxygen content of marine phytoplankton, *Deep-Sea Research*, *42*, 1675–1680, 1995.
- Anderson, L. A., and J. L. Sarmiento, Redfield ratios of remineralization determined by nutrient data analysis, *Global Biogeochemical Cycles*, *8*, 65–80, 1994.
- Arakawa, A., and V. R. Lamb, Computational design of the basic dynamical process of the UCLA general circulation model, *Methods of Computational Physics*, *17*, 173–265, 1977.
- Archer, D., H. Kheshgi, and E. Maier-Reimer, Dynamics of fossil CO_2 neutralization by marine CaCO_3 , *Global Biogeochemical Cycles*, *12*, 259–276, 1998.
- Archer, D., A. Winguth, D. Lea, and N. Mahowald, What caused the glacial/interglacial pCO_2 cycles?, *Reviews of Geophysics*, *38*, 159–189, 2000.
- Aumont, O., J. C. Orr, P. Monfray, G. Madec, and E. Maier-Reimer, Nutrient trapping in the equatorial Pacific: the ocean circulation solution, *Global Biogeochemical Cycles*, *13*, 351–369, 1999.
- Bacastow, R., and E. Maier-Reimer, Ocean-circulation model of the carbon cycle, *Climate Dynamics*, *4*, 95–125, 1990.
- Banse, K., Uptake of inorganic carbon and nitrate by marine plankton and the Redfield ratio, *Global Biogeochemical Cycles*, *8*, 81–84, 1994.
- Bard, E., Correction of accelerator mass spectrometry ^{14}C ages measured in planktonic foraminifera: paleoceanographic implications, *Palaeoceanography*, *3*, 635–645, 1988.

- Baricco, A., *Océan mer*, Gallimard, Paris, 1993, 283p.
- Bengtsson, L., A numerical simulation of anthropogenic climate change, *Ambio*, XXVI, 58–65, 1997.
- Berger, A., and C. Tricot, The Greenhouse effect, *Surveys in Geophysics*, 13, 523–549, 1992.
- Berger, W. H., K. Fischer, C. Lai, and G. Wu, Ocean productivity and organic carbon flux. Part I. overview and maps of primary production and export production, *Tech. Rep. SIO Ref 87-30*, University of California, SCRIPPS Institution of Oceanography, 1987, 66p.
- Berkman, P. A., and S. L. Forman, Pre-bomb radiocarbon and the reservoir correction for calcareous marine species in the Southern Ocean, *Geophysical Research Letters*, 23, 363–366, 1996.
- Berner, R. A., The carbon cycle and CO₂ over Phanerozoic time: the role of land plants, *Philosophical Transactions of the Royal Society of London*, 353, 75–82, 1998.
- Betzer, P. R., W. J. Showers, E. A. Laws, C. D. Winn, G. R. DiTullio, and P. M. Kroopnick, Primary productivity and particule fluxes on a transect of the equator at 153 W in the Pacific Ocean, *Deep-Sea Research*, 31, 1–12, 1984.
- Bidle, K. D., M. Manganalli, and F. Azam, Regulation of oceanic silicon and carbon preservation by temperature control on bacteria, *Science*, 298, 1980–1984, 2002.
- Bolin, B., and H. Rodhe, A note on the concepts of age distribution and transit time in natural reservoirs, *Tellus*, 25, 58–62, 1973.
- Boyer, T., J. Antonov, H. Garcia, D. Johnson, R. Locarnini, A. Mishonov, M. Pitcher, O. Baranova, and I. Smolyar, World ocean database 2005, *Tech. Rep. 60*, U.S. Government Printing Office, Washington, D.C., 2006, DVDs.
- Boyle, E. A., and L. D. Keigwin, North Atlantic thermohaline circulation during the last 20,000 years: link to high latitude surface temperature, *Nature*, 330, 35–40, 1987.
- Bradley, R. S., *PALEOCLIMATOLOGY Reconstructing climates of the Quaternary*, vol. 64 of *International Geophysics Series*, second ed., Academic Press, San Diego, 1999, 613p.
- Broecker, W. S., Paleoocean circulation during the last deglaciation: a bipolar seasaw?, *Palaeoceanography*, 13, 119–121, 1998.

- Broecker, W. S., and E. Maier-Reimer, The influence of air and sea exchange on the carbon isotope distribution in the sea, *Global Biogeochemical Cycles*, 6, 315–320, 1992.
- Broecker, W. S., and T.-H. Peng, Gas exchange rates between air and sea, *Tellus*, 26, 21–35, 1974.
- Broecker, W. S., and T.-H. Peng, *Tracers in the Sea*, Lamont Doherty Geological Observatory, Columbia University, New York, 1982, 690p.
- Broecker, W. S., and T.-H. Peng, Interhemispheric transport of carbon dioxide by ocean circulation, *Nature*, 356, 587–589, 1992.
- Broecker, W. S., and T.-H. Peng, Evaluation of the ^{13}C constraint on the uptake of fossil fuel CO_2 by the ocean, *Global Biogeochemical Cycles*, 7, 619–626, 1993.
- Broecker, W. S., and T.-H. Peng, Stratospheric contribution to the global bomb radiocarbon inventory: model versus observation, *Global Biogeochemical Cycles*, 8, 377–384, 1994.
- Broecker, W. S., and T.-H. Peng, Comparison of ^{39}Ar and ^{14}C ages for waters in the deep ocean, *Nuclear Instruments and Methods in Physics Research Section B*, 172, 473–478, 2000.
- Broecker, W. S., R. D. Gerard, M. Ewing, and B. C. Heezen, Geochemistry and physics of ocean circulation, in *Oceanography*, edited by M. Sears, pp. 301–322, AAAS, Washington, 1961, publication 67.
- Broecker, W. S., T. Takahashi, H. J. Simpson, and T.-H. Peng, Fate of fossil fuel carbon dioxide and the global carbon budget, *Science*, 206, 409–418, 1979.
- Broecker, W. S., T.-H. Peng, G. Ostlund, and M. Stuiver, The distribution of bomb radiocarbon in the ocean, *Journal of Geophysical Research*, 90, 6953–6970, 1985.
- Broecker, W. S., A. Virgilio, and T.-H. Peng, Radiocarbon age of waters in the deep Atlantic revisited, *Geophysical Research Letters*, 18, 1–3, 1991.
- Broecker, W. S., S. Sutherland, W. Smethie, T.-H. Peng, and G. Ostlund, Oceanic radiocarbon: Separation of the natural and bomb components, *Global Biogeochemical Cycles*, 9, 263–288, 1995.
- Broecker, W. S., S. Sutherland, and T. Peng, A possible 20th-century slowdown of Southern Ocean deep water formation, *Science*, 286, 1132–1135, 1999.

- Bryan, F., Parameter sensitivity of primitive equation OGCMs, *Journal of Physical Oceanography*, *17*, 970–985, 1987.
- Burchard, H., and H. Rennau, Comparative quantification of physically and numerically induced mixing in ocean models, *Ocean Modelling*, *20*, 293–311, 2008.
- Butzin, M., M. Prange, and G. Lohmann, Radiocarbon simulations for the glacial ocean: The effects of wind stress, Southern Ocean sea ice and Heinrich events, *Earth and Planetary Science Letters*, *235*, 45–61, 2005.
- Campin, J.-M., Modélisation tridimensionnelle de la circulation générale océanique lors du dernier maximum glaciaire, Ph.D. thesis, Université Catholique de Louvain, Louvain-la-Neuve, Belgium, 1997, 342pp.
- Campin, J.-M., and H. Goosse, Parameterization of density-driven downsloping flow for a coarse-resolution ocean model in z-coordinate, *Tellus*, *51*, 412–430, 1999.
- Campin, J.-M., T. Fichefet, and J.-C. Duplessy, Problems with using radiocarbon to infer ocean ventilation rates for past and present climates, *Earth and Planetary Science Letters*, *165*, 17–24, 1999.
- Cao, L., et al., The role of ocean transport in the uptake of anthropogenic CO₂, *Biogeosciences*, *6*, 375–390, 2009.
- Chen, C.-T. A., The oceanic anthropogenic CO₂ sink, *Chemosphere*, *27*, 1041–1064, 1993.
- CILF (Ed.), *Dictionnaire de l'océan*, Conseil international de la langue française, Paris, 1989, 761p.
- Conkright, M., S. Levitus, and T. Boyer, World Ocean atlas 1994. Volume 1: nutrients, *Tech. Rep. 1*, NODC, 1994.
- Craig, H., The natural distribution of radiocarbon and the exchange time of carbon dioxide between atmosphere and sea, *Tellus*, *9*, 1–17, 1957.
- Craig, H., Abyssal carbon and radiocarbon in the Pacific, *Journal of Geophysical Research*, *74*, 5491–5506, 1969.
- Craig, H., The deep metabolism: oxygen consumption in abyssal ocean water, *Journal of Geophysical Research*, *76*, 5078–5086, 1971.
- Darras, J., *Le Petit Affluent de la Maye*, Le Cri, Bruxelles, 1993.

- Deleersnijder, E., and J.-M. Campin, On the computation of the barotropic mode of a free-surface world ocean model, *Annales Geophysicae*, *13*, 675–688, 1995.
- Deleersnijder, E., J.-M. Campin, and E. Delhez, The concept of age in marine modelling. I. Theory and preliminary model results, *Journal of Marine Systems*, *28*, 229–267, 2001.
- Deleersnijder, E., A. Mouchet, E. Delhez, and J.-M. Beckers, Transient behaviour of water ages in the world ocean, *Mathematical and Computer Modelling*, *36*, 121–127, 2002.
- Delhez, E., and E. Deleersnijder, The concept of age in marine modelling: II. Concentration distribution function in the English Channel and the North Sea, *Journal of Marine Systems*, *31*, 279–297, 2002.
- Delhez, E., J.-M. Campin, A. C. Hirst, and E. Deleersnijder, Toward a general theory of the age in ocean modelling, *Ocean Modelling*, *1*, 17–27, 1999.
- Delhez, E., E. Deleersnijder, A. Mouchet, and J.-M. Beckers, A note on the age of radioactive tracers, *Journal of Marine Systems*, *38*, 277–286, 2003.
- Denman, K., et al., Couplings between changes in the climate system and biogeochemistry, in *Solomon et al.* (2007), chap. 7.
- Dickson, A., and C. Goyet (Eds.), *Handbook of methods for the analysis of the various parameters of the carbon dioxide system in sea water. Version 2*, Department of energy, Washington, 1994, oRNL/CDIAC-74.
- Dickson, A. G., An exact definition of total alkalinity and a procedure for the estimation of alkalinity and total inorganic carbon from titration data, *Deep-Sea Research*, *28A*, 609–623, 1981.
- Dickson, A. G., Thermodynamics of the dissociation of borid acid in synthetic seawater from 273.15 to 318.15 K, *Deep-Sea Research*, *37*, 755–766, 1990.
- Dickson, A. G., and F. Millero, A comparison of the equilibrium constants for the dissociation of carbonic acid in seawater media, *Deep-Sea Research*, *34*, 1733–1743, 1987.
- Dickson, A. G., and J. P. Riley, The estimation of acid dissociation constants in seawater media from potentiometric titrations with strong base. I. The ionic product of water - K_W , *Marine Chemistry*, *7*, 89–99, 1979.
- Doney, S. C., et al., Evaluating global ocean carbon models: The importance of realistic physics, *Global Biogeochemical Cycles*, *18*, GB3017, 2004.

- Duffy, P. B., and K. Caldeira, Three-dimensional model calculation of ocean uptake of bomb ^{14}C and implications for the global budget of bomb ^{14}C , *Global Biogeochemical Cycles*, *9*, 373–375, 1995.
- Duffy, P. B., K. Caldeira, J. Selvaggi, and M. I. Hoffert, Effect of subgrid-scale mixing parameterizations on simulated distributions of natural ^{14}C , temperature, and salinity in a three-dimensional ocean general circulation model, *Journal of Physical Oceanography*, *27*, 498–523, 1997.
- Dugdale, R. C., and F. P. Wilkerson, Silicate regulation of new production in the equatorial Pacific upwelling, *Nature*, *391*, 270–273, 1998.
- Duplessy, J.-C., CO_2 air-sea exchange during glacial times: importance of deep sea circulation changes, in *The role of air-sea exchange in geochemical cycling*, edited by P. Buat-Ménard, vol. C185 of *NATO ASI Series*, pp. 249–267, D. Reidel Publishing Company, Dordrecht, Holland, 1986.
- Dutay, J.-C., et al., Evaluation of ocean model ventilation with CFC-11: comparison of 13 global ocean models, *Ocean Modelling*, *4*, 89–120, 2002.
- Dutay, J.-C., et al., Evaluation of OCMIP-2 ocean models' deep circulation with mantle helium-3, *Journal of Marine Systems*, *48*, 15–36, 2004.
- Engge, J. K., and D. L. Aksnes, Silicate as regulating nutrient in phytoplankton competition, *Marine Ecology Progress Series*, *83*, 281–289, 1992.
- England, M. H., The age of water and ventilation timescales in a global ocean model, *Journal of Physical Oceanography*, *25*, 2756–2777, 1995.
- England, M. H., and E. Maier-Reimer, Using chemical tracers to assess ocean models, *Reviews of Geophysics*, *39*, 29–70, 2001.
- England, M. H., and S. Rahmstorf, Sensitivity of ventilation rates and radiocarbon uptake to subgrid-scale mixing in ocean models, *Journal of Physical Oceanography*, *29*, 2802–2827, 1999.
- Enting, I. G., T. M. L. Wigley, and M. Heimann, Future emissions and concentrations of carbon dioxide : Key Ocean/Atmosphere/Land Analyses, *Tech. Rep. 31*, CSIRO, 1994.
- Falkowski, P. G., R. T. Barber, and V. Smetacek, Biogeochemical controls and feedbacks on ocean primary production, *Science*, *281*, 200–206, 1998.
- Fasham, M. J., Modelling the marine biota, in *The Global Carbon Cycle*, edited by M. Heimann, vol. I15 of *NATO ASI Series*, pp. 457–504, Springer Verlag, Berlin Heidelberg, 1993.

- Fichefet, T., E. Driesschaert, H. Goosse, P. Huybrechts, I. Janssens, A. Mouchet, and G. Munhoven, Modelling the evolution of climate and sea level over the third millennium (MILMO), *Scientific project final report*, BELSPO, Bruxelles, Belgium, 2007.
- Frakes, L. A., *Climates throughout geologic times*, Elsevier, Amsterdam, 1979.
- Francey, R. J., C. Allison, D. Etheridge, C. M. Trudinger, I. G. Enting, M. Leuenberger, R. L. Langenfelds, E. Michel, and L. P. Steele, A 1000 year high precision record of $\delta^{13}C$ in atmospheric CO_2 , *Tellus*, *51B*, 170–193, 1999.
- Friedlingstein, P., et al., Climatecarbon cycle feedback analysis: Results from the C4MIP model intercomparison, *Journal of Climate*, *19*, 3337–3353, 2006.
- Fujii, M., and F. Chai, Effects of biogenic silica dissolution on silicon cycling and export production, *Geophysical Research Letters*, *32*, L05,617, 2005.
- Gent, P., and J. McWilliams, Isopycnal mixing in ocean circulation models, *Journal of Physical Oceanography*, *20*, 150–155, 1990.
- Gérard, J.-C., C. Delire, L. François, Y. Goddérès, D. Hauglustaine, A. Mouchet, G. Munhoven, B. Nemry, and P. Warnant, Global modelling of the coupled chemical-climatic changes due to human activities, *Scientific project final report*, BELSPO, Bruxelles, Belgium, 1996.
- Gnanadesikan, A., A global model of silicon cycling: sensitivity to eddy parameterization and dissolution, *Global Biogeochemical Cycles*, *13*, 199–220, 1999.
- Gnanadesikan, A., R. D. Slater, N. Gruber, and J. Sarmiento, Oceanic vertical exchange and new production: a comparison between models and observations, *Deep-Sea Research*, *49*, 363–401, 2001.
- Godwin, H., Half-life of radiocarbon, *Nature*, *195*, 984, 1962.
- Goosse, H., et al., Description of the earth system model of intermediate complexity loveclim version 1.2, *Geoscientific Model Development*, *3*, 603–633, 2010.
- Gruber, N., et al., Oceanic sources, sinks, and transport of atmospheric CO_2 , *Global Biogeochemical Cycles*, *23*, GB1005, 2009.
- Hall, T., T. Haine, and D. Waugh, Inferring the concentration of anthropogenic carbon in the ocean from tracers, *Global Biogeochemical Cycles*, *16*, 1131–273, 2002.

- Hall, T. M., and T. W. N. Haine, On ocean transport diagnostics: The idealized age tracer and the age spectrum, *Journal of Physical Oceanography*, *32*, 1987–1991, 2002.
- Hall, T. M., D. W. Waugh, T. W. N. Haine, P. E. Robbins, and S. Khatiwala, Estimates of anthropogenic carbon in the Indian Ocean with allowance for mixing and time-varying air-sea CO₂ disequilibrium, *Global Biogeochemical Cycles*, *18*, GB1031, 2004.
- Hedges, J. I., and R. G. Keil, Sedimentary organic matter preservation: an assessment and speculative synthesis, *Marine Chemistry*, *49*, 81–115, 1995.
- Hegerl, G., F. W. Zwiers, P. Braconnot, Gillett, Y. Luo, J. Marengo Orsini, N. Nicholls, J. Penner, and P. Stott, Understanding and attributing climate change, in *Solomon et al.* (2007), chap. 9.
- Heimann, M., and E. Maier-Reimer, On the relations between the oceanic uptake of CO₂ and its carbon isotopes, *Global Biogeochemical Cycles*, *10*, 89–110, 1996.
- Heinze, C., and N. Dittert, Impact of paleocirculations on the silicon redistribution in the world ocean, *Marine Geology*, *214*, 201–213, 2005.
- Heinze, C., E. Maier-Reimer, and K. Winn, Glacial pCO₂ reduction by the world ocean: experiments with the Hamburg carbon cycle model, *Palaeoceanography*, *6*, 395–430, 1991.
- Heinze, C., A. Hupe, E. Maier-Reimer, N. Dittert, and O. Ragueneau, Sensitivity of the marine biospheric Si cycle for biogeochemical parameter variations, *Global Biogeochemical Cycles*, *17*, 1086, 2003.
- Hesshaimer, V., M. Heimann, and I. Levin, Radiocarbon evidence for a smaller oceanic carbon dioxide sink than previously believed, *Nature*, *370*, 201–203, 1994.
- Hinga, K. R., M. A. Arthur, M. E. Q. Pilson, and D. Whitaker, Carbon isotope fractionation by marine phytoplankton in culture: the effects of CO₂ concentration, pH, temperature, and species, *Global Biogeochemical Cycles*, *8*, 91–102, 1994.
- Hoefs, J., *Stable isotope geochemistry*, fourth ed., Springer, Berlin, 1997, 201p.
- Holzer, M., and F. W. Primeau, The diffusive ocean conveyor, *Geophysical Research Letters*, *33*, L14,618, 2006.

- Houghton, J. T., L. Meira Filho, B. A. Callander, N. Harris, A. Kattenberg, and K. Maskell (Eds.), *Climate Change 1995. The science of climate change*, Cambridge University Press, U.S.A., 1996.
- Jacques, G., and P. Tréguer, *Ecosystèmes pélagiques marins*, vol. 19 of *Collection d'écologie*, Masson, Paris, 1986, 243p.
- Jahnke, R. A., The global ocean flux of particulate organic carbon: areal distribution and magnitude, *Global Biogeochemical Cycles*, 10, 71–88, 1996.
- Jain, A. K., H. S. Kheshgi, M. I. Hoffert, and D. J. Wuebbles, Distribution of radiocarbon as a test of global carbon cycle models, *Global Biogeochemical Cycles*, 9, 153–166, 1995.
- Jansen, E., et al., Palaeoclimate, in *Solomon et al.* (2007), chap. 6.
- Jasper, J. P., J. M. Hayes, A. C. Mix, and F. G. Prahl, Photosynthetic fractionation of ^{13}C and concentrations of dissolved CO_2 in the central equatorial Pacific during the last 255,000 years, *Palaeoceanography*, 9, 781–798, 1994.
- Jenkins, W. J., ^3H and ^3He in the Beta Triangle: observations of gyre ventilation and oxygen utilisation rates, *Journal of Physical Oceanography*, 17, 763–783, 1987.
- Jenkins, W. J., and J. C. Goldman, Seasonal oxygen cycling and primary production in the Sargasso Sea, *Journal of Marine Research*, 43, 465–491, 1985.
- Joos, F., Imbalance in the budget, *Nature*, 370, 181–182, 1994.
- Joos, F., and M. Bruno, Long-term variability of the terrestrial and oceanic carbon sinks and the budgets of carbon isotopes ^{13}C and ^{14}C , *Global Biogeochemical Cycles*, 12, 277–295, 1998.
- Joos, F., J. C. Orr, and U. Siegenthaler, Ocean carbon transport in a box-diffusion versus a general circulation model, *Journal of Geophysical Research*, 102, 12,367–12,388, 1997.
- Jouzel, J., et al., Orbital and millennial antarctic climate variability over the past 800,000 years, *Science*, 317, 793e796, 2007.
- Karstensen, J., and M. Tomczak, Age determination of mixed water masses using CFC and oxygen data, *Journal of Geophysical Research*, 103, 18,599–18,610, 1998.
- Keeling, C. D., Standardization of notations and procedures. 3.3 The modelling of rare isotopic carbon with regards to notation, in *Carbon Cycle Modelling*, edited by B. Bolin, pp. 89–101, John Wiley & Sons, New York, 1981.

- Keeling, R. F., S. Piper, A. Bollenbacher, and S. Walker, Monthly atmospheric $^{13}\text{C}/^{12}\text{C}$ isotopic ratios, in *Trends: A compendium of data on global change*, Carbon Dioxide Information Analysis Center, Oak Ridge National Laboratory, U.S. Department of Energy, Oak Ridge, Tenn., U.S.A., 2010.
- Key, R. M., Changes in the Pacific Ocean distribution of radiocarbon, Princeton University, <http://geoweb.princeton.edu/people/key/woce/C14.Changes/key.html>, 2004.
- Key, R. M., et al., A global ocean carbon climatology: Results from GLODAP, *Global Biogeochemical Cycles*, 18, GB4031, 2004.
- Khatiwala, S., M. Visbeck, and P. Schlosser, Age tracers in an ocean GCM, *Deep-Sea Research*, 48, 1423–1441, 2001.
- Kiehl, J. T., and K. E. Trenberth, Earth's annual global mean energy budget, *Bulletin of the American Meteorological Society*, 78, 197–208, 1997.
- Kitagawa, H., and J. van der Plicht, Atmospheric radiocarbon calibration to 45000 yr B.P.: Late glacial fluctuations and cosmogenic isotope production, *Science*, 279, 1187–1190, 1998.
- Klinck, J. M., and D. A. Smith, Association of sinking organic matter with various types of mineral ballast in the deep sea: Implications for the rain ratio, *Global Biogeochemical Cycles*, 16, 1116, 2002.
- Kohfeld, K. E., C. Le Quor, S. P. Harrison, and R. F. Anderson, Role of marine biology in glacial-interglacial CO_2 cycles, *Science*, 308, 74–78, 2005.
- Krakauer, N. Y., J. T. Randerson, F. W. Primeau, N. Gruber, and D. Menemenlis, Carbon isotope evidence for the latitudinal distribution and wind speed dependence of the air-sea gas transfer velocity, *Tellus*, 58, 390–417, 2006.
- Kuhlbrodt, T., A. Griesel, M. Montoya, A. Levermann, M. Hofmann, and S. Rahmstorf, On the driving processes of the Atlantic meridional overturning circulation, *Reviews of Geophysics*, 45, RG2001, 2007.
- Kulp, J., L. Tryon, W. Eckelman, and W. Snell, Lamont natural radiocarbon measurements, II, *Science*, 116, 409–414, 1952.
- Kunze, E., E. Firing, J. M. Hummon, T. K. Chereskin, and A. M. Thurnherr, Global abyssal mixing inferred from lowered ADCP shear and CTD strain profiles, *Journal of Physical Oceanography*, 36, 1553–1576 (Corrigendum pp 2350–2352), 2006.

- Lal, D., and H. E. Suess, The radioactivity of the atmosphere and hydrosphere, *Annual Review of Nuclear Science*, 18, 407–434, 1968.
- Laws, E. A., P. G. Falkowski, W. O. Smith Jr., H. Ducklow, and J. J. McCarthy, Temperature effects on export production in the open ocean, *Global Biogeochemical Cycles*, 14, 1231–1246, 2000.
- Leboucher, V., J. Orr, P. Jean-Baptiste, M. Arnold, P. Monfray, N. Tisnerat-Laborde, A. Poisson, and J.-C. Duplessy, New accelerator mass spectrometry radiocarbon measurements on WOCE I6 section between Antarctica and South Africa, *Radiocarbon*, 41, 51–73, 1999.
- Ledwell, J. R., A. J. Watson, and C. S. Law, Evidence for slow mixing across the pycnocline from an open-ocean tracer-release experiment, *Nature*, 364, 701–703, 1993.
- Louanchi, F., and R. G. Najjar, A global monthly climatology of phosphate, nitrate, and silicate in the upper ocean: Spring-summer export production and shallow remineralization, *Global Biogeochemical Cycles*, 14, 957–978, 2000.
- Mahadevan, A., An analysis of surface trends of bomb radiocarbon in the Pacific, *Marine Chemistry*, 73, 273–290, 2001.
- Maier-Reimer, E., Geochemical cycles in an ocean general circulation model. Preindustrial tracer distributions, *Global Biogeochemical Cycles*, 7, 645–677, 1993.
- Maier-Reimer, E., and K. Hasselmann, Transport & storage of CO₂ in the ocean - an inorganic ocean-circulation carbon cycle model, *Climate Dynamics*, 2, 63–90, 1987.
- Maier-Reimer, E., U. Mikolajewicz, and K. Hasselmann, Mean circulation of the Hamburg LSG OGCM and its sensitivity to the thermohaline surface forcing, *Journal of Physical Oceanography*, 23, 731–757, 1993.
- Maier-Reimer, E., U. Mikolajewicz, and A. Winguth, Future ocean uptake of CO₂: interaction between ocean circulation and biology, *Climate Dynamics*, 12, 711–721, 1995.
- Marotzke, J., Influence of convective adjustment on the stability of the thermohaline circulation, *Journal of Physical Oceanography*, 21, 903–907, 1991.
- Martin, J. H., G. A. Knauer, D. M. Karl, and W. W. Broenkow, VERTEX: carbon cycling in the northeast Pacific, *Deep-Sea Research*, 34, 267–285, 1987.

- Maslin, M., D. Seidov, and J. Lowe, Synthesis of the nature and causes of rapid climate transitions during the quaternary, in *The oceans and rapid climate change: Past, present, and future*, vol. 126 of *Geophysical Monographs*, p. 952, AGU, Washington DC, 2001.
- Maslin, M. A., M. A. Hall, N. J. Shackleton, and E. Thomas, Calculating surface water pCO₂ from foraminiferal organic $\delta^{13}\text{C}$, *Geochimica et Cosmochimica Acta*, *60*, 5089–5100, 1996.
- Matsumoto, K., Radiocarbon-based circulation age of the world oceans, *Journal of Geophysical Research*, *112*, C09,004, 2007.
- Matsumoto, K., and N. Gruber, How accurate is the estimation of anthropogenic carbon in the ocean? An evaluation of the ΔC^* method, *Global Biogeochemical Cycles*, *19*, GB3014, 2005.
- Matsumoto, K., et al., Evaluation of ocean carbon cycle models with data-based metrics, *Geophysical Research Letters*, *31*, L07,303, 2004.
- McManus, J., R. Francois, J. Gherardi, L. Keigwin, and S. Brown-Leger, Collapse and rapid resumption of atlantic meridional circulation linked to deglacial climate changes, *Nature*, *428*, 834e837, 2004.
- Menviel, L., Climate-carbon cycle interactions on millennial to glacial timescales as simulated by a model of intermediate complexity, Ph.D. thesis, University of Hawaii, Mauna Loa, Hawaii, U.S., 2008.
- Menviel, L., A. Timmermann, A. Mouchet, and O. Timm, Meridional reorganizations of tropical marine and terrestrial productivity during heinrich events, *Palaeoceanography*, *23*, PA1203, 2008a.
- Menviel, L., A. Timmermann, A. Mouchet, and O. Timm, Climate and marine carbon cycle response to changes in the strength of the southern hemispheric westerlies, *Palaeoceanography*, *23*, PA4201, 2008b.
- Menviel, L., A. Timmermann, A. Mouchet, and O. Timm, Climate and biogeochemical response to a rapid melting of the West Antarctic Ice Sheet during interglacials and implications for future climate, *Palaeoceanography*, *25*, PA4231, 2010.
- Menviel, L., A. Timmermann, O. Timm, and A. Mouchet, Deconstructing the last glacial termination: the role of millennial and orbital-scale forcings, *Quaternary Science Reviews*, *30*, 1155–1172, 2011a.

- Menziel, L., A. Timmermann, O. Timm, A. Mouchet, A. Abe-Ouchi, M. O. Chikamoto, N. Harada, R. Ohgaito, and Y. Okazaki, Removing the north pacific halocline: effects on global climate, ocean circulation and the carbon cycle, *Deep-Sea Research, II*, in press, 2011b.
- Mikolajewicz, U., E. Maier-Reimer, T. J. Crowley, and K. Kim, Effect of Drake and Panamanian Gateways on the circulation of an ocean model, *Palaeoceanography*, *8*, 4, 1993.
- Mikolajewicz, U., T. J. Crowley, A. Schiller, and R. Voss, Modeling North Atlantic/North Pacific teleconnections during the Younger Dryas, *Nature*, *387*, 384–387, 1997.
- Millero, F. J., Thermodynamics of the carbon dioxide system in the oceans, *Geochimica et Cosmochimica Acta*, *59*, 661–677, 1995.
- Mook, W. G., J. C. Bommerson, and W. H. Staverman, Carbon isotope fractionation between dissolved bicarbonate and gaseous carbon dioxide, *Earth and Planetary Science Letters*, *22*, 169–176, 1974.
- Mouchet, A., and E. Deleersnijder, The leaky funnel model, a metaphor of the ventilation of the World Ocean as simulated in an OGCM, *Tellus*, *60A*, 761–774, 2008.
- Mouchet, A., and L. François, Sensitivity of a global ocean carbon cycle model to the circulation and to the fate of organic matter: preliminary results, *Physics and Chemistry of the Earth*, *21*, 511–516, 1996.
- Mouchet, A., E. Deleersnijder, and F. Primeau, The leaky funnel model revisited, *Tellus*, 2011, submitted.
- Mucci, A., The solubility of calcite and aragonite in seawater at various salinities, temperatures, and one atmosphere total pressure, *American Journal of Science*, *283*, 780–799, 1983.
- Müller, S. A., F. Joos, N. R. Edwards, and T. F. Stocker, Water mass distribution and ventilation time scales in a cost-efficient, three-dimensional ocean model, *Journal of Climate*, *19/21*, 5479–5499, 2006.
- Müller, S. A., F. Joos, G.-K. Plattner, N. R. Edwards, and T. F. Stocker, Modeled natural and excess radiocarbon: Sensitivities to the gas exchange formulation and ocean transport strength, *Global Biogeochemical Cycles*, *22*, GB3011, 2008.
- Munhoven, G., Modelling glacial-interglacial atmospheric CO₂ variations : The role of continental weathering, Ph.D. thesis, Université de Liège, Liège, 1997.

- Munhoven, G., Glacial–interglacial rain ratio changes: Implications for atmospheric CO₂ and oceansediment interaction., *Deep-Sea Research*, *54*, 722–746, 2007.
- Munk, W., Abyssal recipes, *Deep-Sea Research*, *13*, 707–730, 1966.
- Munk, W., and C. Wunsch, Abyssal recipes II: energetics of tidal and wind mixing, *Deep-Sea Research*, *45*, 1977–2010, 1998.
- Naegler, T., Reconciliation of excess ¹⁴C-constrained global CO₂ piston velocity estimates, *Tellus*, *61*, 372–384, 2009.
- Najjar, R. G., J. L. Sarmiento, and J. R. Toggweiler, Downward transport and fate of organic matter in the ocean: simulations with a general circulation model, *Global Biogeochemical Cycles*, *6*, 45–76, 1992.
- Najjar, R. G., et al., Impact of circulation on export production, dissolved organic matter, and dissolved oxygen in the ocean: Results from Phase II of the Ocean Carbon-cycle Model Intercomparison Project (OCMIP-2), *Global Biogeochemical Cycles*, *21*, GB3007, 2007.
- Nelson, D. M., P. Tréguer, M. A. Brzezinski, A. Leynaert, and B. Quéguiner, Production and dissolution of biogenic silica in the ocean: revised global estimates, comparison with regional data and relationship to biogenic sedimentation, *Global Biogeochemical Cycles*, *9*, 359–372, 1995.
- Niiler, P. P., The ocean circulation, in *Climate System Modeling*, edited by K. E. Trenberth, chap. 4, Cambridge University Press, U.S.A., 1992.
- Okazaki, Y., A. Timmermann, L. Menviel, N. Harada, A. Abe-Ouchi, M. Chikamoto, A. Mouchet, and H. Asahi, Deep water formation in the north pacific during the last glacial termination, *Science*, *329*, 200–204, 2010.
- Orr, J., R. Najjar, C. Sabine, and F. Joos, Abiotic-HOWTO. Ocean-Carbon Cycle Model Intercomparison Project (OCMIP), 2000.
- Orr, J. C., et al., Estimates of anthropogenic carbon uptake from four three-dimensional global ocean models, *Global Biogeochemical Cycles*, *15*, 2001.
- Oschlies, A., Equatorial nutrient trapping in biogeochemical ocean models: the role of advection numerics, *Global Biogeochemical Cycles*, *14*, 655–667, 2000.
- Pacanowski, R. C., and S. G. H. Philander, Parameterization of vertical mixing in numerical models of tropical oceans, *Journal of Physical Oceanography*, *11*, 1443–1451, 1981.

- Peacock, S., Debate over the ocean bomb radiocarbon sink: closing the gap, *Global Biogeochemical Cycles*, *18*, GB202,210, 2004.
- Peters, G. P., and E. G. Hertwich, CO₂ embodied in international trade with implications for global climate policy, *Environmental Science & Technology*, *42*, 1401–1407, 2008.
- Petit, J. R., et al., Climate and atmospheric history of the past 420000 years from the Vostok ice core, Antarctica, *Nature*, *399*, 429–436, 1999.
- Plattner, G.-K., et al., Long-term climate commitments projected with climate - carbon cycle models, *Journal of Climate*, *21*, 2721–2751, 2008.
- Polzin, K. L., J. M. Toole, J. R. Ledwell, and R. W. Schmitt, Spatial variability of turbulent mixing in the Abyssal Ocean, *Science*, *276*, 93–96, 1997.
- Prentice, I. C., et al., The carbon cycle and atmospheric carbon dioxide, in *Climate Change 2001. The scientific basis.*, edited by J. T. Houghton, Y. Ding, D. J. Griggs, M. Noguer, P. van der Linden, X. Dai, K. Maskell, and C. A. Johnson, chap. 3, Cambridge University Press, U.S.A., 2001.
- Prévert, J., *Fatras*, Gallimard, Paris, 1966, p. 146.
- Quay, P. D., B. Tilbrook, and C. S. Wong, Oceanic uptake of fossil fuel CO₂: carbon-13 evidence, *Science*, *256*, 74–79, 1992.
- Rahmstorf, S., Ocean circulation and climate during the past 120,000 years, *Nature*, *419*, 207–214, 2002.
- Raper, S. C. B., J. M. Gregory, and R. J. Stouffer, The role of climate sensitivity and ocean heat uptake on aogcm transient temperature response, *Journal of Climate*, *15*, 124–130, 2002.
- Rau, G. H., U. Riebesell, and D. Wolf-Gladrow, CO_{2aq}-dependent photosynthetic ¹³C fractionation in the ocean: a model versus measurements, *Global Biogeochemical Cycles*, *11*, 267–278, 1997.
- Redfield, A., B. Ketchum, and F. Richards, The influence of organisms on the composition of seawater, in *The Sea*, edited by M. N. Hill, vol. 2, pp. 26–77, Wiley Interscience, New York, 1963.
- Rixen, T., M. Guptha, and V. Ittekkot, Deep ocean fluxes and their link to surface ocean processes and the biological pump, *Progress in Oceanography*, *65*, 240–259, 2005.

- Roache, P., On artificial viscosity, *Journal of Computational Physics*, *10*, 169–184, 1972.
- Robinson, L. F., J. F. Adkins, L. D. Keigwin, J. Southon, D. P. Fernandez, S.-L. Wang, and D. S. Scheirer, Radiocarbon variability in the western North Atlantic during the last deglaciation, *Science*, *310*, 1469–1473, 2005.
- Rodgers, K. B., D. P. Schrag, M. A. Cane, and N. H. Naik, The bomb ^{14}C transient in the Pacific Ocean, *Journal of Geophysical Research*, *105*, 8489–8512, 2000.
- Rodhe, H., Modeling biogeochemical cycles, in *Global Biogeochemical Cycles*, edited by S. S. Butcher, R. J. Charlson, G. H. Orians, and G. V. Wolfe, chap. 4, Academic Press, London, 1992.
- Rubin, S. I., and R. M. Key, Separating natural and bomb-produced radiocarbon in the ocean: The potential alkalinity method, *Global Biogeochemical Cycles*, *16*, 1105, 2002.
- Sackett, W. M., A history of the $\delta^{13}\text{C}$ composition of oceanic plankton, *Marine Chemistry*, *34*, 153–156, 1991.
- Schlitzer, R., Carbon export fluxes in the Southern Ocean: results from inverse modeling and comparison with satellite based estimates, *Deep-Sea Research*, *49*, 1623–1644, 2002.
- Schmittner, A., and A. Weaver, Dependence of multiple climate states on ocean mixing parameters, *Geophysical Research Letters*, *28*, 1027–1030, 2001.
- Schmittner, A., N. M. Urban, K. Keller, and D. Matthews, Using tracer observations to reduce the uncertainty of ocean diapycnal mixing and climate carbon cycle projections, *Global Biogeochemical Cycles*, *23*, GB4009, 2009.
- Schmitz, M., Les conflits verts: aperçu général sur la menace de l’an 2000, in *Les conflits verts. La dégradation de l’environnement, source de tensions majeures*, pp. 63–89, GRIP - Institut de recherche et d’information sur la paix et la sécurité, Bruxelles, Belgium, 1992.
- Shackleton, N. J., and N. G. Pisias, Atmospheric carbon dioxide, orbital forcing, and climate, in *The Carbon cycle and atmospheric CO₂: natural variations Archean to present*, edited by E. Sundquist and W. Broecker, vol. 32 of *Geophysical Monograph*, pp. 412–417, AGU, Washington DC, 1985.
- Siedler, G., J. Church, and J. Gould (Eds.), Academic Press, San Diego, U.S.A., 2001.

- Siegenthaler, U., Carbon dioxide: its natural cycle and anthropogenic perturbation, in *The Role of Air-Sea Exchange in Geochemical Cycling*, edited by P. Buat-Ménard, vol. C185 of *NATO ASI Series*, pp. 209–247, D. Reidel Publishing Company, Dordrecht, Holland, 1986.
- Siegenthaler, U., and K. O. Münnich, $^{13}\text{C}/^{12}\text{C}$ fractionation during CO_2 transfer from air to sea, in *Carbon Cycle Modelling*, edited by B. Bolin, pp. 249–257, John Wiley & Sons, New York, 1981.
- Smith, H. J., H. Fischer, M. Wahlen, D. Mastroianni, and B. Deck, Dual modes of the carbon cycle since the last glacial maximum, *Nature*, *400*, 248–250, 1999.
- Solomon, S., D. Qin, M. Manning, Z. Chen, M. Marquis, K. Averyt, M. Tignor, and H. Miller (Eds.), *Climate Change 2007. The scientific basis.*, Cambridge University Press, Cambridge, UK, 2007.
- St. Laurent, L., and H. Simmons, Estimates of power consumed by mixing in the ocean interior, *Journal of Climate*, *19*, 4877–4890, 2006.
- Stocker, T. F., W. S. Broecker, and D. G. Wright, Carbon uptake experiments with a zonally-averaged global ocean circulation model, *Tellus*, *46B*, 103–122, 1994.
- Stommel, H., and A. Arons, On the abyssal circulation of the world ocean - I. Stationary planetary flow patterns on a sphere, *Deep-Sea Research*, *6*, 140–154, 1960a.
- Stommel, H., and A. Arons, On the abyssal circulation of the world ocean - II. An idealized model of the circulation pattern and amplitude in ocean basins, *Deep-Sea Research*, *6*, 217–233, 1960b.
- Stuiver, M., and T. F. Braziunas, Anthropogenic and solar component of hemispheric ^{14}C , *Geophysical Research Letters*, *25*, 329–332, 1998.
- Stuiver, M., and H. A. Polach, Reporting of ^{14}C data, *Radiocarbon*, *19*, 355–363, 1977.
- Stuiver, M., and P. D. Quay, Atmospheric ^{14}C changes resulting from fossil fuel CO_2 release and cosmic ray flux variability, *Earth and Planetary Science Letters*, *53*, 349–362, 1981.
- Stuiver, M., H. Östlund, and T. McConnaughey, GEOSECS Atlantic and Pacific ^{14}C distribution, in *Carbon Cycle Modelling*, edited by B. Bolin, pp. 201–221, John Wiley & Sons, New York, 1981.

- Stuiver, M., P. Quay, and H. G. Östlund, Abyssal water carbon-14 distribution and the age of the world oceans, *Science*, *219*, 849–851, 1983.
- Stuiver, M., et al., INTCAL98 radiocarbon age calibration, 24000–0 cal BP, *Radiocarbon*, *40*, 1041–1083, 1998.
- Stumm, W., and J. J. Morgan, *Aquatic chemistry. Chemical equilibria and rates in natural waters*, Wiley, New York, 1996, 1022p.
- Suess, E., Particulate organic carbon flux in the ocean – surface productivity and oxygen utilization, *Nature*, *288*, 260–263, 1980.
- Sundquist, E. T., L. Plummer, and T. Wigley, Carbon dioxide in the ocean surface: the homogeneous buffer factor, *Science*, *204*, 1203–1205, 1979.
- Supervielle, J., *La mer secrète*, Gallimard, Paris, 1938.
- Sweeney, C., E. Gloor, A. R. Jacobson, R. M. Key, G. McKinley, J. L. Sarmiento, and R. Wanninkhof, Constraining global air-sea gas exchange for CO₂ with recent bomb 14C measurements, *Global Biogeochemical Cycles*, *21*, GB2015, 2007.
- Sylvestre, A., *Le lac Saint-Sébastien*, EPM Musique, 2000.
- Takahashi, T., W. S. Broecker, and S. Langer, Redfield ratio based on chemical data from isopycnal surfaces, *Journal of Geophysical Research*, *90*, 6907–6924, 1985.
- Takahashi, T., et al., Global sea-air CO₂ flux based on climatological surface ocean pCO₂ and seasonal biological and temperature effects, *Deep-Sea Research*, *49*, 1601–1622, 2002.
- Takahashi, T., et al., Climatological mean and decadal changes in surface ocean pCO₂, and net sea-air CO₂ flux over the global oceans, *Deep-Sea Research*, *56*, 554–577, 2009.
- Takeoka, H., Fundamental concepts of exchange and transport time scales in a coastal sea, *Continental Shelf Research*, *3*, 311–326, 1984.
- Takeoka, H., Effects of the deep ocean circulation on the reservoir characteristics of the ocean, *Journal of the Oceanographical Society of Japan*, *47*, 27–32, 1991.
- Talley, L. D., Some aspects of ocean heat transport by the shallow, intermediate and deep overturning circulations, in *Mechanisms of Global Climate Change at Millennial Time Scales*, edited by P. U. Clark, R. S. Webb, and L. D. Keigwin, vol. 112 of *Geophys. Monogr. Ser.*, pp. 1–22, AGU, Washington, DC, 1999.

- Tans, P. P., A. F. De Jong, and W. G. Mook, Natural atmospheric ^{14}C variation and the Suess effect, *Nature*, *280*, 826–828, 1979.
- Tans, P. P., J. A. Berry, and R. F. Keeling, Oceanic $^{13}\text{C}/^{12}\text{C}$ observations: a new window on ocean CO_2 uptake, *Global Biogeochemical Cycles*, *7*, 353–368, 1993.
- Taylor, K. E., Summarizing multiple aspects of model performance in a single diagram, *Journal of Geophysical Research*, *106*, 7183–7192, 2001.
- Thiele, G., and J. Sarmiento, Tracer dating and ocean ventilation, *Journal of Geophysical Research*, *95*, 9377–9391, 1990.
- Thomas, H., and V. Ittekkot, Determination of anthropogenic CO_2 in the North Atlantic Ocean using water mass ages and CO_2 equilibrium chemistry, *Journal of Marine Systems*, *27*, 325–336, 2001.
- Toggweiler, J. R., and B. Samuels, New radiocarbon constraints on the upwelling of abyssal water to the ocean's surface, in *The Global Carbon Cycle*, edited by M. Heimann, vol. I15 of *NATO ASI Series*, pp. 333–366, Springer Verlag, Berlin Heidelberg, 1993.
- Toggweiler, J. R., K. Dixon, and K. Bryan, Simulations of radiocarbon in a coarse-resolution world ocean model. 1. Steady state prebomb distributions, *Journal of Geophysical Research*, *94*, 8217–8242, 1989a.
- Toggweiler, J. R., K. Dixon, and K. Bryan, Simulations of radiocarbon in a coarse-resolution world ocean model. 2. Distributions of bomb-produced carbon 14, *Journal of Geophysical Research*, *94*, 8243–8264, 1989b.
- Toole, J., and T. McDougall, Mixing and stirring in the ocean interior, in *Siedler et al.* (2001), chap. 5.2, pp. 337–356.
- Trenberth, K. E., J. G. Olson, and W. G. Large, A global ocean wind stress climatology based on ECMWF analyses, *Tech. Rep. NCAR/TN-338+STR*, National Center for Atmospheric Research, Boulder, Colorado, 1989.
- Tsunogai, S., and S. Noriki, Particulate fluxes of carbonate and organic carbon in the ocean. is the marine biological activity working as a sink of the atmospheric carbon?, *Tellus*, *43*, 256–266, 1991.
- Vogel, J. C., P. M. Grootes, and W. G. Mook, Isotopic fractionation between gaseous and dissolved carbon dioxide, *Zeitschrift für Physik*, *230*, 225–238, 1970.

- Volk, T., and M. I. Hoffert, Ocean carbon pumps: Analysis of relative strengths and efficiencies in ocean-driven atmospheric CO₂ changes, in *The carbon cycle and atmospheric CO₂: natural variations archean to present*, edited by E. T. Sundquist and W. S. Broecker, vol. 32 of *Geophysical Monograph*, pp. 99–110, AGU, Washington DC, 1985.
- Wanninkhof, R., Relationship between wind speed and gas exchange over the ocean, *Journal of Geophysical Research*, *97*, 7373–7382, 1992.
- Wanninkhof, R., and M. Knox, Chemical enhancement of CO₂ exchange in natural waters, *Limnology and Oceanography*, *41*, 689–697, 1996.
- Watson, A. J., and P. S. Liss, Marine biological controls on climate via the carbon and sulfur geochemical cycles, *Philosophical Transactions of the Royal Society of London*, *353*, 41–51, 1998.
- Waugh, D. W., T. M. Hall, and T. W. N. Haine, Relationships among tracer ages, *Journal of Geophysical Research*, *108*, 3138, 2003.
- Webb, D. J., and N. Suginohara, The interior circulation of the ocean, in *Siedler et al.* (2001), chap. 4.2, pp. 205–213.
- Weiss, R., Carbon dioxide in water and seawater: the solubility of a non-ideal gas, *Marine Chemistry*, *2*, 203–215, 1974.
- Winguth, A. M. E., D. Archer, J.-C. Duplessy, E. Maier-Reimer, and U. Mikolajewicz, Sensitivity of paleonutrient tracer distributions and deep-sea circulation to glacial boundary conditions, *Palaeoceanography*, *14*, 304–323, 1999.
- Wolf-Gladrow, D. A., R. E. Zeebe, C. Klaas, A. Krtzinger, and A. Dickson, Total alkalinity: The explicit conservative expression and its application to biogeochemical processes, *Marine Chemistry*, *106*, 287–300, 2007.
- Wollast, R., The silica problem, in *The Sea*, edited by E. D. Goldberg, vol. 5, pp. 359–392, Wiley Interscience, New York, 1974.
- Wyrtki, K., The oxygen minima in relation to ocean circulation, *Deep-Sea Research*, *9*, 11–23, 1962.
- Zhang, J., R. W. Schmitt, and R. X. Huang, The relative influence of diapycnal mixing and hydrologic forcing on the stability of the thermohaline circulation, *Journal of Physical Oceanography*, *29*, 1096–1108, 1999.

